



# University of HUDDERSFIELD

## University of Huddersfield Repository

Camara, Osmane

Ion irradiation of germanium foils and germanium nanowires

### Original Citation

Camara, Osmane (2019) Ion irradiation of germanium foils and germanium nanowires. Doctoral thesis, University of Huddersfield.

This version is available at <http://eprints.hud.ac.uk/id/eprint/35132/>

The University Repository is a digital collection of the research output of the University, available on Open Access. Copyright and Moral Rights for the items on this site are retained by the individual author and/or other copyright owners. Users may access full items free of charge; copies of full text items generally can be reproduced, displayed or performed and given to third parties in any format or medium for personal research or study, educational or not-for-profit purposes without prior permission or charge, provided:

- The authors, title and full bibliographic details is credited in any copy;
- A hyperlink and/or URL is included for the original metadata page; and
- The content is not changed in any way.

For more information, including our policy and submission procedure, please contact the Repository Team at: [E.mailbox@hud.ac.uk](mailto:E.mailbox@hud.ac.uk).

<http://eprints.hud.ac.uk/>

# **Ion irradiation of germanium foils and germanium nanowires**

OSMANE CAMARA

A thesis submitted to the University of Huddersfield in partial  
fulfilment of the requirements for the degree of Doctor of  
Philosophy

November 2019



## Copyright Statement

- i. The author of this thesis (including any appendices and/ or schedules to this thesis) owns any copyright in it (the “Copyright”) and s/he has given The University of Huddersfield the right to use such Copyright for any administrative, promotional, educational and/or teaching purposes.
  
- ii. Copies of this thesis, either in full or in extracts, may be made only in accordance with the regulations of the University Library. Details of these regulations may be obtained from the Librarian. Details of these regulations may be obtained from the Librarian. This page must form part of any such copies made.
  
- iii. The ownership of any patents, designs, trademarks and any and all other intellectual property rights except for the Copyright (the “Intellectual Property Rights”) and any reproductions of copyright works, for example graphs and tables (“Reproductions”), which may be described in this thesis, may not be owned by the author and may be owned by third parties. Such Intellectual Property Rights and Reproductions cannot and must not be made available for use without permission of the owner(s) of the relevant Intellectual Property Rights and/or Reproductions.

## Contents

Copyright Statement.....	3
Declaration.....	8
Acknowledgements.....	8
Published and under review articles.....	10
List of figures.....	12
List of tables.....	28
List of abbreviations.....	30
Abstract.....	33
Chapter 1: Introduction.....	36
1. Motivation for this work.....	36
2. Structure of the thesis.....	40
Chapter 2: Background & Literature Review.....	42
1. Introduction.....	42
2. Germanium and its properties.....	43
2.1. Context.....	43
2.2. General properties of germanium.....	44
2.3. Properties as a semiconductor.....	45
2.3.1. Valence band and conduction band.....	45
2.3.2. Empty or full: occupation of the band.....	47
2.3.3. Doping germanium.....	50
3. Ion implantation.....	53
3.1. Outline of ion implantation.....	53
3.2. Electronic stopping.....	53
3.3. Nuclear stopping.....	54
3.4. Range.....	56
3.5. Channelling.....	58
3.6. MONTE CARLO SIMULATIONS: SRIM.....	58
4. Defects.....	59
4.1. Overview.....	59
4.2. Vacancies.....	60
4.3. Interstitials.....	61
4.4. Defects at thermal equilibrium.....	62
4.5. Diffusion.....	63

4.6.	Interaction of Vacancies with dopants in germanium .....	65
4.7.	Clusters of defects.....	69
4.8.	Displacement spike and thermal spike .....	70
4.9.	Dangling bonds.....	72
5.	Amorphisation .....	73
5.1.	Properties of amorphous material.....	73
5.2.	Amorphisation models.....	77
5.2.1.	Critical density model .....	77
5.2.2.	Heterogeneous model .....	81
5.2.3.	Intermediate models.....	85
6.	Recrystallisation .....	86
6.1.	Thermal recrystallisation .....	86
6.2.	Preventing amorphisation via irradiation at elevated temperatures.....	88
6.3.	Annealing effects of electron beams .....	89
7.	Nanowires .....	91
7.1.	Top-down / bottom-up .....	91
7.2.	Nanowire applications .....	92
7.3.	Ion irradiation of nanowires .....	93
7.4.	Ion induced bending (IIB).....	95
7.4.1.	Context.....	95
7.4.2.	Typical characteristic of shape modification induced by IIB.....	97
7.4.3.	Thermal Gradients .....	98
7.4.4.	Surface rearrangement .....	99
7.4.5.	Distribution of self-interstitials and vacancies.....	102
7.4.6.	Amorphisation based mechanism .....	106
Chapter 3: Experimental method .....		110
1.	TEM .....	110
1.1.	History.....	110
1.2.	Magnification .....	111
1.3.	Structure of the microscope .....	112
1.3.1.	Emission of electrons .....	112
1.3.2.	Lens system.....	117
1.3.3.	Vacuum system.....	121
1.3.4.	Sample Chamber.....	123
1.3.5.	Type of sample holders .....	124
1.3.6.	Eucentric height .....	126

1.3.7.	Viewing system .....	129
1.4.	Image formation .....	131
1.4.1.	Ensemble view .....	131
1.4.2.	From the Electron Gun to the sample.....	133
1.4.3.	Sample and objective lens .....	135
1.4.4.	Bragg angle.....	137
1.4.5.	Reciprocal space and Ewald Sphere.....	140
1.4.6.	Diffraction patterns.....	142
1.4.7.	Kikuchi line .....	144
1.4.8.	Bright Field and Dark Field .....	147
1.4.9.	Amplitude and mass-thickness contrast .....	150
1.4.10.	Phase contrast.....	152
1.5.	EELS and EFTEM .....	154
1.5.1.	Basic idea .....	154
1.5.2.	Typical EELS spectra .....	154
2.	Sample Preparation .....	157
2.1.	Nanowires .....	157
2.2.	Bulk Germanium .....	159
3.	SRIM calculation tools.....	160
4.	MIAMI-1 and -2 .....	165
4.1.	Overview .....	165
4.2.	Creation of ions .....	165
4.3.	Mass selection.....	166
4.4.	Accelerations of ions .....	166
4.5.	Targeting with ions .....	166
4.6.	Monitoring the ion beam .....	167
4.7.	MIAMI-1 .....	167
4.8.	MIAMI-2 .....	170
5.	Angle between freely hanging nanowires and the ion beam .....	172
5.1.	Reasons for the calculation.....	172
5.2.	Calculation of $i$ .....	173
5.3.	Calculation of the angle between the ion beam and the nanowires.....	176
Chapter 4: Ion induced bending of nanowires at elevated temperatures.....		180
1.	Motivation for irradiation at elevated temperatures .....	180
2.	Design of the experiment .....	183
3.	Results and discussion .....	184

3.1.	Bending of germanium nanowires towards the ion beam at 400°C.....	184
3.2.	IIB mechanisms .....	189
4.	Conclusion, remarks and perspectives .....	200
Chapter 5: Ion induced bending of nanowires at RT and subsequent annealing .....		205
1.	Context.....	205
2.	Method .....	207
3.	Results and discussion .....	208
3.1.	Irradiation of germanium nanowires at RT.....	208
3.1.1.	Results.....	208
3.1.2.	Case of nanowires bending towards the ion beam whilst $\Omega < 0.5$ .....	213
3.1.3.	Competition of mechanisms .....	217
3.2.	Annealing of nanowires bent via IIB .....	225
3.2.1.	Annealing of fully amorphous nanowires .....	225
3.2.2.	Annealing of partially amorphous nanowires.....	226
3.2.3.	Annealing of the partially amorphous nanowires which bent away from the ion beam 227	
3.2.4.	Annealing of the partially amorphous nanowires which bent towards the ion beam	228
4.	Conclusion, remarks and perspectives .....	232
Chapter 6: Amorphisation mechanisms in germanium.....		237
1.	Introduction .....	237
2.	Experimental methods.....	242
3.	Results.....	245
4.	DISCUSSION.....	254
4.1.	Mechanism for amorphisation according to the SADP .....	254
4.2.	Influence of the distribution of defects on the dpa threshold for amorphisation .....	255
4.3.	Influence on the stochastic nature of the collision cascade induce by helium ions on the dpa threshold for amorphisation.....	261
5.	Conclusion and remarks.....	262
Chapter 7: Conclusion.....		264
1.	Ion induced bending of nanowires at elevated temperatures .....	264
2.	1. Ion induced bending of nanowires at RT and subsequent annealing.....	265
3.	Amorphisation .....	266
References .....		269
Appendix.....		299

## Declaration

I, Osmane Camara, certify that this thesis is my own work and I have not obtained a degree in this University, or elsewhere, on the basis of this thesis.

## Acknowledgements

I would like to express gratitude to my supervisors Doctor Jonathan Hinks, Professor Stephen Donnelly and Doctor Graeme Greaves for letting me join the EMMA group and having this opportunity to work in such a dynamic environment.

Upon my arrival in the group, I was pleased to see how friendly, reachable and reliable all the researchers were. Thanks to this, I could literally bombard you with questions at a flux higher than any ion accelerators (no, I am not exaggerating... not even a bit). I have to thank my supervisors as well as the postdocs: Doctor Robert Harrison, Doctor Anamul Mir, Doctor Emily Aradi and Doctor Houari Amari, for all the knowledge I have gained through our discussions and debates.

When I arrived here, I did not know much about transmission electron microscopes and ion beam accelerators; to me these machines were impressively beautiful (they still are) but at the same time scary and full of a dark art. However, my apprehension did not last and thanks to the collective effort, I was surprised to quickly find myself operating them. I believe it is because there is, in this group, a mentality which ensures students feel comfortable enough to “do things” knowing that the support is there. I am also grateful that this extended beyond the place of work: the eating out, the pub evenings, the debates and laughter, which helped me to let off steam.

I would also like to express my thanks to Professor Vladimir Vishnyakov, as it is his valuable advice that allowed me to investigate the amorphisation mechanisms, hence to write chapter 6 of this thesis. I am not forgetting Dr Imran Hanif who was working on nanowires as a PhD candidate when I joined the team and who kindly showed me the tricks of this trade. Of course, I cannot leave out my fellow PhD candidates who are all so cool: Matheus Tunes who was my awesome travel companion during this journey, Benjamin Clay, Jacob Lewis, Hoang Lee, Mohammed Hussien, Walled Muftah, Mohammed Imtyaz Uddin and Italo Oyarzabal.

I would like to also extend my thanks to my mother who gave me the confidence I needed as I was growing up. She made sure I knew that I had the learning capacity which would allow me to do the things I wanted to do, even going back to “school” after dropping out for many years.

And last but one, I want to say thank you to Emma, my wife. She has supported me through all these years of study, taking care of so many things and was the one who pushed me into going back to my studies.

Lastly, I want to thank God for leading me here, I am sorry I doubt you and question you, I guess it is because you made me a scientist...

## Published and under review articles

**June 2019**, Anomalous nucleation of crystals within amorphous germanium nanowires during thermal annealing. **Osmane Camara**, Anamul H.Mir, Stephen E. Donnelly and Jonathan A. Hinks (Under review: *Nanoscale Advances*)

**May 2019**, Understanding amorphization mechanisms using ion irradiation in situ a TEM and 3D damage reconstruction. **Osmane Camara**, Matheus A. Tunes, Graeme Greaves, Anamul H.Mir, Stephen E. Donnelly and Jonathan A. Hinks (Under review: *Ultramicroscopy*).

**Chapter 6 is partially based on this article.** My contribution in this article: The experimental work, the treatment and analysis of the data, the writing of the manuscript plus a 50 percent contribution to the elaboration of the modified version of IDRAGON

**April 2019**, A candidate accident tolerant fuel system based on a highly concentrated alloy thin film. Matheus A. Tunes, Vladimir Vishnyakov, **Osmane Camara**, Graeme Greaves, Phil Edmondson, Yanwen Zhang, Stephen E. Donnelly. *Materials Today Energy* 12 (2019): 356-362.

**December 2018**, Energetic particle irradiation study of TiN coatings: are these films appropriate for accident tolerant fuels? Matheus A. Tunes, Felipe C. da Silva, **Osmane Camara**, Claudio G. Schön, Julio C. Sagás, Luis C. Fontana, Stephen E. Donnelly, Graeme Greaves, and Philip D. Edmondson. *Journal of Nuclear Materials* 512 (2018): 239-245.

**June 2018**, Shape Modification of Germanium Nanowires during Ion Irradiation and Subsequent Solid-Phase Epitaxial Growth. **Osmane Camara**, Imran Hanif, Matheus Tunes, Robert Harrison, Graeme Greaves, Stephen Donnelly, and Jonathan Hinks. *Advanced Materials Interfaces* 5, no. 13 (2018): 1800276. **Chapter 5 is partially based on this article.** My contribution in this article: The experimental work, the treatment and analysis of the data, the writing of the manuscript plus a 10 percent contribution to the elaboration of the modified version of IDRAGON

**May 2018**, Ion-beam-induced bending of semiconductor nanowires. Imran Hanif, **Osmane Camara**, Matheus A. Tunes, Robert W. Harrison, Graeme Greaves, Stephen E. Donnelly, and Jonathan A. Hinks. *Nanotechnology* 29, no. 33 (2018): 335701.

**July 2017**, Effects of temperature on the ion-induced bending of germanium and silicon nanowires. **Osmane Camara**, Imran Hanif, Matheus Tunes, Robert Harrison, Graeme Greaves, Stephen Donnelly, and Jonathan Hinks. *Materials Research Express* 4, no. 7 (2017): 075056. **Chapter 4 is partially based on this article.** My contribution in this article: The experimental work, the treatment and analysis of the data, the writing of the manuscript plus a 10 percent contribution to the elaboration of the modified version of IDRAGON

## List of figures

**Figure 1.1:** Graph showing the number of transistors in a central processing unit from 1972 to 2016. From [14].

**Figure 2.1:** (a) Unit cell showing the crystalline structure of germanium, from [46] along with (b) a representation of the unit cell from a [100] direction where atom positions are shown as a fraction of the cube edge length, from [47].

**Figure 2.2:** Structure of the bands showing the energy differences of 0.66 eV and 0.80 eV between the valence band and the conduction band of germanium. The semiconductor has an indirect band gap of 0.66 eV.

**Figure 2.3:** Distribution of the electrons as a function of temperature and energy according to equation 2.2, showing the Fermi-Dirac distribution at four different temperatures.

**Figure 2.4:** Graphs showing (a), an energy distribution of electrons defined via  $f(E,T)$ , (b) the valence and the conduction band defined via  $(D_e)$  and (c) the convolution of the two, defined via  $f(E,T)(D_e)$  where the empty and occupied energy levels can be seen.

**Figure 2.5:** Schematic showing how the introduction of a dopant from column V or III can result in a free electron and a hole, respectively, as just four electrons are required to form a covalent bond in the germanium material. From [55].

**Figure 2.6:** Graph showing a typical example of the relative contribution of the nuclear energy loss (in green) and the electronic energy loss (in red) as well as their sum (in blue) as a function of the particle energy. From [61].

**Figure 2.7:** The concentration of boron implanted in silicon is shown by the continuous line as a function of depth for four different acceleration energies (30, 100, 300 and 800 keV) and can be compared with the concentration which would result if their distribution followed a Gaussian distribution (shown by the dashed lines). From [69].

**Figure 2.8.** Schematic summarising the main types of defects in a crystal. From [92].

**Figure 2.9:** Type of interstitials in germanium as they can be of type: (a) split, (b) hexagonal (c) tetrahedral and (d) distorted hexagonal. From [21].

**Figure 2.10:** Vacancy diffusion (top) and interstitial diffusion (bottom) are shown as well as the energy barrier corresponding to each of these two diffusion mechanisms (where the interstitial shown in the picture represents a smaller atom than these of the material). From [101].

**Figure 2.11:** In the graph the diffusion coefficient as a function of temperature in germanium of the p-dopants (in green), n-dopants (in red) can be compared with the self-diffusion coefficient of germanium (in black). At temperatures at which diffusion coefficients have not been experimentally observed, the extrapolated values are shown as dashed lines instead of continuous lines. From [84].

**Figure 2.12:** Logarithmic timescale of the main events, which can occur following an atomic collision. It must be noted that the typical duration of a video frame shows the technological limitations, which prevent the monitoring of these events. Courtesy of Dr Jonathan Hinks.

**Figure 2.13:** Schematic showing a dangling bond (in green) at the interface between a germanium crystal and an oxide layer. The germanium atoms are represented in grey and the oxygen atoms are shown in black. From [21].

**Figure 2.14:** Radial density function (RDF) of single crystal, amorphous and liquid germanium. From [124].

**Figure 2.15:** Scanning electron microscopy (SEM) images showing the evolution of the germanium surface during irradiation at RT by a 30 and a 60 keV bismuth ion beam at fluences ranging from  $5 \times 10^{13} \text{ cm}^{-2}$  to  $1 \times 10^{17} \text{ cm}^{-2}$  at normal incidence. From [121].

**Figure 2.16:** Nuclear energy absorbed by the target material as a function of depth in germanium irradiated with 300 keV xenon ions at normal incidence calculated using SRIM.

**Figure 2.17:** Measured amorphous depth due to irradiation of germanium as reported in various experiments reported in the literature and summarised in [26] to be compared with the predicted amorphous depth if  $E_{dc} = 5 \text{ eV}$ . From [26].

**Figure 2.18:** BF-TEM images of crystalline silicon with black spots, identified as amorphous pockets due to irradiation by 30 keV germanium, lead or tellurium at either 77 K or RT. From [139].

**Figure 2.19:** Schematic showing the original disordered region of radius  $R_0$  along the path of the ion and the resulting amorphous region of radius  $R_0 - \delta R$  (referred to in the text). From [140].

**Figure 2.20:** Relative increment of refractive index (proportional to  $f_a$ ) as a function of fluence during irradiation of silicon by several ions at RT. From [27].

**Figure 2.21:** Schematic of a diamond type crystal lattice in  $\langle 110 \rangle$  projection showing the (100) (111) and (110) interfaces and six fold rings formed via epitaxial crystallisation represented in crosshatched. From [143].

**Figure 2.22:** Regrowth rate of amorphous pockets observed via TEM in germanium, silicon and gallium phosphide as a function of the electron beam energy. From [153].

**Figure 2.23:** Schematic to illustrate (a) the interaction between an ion and a solid where the recoils can leave the target material from the surface (as illustrated by the red arrow), whilst in the case of a nanostructure (b) more surface is available for recoils to be sputtered away. From [35].

**Figure 2.24:** Schematic illustrating how (a) a straight nanowire will (b) first become curved during IIB towards the ion beam until (c) it becomes aligned with the ion beam.

**Figure 2.25:** Schematic showing the correlation between the temperature and the volume expansion within the nanopillar. The extent of the volume expansion is qualitatively illustrated by the length of the arrows within the nanopillars. From [179].

**Figure 2.26:** MD simulations displaying the evolution of the displaced atoms (shown in blue) as a function of time. The figure shows (a) the temperature evolution during the thermal spike phase, (b) the displaced atoms at 0.054 ps (when the temperature reaches a maximum). The region with the highest temperature of 1254.4 K is delimited by the white line. (c) A transitional phase at which sputtering occurs where the sputtered atoms are shown within the region delimited by the white line. (d) At 0.26 ps, the stage at which the disorder reaches its peak. (e) The remaining defects after the system is cooled down to 298K. From [122].

**Figure 2.27:** Iradina MC simulation results and schematic depicting shallow and deep implantation in the top and the bottom row, respectively. In the left column (a), (d), implanted ions are represented in a purple colour gradient. In the middle column (b), (e), excess of interstitials are represented in purple whilst excess of vacancies are shown in red. In the right column (c), (f), the direction of the ion beam is represented by the dark blue arrow and the part of the nanowire affected by the ions is coloured in light blue. From [114].

**Figure 2.28:** SEM images of germanium nanowires under 30 keV gallium irradiation. The direction of the ion beam is indicated by the white arrows. As indicated, the incidence direction is changed during irradiation, inducing a change in the bending direction. From [120].

**Figure 3.1:** Schematic showing how individual rays (represented with coloured lines) are bent depending on their optical pathways and the angle they form with the central plane of the convergent lens. In front of the lens in the image plane an image of the object is formed where the rays meet.

**Figure 3.2:** Schematic showing a typical thermionic electron gun structure with photographs of the two most common thermionic sources used in TEM (tungsten and LaB<sub>6</sub>). From [204]–[206].

**Figure 3.3:** Schematic showing a field-emission type of electron gun where two anodes under a voltage shown in the picture by V1 and V2 are used as electrostatic lens to guide and focus the beam. Furthermore, as stated in [203], V1 typically delivers a voltage to extract the electrons from the tip whilst anode 2 is used to accelerate the electrons.

**Figure 3.4:** Schematic of an electromagnetic lens system and associated components. In the example depicted in the figure the electron beam shown in red is tilted towards the optical axis of the lens by the deflectors. As illustrated in the image on the right bottom-corner the astigmatism (represented by a distorted electron beam) is corrected when the electron beam passes through the stigmators (or more precisely by the field they generate) and is then skimmed by the aperture.

**Figure 3.5:** Schematics of: (a) a rotary pump, from [209]; (b) a turbo-molecular pump, from [210]; (c) an oil diffusion pump, from [203]; and (d) an ion getter pump, from [203].

**Figure 3.6:** TEM holder with the two tilting directions represented by the green arrows.

**Figure 3.7:** Schematic illustrating situations where the conjugate image of an object is either well focused onto the object plane of the lens positioned below in the TEM column (red line), underfocused (green lines) and overfocused (blues lines). In the example shown here the lens below in the TEM (not shown for clarity of the figure) is set such as its object plane is at a fixed height.

**Figure 3.8:** Schematic of a camera based on a CCD showing how an electron is captured by the scintillator that translates the electronic signal into photons to ultimately give rise to a signal via the CMOS. Modified from [214].

**Figure 3.9:** Ensemble view showing the main sections of the TEM. The image shown in the figure illustrates a simplified example as the actual TEM is more complex and may possess more lenses.

**Figure 3.10:** Electron ray path from the gun crossover to the sample showing how the C2 lens focuses the beam onto the specimen and how the diaphragm can act as a beam skimmer in a simplification of an actual TEM which is more complex and typically will possess more lenses. From [203].

**Figure 3.11:** The ray diagram on the left shows an example of how a TEM can be operated to produce a diffraction pattern on the viewing system and on the right to produce an image. As shown in the picture the projector lens has a fixed height at which its object plane is positioned (i.e. Intermediate image 2). Consequently, the formation of a DP or an image will depend on whether at this position (i.e. the intermediate image 2) the intermediate lens forms a DP or an image. From [203].

**Figure 3.12:** Scattering occurs from B and C, which are two points lying on the planes  $P_1$  and  $P_2$ . The path difference between the two beams is equivalent to  $AC+CD$ . From [203].

**Figure 3.13:** Illustration of vectors, which represent the wavefront prior to scattering,  $k_i$ , and after diffraction,  $k_d$ . The difference between these two is the vector  $K$ .

**Figure 3.14:** The Ewald sphere and the relrods in 2 D: as the relrods are not discrete points, a sphere with a large radius may encounter numerous relrods. From [203].

**Figure 3.15:** Examples of typical diffraction patterns: (a) single crystal diffraction pattern with the characteristic distinct bright spots; (b) fully amorphous specimen diffraction pattern with the characteristic faint rings and no bright spot apart from the 000 spot and (c) polycrystalline crystal diffraction pattern with the characteristic rings made from a multitude of bright spots.

**Figure 3.16:** Illustration of the formation of Kikuchi lines during interaction of the electron beam with a sample: (a) the intensities of the two lines which each represents one Kossel cone differ as they emerge close to the incident electron beam; and (b) are approximated as lines on the camera or the phosphorescent screen. From [203].

**Figure 3.17:** Summary of the principal possibilities for the electrons which are accelerated towards a specimen: (a) unscattered; (b) inelastically scattered; or (c) elastically scattered. From [215].

**Figure 3.18:** Schematics illustrating various imaging modes using the objective aperture: (a) BF imaging by selecting the direct beam on the optical axis; (b) a DF imaging mode by moving the objective aperture to select an off-axis diffracted beam; and (c) centred DF imaging where the incident electron beam is tilted in such a way that the diffracted beam becomes aligned with the optical axis.

**Figure 3.19:** BF-TEM image of a wedge-shaped single-crystal germanium specimen, the darker regions corresponds to the thicker parts.

**Figure 3.20:** (a) HRTEM micrograph of a germanium nanowire obtained at the MIAMI-2 facility on a Hitachi H-9500. Measurements have confirmed that the representation of (111) lattices are shown in the image. (b) HRTEM micrograph captured at the MIAMI-1 facility on a JEOL JEM-3010 showing of a gold nanoparticle.

**Figure 3.21:** Typical EELS spectrum with the typical most-intense signals in the spectrum, (the zero loss peak and the plasmon resonance) as well as the less-intense signals which can be found at higher energy losses. From [218].

**Figure 3.22:** BF-TEM image of germanium nanowires. Some nanowires are potentially entangled together whilst others are isolated enough to bend without interference from neighbouring nanowires.

**Figure 3.23:** Schematic showing the main steps of the preparation of an electron transparent germanium foil. The electron transparent region is located in the vicinity of the hole made by ion milling. From [220].

**Figure 3.24:** The cross-section of a nanowire is divided into slices that will be treated individually in SRIM as flat targets. Typically, the nanowires were divided into 100 slices that were recomposed in the IDRAGON MATLAB code to model the nanowire cross-section. For clarity, the nanowire is divided in only 10 slices in the figure.

**Figure 3.25:** The modified DRAGON 3d plot showing the recoils (in blue) and the PKAs (in red) after a zirconium flat target is irradiated with 5 xenon ions accelerated to 300 keV at normal incidence.

**Figure 3.26** Picture of MIAMI-1 and schematic displaying the layout of the system. From [208].

**Figure 3.27:** Picture of MIAMI-2 and schematic displaying the layout of the system. From [228].

**Figure 3.28:** Example of how tilting can reveal the bent shape of a nanowire using the x-tilt of a TEM holder: (a) the nanowires appears bent towards the left when tilted at  $+45^\circ$ ; (b) straight when untilted; and (c) bent towards the right when tilted at  $-45^\circ$ . At  $0^\circ$  the nanowire is actually bent upward as revealed by the tilting. It is worth noting that if the nanowire were bent downward it would appear bent towards the right when tilted at  $+45^\circ$  and bent towards the left when tilted at  $-45^\circ$ .

**Figure 3.29:** (a) Schematic showing the nanowire (brown) and the vector (orange) of length  $t$  (i.e.  $KB = KC = t$ ), (b) the nanowire and its projections are shown (b) before and (c) after tilting. The abbreviations used to name distances are shown in (d).

**Figure 3.30:** (a) Schematic showing the vector (orange) of length  $t$ , and its projection as seen along the axis of the tilt before and after tilting, (b) the nanowire (brown) and its projections are shown before and (c) after tilting. The abbreviations used to name distances are shown in (d).

**Figure 3.31:** Schematic showing a nanowire in the MIAMI-1 system. The ion beam forms an angle of  $30^\circ$  with the x-axis whilst its projection forms an angle of  $45^\circ$  with x-axis and the y-axis.

**Figure 4.1:** BF-TEM images and SADP of a nanowire: (a) before irradiation; and (b) after 30 keV xenon ion irradiation at  $400^\circ\text{C}$  to a fluence of  $7.1 \times 10^{14}$  ions. $\text{cm}^{-2}$ . The projection of the ion beam direction onto the image plane is indicated by the red arrow in (a). The scale bar in (a) also applies to image (b). The SADPs before and after irradiation are characteristic of single crystalline material.

**Figure 4.2:** SADPs of a nanowire captured during irradiation to fluences of (a)  $8.8 \times 10^{14}$  ions.cm<sup>-2</sup> and (b)  $9.6 \times 10^{14}$  ions.cm<sup>-2</sup>. The diffraction spots indicated by the blue arrows have been chosen to illustrate the evolution of the SADP. A diffraction spot chosen as reference is indicated by the dashed black arrow. During the bending of the nanowires, several spots such as spots (i) and (ii) moved during the motion of the nanowire. However, whilst the intensity of the diffraction spot chosen as a reference varied, it did not move during irradiation. Indeed, the intensities of the diffraction spots may vary during the ion irradiation and some may appear and disappear as the intensities of the spots depend on how close to the Bragg conditions the diffracting planes are during the nanowire motion.

**Figure 4.3:** (a) BF-TEM image of a nanowire before irradiation at elevated temperature and (b) after irradiation to a fluence of  $2.4 \times 10^{15}$  ions.cm<sup>-2</sup> inducing bending and sputtering of the nanowire. The SADP in (b) shows that amorphisation has not been detected after the bending of the nanowire towards the ion beam. The same nanowire after irradiation is shown in (c) at another tilt angle in BF-TEM image mode and in a CDF-TEM image mode which correspond to (d) a (004) condition and in (e) to a  $(1\bar{3}1)$  condition. The projection of the ion beam direction onto the image plane is indicated by the red arrow in (a). The scale bar in (a) is also valid for the other images in the figure. It must be specified that the images (b), (c) and (d) were taken at a different tilt angle (close to zone axis) for the reason that they were captured during a post-analysis whose aim was to perform HRTEM.

**Figure 4.4:** BF-TEM image and SADP of a germanium nanowire irradiated at elevated temperature to a fluence of  $2.7 \times 10^{15}$  ions.cm<sup>-2</sup> showing that in this case the elevated temperature may have prevented the bending from occurring. The projection of the ion beam direction onto the image plane is indicated by the red arrow.

**Figure 4.5:** IDRAGON profile showing the distribution of implanted xenon atoms in the cross section of the nanowire shown in figure 4.1. According to this calculation, most of the ions were implanted within the half of the nanowire nearest to the irradiated surface.

**Figure 4.6:** BF-TEM images of a nanowire (a) before and (b) after 30 keV xenon ion irradiation at 400°C to a fluence of  $1.2 \times 10^{15}$  ions.cm<sup>-2</sup>. The projection of the ion beam direction onto the image plane is indicated by the red arrow in (a) and the zones corresponding to the sections where the sputtering yield was measured are shown by the red arrows. The scale bar in (b) also applies to image (a). The SADP after irradiation is indicative of single crystal material.

**Figure 4.7:** BF-TEM images and SADPs of a nanowire (a) after a 30 keV xenon ion irradiation at 400°C to a fluence of  $2.7 \times 10^{15}$  ions.cm<sup>-2</sup> and (b) after a subsequent irradiation at RT to a further fluence of  $7.5 \times 10^{13}$  ions.cm<sup>-2</sup>. The projection of the ion beam direction onto the image plane is indicated by the red arrow in (a). The scale bar in (a) applies to image (b). The SADPs show that the irradiation induced considerably more damage accumulation (leading to amorphisation) when it was performed at RT.

**Figure 4.8:** Superimposed BF-TEM images taken from an in situ video showing the evolution of a germanium nanowire during a 30 keV xenon ion irradiation at elevated temperature. The projection of the ion beam direction onto the image plane is indicated by the red arrow in (a). The SADP before and after irradiation are characteristic of crystalline material. The nanowire is shown to align towards the ion beam without taking a curved shape.

**Figure 4.9:** Schematic of a nanowire bending towards the ion beam whilst taking a circular shape. The radius ( $r_{arc}$ ) should be measured using the neutral axis of the nanowire to determine the strain as a function of  $d_y$  according to equation 4.7.

**Figure 5.1:** BF-TEM images and SADPs of (a) a germanium nanowire before a 30 keV xenon irradiation at RT and (b) after the irradiation which has prompted IIB away from the ion beam. On the bottom row the BF-TEM images and the SADPs show (c) a germanium nanowire before a 30 keV xenon irradiation at RT and (d) after the irradiation which has prompted IIB towards the ion beam. For each case,  $\Omega$  is given in (a) and (c). The projection of the ion beam onto the image plane is indicated by the red arrow in (a). The scale bar in (a) also applies to the other images in the figure. The conditions of irradiation of the nanowire in (a), (b) and in (c),(d) are resumed in table 1(xi) and (vi), respectively.

**Figure 5.2:** IDRAGON implantation profile of the nanowire shown in figure 5.1 under irradiation by a 30 keV xenon ion beam at  $\alpha=37^\circ$ .

**Figure 5.3:** BF-TEM images of (a) a germanium nanowire before 30 keV xenon irradiation at RT, (b) after irradiation at a fluence of  $1 \times 10^{14}$  ions.cm<sup>-2</sup> which has prompted IIB towards from the ion beam and (c) at a fluence of  $3 \times 10^{14}$  ions.cm<sup>-2</sup> showing that the nanowire bending direction has changed during subsequent irradiation as it then bends away from the ion beam. The projection of the ion beam onto the image plane is indicated by the red arrow in (a). The scale bar in (a) also applies for the other images in the figure. The ratio  $\Omega$  illustrating the initial condition of irradiation corresponds to a value of 0.35 and is thus close to the threshold value for bending direction reversal.

**Figure 5.4:** DF-TEM image of a germanium nanowire after a 30 keV xenon irradiation at RT to a fluence of  $4.7 \times 10^{14}$  ions.cm<sup>-2</sup> which has prompted IIB away from the ion beam. The presence of a crystalline structure is evidenced by the bright features. The nanowire was single crystalline before irradiation (as shown by its SADP in figure 5.1(a)). On the ion-beam-facing side, the nanowire is dark all along its length in the DF image even in the vicinity of the bright section – thus suggesting that the side facing the ion beam is fully amorphous as a result of the damage accumulation due to the xenon ion beam irradiation. The projection of the ion beam onto the image plane is indicated by the white arrow.

**Figure 5.5:** Schematic of the bending of a thin film and its substrate. On the figure the variables (described in the text) required for the calculation via the Stoney equation are based on two distinct portions, which are the thin film and the substrate. However, as stated above, in a nanowire the two distinct portions must be replaced by two phases of the irradiated nanowire for which properties and thickness are difficult to determine and which will evolve during the irradiation. From [248].

**Figure 5.6:** BF-TEM images and SADPs of (a) germanium nanowire before 30 keV xenon irradiation at RT and (b) after irradiation to a fluence of  $7.3 \times 10^{13}$  ions.cm<sup>-2</sup> which has prompted IIB towards the ion beam. The SADPs indicate that the nanowire was single crystalline before and became fully amorphous during irradiation. (c) Annealing at a temperature of 440°C was performed on the bent nanowire for 25 minutes. No noticeable change of shape was observed during the annealing and the SADP remained unchanged showing that neither SPEG nor RNG has been induced by the thermal treatment. The projection of the ion beam onto the image plane is indicated by the red arrow in (a). The scale bar in (c) also applies for the other images in the figure.

**Figure 5.7:** BF-TEM images and SADPs of (a) germanium nanowire (indicated by the black arrow) before a 30 keV xenon irradiation at RT and (b) after the irradiation to a fluence of  $9.1 \times 10^{13}$  ions.cm<sup>-2</sup> which caused IIB away from the ion beam. (c) Annealing at a temperature of 440°C was performed on the bent nanowire for 5 minutes during which time the shape of the nanowire changed becoming straight once more. The projection of the ion beam onto the image plane is indicated by the red arrow in (a). The scale bar in (a) is also valid for the other images of the figure.

**Figure 5.8:** BF-TEM images and SADPs of (a) a germanium nanowire (indicated by the black arrow) before a 30 keV xenon irradiation at RT and (b) after irradiation to a fluence of  $7.3 \times 10^{13}$  ions.cm<sup>-2</sup> which has prompted IIB towards the ion beam. The SADPs indicate that the nanowire was a single crystal and (b) became partially amorphous after irradiation. (c) Annealing at a temperature of 440°C was performed on the bent nanowire for 18 minutes during which the shape of the nanowire changed as the curvature increased during annealing. Additionally, as evidenced by the SADP, recrystallisation occurred during the thermal treatment making the nanowire polycrystalline. The projection of the ion beam onto the image plane is indicated by the red arrow in (a). The scale bar in (a) also applies for the other images in the figure.

**Figure 5.9:** The orientation of crystallites relative to each other in a partially amorphous nanowire and the way it can impact the diffraction pattern is shown (a) in the case where the crystallites did not rotate during the bending, thus, making sets of planes in several crystallites parallel and consequently diffracting in the same fashion, whilst in (b) the crystallites have rotated during the bending making a similar set of planes misoriented relative to each other and consequently leading to a rotation of the diffracting spots from the crystallites. In order to make the figure clearer, only one diffracted beam is taken into account for each set of planes.

**Figure 5.10:** Superimposed BF-TEM images taken from an in situ video showing the evolution of a germanium nanowire during a 30 keV xenon ion irradiation at RT. The projection of the ion beam onto the image plane is indicated by the red arrow. The nanowire is shown to have bent away from the ion beam as the fluence increased. It is worth noting that the curvature of the nanowire has increased until the nanowire came into contact with the TEM grid.

**Figure 6.1:** Schematic showing the cross section of a calculated volume  $V$  made of an amorphous core  $V_a$  (in red) and a crystalline damaged region  $V_d$  (in orange) requiring  $m$  overlaps to become amorphous.

**Figure 6.2:** Evolution of the amorphous fraction as a function of fluence for different amorphisation mechanisms. In this simple illustration, the target material is considered fully amorphous (i.e.  $f_a = 1$ ) at the same fluence for each mechanism. In the three heterogeneous models the curves have been generated using equation 6.4 whilst keeping the value of  $V$  similar whether  $V = V_a$ ,  $V = V_d$ , or  $V = V_a + V_d$ .

**Figure 6.3:** (a) Schematic showing how  $V_a$  is determined based on the defect densities distribution indicated by the red line and (b) example showing a section of the 3D plot of the recoils within  $V_a$  and the PKAs after irradiation by 300 keV xenon ions, where all the recoils within  $V_a$  are indicated by a blue spot and the PKAs are shown by red spots. The plot shown in (b) is generated after 1000 ions.

**Figure 6.4:** SADP of a germanium sample (a) before irradiation (b) after irradiation with 300 keV xenon ion at a fluence of  $1.3 \times 10^{13}$  ions.cm<sup>-2</sup> and a dpa of 0.13 (c) at a fluence of  $3.0 \times 10^{13}$  ions.cm<sup>-2</sup> and a dpa of 0.37, this is when the sample becomes fully amorphous as characterised by the presence of amorphous rings without any spots apart from the direct beam spot.

**Figure 6.5:** Evolution of  $f_a$  as function of the fluence during irradiation at RT according to equation 6.4 (as indicated by the curves) and according to the experiments (as shown by the data points) for the irradiation conditions: (a) 300 keV xenon (b) 200 keV krypton (c) 100 keV argon (d) 80 keV neon and (e) 70 keV helium ions. The labels of the axis in (e) also applies for (a) - (d).

**Figure 6.6:** Using the MATLAB code and SRIM, the calculated fraction of defects as a function of the cylindrical volumes of radii,  $r_x$  defined in the experimental section is shown for all ions with the exception of the helium irradiation.

**Figure 6.7:** The percentage of recoils induced (a) in  $V_a$  and in (b)  $V$  as function of the ion mass for each irradiation condition. In (c) is shown  $1/\text{dpa}$  as a function of the ion mass for each case. The ions labelled in (a) and are also applicable for (b) and (c). The lines in (a), (b) and (c) are included as guides for the eye.

**Figure A.1:** Superimposition of BF-TEM images captured from a video during 40 keV xenon ion irradiation in situ in the TEM inducing the bending of the silicon nanowires at 500°C. The SADPs before irradiation and after irradiation are shown to illustrate the single crystalline character of the nanowire after bending.

## List of tables

**Table 1.1:** Comparison between the ENIAC and an Intel Core Duo Chip circa 2006. The table shows that whilst the performance has increased, the price, size, weight and conception have decreased. From [12].

**Table 2.1:** Conductivity of example insulators, semiconductors and conductors according to [54].

**Table 3.1** Typical values of energy distribution and source sizes of the main type of sources used in TEM according to [207].

**Table 3.2:** The table shows the main characteristics of the MIAMI-1 system. It is worth noting that these characteristics were accurate at the time when the work presented in this thesis was undertaken and consequently may not reflect the newest upgrades made to MIAMI-1.

**Table 3.3:** The table shows the main characteristics of the MIAMI-2 system.

**Table 5.1** The table summarises the experimental conditions and results obtained when 11 germanium nanowires were irradiated by xenon ion irradiation at RT. The colour scale under the table is valid for all the IDRAGON profiles with “maximum” referring to the highest level of damage within each individual nanowire (i.e. not the maximum damage level across all 11 nanowires).

**Table 6.1:** For each case, as well as the average total number of recoils per ion determined by SRIM are shown the value of  $m$  determined via the correlation between the experimental results and equation 6.4,  $V_a$  determined via the MATLAB analysis of the collision cascades using the theoretical defect fraction for amorphisation,  $V_d$  determined via the correlation between the experimental results and equation 6.4, the threshold dpa for amorphisation and the fluence at

full amorphisation were determined using the experimental results (i.e. the SADPs) and  $S_e/S_n$  as given by SRIM.

## List of abbreviations

BF	Bright field
CBED	Convergent-beam electron diffraction
CCD	Charge coupled device
CDF	Centred dark-field
CMOS	Complementary metal-oxide-semiconductor
DF	Dark-field
DFT	Density functional theory
dpa	Displacement per atom
EELS	Electron energy loss spectroscopy
EFTEM	Energy-filtered transmission electron microscopy
ELNES	Energy-loss near-edge structure
EMMA	Electron Microscopy and Materials Analysis
EOR	End of range
EXELFS	Extended energy-loss fine structure
fcc	Face-centred cubic
FEG	Field emission gun
FIB	Focused ion beam
HRTEM	High resolution transmission electron microscopy

IDRAGON	Ion Damage and RAnge in the Geometry Of Nanowires
IIB	Ion induced bending
ITRS	International technology roadmap for semiconductors
MC	Monte Carlo
MD	Molecular dynamic
MIAMI	Microscope and Ion Accelerator for Materials Investigation
MOSFET	Metal-oxide-semiconductor field-effect transistor
PIPS	Precision ion polishing system
PKA	Primary knock-on atom
RDF	Radial density function
RNG	Random nucleation and growth
RT	Room temperature
SAD	Selected area diffraction
SADP	Selected area diffraction patterns
SEM	Scanning electron microscopy
SIMS	Secondary ion mass spectrometry
SPEG	Solid phase epitaxial growth
SRIM	Stopping and Range of Ions in Matter
STEM	Scanning transmission electron microscopy
TEM	Transmission electron microscope

UHV

Ultra-high vacuum

VLS

Vapor liquid solid growth

X-TEM

Cross section transmission electron microscopy

## Abstract

In the work presented in this thesis, ion irradiations were carried in situ within a transmission electron microscope (TEM) allowing the consequences of radiation damage on germanium to be investigated. In general, the study of radiation damage on semiconductors is of utmost importance as the use of ion beams during the processing of semiconductors is now a standard technique. Furthermore, as germanium materials in general, and germanium nanowires especially, are currently being considered as replacements for bulk silicon in future microelectronic devices, this thesis will address the effects of radiation damage on both germanium thin foils and germanium nanowires.

Concerning, the use of ion beam on nanowires, a remarkable, but yet to be fully explained consequence of radiation damage, is investigated in this work: the ion induced bending (IIB) effect. In the literature, it has been reported that during ion irradiation of nanostructures they may bend towards or away from the ion beam. However, the mechanisms invoked to explain IIB are various and still debated.

Following 30 and 70 keV xenon ion irradiation experiments, it is shown in this thesis that out of the proposed mechanisms only those based on dynamical rearrangement of the damage can explain the bending of the irradiated germanium nanowires towards the ion beam. In contrast, it is demonstrated that the mechanisms based on the accumulation of point defects or on the presence of an amorphous phase cannot explain the bending of the germanium nanowires irradiated in the current work. In a set of experiments where germanium nanowires were irradiated by 30 keV xenon ions at 400°C, bending was observed even though the accumulation of point defects and the collapse of the crystalline phase into an amorphous one is prevented by the relatively elevated temperature (i.e. 400°C). Similarly, in another set of experiments performed at room temperature it is shown via Monte Carlo calculations that there is a

discrepancy between the distribution of the damage within the nanowires and that which would be required in order for the mechanisms based on damage accumulation to operate.

Furthermore, the work in this thesis also solves several issues regarding the use of IIB as a potential technique in industrial processing of nanowires. Whilst IIB can be considered as an unwanted side effects occurring during the ion beam doping of nanostructures, it also represents a powerful nanomanipulation technique. However, to make full use of IIB as such a technique, the bending direction must be controllable. For this reason, using an in-house MATLAB code combined with Monte Carlo calculations it was determined that the damage depth normalised with respect to the diameter of the nanowire could be used to forecast the bending direction. Lastly, as germanium nanowires became amorphous or partially amorphous during IIB, annealing experiments were performed. However, it is shown in this work that the shape modification obtained via ion beam irradiation can be unstable during recrystallisation. Consequently, irradiating the germanium nanowires at elevated temperature (e.g. 400°C in this work) is proposed as a novel way to use the IIB effect as it allows the nanowires to maintain their single-crystalline character during the nanomanipulation.

As stated above, ion beams are routinely used to process semiconductors. However, unless the irradiation is performed at elevated temperature, the damage accumulation may induce amorphisation. To investigate the currently debated mechanisms behind amorphisation and the effect of the ion mass on the amorphization rate, germanium foils were irradiated in situ within the TEM using either 300 keV xenon, 200 keV krypton, 100 keV argon, 80 keV neon or 70 keV helium ions. By monitoring the diffraction patterns during the in situ ion irradiations and modelling the collision cascades, it was shown that amorphisation must occur gradually via a heterogeneous damage accumulation mechanism where each ion induces an amorphous region at the core of the cascade surrounded by a highly defective crystalline shell. It was also revealed that the threshold displacement per atom (dpa) for amorphisation was not always lower for

heavier ions as may be expected. This feature of the threshold dpa trend was shown to depend on the spatial distribution of the point defects in a collision cascade. Furthermore, the correlation between the experiments and the modelling of 1000 collision cascades induced by helium ions has shown that, in the case of helium, the amorphisation mechanism can be understood only when taking into account the stochastic nature of collision cascades. Indeed, it is revealed that the average collision cascade induced by helium ions could not induce amorphisation. On the other hand, it is shown that it is only occasional collision cascades involving a relatively larger number of defects which are responsible for the amorphisation process.

# Chapter 1: Introduction

## 1. Motivation for this work

The Z1, the COLOSSUS, the ENIAC or the ABC: These machines may prompt endless debates amongst computer experts regarding which of them should be branded as the first real computer [1]–[3]. However, there is no disputing the fact that the computer-based technologies have, and continue to have, tremendous impact on our society [4]–[7]. Whilst these pioneering devices were small in number and dedicated to a limited number of tasks (for example the ENIAC was initially built for military purposes [8]), nowadays computers are almost everywhere and perform an almost unlimited number of different tasks. They can be utilised to assist a surgeon during a delicate procedure, they ensure the automation of numerous actions during flights [9] and are routinely used in everyday life in the form of personal computers, laptops or smartphones [6].

However, not only has the proliferation of computer-based technologies been impressive but also the evolution of computational power has also been remarkable. For instance, when comparing (as illustrated by table 1.1) aspects of ENIAC with a microprocessor circa 2006, it becomes obvious that intense research and funding must have been deployed to achieve the making of more powerful electronic devices in a smaller space [10], [11].

**DOWNSIZING AND UPGRADING**

The inception of computing inspired a remarkable race for faster, smaller, lighter, cheaper hardware.

	<b>ENIAC</b>	<b>Intel Core Duo chip</b>
Debut	1946	2006
Performance	5,000 addition problems/sec	21.6 billion ops/sec
Power use	170,000 watts	31 watts max
Weight	28 tons	negligible
Size	80' w x 8' h	90.3 sq. mm.
What's inside	17,840 vacuum tubes	151.6 M transistors
Cost	\$487,000	\$637

**Table 1.1:** Comparison between the ENIAC and an Intel Core Duo Chip circa 2006. The table shows that whilst the performance has increased, the price, size and weight have decreased. From [12].

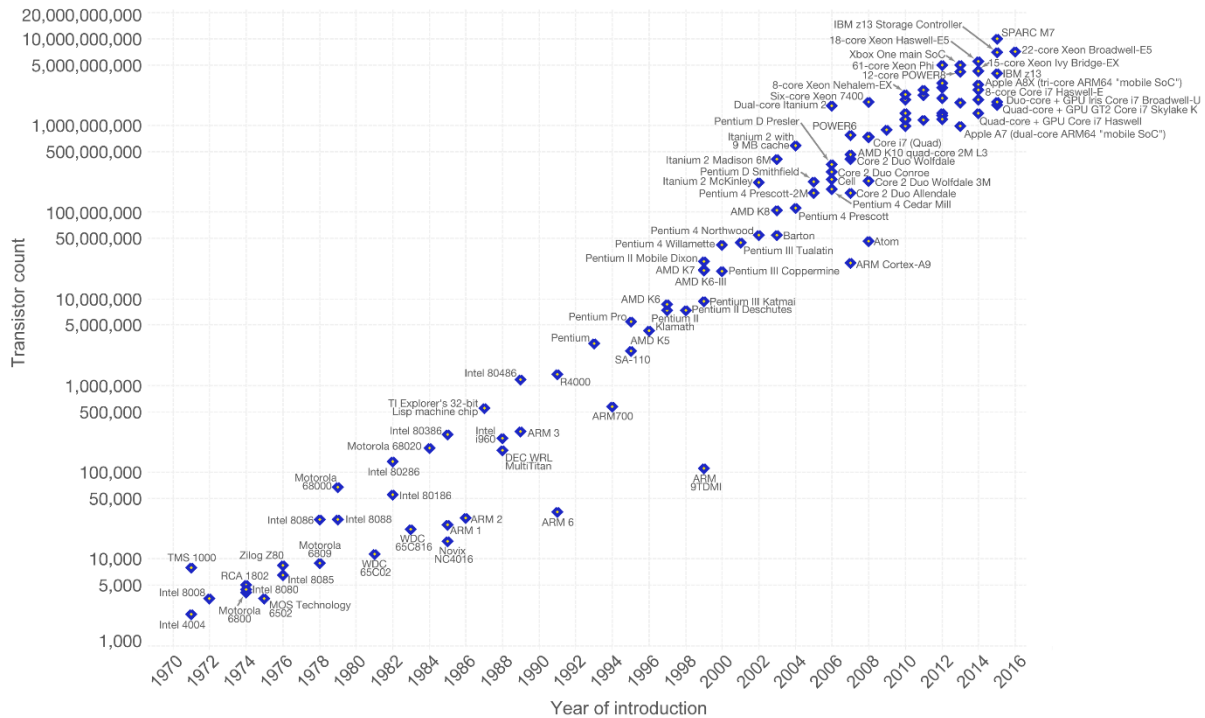
The evolution of computational power over time is related to the number of transistors (or valves) and is usually described by what is known as the Moore's Law which in 1975 stated that the number of transistors on a microprocessor chip was doubling every two years and predicted the continuation of such a trend [11].

Moore's Law is not a fundamental physical law but has been relatively well followed as illustrated by figure 1.1 showing the number of transistors on a chip over a period spanning 1971 to 2016. In the vast majority of cases, the material used in electronic devices was silicon. However, for this law to remain true, the necessity of replacing typical bulk silicon by another class of material is required [13]. This quest for new types of materials has led to the investigations that will be presented in this thesis. Indeed, whilst a great deal of effort has already been made to understand the properties of silicon, the use of other materials in future electronic devices cannot be implemented without comparable knowledge about their

properties and scientists therefore need to probe these. Interestingly, one of the main candidates to replace or be used together with silicon is the material that was first used in 1947 for the fabrication of transistors: germanium.

### Moore's Law – The number of transistors on integrated circuit chips (1971-2016) Our World in Data

Moore's law describes the empirical regularity that the number of transistors on integrated circuits doubles approximately every two years. This advancement is important as other aspects of technological progress – such as processing speed or the price of electronic products – are strongly linked to Moore's law.



Data source: Wikipedia ([https://en.wikipedia.org/wiki/Transistor\\_count](https://en.wikipedia.org/wiki/Transistor_count))  
 The data visualization is available at [OurWorldinData.org](https://ourworldindata.org). There you find more visualizations and research on this topic. Licensed under CC-BY-SA by the author Max Roser.

**Figure 1.1:** Graph showing the number of transistors in a central processing unit from 1972 to 2016. From [14].

Due to the similarities with silicon, germanium could be relatively easily deployed as a replacement or co-material of silicon [15], [16]. As will be addressed in the next chapter, there are several reasons which make germanium a credible material of choice for tomorrow's electronic devices.

In this thesis, the properties of germanium will be studied with and without respect to the scale at which it is being processed. For the former, the experiments on nanowires performed during this doctoral research will be presented. This class of materials (i.e. nanowires) has aroused a

lot of interest in the scientific community as it displays novel properties that may allow the creation of transistors with performances that could exceed the expectations of Moore's law [13]. Nanowires are furthermore proposed for a large number of other applications ranging from optoelectronics to new types of super-hydrophobic clothing [17]–[19]. However, for obvious reasons, handling and assembling nanostructures is a challenge [20]. The answer to this challenge may arise from a technique that has been routinely used during the processing of semiconductor devices to turn them into transistors. This technique is called ion implantation and consist of bombarding the semiconductor with ions that can confer to it the desired electronic properties [21]. However, during ion irradiation it has been observed that nanostructures may bend and be readily manipulated using the so called ion-induced bending (IIB) effect [20][22].

In order to control IIB, the mechanisms behind it must be identified and understood; however, to do so, the consequences of ion irradiation on nanostructures must also be better understood. During ion irradiation, radiation damage may occur leading to an accumulation of numerous type of defects such as interstitials and vacancies, and even lead to amorphisation of the target material [21], [23]. Whilst mechanisms based on amorphisation have been proposed as a cause for the IIB phenomenon [20], amorphisation is itself a process that is still not fully understood and yet is crucial for the electronics industry [24], [25]. For these reasons, much effort has been made to understand how amorphisation occurs during the irradiation of semiconductors [25]–[27]. This thesis aims to investigate both the mechanisms behind IIB and amorphisation resulting from ion bombardment.

## 2. Structure of the thesis

In the next chapter, a review of the literature will provide the scientific concepts that will be used to investigate the IIB effect and the amorphisation mechanisms. Thus, chapter 2 will give an overview of the actual knowledge regarding (among other things) the damage that can occur during ion irradiation, the properties of germanium and the properties of nanowires. Afterwards, a more in-depth review of the state of the art regarding the mechanisms of IIB and the mechanisms of amorphisation in semiconductors will be given.

In chapter 3, the experimental details regarding the experiments that have been carried out during this doctoral work will be provided. This will include the fundamentals of transmission electron microscopy (TEM) as, in the current work, ion irradiations were performed in situ within a TEM.

Chapter 4 will address the effect of ion irradiation in situ in the TEM of germanium nanowires at elevated temperatures. This chapter, which will focus on the IIB phenomenon, will present a work aimed at inducing the manipulation of nanowires whilst preserving their single crystalline character. Additionally, the experiments will provide valuable information about the mechanisms behind the IIB effect.

In chapter 5, germanium nanowires will be subjected to ion irradiation at room temperature (RT) and to a subsequent annealing step. In this chapter, the correlation between Monte-Carlo (MC) calculations and the experimental results are used to determine how the experimental conditions influence the bending of nanostructures. The stability of the germanium nanowires during annealing is also investigated. In this chapter all the main mechanisms which have been proposed in the literature to explain the bending of nanostructures will be examined in light of the experimental results.

In chapter 6, germanium foils are irradiated in situ in the TEM using non-radioactive inert gases (xenon, krypton, argon, neon and helium ions). During the in situ ion irradiations, the amorphisation rate of the specimen is monitored via the evolution of the diffraction patterns. Using ions, with masses which differ by more than a factor of 30, the influence of the ion mass on the amorphisation is revealed. Furthermore, in addition to the experimental results a 3D reconstruction of the collision cascades is made using MC calculations and an in-house developed MATLAB code. Both the 3D reconstruction and the evolution of the diffraction patterns are analysed to understand how amorphisation occurs in semiconductors

In the last chapter, the main results presented in this thesis are summarised and ideas for new experiments related to the current work are detailed.

# Chapter 2: Background & Literature Review

## 1. Introduction

Transistors are the heart of electronics devices and their evolution is continuously shaping our modern world [11]. However, unless novel categories of materials are introduced, a struggle to keep up with the pace of Moore's law will arise [13]. To respond to this challenge, an international technology roadmap for semiconductors (ITRS) has been proposed by the industry. One of the main materials considered as the silicon successor is not an exotic one; in fact, far from being a new material, it is historically the first element used for its semiconductor properties which is today being reconsidered: germanium [28]–[30]. Additionally, a novel group of materials are also proposed as a replacement for bulk silicon: nanowires, which according to the ITRS are considered as key candidates for this purpose, and therefore implicitly so are germanium nanowires [13], [22], [30]–[34].

Germanium is a semiconductor far from being as well documented as silicon; furthermore, nanowires are even less well known than their bulk equivalent, thus several aspects need to be investigated [22], [29], [32], [33], [35], [36].

To tailor the electrical properties of semiconductors it is usual to add impurities inside the material via a process called doping [37], [38]. One of the standard techniques to dope semiconductors is ion implantation [32], [33], [37]. The benefits of this technique compared to diffusion of chemicals into the semiconductor are better control of the implantation depth, more precise control of the dose and the possibility to achieve more-complex profiles [39]. Whilst the benefits of ion implantation are undeniable, it is also necessary to remember that during implantation numerous point defects and extended defects might arise, the target material might be rendered amorphous due to damage accumulation and implanted ions might need to be driven into substitutional sites to be electrically activated [21], [40]. For these reasons, an

annealing step is routinely performed after irradiation as a way of recovering a pristine crystal and activating the dopants [21], [22].

The ion irradiation and the annealing processes, which are routinely performed on bulk silicon, have not been as extensively used on germanium and germanium nanowires. They are therefore less well understood as they lead to different outcomes from those on bulk silicon [35]. For these reasons, if they are to be truly considered as tomorrow's building blocks for modern devices, it is crucial to gain a deeper understanding of both processes and to find a way to forecast their outcome. [22], [32], [35]

In this chapter, the process of damage accumulation during irradiation with an emphasis on ion-induced amorphisation and ion-induced bending (IIB) of nanostructures will be addressed. Thus, the proposed mechanisms which lead to amorphisation will be presented as well as those proposed to explain the IIB phenomenon[41].

## 2. Germanium and its properties

### 2.1. Context

In 1886, germanium was discovered by a German chemist, Clemens Winkler [42]. About 50 years later, Shockley, Brattain and Bardeen designed the first transistor using germanium making it the precursor of electronic semiconductor based devices [16]. Despite the fact that electronics was still in its infancy, materials scientists already knew how to tune the electronic properties of germanium by introducing chemical impurities into the matrix as dopants [16].

Although germanium does not exist as a standalone mineral after its extraction from materials such as zinc ore, high purity single crystalline material can be obtained using the Czochralski technique [16]. Invented in the 1950s for the purpose of producing high quality single

crystalline materials, the Czochralski process was first established on germanium before being transferred to silicon. In fact, the technology transfer to silicon did not only concern the Czochralski process as silicon became the primary material for electronic devices most of the semiconductor processing techniques became centred around silicon [34]. Likewise, scientific investigations into semiconductors properties became more and more focused on silicon at the expense of germanium.

Germanium has a lot in common with silicon (both are indirect band gap semiconductors with the same type of crystalline structure [15]). However, it has a number of drawbacks compared with silicon. Germanium is less abundant than silicon and consequently costlier. Its smaller band gap makes it much more subject to current leakage [21], [29]. Furthermore, one of its major flaws is the instability of its native oxide layer. The oxide layer which plays the role of the insulator in a metal-oxide-semiconductor field-effect transistor (MOSFET) is crucial in those types of device. Therefore, this issue makes it unsuitable to be the material of first choice when building MOSFETs [28], [34]. Yet, in a context where alternative materials need to be envisaged to replace bulk silicon, some of the differences between silicon and germanium are now causing the industry to reconsider germanium as a major candidate to replace silicon in future transistors devices, therefore prompting a new momentum for research on germanium materials [21], [43].

## 2.2. General properties of germanium

Germanium belongs to the group IV in column 14 of the periodic table and is a metalloid. As is the case for silicon, it has four electrons in its valence shell and forms hybridized  $sp^3$  covalent bonds [44]. As shown in figure 2.1, germanium typically crystallises in a diamond-like structure [21]. Each germanium atom is bonded to its four nearest neighbours forming a tetrahedron with an angle of about  $109.5^\circ$  [45]. The crystal can be depicted using a face-

centred cubic (fcc) Bravais lattice with half of the tetrahedral sites occupied or alternatively can be seen as a fcc lattice coupled with another fcc lattice that has been translated by  $\frac{1}{4}$  of the main diagonal of the cube. The diamond structure therefore possesses four atoms from the fcc lattice plus four atoms from the tetrahedral sites making eight atoms. At room temperature (RT) and at atmospheric pressure the lattice constant ( $a$ ) of germanium is about 0.566 nm [21], the distance between each germanium atom is  $\frac{\sqrt{3}}{4}a \approx 0.245$  nm and its nominal density is  $5.3234 \text{ g.cm}^{-3}$  or in atomic density ( $\rho$ ) is  $4.42 \times 10^{22} \text{ cm}^{-3}$  [15].

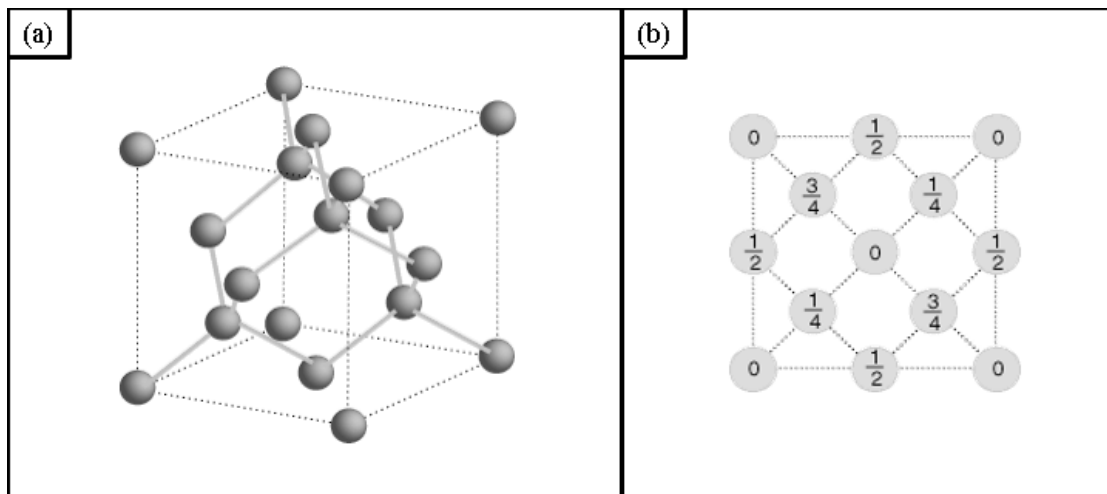


**Figure 2.1:** (a) Unit cell showing the crystalline structure of germanium, from [46] along with (b) a representation of the unit cell from a [100] direction where atom position are shown as a fraction of the cube edge length, from [47].

## 2.3. Properties as a semiconductor

### 2.3.1. Valence band and conduction band

In a single germanium atom, each electron has its own unique quantum state [48]. However, in the case of several atoms, the quantum state of the electrons can be altered depending on the

inter-atomic distances. Indeed, as the distances between atoms get smaller, the electrons of each atom can interact with the electrons of the other atoms. Consequently, as the Pauli exclusion principle forbids two electrons from sharing the same quantum state, their energy levels (which depend on the quantum states) are slightly shifted [48]. In a solid, to avoid violating the Pauli exclusion, the energy levels are shifted relative to each other in such a way to make the energy levels similar to a continuum of available quantum states for electron occupancy [48], [49]. These continuums are known as the permitted energy bands. Between these permitted bands the energy levels with no available quantum states form the forbidden bands [48], [49]. In a solid there are several permitted bands, whose characteristics vary depending on the energy level of the electrons surrounding the atoms nuclei. In germanium, for instance, the band positioned around the 1s level has a width of approximately  $10^{-3}$  eV, whilst the 3s and 3p levels form a permitted occupied energy band of approximately 10 eV (the valence band) plus an empty energy band of 20 eV (the conduction band) separated by a forbidden band gap of approximately 0.66 eV at RT [50].

Providing energy greater than the band gap to the electrons in the valence band enables their promotion from the valence band to the conduction band [48]. Typically, due to its small band gap which allows electrons to be promoted to the conduction band via visible light absorption or via a relatively low thermal energy (below its melting point), germanium is classified as a semiconductor as opposed to insulators which have bigger band gaps [48], [51]. Conversely, in conductors there exists an overlap of the valence and conduction bands [49], [51]. The allowed energy levels are usually described as function of the propagation vector  $\vec{K}$  where  $\vec{K}$  is proportional to the momentum of the electron. As seen in figure 2.2, in germanium the smallest energy transition between the valence band and the conduction band does not correspond to the same value of  $\vec{K}$ , there is thus a difference in the momentum of the electron

when such transition occurs. For these reason germanium is said to be an indirect band gap semiconductor, similarly to silicon [48].

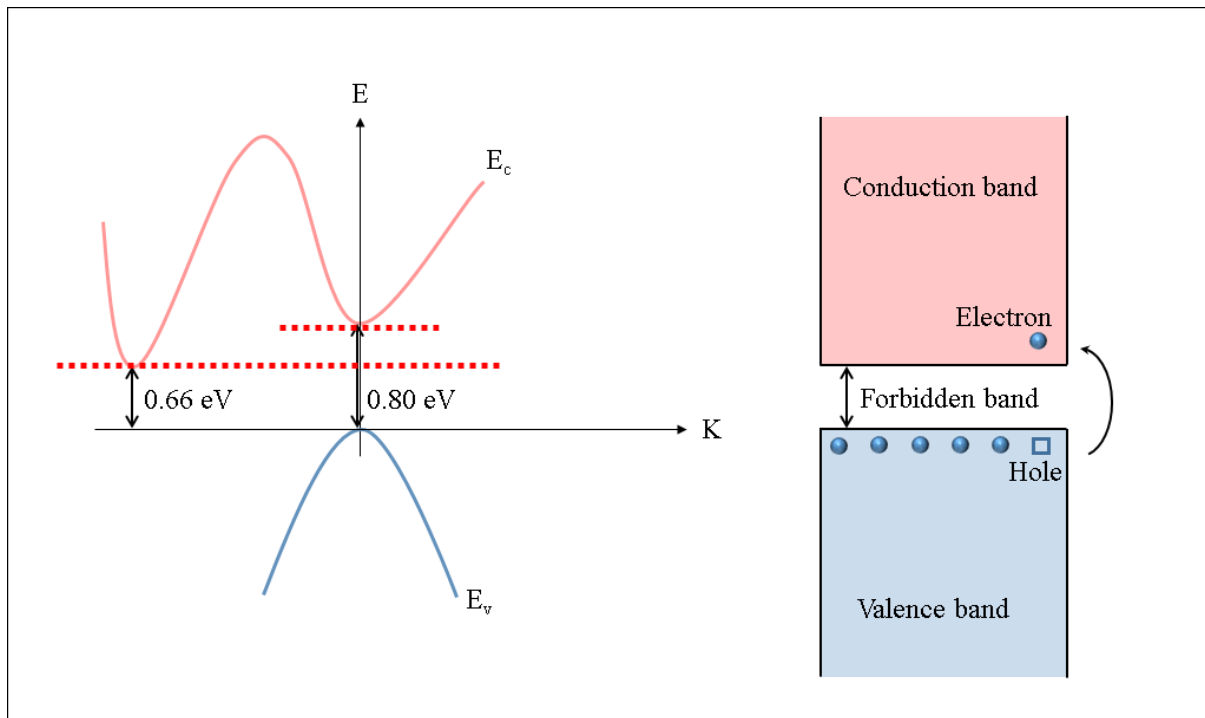


**Figure 2.2:** Structure of the bands showing the energy differences of 0.66 eV and 0.80 eV between the valence band and the conduction band of germanium. The semiconductor has an indirect band gap of 0.66 eV.

### 2.3.2. Empty or full: occupation of the band

Using quantum physics, the density of state ( $D_e$ ) of permitted energy levels for a charge carrier of mass  $m_*$  as a function of energy ( $E$ ) and of the reduced Planck constant ( $\hbar$ ) where  $E_c$  is the energy at the minimum of the conduction band is determined in a bulk using the following equation 2.1 [48]:

$$D_e(E) = \frac{1}{2\pi^2} \left(\frac{2m_*}{\hbar}\right)^3 (E - E_c)^{1/2} \quad (2.1)$$

To define how the electrons are distributed within the available density of states, a probability of occupation is described using an energy level called the Fermi level ( $E_f$ ) and known as the Fermi-Dirac distribution  $f(E, T)$  described by equation 2.2 [48]:

$$f(E, T) = \frac{1}{1 + \exp\left[\frac{E - E_f}{kT}\right]} \quad (2.2)$$

Setting the temperature to 0 K in equation 2.2 where  $k$  is the Boltzmann constant, all electrons have energies below the Fermi level energy [48]. Under conditions where the semiconductor is undoped, this level can be considered as being in the middle of the forbidden band and at 0 K, the electrons are all in the valence band whilst the conduction band is empty. However, as can be seen in figure 2.3, at higher temperatures the distribution of the electrons will be affected as energy is given to electrons [48], [51]. Indeed, if the electrons gain enough energy they might be promoted from the valence to the conduction band as the final distribution of the charges depends on the probability of occupation of energy levels (defined via the Fermi-Dirac distribution) and the available energy levels (defined via the density of states) as illustrated by figure 2.4 [48].

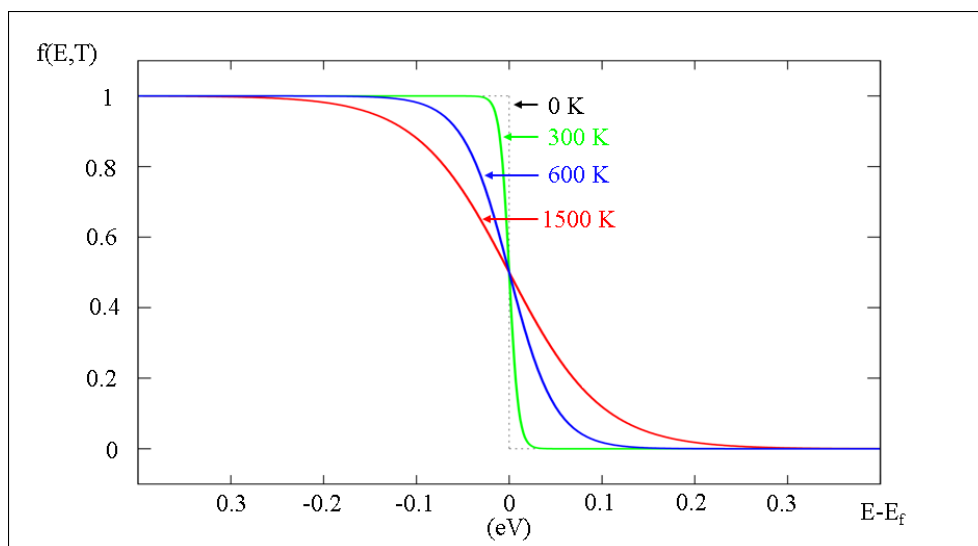


**Figure 2.3:** Distribution of the electrons as a function of temperature and energy according to equation 2.2, showing the Fermi-Dirac distribution at four different temperatures.

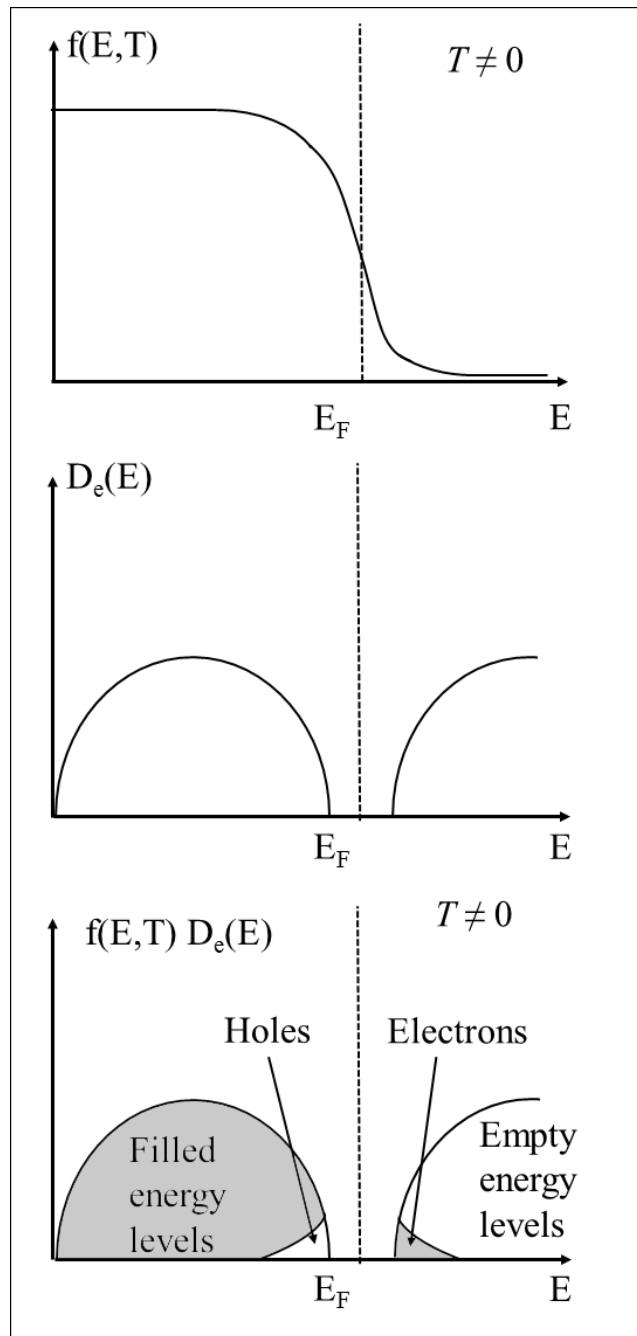


**Figure 2.4:** Graphs showing (a), an energy distribution of electrons defined via  $f(E, T)$ , (b) the valence and the conduction band defined via  $(D_e)$  and (c) the convolution of the two, defined via  $f(E, T)(D_e)$  where the empty and occupied energy levels can be seen.

To model the way an external force affects the electrons distributed within these bands, a mass  $m_e$ , is allocated to the electrons. In a semiconductor, each state left empty in the valence band is referred to as a pseudo-particle called a “hole” which is also allocated a pseudo mass  $m_h$  [21], [48], [51]. According to classical mechanics, the external force applied to the charge ( $F_{ext}$ ) (for instance an electric field) can be expressed via equation 2.3.

$$\sum F_{ext} = m_* \times acceleration \quad (2.3)$$

Where  $m_*$  is the mass of either the electron or the hole (known as charge carriers), and  $F_{ext}$  is the external force applied to the charge. In a semiconductor, the value of these masses  $m_*$  has an important effect on the electrical properties of the semiconductor. Indeed, as described by the previous expression, the smaller these masses are, then the bigger the effect of an exterior force on them (which also means a higher mobility of the charge carriers). In germanium, the masses  $m_e$  and  $m_h$  are both smaller than those in silicon making germanium a valuable material for future electronic devices, giving better conductivity, lower energy consumption as well as higher speed circuits [21], [52], [53]. In fact, the mobility of the charge carriers in germanium compared to other semiconductors is one of the main reason why germanium is now attracting so much interest [34].

### 2.3.3. Doping germanium

Compared to metals, semiconductors have poor conductivity as only a relatively small proportion of electrons are free to travel in the material. In table 2.1, it can be seen that germanium has a conductivity that is many orders of magnitude lower than that of metals [54].

Material	Conductivity (S.m <sup>-1</sup> )
<b>Insulators</b>	
Glass	10 <sup>-15</sup> to 10 <sup>-11</sup>
Hard rubber	10 <sup>-14</sup>
<b>Semiconductors</b>	
Silicon	1.56×10 <sup>-3</sup>
Germanium	2.17
<b>Conductors</b>	
Platinum	9.43×10 <sup>6</sup>
Tungsten	1.79×10 <sup>7</sup>
Aluminium	3.77×10 <sup>7</sup>
Gold	4.1×10 <sup>7</sup>
Copper	5.96×10 <sup>7</sup>
Silver	6.30×10 <sup>7</sup>

**Table 2.1:** Conductivity of example insulators, semiconductors and conductors according to [54].

Undoped semiconductors are described as being intrinsic [21], [48]. In order to introduce additional charge carriers into an intrinsic semiconductor, impurities can be implanted into the material during a process called doping. In germanium and silicon, the common doping method consist of putting in substitutional lattice-site dopants from column III or VI of the periodic table of the elements [21], [48], [55]. The introduction of the dopants from these columns will result in p-type doping or n-type doping, respectively. As illustrated in figure 2.5, when a dopant from column VI is introduced in a lattice site, its extra electron can become a charge carrier in the material, otherwise, when a dopant from column III is introduced to a lattice site the lack of electron is assimilated to a hole which will also be free to participate in the conduction of current [48], [55].

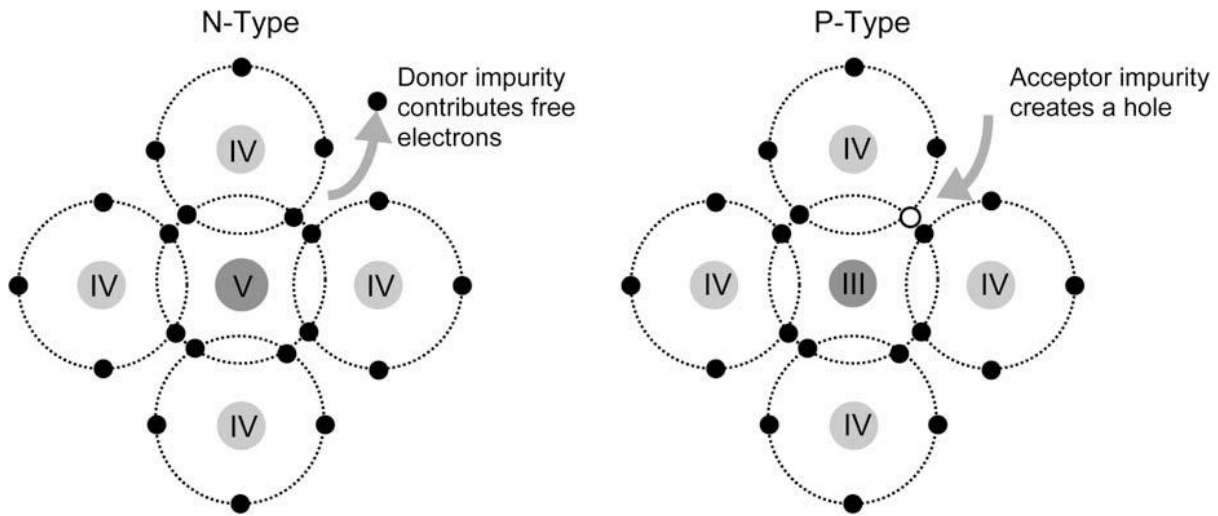


**Figure 2.5:** Schematic showing how the introduction of a dopant from column V or III can result in a free electron and a hole, respectively, as just four electrons are required to form a covalent bond in the germanium material. From [55].

In each of these cases, the conductivity,  $\sigma_c$ , of the doped material can be expressed as a function of the dopant concentration  $N_d$  and the mobility  $\mu$  of the carrier having a charge  $q$  [48]:

$$\sigma_c = qN_d\mu \quad (2.4)$$

The mobility of the electrons and the mobility of the holes are given by the following equation where  $\tau_c$  is the mean free time between collisions [48]:

$$\mu_c = \frac{q\tau_c}{m_*} \quad (2.5)$$

To tune the properties of an intrinsic semiconductor via doping (and make it extrinsic), two ways are usually used: the diffusion of the chemical elements into the semiconductor (which is not the subject of this work) and ion implantation which is discussed below.

### 3. Ion implantation

#### 3.1. Outline of ion implantation

Often used for the purposes of making transistors, and in particular MOSFETs, ion implantation was first patented by Ohl, Moyer and Shockley in the 1940s [56]. In this technique, ions are accelerated towards a target material inducing several effects such as atomic displacement, sputtering or implantation which as will be addressed later can modify the target material in various ways [56], [57]. Compared to chemical diffusion, ion implantation presents many advantages such as better control of both the dose and the depth [38].

For an accelerated ion to be implanted into a target material, it needs to lose its kinetic energy. The interaction between the particle and the solid is the result of the ion interacting with the target material nuclei (nuclear stopping) and with the target material electrons (electronic stopping) [20], [57].

#### 3.2. Electronic stopping

The energetic ion may lose a part of its energy via its interaction with the target atoms' electrons [58]. Such interactions are characterised by an electronic stopping power ( $S_e$ ) and can be approximated by equation 2.6 in which  $S_e$  is a function of the atomic number of the target material,  $Z_1$ , and the ion,  $Z_2$ , the velocity of the ion,  $v$ , the atomic density of the target material,  $N$ , and the Bohr radius,  $a_0$  [59].

$$S_e = \frac{Z_1^7 Z_2^4 a_0 N v}{\left( Z_1^{\frac{2}{36}} + Z_2^{\frac{2}{3}} \right)^{\frac{3}{2}}} \quad (2.6)$$

The slowing down via electronic loss is a continuous deceleration of the ion [59]. During this process, the Coulomb interactions lead to the ion losing its kinetic energy and the electronic stopping is thus described as leading to inelastic energy losses [60]. During the inelastic loss, the energy lost to the target material may sometimes modify its electronic properties and/or promote electrons to higher energy levels. The lighter the ions and the higher their energy, the more the electronic stopping dominates over the nuclear stopping [60]. An example of the relative contribution of the nuclear and electronic stopping is shown in figure 2.6.

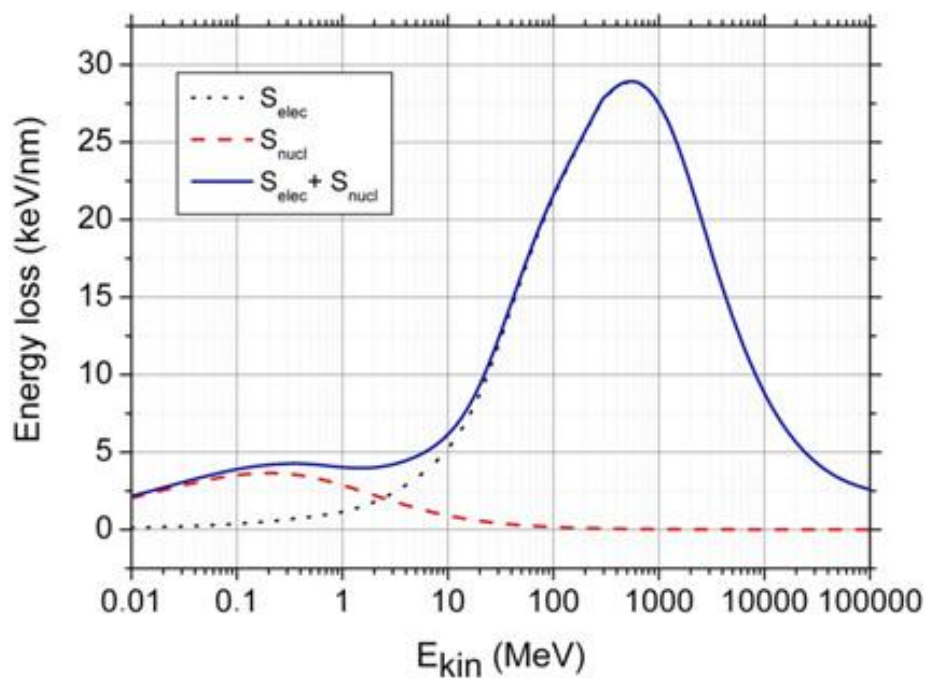


**Figure 2.6:** Graph showing a typical example of the relative contribution of the nuclear energy loss (in red) and the electronic energy loss (in black) as well as their sum (in blue) as a function of the particle energy. This example corresponds to the irradiation of SrTiO<sub>3</sub> via xenon ions as determined using Monte-Carlo calculations. From [61].

### 3.3. Nuclear stopping

Unlike electronic energy loss where the ions continuously lose energy, the nuclear energy loss occurs in discrete events [60], [62]. The nuclear energy loss can be described as a ballistic

phenomenon where the ion interacts with the nucleus of an atom of the target material. It is therefore commonly treated as a binary collision which can generate displacements and thus, defects [63]. However, the binary collision approximation which only considered a two-body collision, (i.e. meaning that effects from neighbouring atoms are not taken into account during the energy transfer between the ion and the target atom) can only be made when the mean free path does not approach the interatomic spacing. Accordingly, if collision events cannot be treated individually (which can for instance happen when the ion has a low energy) the binary collision approximation cannot be applied [62], [64].

In this work, the energy regime used for ion irradiation (30 to 300 keV) will make the nuclear stopping contribution most significant; consequently, the radiation damage is mainly induced by the nuclear collisions. If the incident ion transmits enough energy to displace the target atom, that atom will be knocked out from its lattice site whilst the ion may carry on its course within the material displacing more atoms. For germanium, the energy required to displace an atom is approximately 21 eV (according to DFT simulations reported in [65]). After being displaced by the incoming ion, this primary knock-on atom (PKA) can then also travel in the material and, similarly to the ion, will be slowed down by electronic and nuclear energy losses until it comes to rest in or exits from the target material. Thus, along its path the PKA can also induce lattice disorder via recoils through nuclear stopping. Consequently, not only must the damage caused by the ion be taken into account for the crystal disorder but also that by the recoiling target atoms. The displaced PKAs and their subsequent recoiling targets form what is termed an atomic collision cascade [66]. The number of displaced atoms can be calculated using the Kinchin-Pease model [66], where the number of displaced atoms is proportional to the energy lost by the incoming ion. In a monoatomic material such as germanium the number of displaced atom ( $n_d$ ) can be expressed as a function of the PKA energy ( $E_I$ ) using equation

2.7 via the Kinchin-Pease formalism. The contribution of electronic loss is often taken into account by modifying the previous expression which becomes equation 2.8 [67], [68].

$$n_d \approx \frac{E_1}{2 \times E_d}, \quad (2.7)$$

$$n_d \approx 0.8 \times \frac{E_1}{2 \times E_d}, \quad (2.8)$$

It is worth noting that whilst equation 2.8 gives an approximation of the number of displaced atoms during irradiation, the final state of the material is dependent on many dynamic processes such as the recombination of defects. Such recombination of defects will greatly reduce the final defect concentration in an irradiated material and may be estimated via molecular dynamic (MD) simulations.

### 3.4. Range

The incoming ions may experience a succession of nuclear collisions and electronic interactions and ultimately come to rest in, or exit from the material [35]. To an initial approximation where diffusion effects are neglected, if the particle is implanted in the target material, its implantation depth will depend on both the nuclear and electronic stopping interactions (and will typically be smaller for heavy ions than for light ions for a given energy). Theoretically, the implantation profile can be approximated as having a Gaussian distribution centred on the projected range,  $R_p$ . (It worth noting that this Gaussian distribution for implanted ions is more accurate when it comes to amorphous materials). To describe the distribution of the ions it is also common to use other parameters such as the straggle, which indicates the width of the Gaussian at 60% of the maximum of the implanted ions concentration. The straggle thus gives information about how peaked or spread the ion distribution is. Additionally, the skewness, is used to show how the distribution of the ions differs from an

idealised Gaussian distribution. Instead of a perfect Gaussian, the distribution of implanted ion will show a tail towards the surface or towards the backside of the irradiated material. The skewness, can therefore be negative if the distribution shows that the ions are relatively more located towards the surface or positive if the ions are implanted deeper than the profile depicted by the Gaussian. Typically, as shown in figure 2.7, the greater the energy is the more pronounced the positive skewness is. In crystalline materials, the profile of the distributed ions can be heavily disturbed with a large positive skewness if channelling (described below) occurs.

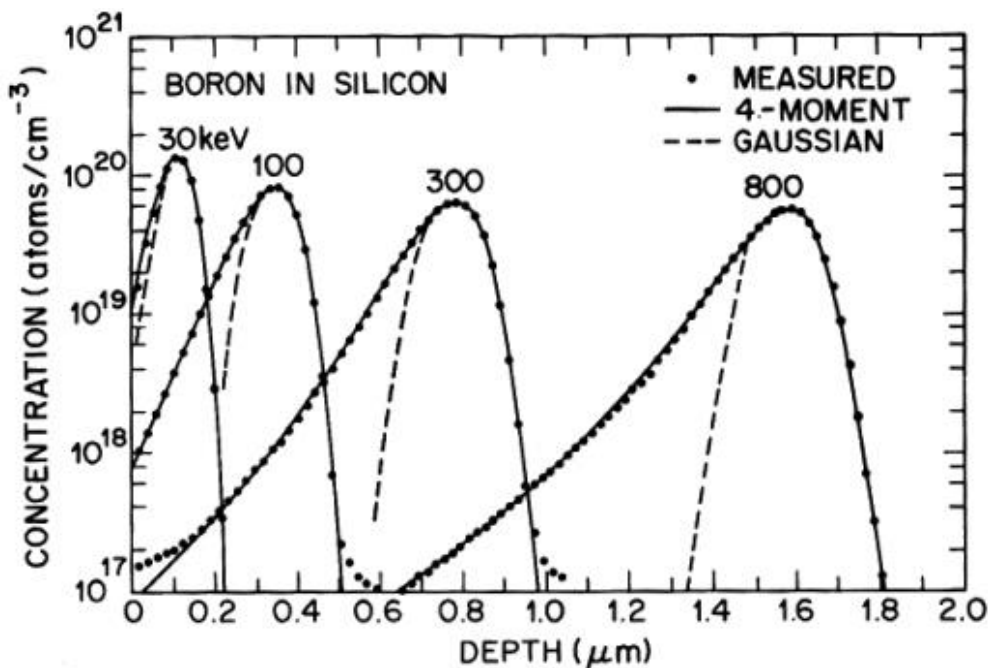


**Figure 2.7:** The concentration of boron implanted in silicon is shown by the continuous line as a function of depth for four different acceleration energies (30, 100, 300 and 800 keV) and can be compared with the concentration which would result if their distribution followed a Gaussian distribution (shown by the dashed lines). Whilst the experimental results do not overlap with the Gaussian curves, as shown in the figure, they can be fitted with the algebraic curves indicated by black lines in the figure. (These curves are called four moment curves and can be used to model skew curves). From [69].

### 3.5. Channelling

For the purposes of ion implantation into crystalline semiconductors, the relative angle between the ion beam and the crystal must be chosen carefully as it can affect the probability of the ions being scattered and thus alter the implantation range [57], [70]. Some crystallographic orientations are more open than others, giving the ions less probability of colliding with atoms in the material [57]. For instance, in germanium the direction [100] is so open that many ions may travel in the relatively “hollow” direction, undergoing so-called channelling effects. As the channelled ions will encounter fewer atoms, they will travel deeper inside the material.

For this reason, it is common to tilt the sample in order to avoid irradiation parallel to such crystallographic directions [57], [71]. However, as the tilting procedure does not prevent all channelling effects, it is common to preamorphise the sample so that the profile and the projected range can be better forecast [27], [72]–[74]. Typically, software such as SRIM [75], TRIDYN [76] or MARLOWE [77] allow the forecasting of many of the consequences of ion irradiation.

### 3.6. MONTE CARLO SIMULATIONS: SRIM

Of the various computer codes used to calculate the interaction between ions and matter, the Stopping and Range of Ions in Matter (SRIM) code is the most popular one and the one that will be used in the current work (this will be described in the next chapter) [75]. Based on Monte Carlo (MC) calculations, it includes a suite of programs from which TRIM is the most comprehensive one. Using quantum mechanics and statistical algorithms, it treats the interaction between ions and amorphous solids at 0 K thus under circumstances where the induced defects are immobile. In the simulation which will be described in the next chapter, the chosen ion is sent to the target under conditions which can be customised via variables such

as its incident angle, its energy and the chemical composition of the materials being subject to irradiation [75].

SRIM gives various information regarding the irradiation, such as the displacement events (which allows the displacement per atom (dpa) to be consequently calculated), the nuclear energy loss and the range of the ions. However, as SRIM calculations are performed for amorphous bulk material with a planar surface, they do not take into account the crystallinity and cylindrical shape of a nanowire. To compensate for the issues regarding the shape of nanowires, a MATLAB script designed within the Electron Microscopy and Materials Analysis (EMMA) group has been used. Whilst other code such as Iradina and 3DTRIM can also be used for this purpose, the MATLAB script has two main advantages. It actually relies on SRIM calculations and not on lookup-tables, therefore, its calculations are more accurate (but slower) than those of Iradina and it benefits from the fact that SRIM calculations have been intensively benchmarked over time [78], [79]. The script is called *Ion Damage and Range in the Geometry Of Nanowires* (IDRAGON) and will be described in the Chapter 3 [80].

## 4. Defects

### 4.1. Overview

As nuclear stopping tends to displace atoms within the irradiated material, many kinds of defects are expected [81]–[83]. The ion-induced damage can be one of the main drawbacks resulting from ion implantation. When doping semiconductors, the defects might interact with the dopants altering their distribution and/or prohibiting their activation. For instance, indium (n-type dopant) in germanium is known to bond with vacancy-type defects enhancing their diffusion [84], [85].

Furthermore, the introduction of defects inside the material might induce density changes i.e. volume expansion, compressive stress, or strain [86]–[88]. Lastly, accumulation of defects might lead to an amorphisation of the crystal [25], [89].

#### 4.2. Vacancies

A vacancy is a type of defect which corresponds to a lack of an atom on a lattice site, as illustrated in figure 2.8 [90]. When a vacancy is introduced into a crystal, there is a relaxation around the missing atom leading to a contraction around the point defect [86].

In germanium, the study of point defects is mostly done via quantum calculations but the direct observation of vacancies has been possible after creation via electron irradiation at cryogenic temperatures. The low temperature permitted freezing of the defects and thus limited their recombination to make such observations possible [52], [91].

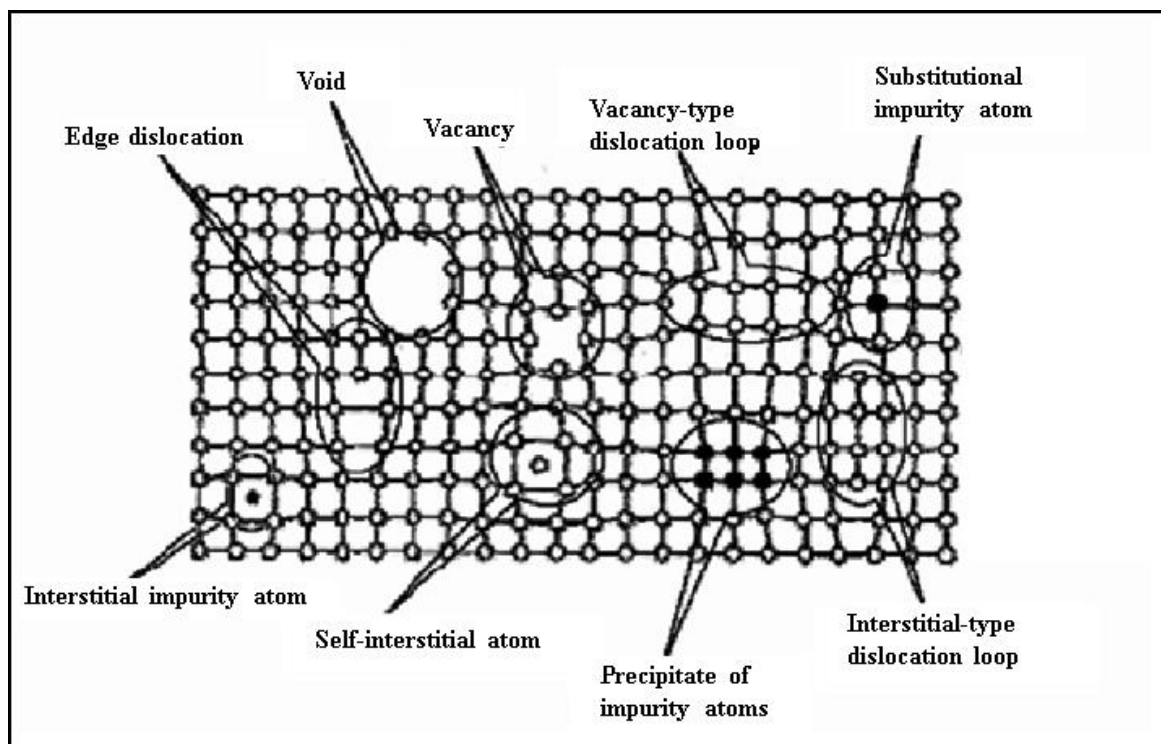


**Figure 2.8.** Schematic summarising the main types of defects in a crystal. From [92].

### 4.3. Interstitials

As shown in figure 2.8, interstitials are found in positions that should not be occupied in a perfect crystal [21]. If these are native atoms, then they are called self-interstitials. As will be addressed later, the fact that in germanium, self-interstitials are expected to have no role, or a very limited one, in the diffusion of dopants and for this reason suggests that they only exist at a low concentration [43], [84], [93]–[96]. Even though creation of these point defects via electron irradiation has been observed at cryogenic temperature [84] their presence under thermal equilibrium at RT is suspected to be negligible as compared to that of vacancies [84], [93].

In germanium the self-interstitials can in principle occupy several atomic-configurations [21], as illustrated in figure 2.9. Two atoms can be put on a single lattice site creating what is called a split interstitial. Alternatively, as shown in figure 2.9, a hexagonal type of self-interstitial can also be placed at the centre of a hexagon formed by the germanium atoms from the lattice. Lastly, a tetrahedral type of self-interstitial will be formed when it bonds to four atoms of the lattice [21].

If an atomic displacement occurs during ion irradiation, an atom in the material can leave a vacant site and travel until stopping in an interstitial position [97]. Therefore, as a result of ion irradiation pairs of self-interstitials and vacancies known as Frenkel pairs are formed. Similarly, to the vacancy, the interstitial stabilizes itself via relaxation. However, in this case the relaxation volume corresponds to an expansion [52], [86], [98].

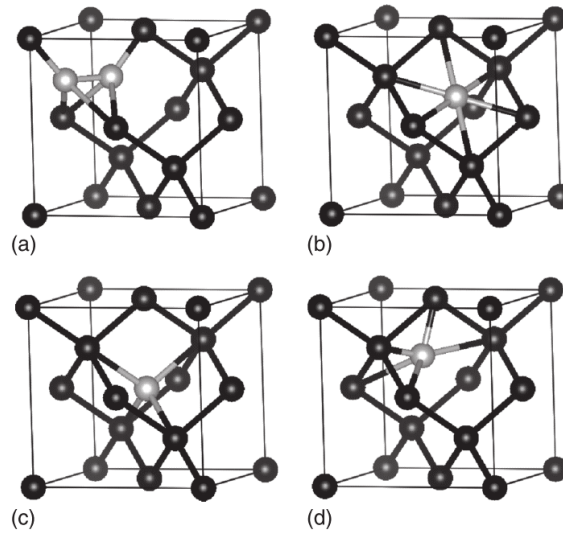


**Figure 2.9:** Type of interstitials in germanium as they can be of type: (a) split, (b) hexagonal (c) tetrahedral and (d) distorted hexagonal. From [21].

#### 4.4. Defects at thermal equilibrium

As a result of irradiation, atomic displacements can occur resulting in the formation of several types of defects. However, even without radiation damage there will be defects within a crystal (typically interstitials and vacancies) [84]. Indeed, it is thermodynamically favourable for the crystal to have a fixed number of defects at a given temperature, there is thus for the defects, a thermal equilibrium [99], [100]. Using thermodynamics, the intrinsic concentration of defects can be deduced from the Gibbs free energy ( $G$ ) which under equilibrium condition is minimised (i.e. equation 2.9 is equal zero and the symbol  $\Delta$  means the difference between an initial and a final state) [99].

$$\Delta G = \Delta H - T\Delta S \quad (2.9)$$

Therefore, under conditions where the temperature ( $T$ ) is constant, the concentration of defects will depend on the enthalpy ( $H$ ) and the entropy ( $S$ ). As will be now shown, equation 2.9 means that vacancies have an opposite effect on the evolution of the equation and thus on the

minimisation of the Gibbs free energy. Indeed,  $\Delta G$  will be increased by the presence of the point defects due to their enthalpy of formation  $\Delta H_f$ , whilst on the other hand  $\Delta G$  will be decreased by their presence as they will induce more disorder within the crystal thus increasing  $\Delta S$ . Consequently, there is a concentration of point defects at a temperature  $T$  (i.e. the thermal equilibrium concentrations of point defects) at which the terms  $\Delta S$  and  $\Delta H$  will be such that  $\Delta G=0$ . It is worth noting that equation 2.9 also shows the importance of the temperature on the final concentration of point defects as a higher temperature will induce a greater effect of  $\Delta S$  on equation 2.9. In semiconductors, the effect of temperature will be critical as it implies that a semiconductor will intrinsically have a higher quantity of defects at higher temperatures as their presence will tend to minimise the entropy [99].

#### 4.5. Diffusion

In germanium, the diffusion of point defects (and particularly of vacancies) is an important feature as it mediates the diffusion of the implanted dopants [84], [93]. Diffusion is dependent on temperature as the thermal energy is used to activate the motion of atoms. Depending on the type of diffusion mechanism, different energy barriers ( $E_m$ ) need to be overcome [99]. As shown in figure 2.10, in a vacancy diffusion mechanism the motion of the vacancy is opposite to the motion of the atom. Furthermore, as compared with interstitial diffusion, (also shown in the figure 2.10), the energy barrier  $E_m$  to overcome for vacancy diffusion is higher as it necessitates stronger inter-atomic bond breaking [99].

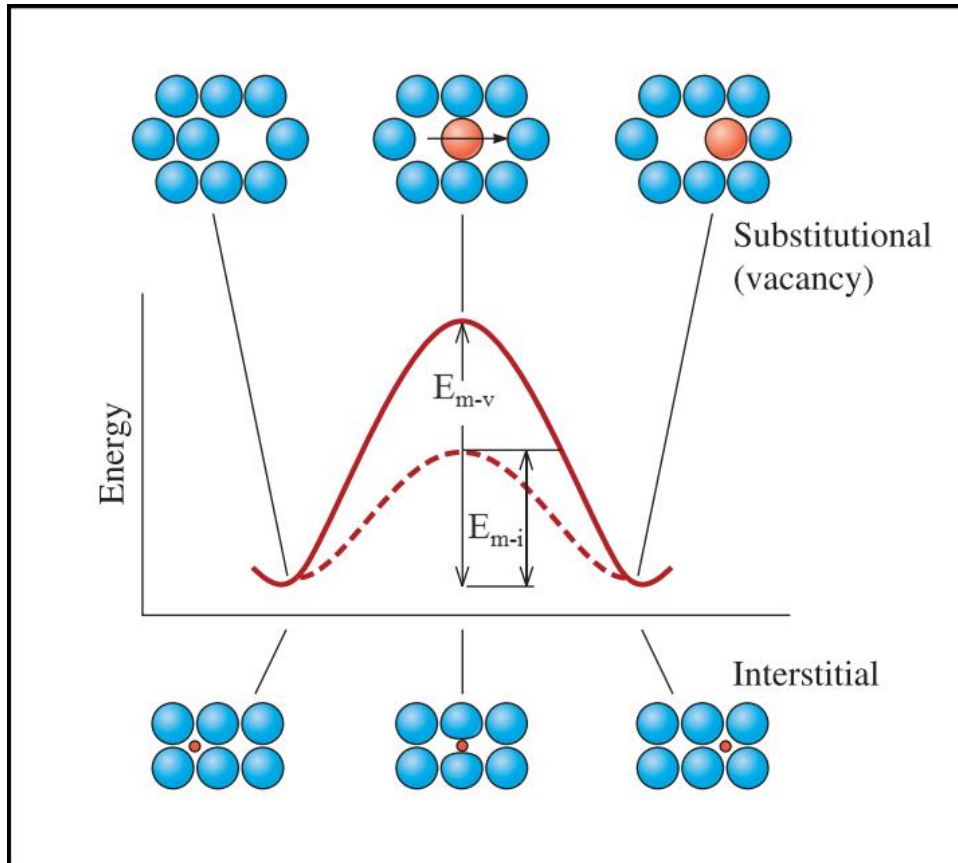


**Figure 2.10:** Vacancy diffusion (top) and interstitial diffusion (bottom) are shown as well as the energy barrier corresponding to each of these two diffusion mechanisms (where the interstitial shown in the picture represents a smaller atom than these of the material). From [101].

The flux of atoms  $J_x$  (in  $\text{kg}\cdot\text{m}^{-2}\cdot\text{s}^{-1}$ ) during diffusion indicates the rate of diffusion and necessarily depends on the diffusion mechanism. It can be mathematically described using Fick's laws. When the assumption is made that the concentration profile within the sample does not vary with time, Fick's first law shown by equation 2.10 can be invoked and depends on the gradient of the concentration ( $C$ ) (in  $\text{kg}\cdot\text{m}^{-3}$ ) and on the diffusion coefficient ( $D$ ) (in  $\text{m}^2\cdot\text{s}^{-1}$ ). When the concentration profile evolves during diffusion, the non-steady-state of the system requires the use of Fick's second law via equation 2.11 [90], [99].

$$J_x = -D \frac{dC}{dx} \quad (2.10)$$

$$\frac{\partial C}{\partial t} = D \frac{\partial^2 C}{\partial x^2} \quad (2.11)$$

The diffusion coefficient can be estimated via equation 2.12 and follows an Arrhenius dependence where  $D_0$  is a temperature independent constant (in  $\text{m}^2.\text{s}^{-1}$ ) and  $Q_d$  is the activation energy for the diffusion process (in  $\text{eV}.\text{atom}^{-1}$ ) and is the sum of  $E_m$  and of  $Q_v$  which is the energy formation of the defect [99].

$$D = D_0 e^{-\frac{Q_d}{k_b T}} \quad (2.12)$$

#### 4.6. Interaction of Vacancies with dopants in germanium

A useful way of indirectly observing and characterising point defects is by studying the diffusion of metal impurities, dopants or isotopes and to subsequently deduce information regarding the defects which mediate their diffusion [84], [93], [102], [103]. Some of the earliest work by Valenta and Ramasastry [102] in 1957 showed that, unlike in silicon where the both the concentration of interstitials and vacancies are comparable, vacancies are the main point defects present in germanium [102]. To do so, they used a method developed by Reiss and Fuller [104] based on the fact that the solubility of acceptor content within n-doped semiconductors increases with the concentration of n-type dopants (i.e. dopants which are donor species and thus donate electrons), whilst conversely the solubility of donor content in the semiconductor increases with the concentration of p-type dopants [104]. As vacancies are considered as acceptor content (i.e. they tend to attract negative charges), Valenta and Ramasastry managed to increase the concentration of vacancies within the germanium specimen using heavy n-type doping. They consequently observed an increase in the self-

diffusion coefficient of the germanium atoms which was proportional to the increase of the vacancy concentration, thus showing that self-diffusion of germanium was mediated by vacancies [102].

More works have since confirmed that self-diffusion and dopant diffusion in germanium is mainly controlled by vacancies and that the vacancies are in most doping conditions in a negative charge state [84], [94], [103].

Furthermore, experimental works and DFT calculations have also shown that the concentration of self-interstitials in germanium at thermal equilibrium is low and that the diffusion of dopants is not mediated by self-interstitials [84], [94], [102], [103]. It must be noted that a higher concentration of vacancies can indeed be expected due to the lower formation energy of vacancies compared with that of the interstitials as it is reported to be around 2 eV for the vacancy (with a migration barrier of approximately 0.6 eV) [21], [84], [105]–[108], whilst the formation energy of the interstitial is about 3 eV (with a migration barrier of approximately 0.3 eV) [84], [109]–[111]. Furthermore, it was demonstrated that vacancies regulate the diffusion rate of dopants [84], [96]. Figure 2.11 shows the diffusion coefficient of several n-dopants (antimony, arsenic and phosphorus) and p-dopants (indium gallium, aluminium and boron) in germanium as well as of germanium self-diffusion [84]. Interestingly, the diffusion coefficient of the donor species is greater than that for self-diffusion. According to several articles in the literature, the explanation for the greater coefficient of diffusion is related to the fact that there is an attractive Coulomb interaction between the donor species (the n-type dopants) and the acceptor vacancies responsible for diffusion. On the other hand, the p-type dopants which are also acceptor species do not benefit from the Coulomb attraction and their diffusion coefficient is consequently close to that of the self-diffusion [84]. In addition to electronic affinity, steric considerations are also proposed as factors that further influence the attraction between vacancies and dopants. In this aspect it is proposed that lattice deformations are minimised

when a vacancy is in the vicinity of a relatively-big atom, thus enhancing the bonding between the dopant and the vacancy and consequently the vacancy-mediated diffusion of relatively large atoms such as antimony, whilst reducing that of the smaller atoms such as boron [84].

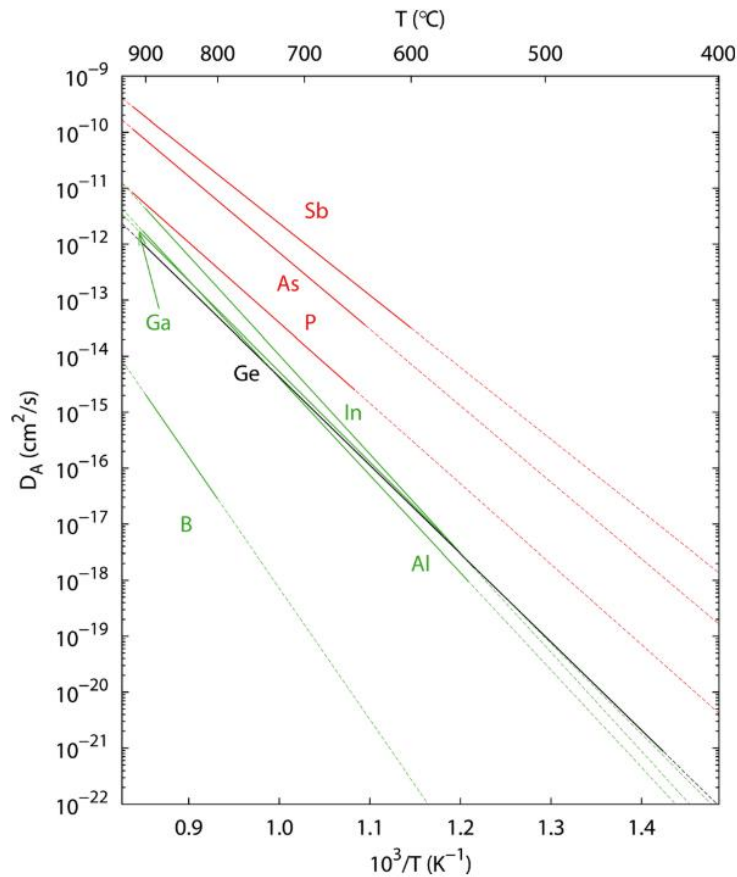


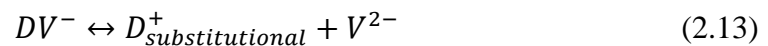
**Figure 2.11:** In the graph the diffusion coefficient as a function of temperature in germanium of the p-dopants (in green), n-dopants (in red) can be compared with the self-diffusion coefficient of germanium (in black). At temperatures at which diffusion coefficients have not been experimentally observed, the extrapolated values are shown as dashed lines instead of continuous lines. From [84].

Lastly, it is interesting to note that according to DFT calculations self-interstitials are expected to be subject to a Coulomb attraction with boron atoms which are acceptor species [84]. Consequently, the presence of self-interstitials in germanium should therefore enhance diffusion of the acceptor dopants such as boron. The fact that the diffusion of p-type dopants

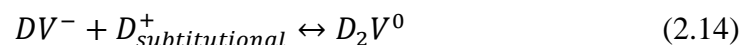
is slow in germanium, thus provides further evidence that the concentration of interstitials is negligible [37], [84], [94], [96].

In semiconductors, during high temperature annealing, the thermal energy ensures the diffusion of dopants into substitutional sites [22], [112], [113]. However, it is worth noting that the fast diffusion of dopants is typically considered as detrimental to the conductivity of the semiconductor and that during annealing their interaction with point defects may lead to the deactivation (making them incapable of providing the charges carriers) as well as modifying the implantation profile of the dopants within the semiconductor [37], [84], [94], [96].

The equation describing the interactions between the vacancy and the n-type dopants is shown in equation 2.13 where  $D$  represent the donor atom,  $V$  the vacancy and the charge states are indicated by the superscripts [84]:



As secondary ion mass spectrometry (SIMS) characterisation has shown that there is a difference between the concentration of dopants within doped germanium and the expected extent of electrically active dopants, it has been suggested that dopants and defects must form a neutral complex [84]. Typically, the electrical deactivation of the donor is highly pronounced in heavily-doped materials and the main reaction which forms neutral clusters has been reported as being described by equation 2.14 [84]:



## 4.7. Clusters of defects

As previously stated, vacancies and self-interstitials can interact and annihilate each other via recombination [114], [115]. However, the opposite can also arise and point defects might agglomerate to form more complex defects such as dislocation loops or precipitates as shown in figure 2.8 [57].

Formation of defect clusters has been shown to happen more often when a semiconductor is irradiated by heavy ions than when irradiated by light ions. This has for instance been evidenced via MD simulations of the irradiation of silicon with boron and arsenic by Caturla et al. [116]. When comparing the collision cascades induced by the two ions, the authors kept either the range  $R_p$  or the energy density identical for the two ions. It was shown that the cascade formed by the heavier ion was denser than the one resulting from irradiation with the lighter ion. Furthermore, the authors showed that as a result of the irradiation with the heaviest ion (arsenic) more clusters were formed [116].

Apart from the mass of the ions, other factors can also influence the damage density within collision cascades. Nord et al. have demonstrated via MD simulations that the energy of the recoil might play a role in the way defects accumulate [117]. In their work on silicon, they observed that amorphisation occurs less readily when a semiconductor has relatively high energy recoils (recoils of 1 keV as compared with 100 eV). The authors concluded that this difference in amorphisation behaviour was the result of more-pronounced dynamic annealing as energetic recoils induced a heating effect within the cascade, thus leading to defect recombination. Lastly, dense regions of defects and clusters have also been shown to depend on the semiconductor material subject to irradiation. In this instance, clusters of defects and amorphous pockets are more likely to arise during the irradiation of germanium than during the irradiation of silicon or gallium arsenide [117].

The possible structure of agglomerates of defects are numerous, for instance, two vacancies might interact to become a di-vacancy [26], more vacancies can also interact together to form structures such as tri-vacancies, voids or vacancy loops [26], [57]. Likewise, interstitials may agglomerate and form interstitial clusters or interstitial loops [26], [57].

#### 4.8. Displacement spike and thermal spike

As stated previously, during nuclear collisions, atoms can be displaced resulting in what is known as a collision cascade. However, as the mean free path between atomic displacements comes close to the interatomic distance, the binary collision approximation is not valid anymore [118]. Typically, such a situation occurs when the velocity of the ion is low. At reduced velocity, the nuclear cross section greatly increases and consequently the ion may collide with several atoms in a confined place, these near-simultaneous displacements of neighbouring atoms occurs during what is termed a displacement spike [118], [119]. In the displacement spike volume, the binary collision approximation cannot be applied as the displacements cannot be considered as a series of individual events [118]. For instance, in silicon and germanium the displacement spike generally occurs mainly in the end of range (EOR) region, when the ion is about to come to rest in the semiconductor and the nuclear cross section is high [27].

After the displacement spike, which according to Brinkman occurs in approximately  $10^{-13}$  seconds, comes a phase known as the thermal spike. The thermal spike phase, as shown in the timescale in figure 2.12, occurs in a region of the target material as a relatively high density of atoms in such region dissipate their energy thermally. In most cases, the thermal spike thus occurs when the atoms involved in the displacement spike do not provide enough energy to dislodge other atoms their lattice sites [27], [120]. Rather, the atoms have an increased vibration amplitude and their remaining energy thus dissipates via heat during the thermal spike.

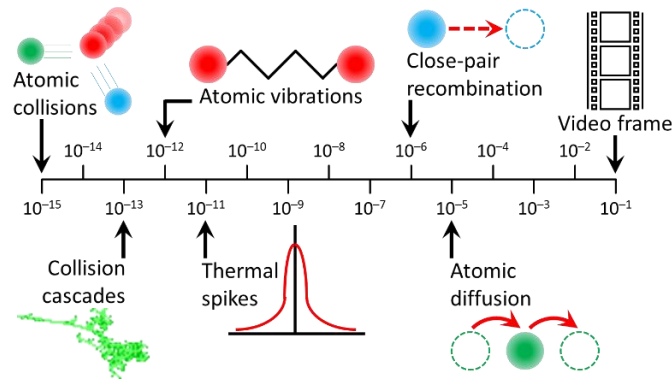


**Figure 2.12:** Logarithmic timescale of the main events, which can occur following an atomic collision. It must be noted that the typical duration of a video frame shows the technological limitations, which prevent the monitoring of these events. Courtesy of Dr Jonathan Hinks.

The temperature rise due to thermal spikes in semiconductors may be high enough to melt materials such as germanium and silicon [27], [121]. As stated above, Caturla et al. simulated the irradiation of silicon by light (boron) and heavy ions (arsenic) [116]. They concluded that relatively-heavy ions tend to generate disordered regions (amorphous pockets). Indeed, the authors observed melting localised in nanometer-sized volumes during the thermal spike caused by the arsenic ion then followed by a quenching of these volumes, from which amorphous pockets were formed. It is worth noting that the temperature rise was only high enough to induce melting when irradiation was performed via heavy ions in that study.

Furthermore, it has been reported in [27] that as a result of the thermal spike the temperature may induce relaxation of the damaged regions in the spike volume and its vicinity. During this relaxation, defects can migrate and rearrange so that the Gibbs free energy of the region is reduced. It has been reported that during this period (i.e. the dissipation of the thermal spike heat) dynamic annealing can occur and some damage can be repaired due to the enhanced mobility of defects at these higher temperatures, whilst conversely agglomeration of defects can also be observed depending on their initial spatial distributions after their formation,

(which, may for instance impact on the probability of an interstitial encountering another interstitial and form a di-interstitial or contrariwise to encounter a vacancy and thus recombine with it) [116], [118], [122], [123].

#### 4.9. Dangling bonds

Broken bonds also known as dangling bonds, are particularly common at the interface (i.e. where the material terminates) of germanium [21]. As shown in figure 2.13, such bonds are left “dangling” in semiconductors. The presence of dangling bonds is often problematic as they act as traps for charges thus greatly reducing the conductivity of the material [21], [28], [42]. In silicon, in order to suppress dangling bonds at interfaces the use of its native oxide layer (silicon dioxide) is very effective as it can bond with most dangling bonds. Furthermore the oxide layer is also used as an insulator which, as described in chapter 2, is crucial in MOSFET devices [42]. Germanium also grows a native oxide layer; however, the oxide is relatively unstable as it absorbs water and tend to be dissolved [21], [28], [42]. The difficulty of effectively growing a stable native oxide layer on germanium has been the main reason why it has been supplanted by silicon technologically, however, new materials are now proposed to suppress dangling bonds and serve as insulators on germanium based electronic devices [16], [21], [28], [42].

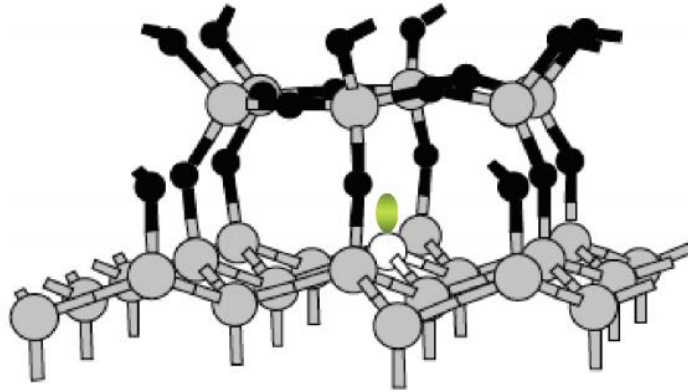


**Figure 2.13:** Schematic showing a dangling bond (in green) at the interface between a germanium crystal and an oxide layer. The germanium atoms are represented in grey and the oxygen atoms are shown in black. From [21].

## 5. Amorphisation

### 5.1. Properties of amorphous material

During ion irradiation of germanium, the long and medium-range order which characterise crystalline materials can be lost due to damage accumulation leading to amorphisation [27], [58], [118]. However, the short-range order is preserved as the equilibrium distances between atoms still remain [27], [58], [118]. In figure 2.14, the radial density of atoms is shown and reflects the probability of finding an atom at a given radius from another atom in germanium. In the figure, the radial density function (RDF) is shown for the crystal, the amorphous phase as well as the liquid phase of the material [124]. Figure 2.14 illustrates the fact that even in an amorphous phase, there is an equilibrium distance between neighbouring atoms (as there is a higher probability of the presence of an atom at approximately 2.5 angstrom). However, the ordering is much more pronounced in the crystal as the RDF illustrates both the short and long-range order that characterise the crystal. Indeed, in the crystal there are multiples distances with

high probabilities of finding an atom whilst at the other distances the probabilities are close to zero. On the other hand, as shown by the RDF, in an amorphous material (or a liquid) the loss of long-range order is characterised by a more diffuse probability of finding a germanium atom at a given distance.

It is worth noting that in an amorphous material, the bond angles are not fixed and the distances between adjacent atoms are more variable compared with the crystalline phase [27]. This characteristic of the interatomic bond distance of the amorphous phase is illustrated by its wider peak at approximately 2.5 angstrom compared with the crystalline one at the same interatomic distance in the RDF. Furthermore, unlike the crystalline germanium material where the atoms are bonded in such a way that they form six membered rings, amorphous germanium has also seven and five folds membered rings [81]. Remarkably, it has been shown by MD simulations that when 25% interstitial-vacancies pairs are present in silicon, the RDF is indistinguishable from that of the amorphous phase. [27] Similarly when 25% interstitial-vacancies pairs are present in silicon the contrast of the structure in a microscope was shown to be analogous to that of an amorphous material as it results in the formation of 5 and 7 membered rings [89]. In the literature, it has thus been suggested that that during irradiation the formation of interstitial-vacancy pairs are responsible for amorphisation [27], [89], [125].

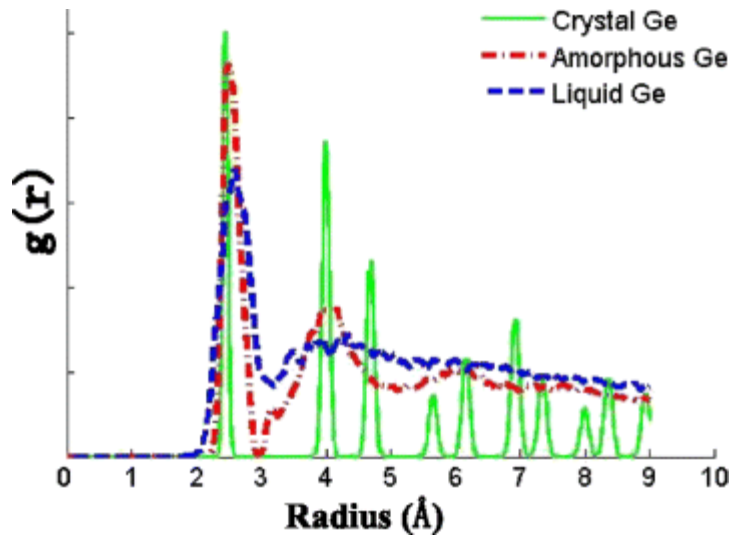


**Figure 2.14:** Radial density function (RDF) of single crystal, amorphous and liquid germanium. From [124].

Amorphisation is routinely observed to happen during ion irradiation [23], [27], [121], [126]. However, the fluence at which this process occurs as well as the manner in which the ion beam induces amorphisation of the crystal is still subject to debate [23], [25]–[27], [89], [117], [125]–[133].

Furthermore, the properties of an amorphous phase are more variable than those of a crystal [27]. For instance, whilst experimental results have shown that densities of both amorphous germanium [20], [121], [134] and amorphous silicon [27] are in most cases lower than their crystalline counterparts, these densities can vary widely depending on how the amorphous phase has been prepared [20], [27]. For instance, amorphous silicon made by physical vapor deposition can be more than 10% less dense than the crystalline structure [27], [135]. On the other hand, silicon rendered amorphous via ion irradiation is typically about 1 to 2% less dense than crystalline silicon [27].

The density of amorphous germanium can vary extensively during ion irradiation and the germanium can even exhibit porosity. The magnitude of such porosity depends on the fluence, the angle of irradiation and the energy of the incoming ions [121], [134], [136]. Therefore, the density of germanium after irradiation does not have a fixed value but is known to sometimes be much lower than its crystalline phase [121], [134], [136]. Porous germanium has for instance been reported to be 30% less dense than the crystal after 1 MeV germanium ion irradiation in [134]. However, in the same work a change in the density of the ion-bombarded material was observed during irradiation as both the emergence and the thickness the porous layer depended on the fluence. Indeed, the thickness of the porous layer induced by the ion beam at RT was at least three times larger at a fluence of  $3 \times 10^{16}$  ions.cm<sup>-2</sup> compared with a fluence of  $1 \times 10^{17}$  ions.cm<sup>-2</sup> [134].

In another work, germanium has been reported to exhibit a foam-like structure after irradiation by a 30 or 60 keV ion beam (i.e. at the energy range used in the current work). As can be seen in figure 2.15, the porosity of the target material reaches a maximum for both energies when the fluence ( $\psi$ ) is about  $5 \times 10^{16}$  ions.cm<sup>-2</sup> but the roughness of the surface is higher for the specimen irradiated at 60 keV [121].

Other authors have also reported such observations when germanium has been irradiated by ions such as gallium or gold [137]. In those studies, the porosity has been attributed to the accumulation of vacancies in the vicinity of the surface which migrate to form clusters and subsequently voids [121]. Interestingly, in a recent publication the swelling of germanium under silver ion irradiation was not observed even though the sponge-like structure was formed; thus the authors concluded that the morphology of germanium during ion bombardment is very sensitive to the irradiation conditions [136].

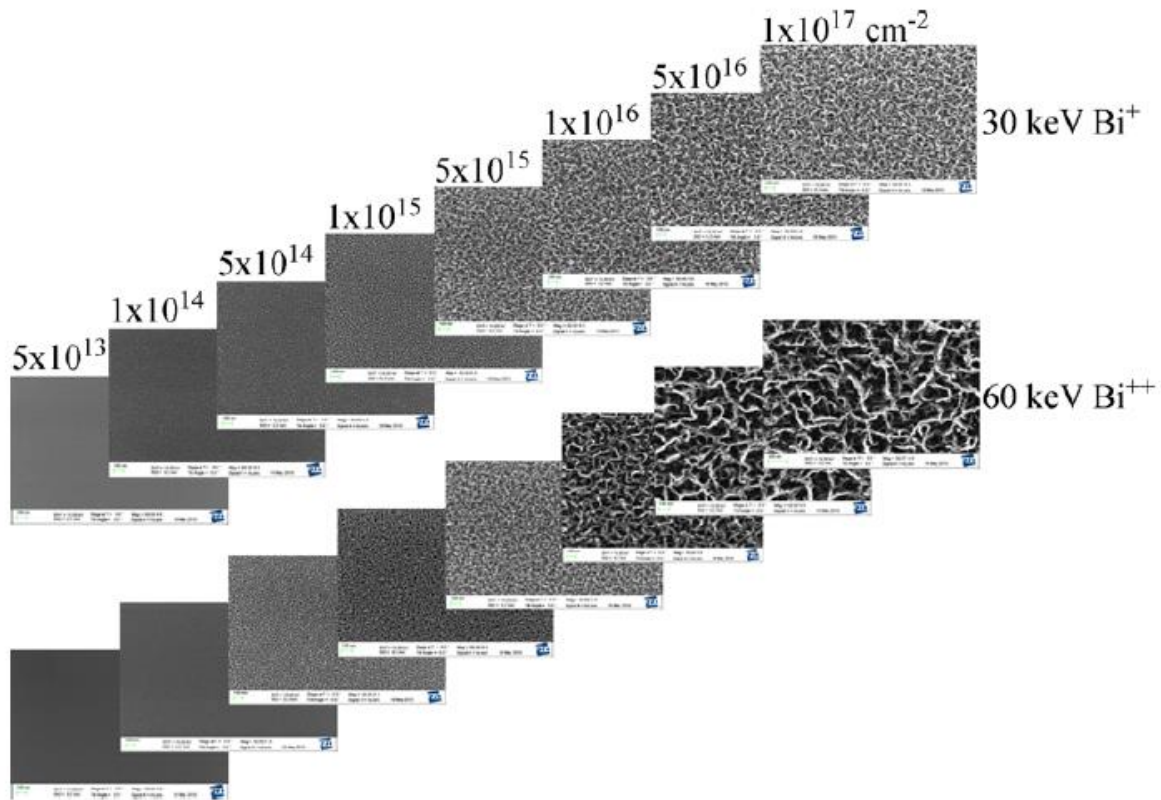


**Figure 2.15:** Scanning electron microscopy (SEM) images showing the evolution of the germanium surface during irradiation at RT by a 30 and a 60 keV bismuth ion beam at fluences ranging from  $5 \times 10^{13} \text{ cm}^{-2}$  to  $1 \times 10^{17} \text{ cm}^{-2}$  at normal incidence. From [121].

## 5.2. Amorphisation models

### 5.2.1. Critical density model

One of the main mechanism explaining amorphisation is based on the density of the defects induced during ion irradiation within the region made amorphous and has been developed via the so-called critical density model, which as will be addressed later, is defined as a homogeneous amorphisation mechanism [23], [26], [27], [127]. According, to this model, when defects accumulate in the crystal there is a certain density at which the crystal should collapse into its amorphous phase [23], [26], [27], [127]. Through irradiation, the Gibbs free energy of the irradiated material increases, thus making it energetically favourable for the

material to be amorphous rather than to be a highly damaged crystal [23], [26], [27], [127]. This model has been developed mainly for silicon in order to predict the appearance of an amorphous layer during implantation as well as the depth of that layer [26].

In line with this, Swanson et al. have proposed that the threshold density of defects in silicon and germanium should be around 0.02 of the atomic fraction [138]. In semiconductors, the density of defects is considered proportional to the energy absorbed in the crystal via nuclear collisions [27]. Therefore, rather than the density of defects, in the critical energy density model the nuclear energy deposited in the target material is instead used to determine when and at which depth amorphisation will occur [23], [26], [27], [127]. As these absorbed energies can be calculated via software such as SRIM (as for instance shown in figure 2.16), the critical density model has been used in the literature to predict the formation of amorphous layers in both silicon and germanium [23], [26].

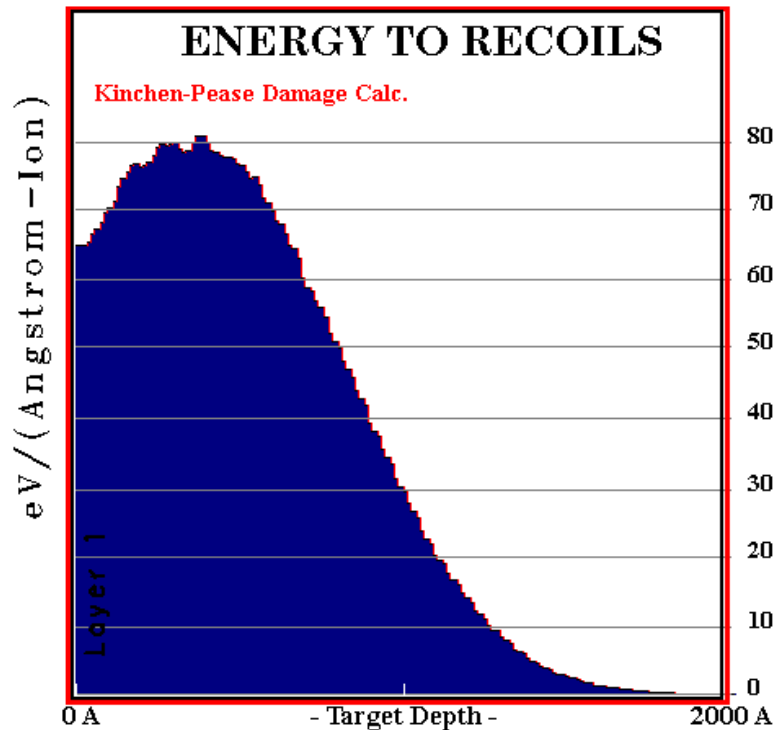


**Figure 2.16:** Nuclear energy absorbed by the target material as a function of depth in germanium irradiated with 300 keV xenon ions at normal incidence calculated using SRIM.

In the critical density model, the strong assumption is that the energy density is homogenous within the damaged layer. This assumption is often disputed as the energy distribution during irradiation depends not only on the overall energy deposited in the crystal but also on the morphology of the collision cascade which might induce localised regions with higher concentrations of defects, whilst others regions of the irradiated region might be defect-free [27], [116]. However, some authors have stated that a homogenous amorphisation mechanism may still hold true as the concentration of defects can become independent of the morphology of the collision cascades if Frenkel pairs diffuse and become homogeneously distributed in the irradiated regions [27]. In such a model, under conditions where dynamical annealing (i.e. annealing effects occurring during damage build-up via the ion beam) can be neglected, the critical energy density at which amorphisation occurs should therefore remain identical irrespective of the ion.

Using the critical dose energy density ( $E_{dc}$ ) at which germanium becomes amorphous, the depth and position of the amorphous layer can be determined as a function of fluence using equation 2.15, where  $\psi$  is the fluence,  $E_d(z)$  is the energy absorbed by the target material at a depth  $z$  and  $\rho$  is the atomic density of the target material [26].

$$\psi \cdot E_d(z) = E_{dc} \cdot \rho \quad (2.15)$$

In germanium, at RT, self-ion irradiation performed at 150 keV has been correlated to the depth,  $z$ , of the amorphous layer using cross section TEM (X-TEM) in [26]. Using equation

2.15, the correlation between critical fluence and the amorphisation depth allowed Claverie et al. to conclude that the threshold energy density ( $E_{dc}$ ) was 5 eV per atom in germanium [26].

Furthermore, as shown in figure 2.17 the authors analysed results from other publications on the irradiation of germanium by phosphorus, germanium and indium ions at RT as well as irradiations performed by phosphorus, germanium, arsenic and bismuth ions at liquid-nitrogen temperature. They concluded that in all those experiments, the same  $E_{dc}$  was shared as the predicted amorphous depth corresponded to what could be expected using an  $E_{dc}$  of 5 eV. They therefore concluded that these results confirmed that the density of defects was irrespective of the bombarding ion. Furthermore, as RT and liquid nitrogen experiments were equivalent in term of critical energy density, it was also concluded that at RT under the conditions used in these experiments the dynamical annealing was low enough to have little effect on the overall defect density [26].

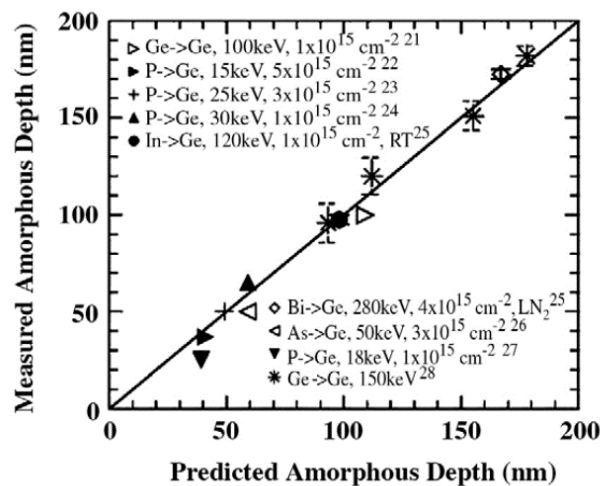


**Figure 2.17:** Measured amorphous depth due to irradiation of germanium as reported in various experiments reported in the literature and summarised in [26] to be compared with the predicted amorphous depth if  $E_{dc} = 5\text{eV}$ . From [26].

However, the authors expressed reservations concerning a value  $E_{dc}$  of 5 eV for lighter ions [26]. As amorphisation by light ions has been shown to be difficult or even impossible, the authors irradiated germanium with boron at RT and at liquid nitrogen temperature. They observed that a reduced amorphisation layer was induced by the ion beam compared with that predicted by the  $E_{dc}$  calculated with heavier ions. Whilst the authors did not explicitly quantify the reduction in the amorphisation layer compared with the model and the value  $E_{dc}$  value of 5 eV, they explained that the discrepancy was due to enhanced Frenkel pair recombination in very dilute cascades. It is also worth noting that unlike in the work of Claverie et al. work (in [26]) the effect of temperature on the density of defects during self-ion irradiation has been reported elsewhere as being an important factor as  $E_{dc} = 5$  eV at RT but only 1.2 eV when the irradiation is performed at liquid nitrogen temperature [23].

### 5.2.2. Heterogeneous model

As stated above, according to [26] the critical energy density model based on a homogenous amorphisation mechanism seems to accurately predict the formation of amorphous layers in several cases [26], [139]. However, TEM observations have shown evidence of discrete amorphous regions heterogeneously distributed within irradiated crystals [27]. As shown in figure 2.18, the presence of amorphous clusters can be directly observed when heavy ions such as bismuth are used to perform the irradiation and are also predicted by MD simulations [116], [125], [139].

According to Morehead and Crowder [140] it is the overlap of these amorphous region which causes the global amorphisation of the irradiated crystal [140]. The amorphous region is generated along the path of the ion. As shown in figure 2.19, the amorphous section with a radius  $R_0 - \delta R$  depends on both the damage generated during irradiation and on subsequent diffusion of defects. Indeed, an original highly disordered region of radius  $R_0$  is induced by the

incoming ion. However, in a sheath  $\delta R$ , the defects can diffuse out of the region  $R_0$ . The highly disordered region will therefore be proportional to a region  $(R_0 - \delta R)^2$ . Consequently, in this model the accumulation of these amorphous regions will lead to complete amorphisation, (at which point the amorphous fraction  $f_a$  of the irradiated material reaches 1) [140].

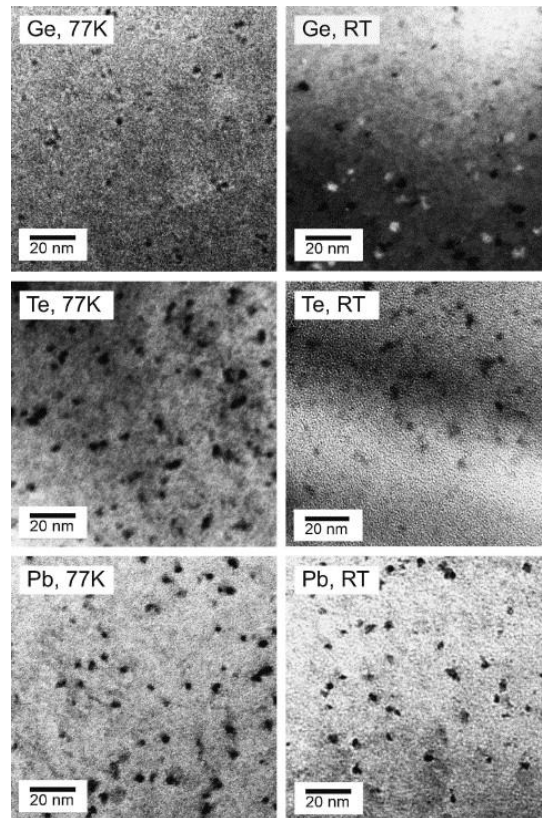


**Figure 2.18:** BF-TEM images of crystalline silicon with black spots, identified as amorphous pockets due to irradiation by 30 keV germanium, lead or tellurium at either 77 K or RT. From [139].

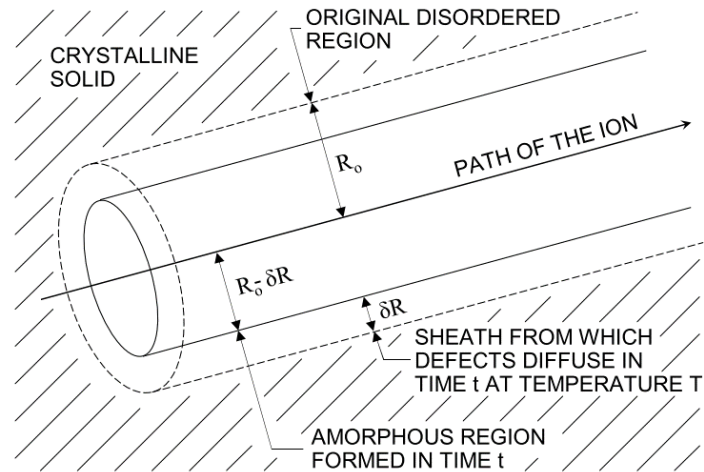


**Figure 2.19:** Schematic showing the original disordered region of radius  $R_0$  along the path of the ion and the resulting amorphous region of radius  $R_0 - \delta R$  (referred to in the text). From [140].

However, the nature of the highly disordered region as well as its size is strongly dependent on the ions used for the irradiations [27], [116]. With light ions, the size of the highly disordered region is smaller whilst heavy ions create larger highly disordered regions. Furthermore, and as stated above, single impacts from heavy ions can generate amorphous pockets [139]. On the other hand, the pure heterogeneous model may not apply for light ions as it is unlikely that a single impact from these ions generates a discrete amorphous region [25], [27], [125], [138]. As the formation of an amorphous region due to a single impact is expected to arise only with heavy ions, a modified version of the heterogeneous model for lighter ions has been proposed by Gibbons [25], [27], [125], [138]. For lighter ions, the collision cascade is less dense and therefore the formation of amorphous pockets is less likely [116], [138]. With lighter ions a number  $m$  of overlapping cascades is needed to render the highly disordered region amorphous [25], [125], [138]. Therefore, equation 2.16 developed by Gibbons [128] is used to describe

the amorphous fraction as a function of the ion per unit volume  $D$  and the volume of an amorphous zone  $V$  with a broader range of ions [25], [27], [125], [138].

$$f_a = 1 - \sum_{k=0}^{m-1} \frac{(V.D)^k}{k!} e^{-V.D} \quad (2.16)$$

A recent study has associated equation 2.16 with the evolution of  $f_a$  via the direct observation of the selected area diffraction patterns (SADPs) during in situ irradiation within a TEM) by 30 keV helium and 80 keV xenon in silicon [25]. Via the fitting between the monitoring of the SADP during irradiation, which allowed the authors to determine experimentally  $f_a$  and the equation 2.16 the authors identified the values  $V$  and  $m$  each of the ions. They noted that xenon was able to cause direct amorphisation whilst four overlapping cascades were needed to make a highly damaged region of volume  $V_{He}$  amorphous when the irradiation was performed via helium ions [25].

Furthermore, it has also been observed experimentally that the mass of the ion has an influence on the shape of the curves describing the build-up of amorphous fraction. As shown in figure 2.20, refractive indexes, which are assumed to be proportional to  $f_a$ , were measured during ion irradiation of silicon in [141]. Consequently figure 2.20 indicates that the amorphous fractions evolve in a linear fashion during heavy ion irradiation and tend to evolve in a super linear fashion (but only after a higher dose is reached) as the ions become lighter as expected by equation 2.16 [27], [142].

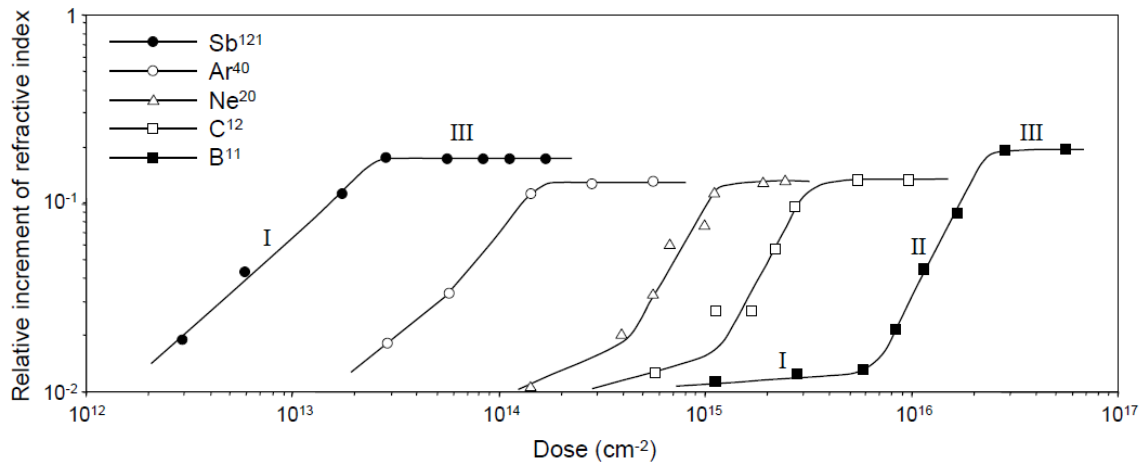


**Figure 2.20:** Relative increment of volume fraction of amorphous material (proportional to  $f_a$ ) as a function of fluence during irradiation of silicon by several ions at RT. From [27].

### 5.2.3. Intermediate models

In [26] the observation of sharp delimitation between the amorphous irradiated semiconductors and the crystalline layer via X-TEM have been reported as being an indication that the region with a high enough density of defects has collapsed into an amorphous phase, thus suggesting a homogenous amorphisation model [26], [27]. However, as stated in [27], [143], the presence of amorphous pockets during heavy ion irradiation seems to indicate otherwise. The nucleation limited model is an intermediate model compatible with both the presence of heterogeneously distributed clusters of defects and the collapse of the crystalline phase into an amorphous one [27], [143].

In this model, the amorphous pockets formed in the crystal during irradiation may act as sites where the remaining defects will interact. The interaction between these sites and the defects can result in the growth of the amorphous regions or, conversely, to them shrinking. In this model, the concentration of defects surrounding the amorphous pocket will determine whether

an amorphous pocket will grow or shrink. Consequently, below a critical defect density the metastable amorphous pockets will shrink due to their interaction with the defects. Conversely, above a critical defect density the interaction between the defects and the nucleated amorphous regions will result in growth of the amorphous phase [143]. This mechanism, therefore, describes an all or nothing type of situation as the presence or non-presence of a continuous amorphous layer will depend on whether amorphous growth is more favourable than shrinkage of the amorphous regions [27], [143]. This would explain why several experimental results seem to indicate that ion irradiation induces two distinct regions delimited by a sharp interface, one which is completely amorphous and one which is crystalline (thus suggesting the collapse of one of the regions into an amorphous state). [26], [27], [143].

To describe the evolution of the amorphous fraction during irradiation several models have been proposed to relate the evolution of the amorphous fractions to two distinct cross sections: one that is related to the direct impact amorphisation cross-section and the other to interaction between the amorphous zones and the defects, with the former mechanism being more pronounced during heavy ion irradiation and the latter during irradiation with light ions [144]–[146].

## 6. Recrystallisation

### 6.1. Thermal recrystallisation

During ion irradiation, a semiconductor can suffer more or less severe degrees of amorphisation but if the damage range and the fluence are adequate then the target material may become fully amorphous [25]. During irradiation of single crystalline semiconductors, it may be possible to adjust the irradiation parameters so that a layer of crystal remains buried within the target material [26], [32]. If so intended, the purpose of this layer is to serve as a seed to regrow a

single crystal via a process called solid phase epitaxial growth (SPEG). For this process to be possible, the specimen must be heated to a temperature high enough to induce the reorganisation of the amorphous phase. Such reorganisation will occur by using the remaining crystalline phase as a template for the reordering of the atoms at the amorphous-to-crystalline interface (as will be described below) [147]. In the absence of a crystal within the irradiated material, recrystallisation typically occurs at a significantly higher temperature ( $\approx 400^\circ\text{C}$  in germanium) via a process called random nucleation and growth (RNG). In this case, the temperature must be high enough to prompt the nucleation of crystallites within the amorphous material. However, in such instances the subsequent growth from the numerous nucleated crystallites leads to a polycrystalline material.

Germanium has the advantage of being able to recrystallise via SPEG at a temperature of approximately  $300^\circ\text{C}$  which corresponds to a temperature substantially lower than SPEG in silicon (about  $200^\circ\text{C}$  lower) [26], [27], [148], [149]. However, some factors such as an applied pressure on the semiconductor or the doping might enhance, delay or even prevent the SPEG process. One of the major factors which affects the recrystallisation rate is the crystallographic nature of the interface between the amorphous region and the crystalline layer [143]. Indeed, it has been observed that the growth rate depends strongly on the growth orientation. For instance, in germanium and silicon, SPEG occurs the fastest in the  $\langle 100 \rangle$  directions and the slowest in the  $\langle 111 \rangle$  directions. According to Faust et al., an atom from the amorphous phase can be subject to recrystallisation, only if it has at least two bonds shared with the crystalline phase [27], [113], [143]. As can be seen in figure 2.21, only one atom from the amorphous region will need to bond with the crystal at a (100) interface to respect this rule, whilst two of them need to bond with a (110) interface and three are needed to satisfy this requirement at a (111) interface. For these reasons the regrowth at the (100) interface is the easiest and therefore the fastest [143].

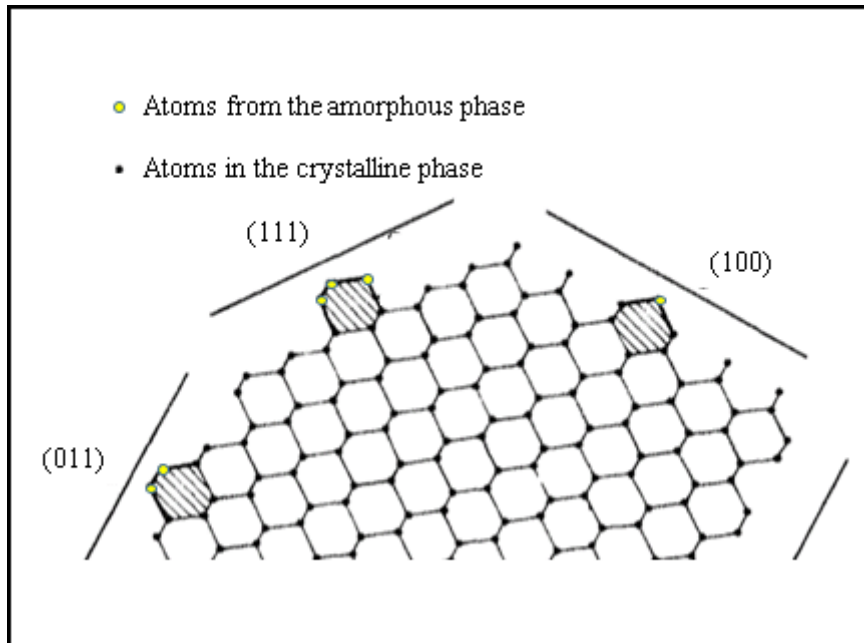


**Figure 2.21:** Schematic of a diamond type crystal lattice in  $\langle 110 \rangle$  projection showing the (100) (111) and (110) interfaces and six-fold rings formed via epitaxial crystallisation represented in crosshatched. Modified from [143].

## 6.2. Preventing amorphisation via irradiation at elevated temperatures

A simple way of preventing the growth of an amorphous layer is to perform irradiation at elevated temperature (also called hot implantation) [33], [150], [151]. This technique has been successfully used with silicon and germanium; however, the minimum temperature at which the growth of an amorphous layer has been prevented depends on many factors such as the ion species and the flux [33], [150]–[152]. For instance, as heavy ions tend to induce amorphisation at a relatively fast rate, a higher temperature is required to successfully prevent amorphisation (the annealing rate must be faster than the amorphisation rate) [150].

Fukata et al. have irradiated silicon nanowires with boron and phosphorus to achieve n doping and p doping, respectively [33]. Their aim was to achieve heavy doping, therefore the nanowires were irradiated to high fluences. Irradiated at RT, the nanowires became fully amorphous at the fluence used during phosphorus ion irradiation (i.e. above  $10^{16}$  ions.cm<sup>-2</sup>). The nanowires were subsequently heated at a temperature of 900°C to activate the dopants and to recrystallise the nanowires. However, because the nanowires were fully amorphous after irradiation, the single crystalline characteristic could not be recovered and the nanowires became polycrystalline after RNG. For the reasons stated above, performing irradiation at 300°C enabled the authors to avoid amorphisation of the silicon nanowires. It is also worth noting that the silicon nanowires irradiated at elevated temperatures presented a higher activation ratio after annealing compared to those irradiated at room temperature with subsequent annealing [33].

### 6.3. Annealing effects of electron beams

Whilst epitaxial recrystallisation can occur via an input of thermal energy into the specimen, several experiments have shown that recrystallisation may also result from the interaction of the specimen with an electron beam. In [153], [154] germanium, silicon and gallium phosphide specimens were irradiated with 50 keV xenon ions under conditions where the flux and the fluences were low enough to induce the formation of isolated amorphous pocket within the single crystalline specimens which were subsequently annealed using electron beams. The authors in [153], [154] clarified that prior to their experiments it was believed that recrystallization of amorphous regions could occur only when the energy transferred by the electrons to the atoms in the target material was elevated enough to exceed the displacement threshold of the specimens [153]–[156]. In germanium, silicon and gallium phosphide crystalline specimens this corresponds to an electron beam with a minimum energy of 350 keV, 145 keV and 200 keV, respectively [153], [154]. It worth noting that due to the small mass of

the electron, the electron beam energy needs to be relatively high (compared with the energy of an ion beams) to displace atoms in the target material.

As illustrated by figure 2.22 showing the regrowth of the crystalline structure as a function the electron beam energy, the authors in [153] observed that the annealing effect of the electron beam started at a value too low to reach the displacement threshold reported above (i.e. between 25 and 50 keV). They concluded that electrons did not need to displace atoms from the target material to induce recrystallisation and that energy transferred to the target material below the displacement threshold could induce bond rearrangements at the interface between the amorphous phase and the crystal. They also concluded that when the electron beam energy was 200 keV, 100 keV and 125 keV, for germanium, silicon and gallium phosphide, respectively, the electron beam annealing effect was minimised. Furthermore, above these energies, the electron beam annealing effect increased as such energies were, according to the authors, high enough to induce atomic displacements and cause recrystallisation of the amorphous pockets via mass transport. The authors speculated on the reason why electrons may be able to displace germanium, silicon and gallium phosphide below their displacement threshold voltages (i.e. 350 keV, 145 keV and 200 keV, respectively), and proposed a lower displacement threshold for atoms in the amorphous phase compared with those in the crystal. It must also be noted that the authors dismissed the electron beam heating effect as a cause for the recrystallisation of amorphous pockets as the maximum temperature increase was calculated to be only 7°C.

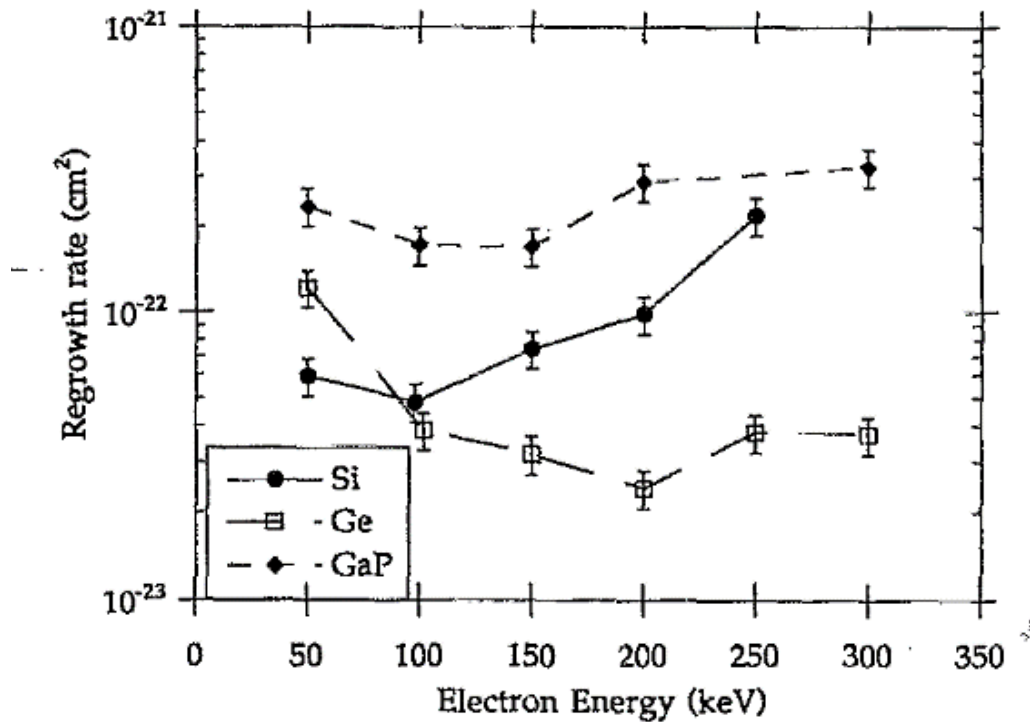


**Figure 2.22:** Regrowth rate of amorphous pockets observed via TEM in germanium, silicon and gallium phosphide as a function of the electron beam energy. From [153].

## 7. Nanowires

### 7.1. Top-down / bottom-up

In 1964 the first paper reporting the growth of a nanowire was published by Wagner and Ellis [157]. As with the germanium and silicon nanowires used in the experiments presented in the current work, Wagner's nanowires were obtained by the vapour liquid solid growth (VLS) method. The germanium and silicon nanowires used in the present work, were commercially acquired from Nanowire Tech Ltd (product number GNWsI15) and Sigma-Aldrich (product number 731498), respectively.

Wagner and Ellis used a gold particle as a seed to grow a single crystalline nanowire [157]. The nanowire was therefore made from “scratch” and is obtained via what is classified as a bottom-up approach [158]. Indeed, there are two main approaches to obtain nanowires, the so called “bottom-up” and “top-down” techniques [158]. The top-down techniques are based on processes that involve cutting through a crystal to obtain the desired structures. This kind of approach offers the advantage of better control over the positioning and alignment of the nanowires [159], [160]. However, bottom-up based processes are more promising for applications requiring high quality nanowires. Indeed, via this approach, the production of high purity nanowires is more likely as well as the production of nanowires which present less surface roughness compared to those processed via top-down techniques. Furthermore, this approach is more suitable for large scale processing [159], [160].

## 7.2. Nanowire applications

Nanowires have numerous properties specific to their reduced sizes that make them interesting for a great number of applications. For instance, these structures have high surface-to-volume ratios as well as novel optical features [35], [161]. In addition to this, their mechanical properties often differ from those of the bulk materials. For instance, whilst bulk germanium is considered a brittle material, germanium nanowires can have an ultimate strength that is orders of magnitude above that of their bulk counterpart [162]. Furthermore, when the diameter of a semiconductor nanowire is below a certain size, they are subject to a quantum confinement that affects their electronic band structure [161]. Therefore when quantum confinement is sought, germanium nanowires may be a better alternative than silicon nanowires as their relatively larger exciton pair Bohr radius make them more readily subject to quantum confinement [163].

As stated in the first part of this chapter, germanium nanowires have been suggested by the ITRS as being integrated into future transistors to replace bulk silicon and satisfy Moore's law by continuing the miniaturisation of devices [71]. However, they may also be interesting for applications unrelated to transistors. Properties of germanium nanowires could for instance be put to good use on future lithium batteries anodes, taking advantage of their large surface to volume ratio which means more available surfaces where electro-chemical reactions can happen [164]. Furthermore, numerous publications have shown the potential of germanium to overcome its indirect band gap nature [165], [166]. In germanium, the indirect band gap is characterised by an energy of 0.66 eV. However, the difference between the bottom of the two conduction bands shown in figure 2.2 is only  $\approx 0.14$  eV (i.e. it is this 0.14 eV that makes it an indirect band gap semiconductor) [166]. It has been predicted via DFT calculations that strain could change the band gap structure of the germanium making it optically active by turning it into a direct band gap semiconductor [166]. As germanium nanowires have the particularity to be more resistant to such strain than the bulk, nanowires have recently been the subject of intensive research on their optoelectronic properties via the possibility of achieving the tuning of their band gap via strain [165]–[170].

### 7.3. Ion irradiation of nanowires

The effects of ion irradiation on nanowires (and nanostructures) have been reported to differ from those in the bulk. As will be addressed below, these differences are both due to the reduced size of the target material and to their shape. For instance, as stated in [35], [171] the sputtering yield can be strongly influenced by the ratio between the implantation depth/nanowire diameter (or nanoparticle) and MC calculations have shown that under conditions where the range of the ion is comparable to the nanostructure diameter the sputtering yield was enhanced. As shown in figure 2.23, this has been attributed to the large surface area from which atoms can be sputtered. Indeed as shown in the figure, in the circular shape of a

nanowire, atoms can leave from many directions whilst in the bulk only the ion-beam facing side of the specimen enable atoms to escape [35]. In [171] the same authors have also observed the enhanced sputtering yield when silicon nanowires of various diameters were irradiated by argon ions. The authors observed that the sputtering yield was maximum when the range of the ion was comparable to the nanowire diameter. On the other hand, as described in [35] if the ion range is smaller than the nanowire diameter most of the atoms are sputtered from the front of the nanowire (the ion beam-facing side) whilst a high ion beam energy will only induce sputtering from the back of the nanowire (i.e. the surface from which the ions will escape the nanowire). It is worth noting that a high surface to volume ratio of nanowires also influences the doping profile as incident ions and sputtered atoms have more opportunities to escape from the target.

Furthermore, as surfaces can be considered as sinks for defects (based on experimental observations and MD simulations [172]–[174]) where they may either recombine and/or be involved in surface rearrangement [35], the interaction between defects and surfaces of nanostructures may have significant consequences. For instance as will be addressed below, rearrangement of the defects near the surface of nanostructures has been proposed as being responsible for the so called “ion-induced bending” phenomenon [122].

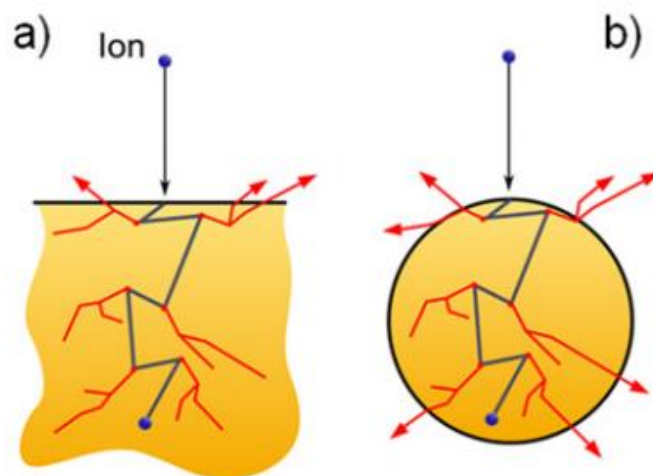


**Figure 2.23:** Schematic to illustrate (a) the interaction between an ion and a solid where the recoils can leave the target material from the surface (as illustrated by the red arrow), whilst in the case of a nanostructure (b) more surface is available for recoils to be sputtered away. From [35].

## 7.4. Ion induced bending (IIB)

### 7.4.1. Context

One of the most noticeable effects of ion irradiation on nanostructures is the deformation that may be induced. This ion-induced bending phenomenon has been observed in a large range of nanostructures such as nanowires, nanotubes, nanopillars and cantilevers [20], [22], [41], [97], [114], [122], [171], [175]–[181]. It also affects a wide range of materials including nanostructures made of germanium, silicon, aluminium, zinc oxide, gallium arsenide, carbon, and silver. Furthermore, several authors have reported that the deformation induced by the ion beam could occur either away from the ion beam or towards it depending on the irradiation conditions (i.e. the ion species, the energy of the incoming ions, the fluence, the angle of irradiation or the nanostructure diameter or width [20], [22], [41], [97], [114], [122], [171], [175]–[183]).

Ion irradiation might be used to modify the properties of the irradiated material and more particularly as stated above, ion beams can be utilised to dope semiconductors [33]. In this case, the IIB may be a side effect of the doping process and the shape modification of the nanostructures may be deleterious. For instance, in [22] whilst performing doping of a silicon nanowire by gallium ions, the authors had to develop a way of making sure that the nanowire was attached at both ends to a substrate in order to prevent the bending effect during irradiation[22].

Conversely, IIB is also considered as an efficient and relatively simple way of manipulating nanostructures after growth. Indeed, because often the spatial orientation of nanostructures is dictated by their crystallographic growth direction on a substrate it is challenging to fully control their spatial orientation. Moreover, the spatial orientation of the nanostructures is lost if they are removed from the growth substrate [158], [177], [184]. In such instances, IIB can be used to readily control the spatial orientation of the nanostructures as reported in [178] where an array of nanowires was aligned towards the ion beam. Consequently, due to the interest of using IIB to align nanostructures a patent has been used to protect an IIB method by Hewlett-Packard company<sup>®</sup> where the authors described a manner of aligning nanowires via irradiation by inert gases [185].

Performing IIB with inert gases can be useful as their effects on the chemical and electronic properties of the target material are relatively small. Moreover, as IIB has been observed to occur via the use of several ion species, including both inert gases and ion species used for doping purposes [114], [178], IIB can be readily used during the fabrication of electronic devices as their fabrication often requires irradiation with both inert gases and dopants [25], [72].

The literature about IIB clearly shows both the opportunities that IIB can offer as well as its detrimental effects. To both master its capabilities and avoid it, the mechanisms behind the phenomenon must be understood. However, the literature shows that no consensus has been reached regarding the cause of the IIB effect. The main mechanisms proposed in the literature at the time when the work presented in this thesis was being carried out will therefore be presented below and tested in later chapters.

#### 7.4.2. Typical characteristic of shape modification induced by IIB

Ion-induced bending may be used to manipulate nanostructures as they can bend away or towards an ion beam [114]. Typically, as shown in figure 2.24 during IIB towards the ion beam, nanostructures such as nanowires may first take on a circular shape while bending towards the beam [176]. Ultimately, they are aligned towards the incoming ions when the fluence reaches a threshold value [176].

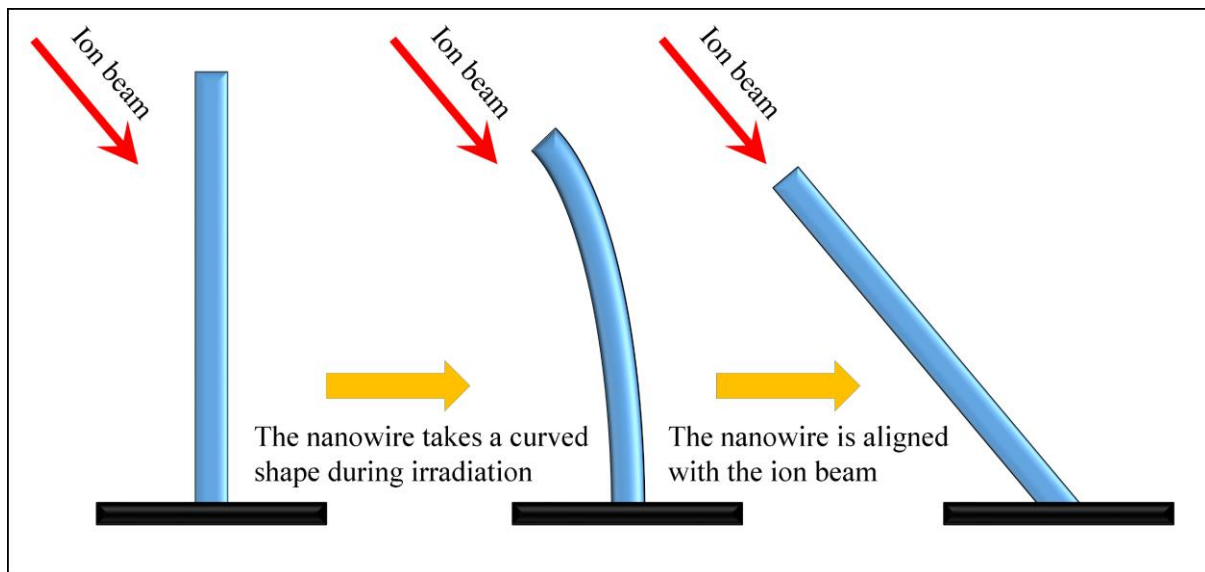


**Figure 2.24:** Schematic illustrating how (a) a straight nanowire will (b) first become curved during IIB towards the ion beam until (c) it becomes aligned with the ion beam.

The degree of bending has been found to depend in all cases on the fluences used during irradiation, meaning that the higher the fluence the more the structure will bend [20], [97], [114], [122]. Thus, unless there is a change of the side exposed to the beam during the shape modification of the nanostructure, once a permanent bending in a given direction is achieved, the end-result is just a function of the fluence and this statement seems to be true whatever the ion or the energy used during the process as shown by several authors [20], [97]. For this reason, the use of in situ ion irradiation within a FIB (Focused ion beam) has enabled the ability

to precisely manipulate nanostructures, because once the desired configurations were obtained irradiation was simply stopped [20], [179].

However, forecasting the behaviour of a nanowire before irradiation is a challenging task as it implies knowing whether bending will occur, in which direction and a correlation between the fluence and the degree of the phenomenon. To be able to answer those questions, the mechanisms behind IIB must be understood. However, as detailed below, there is currently no consensus regarding how bending occurs and several different mechanisms are currently proposed in the literature.

#### 7.4.3. Thermal Gradients

Based on thermal expansion, a mechanism which relies on an uneven heat transfer occurring during irradiation, has been proposed by Tripathi et al. [179]. The authors irradiated composite carbon nanopillars and cantilevers with a 30 keV gallium ion beam using a FIB. During irradiation, the structures bent towards the ion beam and with sufficient fluence became aligned parallel with the ion beam direction. Furthermore, after being bent for the first time, nanopillars irradiated from a different angle realigned once again with the incoming ions. Interestingly, based on the results of many irradiations made at different energies and with different ions, it was noted that at a given radius the nanopillars bent only above a threshold ion beam power (This threshold power, in watts, was irrespective of the combination of current and acceleration voltage used in the FIB) [179].

The authors explained that during a time  $t_p$  (corresponding to the time for which the ion beam was focused on the pillar), the ion beam deposits its energy which is converted into heat [179]. The authors stated that the thermal energy due to the ion beam and the radiative heat loss in the pillar give rise to an uneven thermal distribution in the pillar as shown in figure 2.25. As the composite carbon nanopillars were expected to have a negative thermal expansion coefficient,

it was stated that the thermal distribution shown in figure 2.25 might result in the structure to bending towards the ion beam as the ion-beam-facing-side of the pillar is hotter than its opposite side.

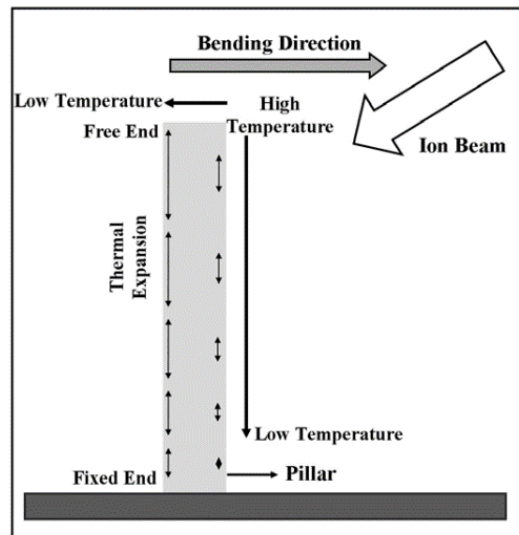


**Figure 2.25:** Schematic showing the correlation between the temperature and the volume expansion within the nanopillar. The extent of the volume expansion is qualitatively illustrated by the length of the arrows within the nanopillars. From [179].

#### 7.4.4. Surface rearrangement

Bettge et al. [178] and Rajput et al. [122], [175], [176] almost concurrently proposed mechanisms based on surface energy reduction to explain the bending of nanostructures. The former authors irradiated silica nanowires with a 30 keV gallium ion beam and reported the alignment of the wires towards the ion beam [178]. The authors considered that a contraction of the surface of the nanowire on the side facing the ion beam was the reason why the nanowires bent towards the beam. As the surface energy per unit volume of a nanowire is inversely proportional to its radius, it was concluded that a tendency to reconfigure the nanowire shape by increasing the nanowire radius (whilst reducing its length) must be expected as this would

result in the diminution of the surface energy. Bettge et al. [178] concluded that such surface relaxation resulting in the shrinkage of the length could be thermally activated and/or be the result of atom transport during irradiation. As ion irradiation can provide both thermal energy and enhanced atom transport in the vicinity of the irradiated surface [178], the authors concluded that ion irradiation can be considered as an ideal technique for inducing such surface rearrangement and consequently the bending of various nanostructures.

Rajput et al. also investigated the role of surface rearrangement in the IIB of nanostructures towards the ion beam and concluded that the bending occurs when their surface layers shrink during irradiation [122], [175], [176]. The contraction of the surface was said to affect the sub layers and thus cause the bending of the nanostructures towards the ion beam.

During irradiation, the incoming ions are expected to induce both damage and dynamic annealing in metallic materials or semiconductors bombarded in [122], [175], [176]. The authors stressed the fact that damage near the surface (such as voids due to agglomeration of vacancies as well as surface roughness due to sputtering) have been reported to potentially induce stress to the same order (several GPa) as that expected during the bending of nanostructures. According to Rajput et al., the damaged surface and subsurface release this stress by rearranging the atoms taking advantage of the thermal energy given by the incoming ions [122], [175], [176].

For instance, in [175] aluminium nanowires were irradiated with 30 keV gallium ions at an angle of 45°. Using SRIM, the authors showed that creation of voids near the surface can be the result of such irradiation as vacancies were mainly generated within the first 15 nm. Also using SRIM, they calculated that each impinging ion would induce a temperature rise of at least 350°C due to phonon generation in the interaction region [175].

The combination of defect generation and rearrangement of these defects near the surface was also investigated by Rajput et al. using MD simulation in [122]. Emulating their experimental conditions, single crystalline silicon nanowires were irradiated with a 16 keV gallium ions. The results indicated dynamic annealing of the defects as well as a recrystallisation which consequently induced nucleation of grains [122].

In figure 2.26 reported in the same work in [122] the evolution of both the temperature and the defects (which are indicated in a purple colour) are shown after a gallium ion has impinged the target material. After 0.26 picoseconds, the temperature due to the thermal spike is about 700°C and the defect concentration is at a maximum. Subsequently, whilst the temperature drops the simulation shows that there is a relatively long period (140 ps) during which the annealing of the defects occurs. According to another of their MD simulations, it is during this period of annealing that an internal compressive stress in the front facing side of the nanowire is induced which also affects the sublayers and causes the bending of the silicon nanowire towards the ion beam [122].

During observation in a TEM of an IIB bent silicon nanowire, Rajput et al. [122] noticed that the tip of the nanowire was slightly deformed. The authors concluded that this deformation might be the result of the reactivation of the surface rearrangement due to an excessive heating localised in the tip of the nanowire under the electron beam [122].

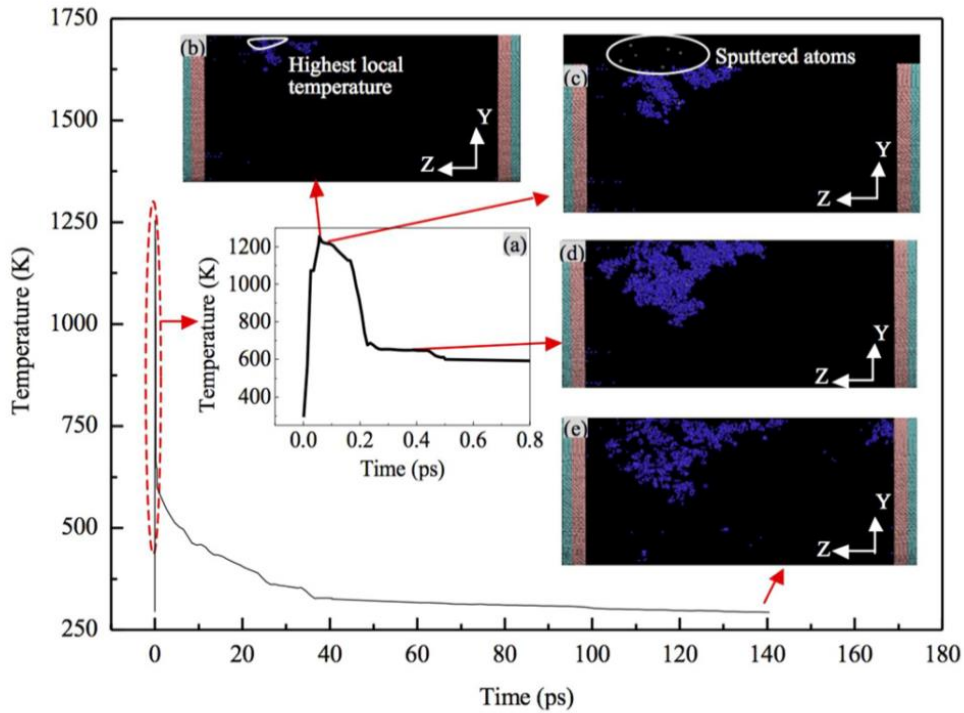


**Figure 2.26:** MD simulations displaying the evolution of the displaced atoms (shown in blue) as a function of time. The figure shows (a) the temperature evolution during the thermal spike phase, (b) the displaced atoms at 0.054 ps (when the temperature reaches a maximum). The region with the highest temperature of 1254.4 K is delimited by the white line. (c) A transitional phase at which sputtering occurs where the sputtered atoms are shown within the region delimited by the white line. (d) At 0.26 ps, the stage at which the disorder reaches its peak. (e) The remaining defects after the system is cooled down to 298K. From [122].

#### 7.4.5. Distribution of self-interstitials and vacancies

As seen previously, a change of bending direction of the whole or a part of the nanowire can sometimes happen due to the motion of the nanowire during bending. Indeed, when the nanowire moves during IIB it may happen that the ion-beam facing side of the nanowire changes due to its motion [122]. However, whilst such geometric considerations (i.e. the ion

beam hitting one side or the other) typically influence the bending direction of nanowires in all proposed mechanisms, nanowires have also been observed to either bend away from or towards the ion beam depending on factors unrelated to a change of the irradiated side [97], [114]. A mechanism based on an uneven distribution of point defects proposed by Borschel et al. has the advantage of explaining both the bending towards the ion beam and the bending away from it.

In their work, Borschel et al. irradiated single-crystal gallium arsenide nanowires or single-crystal zinc oxide nanowires [97], [114]. They observed that the bending direction was dependent on the diameter of the nanowires, the energy of the ion beam and the ion species. In their experiments, they irradiated the nanostructures under conditions that would either promote radiation damage in the whole cross section of the nanowire (deep implantation) or within the first half of it (shallow implantation) [97], [114]. Furthermore, in [97] by choosing medium energy conditions (i.e. such that the range of the ions is somewhere in the middle of the nanowire at the beginning of the irradiation) they observed that the bending direction of the nanowires changed depending on the way in which the implantation varied during the nanowire motion. In their studies, the authors wanted to visualize the distribution of point defects in the irradiated structures which they did using MC calculations [97], [114]. SRIM is routinely used to simulate the interaction of ions with flat target materials. However, due to its inability to reproduce the circular cross section of nanowires, the authors used either a TRIM based program “3dTRIM” or their in-house code “Iradina” [97], [114]. The two aspects that were monitored using the simulation were the distribution within the nanowires of the implanted ions and of the induced point defects.

The authors reported that when shallow implantation was performed such that the range of the ions was less than half of the nanowire cross section, the nanowire bent away from the ion

beam [97], [114]. For instance in [114] 60 nm diameter zinc oxide nanowires were observed to bend away from the ion beam when irradiated with a 20 keV argon ion beam [114].

As explained above, during a nuclear collision when an atom is displaced from its lattice site it can leave behind a vacancy and travel within the material until it comes to rest at some distance. Therefore, as stated by Borschel et al. [97], [114] one might expect that overall more self-interstitials will be located deeper (and more vacancies shallower) within the target material. As annihilations of pairs of self-interstitials and vacancies are more likely to occur when the two point defects are located close to each other, the self-interstitials and vacancies formed within the same simulation voxel were considered as having recombined [97], [114]. As can be seen in figure 2.27, this method showed that an excess of vacancies is expected very close to the surface and an excess of self-interstitials a few nanometres deeper [114]. To determine the final distribution of these point defects, the authors also considered sputtering effects and concluded that a thin surface layer which was rich in vacancies was removed during sputtering thus leading to a net excess of self-interstitials in the irradiated part of the nanowire [114]. The self-interstitials would therefore induce a volume expansion of the upper part (i.e. the ion-beam-facing side) of the nanowire while the lower part (i.e. the opposite side) would remain unaffected. According to the authors, such differences between the two sides of the nanowire would induce opposite stresses and therefore a bending moment leading the nanowire to bend away from the ion beam [97], [114].

On the other hand, as also reported in the same work, for the irradiation of 90 nm zinc oxide nanowires by a 100 keV argon ion beam, the authors observed that deep implantation resulted in the nanowires bending towards the ion beam [114]. As explain above, the nature of nuclear collisions during ion irradiation is likely to generate an uneven distribution of vacancies and self-interstitials. However, as shown in figure 2.27, in the case of the deep implantation conditions the unequal distribution results in an excess of vacancies in the upper part of the

nanowire and an excess of self-interstitials in the lower part. In this case, according to the authors the bending moment will be due to a volume reduction in the upper part richer in vacancies and a volume expansion in the lower part which is richer in self-interstitials and thus, according to the authors, will induce the bending of the nanowire towards the ion beam [114].

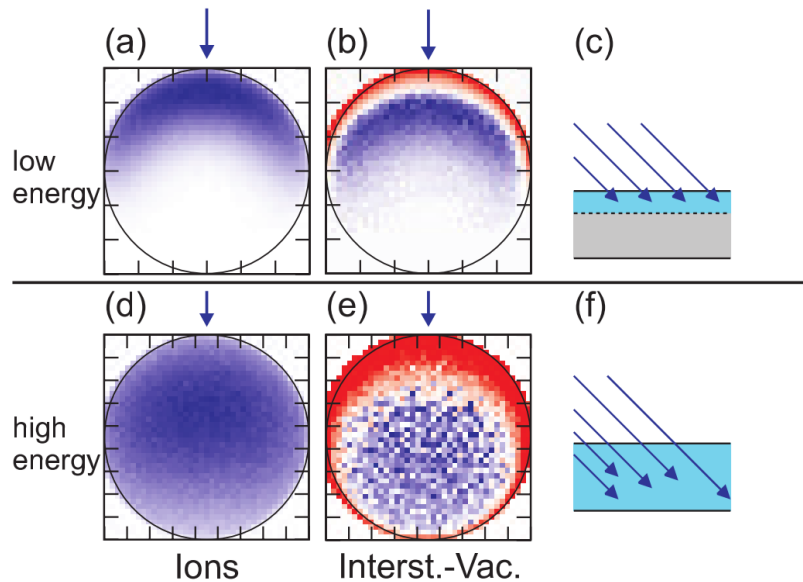


**Figure 2.27:** Iradina MC simulation results and schematic depicting shallow and deep implantation in the top and the bottom row, respectively. In the left column (a), (d), implanted ions are represented in a purple colour gradient. In the middle column (b), (e), excess of interstitials are represented in purple whilst excess of vacancies are shown in red. In the right column (c), (f), the direction of the ion beam is represented by the dark blue arrow and the part of the nanowire affected by the ions is coloured in light blue. From [114].

Furthermore, the same authors dismissed the influence of the implanted ions in the volume change of the nanowires as their effect must be marginal compared to that of the point defects as the number of vacancies and self-interstitials generated during irradiation is much higher (orders of magnitude higher) than the number of implanted ions. For this purpose, the authors showed that the number of point defects generated during the experiments performed on zinc oxide is about  $5 \times 10^3$  per incoming ion [114].

Choosing an energy such that the range of the incoming ions was about half of the nanowire diameter, the authors irradiated gallium arsenide nanowires with xenon ions [97]. By imaging the nanowires ex situ in a scanning electron microscope (SEM) at successive irradiation steps, they observed that the bending direction of the nanowires changed during the experiment. When the irradiation commenced the nanowire initially started to bend away from the ion beam, then during the bending the range was increased as the relative angle of irradiation changed (due to the bending) and the nanowire then started to bend towards the ion beam. In terms of the mechanism described earlier, this bending behaviour was explained by invoking the change of range due to the angle of incidence which affects the distribution of point defects thus, switching the irradiation conditions from shallow implantation to deep implantation conditions, leading to an alternate bending direction [97].

#### 7.4.6. Amorphisation based mechanism

Like the mechanism based on the distribution of point defects, amorphisation based mechanisms can also explain both the bending away from and towards the ion beam [20], [177], [184].

As stated above, ion irradiation of silicon and germanium can lead to amorphisation. It is therefore not surprising that IIB applied to germanium and silicon nanowires has also induced amorphisation when taken above a certain fluence. In [20], 30 keV gallium ion irradiations were performed on single crystal germanium nanowires, by Romano et al., whilst in [177], [184] ion irradiations have been performed by Pecora et al. on tapered single crystal silicon nanowires under 45 keV germanium ions in both cases inducing amorphisation and bending [20], [177], [184].

The work performed on germanium nanowires by Romano et al. gave different results from that on silicon because during irradiation onto the same side of the nanowire, a change of the

bending direction was observed [20]. In addition, Romano et al. showed that it was possible to reverse the bending direction numerous times by irradiating opposite sides of the nanowires. As seen in the top row of figure 2.28, the germanium nanowires at first bent slightly away from the ion beam at low fluence before bending towards the ion beam at higher fluences [20]. On the second and third row of images in figure 2.28, it can be seen that the bending direction can be modified by repositioning the ion beam to the opposite direction prompting the nanowires to then realign with it. However, unlike the IIB towards the ion beam which could be repeated several times, the nanowires did not bend away the ion beam when it was repositioned [20].

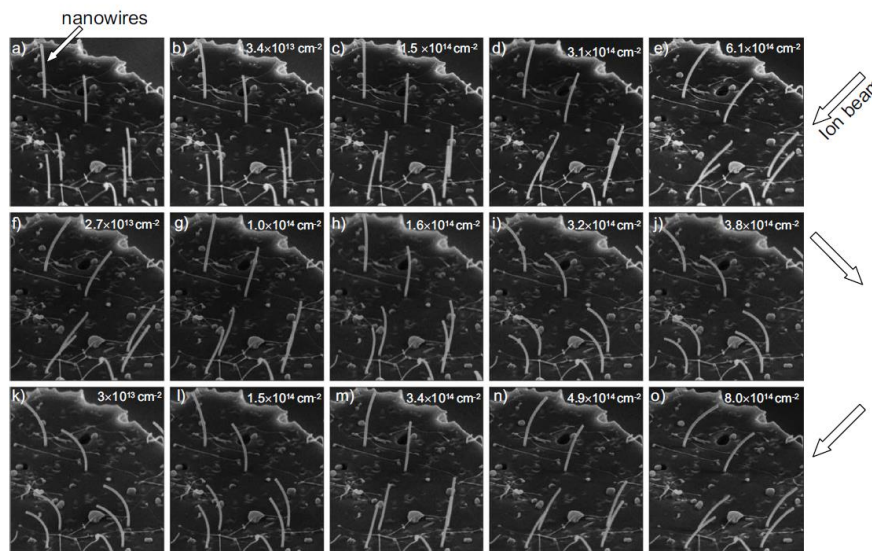


**Figure 2.28:** SEM images of germanium nanowires under 30 keV gallium irradiation. The direction of the ion beam is indicated by the white arrows. As indicated, the incidence direction is changed during irradiation, inducing a change in the bending direction. From [20].

Romano et al. observed that the nanowires became partially amorphous after the irradiation by the 30 keV gallium ion beam to a fluence of  $3.5 \times 10^{13}$  ion.cm<sup>-2</sup>. This fluence matched the moment at which the authors first observed the nanowires bending away from the ion beam. Above this fluence, the germanium nanowires continued to bend away from the ion beam until complete amorphisation was reached. As stated above, germanium is known to become less

dense when it amorphises. Romano et al. invoked the stress between the two germanium phases (the expanded amorphous phase constrained by the denser crystalline phase) to explain the bending away of germanium nanowires under irradiation [20]. According to the authors, as the bending away from the ion beam is dependent on the existence of such stress (and consequently on the presence of both phases), the absence of bending away from the ion beam can be expected when the nanowires are fully amorphous as the stress between the two phases is cancelled at this point. Consequently this would explain why germanium nanowires did not bend away repeatedly upon changing of the irradiation direction as the nanowires were already fully amorphous [20].

Once the nanowires became fully amorphous the same authors observed the bending towards the ion beam. After sufficient irradiation, the germanium nanowires were aligned with the beam and could endure at least six iterations of the IIB reversal before suffering noticeable sputtering. As the bending towards seemed to be activated only once the nanowires became fully amorphous, the authors proposed two mechanisms related to amorphisation. One of the mechanisms they suggested was a possible relaxation of the amorphous phase during irradiation leading to densification, the other mechanism was a viscoelastic flow process known as ion hammering [20], [186]. Also proposed by Pecora et al. [177], [184] to explain tapered silicon nanowires bending towards the ion beam, this viscoelastic flow process occurs only in amorphous material. Ion hammering is due to an anisotropic heating during electronic energy loss. By the transiting ion, this anisotropic heating leads to an anisotropic thermal expansion, which, after relaxation, will lead to a net deformation of the amorphous material. Ultimately, as a result of ion hammering, an expansion perpendicular to the ion beam will be observed as well as a shrinkage of the irradiated material in the direction parallel to the ion beam [20], [177], [184], [186]. This effect, whilst inducing a macroscopic deformation of the irradiated material, depends on the cumulative deformation induced by each impinging ion and increases

with the electronic energy per ion deposited in the system [187]. Indeed, the anisotropic thermal expansion mentioned above occurs in the cylindrical track formed by each ion and most importantly at energy regimes where thermalization occurs largely due to electronic loss [187], [188]. As a result, ion hammering typically necessitates ions to be accelerated at least at a few MeV to be observed [187], [188]. As this crucial feature of the ion hammering effect normally means that it must not occur in the experiments reported by Romano et al. in [20], the authors suggested that the bending of the germanium nanowires towards the ion beam under the 30 keV gallium ion beam indicates that ion hammering might occur in nanostructures even when the electronic energy deposited is relatively low [20].

Pecora et al. irradiated tapered silicon nanowires in a way that would render fully amorphous the top part of the nanowires but would not have sufficient range to make the nanowires fully amorphous in the larger part of the tapered nanowires [177], [184]. Using TEM diffraction and imaging techniques to observe the microstructure, they observed that the bent parts of the nanowires were fully amorphous, while on the unbent part a thin crystalline strip was coexisting with the amorphous phase. Pecora et al. suggested that the rigid crystalline part was preventing the nanowire from bending towards the ion beam. Thus, they concluded a necessity for the nanowire to be fully amorphous for the hammering effect to be able to induce bending towards the ion beam [177], [184].

Annealing of the bent tapered silicon nanowires was performed afterwards at 600°C and 800°C by the same authors [177], [184]. They observed that the nanowires unbent during SPEG but remain bent when RNG was induced. They concluded that during SPEG the aforementioned crystalline strip acted as a seed for the regrowth. Furthermore, as they observed that the removal of the amorphous phase during SPEG was accompanied by the unbending of the structure, they concluded that the unbending was further proof that the presence of the amorphous phase was responsible for the initial bending towards the ion beam [177], [184].

# Chapter 3: Experimental method

## 1. TEM

### 1.1. History

Often, relatively small things will govern the relatively large ones and whilst this preceding statement might at first seem paradoxical, numerous scientific investigations have proven that it is often by looking into what can be considered small details of a specimen that we can unravel features having a dramatic effect at a much larger scale. For these reasons, scientists study proteins to help cure cancer [189], observe defects in crystals in order to understand how more-resistant materials can be designed to be used in future nuclear plants [190] or study how the geometry of nanomaterials can influence the future quantum computers [191]. For centuries, the natural reflex when observation was needed was to use light [192]. Indeed, microscopes were, until the 20<sup>th</sup> century, always based on focusing visible light onto the specimen that one wanted to study.

It was only in the 1930s that the first rudimentary TEM was designed [193]. However, as with many innovations in science, the invention of the TEM was not solely due to the spontaneous genius of one individual, but the result of decisive discoveries which were shaping and redefining science.

For instance, Thomson [194], [195] and Millikan [196] provided fundamental information regarding the electron. The former determined the ratio between the charge of the electron and its mass in 1897 whilst the latter calculated its charge and mass. In the 1900s, scientists such as Birkland and Poincaré showed that electron trajectories can be influenced and guided via the use of magnetic fields [197]. Investigations, which, led to the ability to control the trajectories of electrons using the kind of magnetic field now used in TEMs permitted Busch

to establish what became known as electron optics [198]. Out of those advances, one of the most crucial must be credited to Louis de Broglie. By establishing in 1924 that electrons are not only particles but also have wave-like properties, he opened the possibility that similarly to light they might be used to observe matter [199].

A few years later, the big step was taken by Max Knoll and Ernst Ruska who on the 4<sup>th</sup> June 1931 unveiled the first image obtained by an electron microscope during a conference in Berlin [193]. As the resolution of their images was already below 10 nanometres, their work had a consequent impact and triggered the urge to develop TEM, thus earning Ruska a Nobel prize in 1986 [193].

## 1.2. Magnification

In order to distinguish what cannot be observed by an unaided human eye, an object of interest must be magnified [200]. In a TEM, this is done by transiting electrons through the object and then guiding them using a series of lenses in such a way that an enlarged image of the object is formed (and then converted into light). [201].

In a TEM, it is the magnetic lenses that are typically used to guide the electrons [201]–[203]. These lenses are able to converge and focus electron beams. As can be seen in figure 3.1, a convergent lens will bend the incoming rays depending on the angle  $\hat{C}$  that they make with the plane of the lens. The lens will converge more strongly the ray forming a small angle  $\hat{C}$  as compared with those forming a larger angle  $\hat{C}$ . Via this process, an image of the object will be formed behind the TEM lens to a specific distance from the lens' central plane. As shown in the picture at such distance all the rays coming from a point of the object will have been focused at the same position behind the lens, on the image plane [201]–[203].

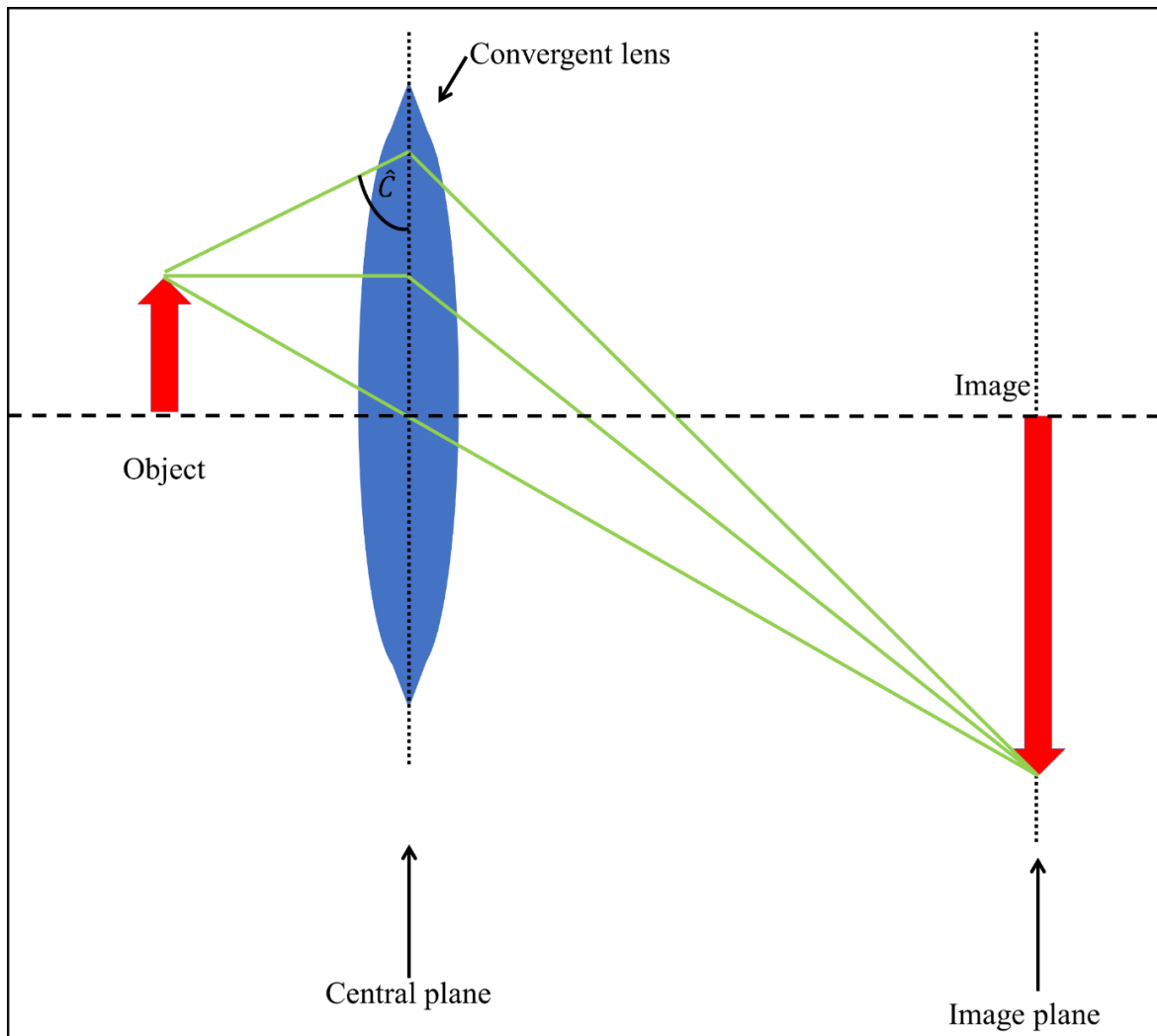


**Figure 3.1:** Schematic showing how individual rays (represented with coloured lines) are bent depending on their optical pathways and the angle they form with the central plane of the convergent lens. In front of the lens in the image plane an image of the object is formed where the rays meet.

### 1.3. Structure of the microscope

#### 1.3.1. Emission of electrons

As will be addressed later, during the interaction between the electron and the sample some important imaging properties (such as the diffracting effects, the resolution and the brightness)

are improved if the electron has a lower wavelength (i.e. a higher velocity), however, before being accelerated, electrons need to be emitted from a source. The most common ones are the so-called thermionic sources. In addition to be easily engineerable these sources must be able to provide electrons. To escape from the source, enough energy must be provided to the electrons so that they can overcome the work function,  $\Phi$ , of the material. The work function defines the minimum energy that need to be given to an electron to be removed from this material, and thus reach the vacuum level. To provide such energy, a filament may be heated so that enough thermal energy is given to the electrons allowing them to escape from the tip of the source. In these cases, the sources are referred to as working via thermionic emission. They must therefore be able to withstand high temperature (or have a low enough work function) and be formed into a tip. As they satisfy those conditions, the thermionic tips typically chosen in TEM are made of LaB<sub>6</sub> or tungsten. The density of current,  $J$ , they emit is given by equation 3.1 where  $A$  is Richardson's constant ( $\text{A.m}^{-2}.\text{K}^{-2}$ ) [201]–[203].

$$J = AT^2 e^{-\frac{\Phi}{k_B T}} \quad (3.1)$$

Most TEMs based on such type of emission were equipped with an electron gun made of a V-shaped tungsten filament [203] as shown in figure 3.2. The tungsten filament is heated to a temperature of about 2500°C in order to emit electrons [201]–[203]. However, this type of electron gun has been gradually replaced by those made of LaB<sub>6</sub> crystals as shown in figure 3.2 [203]. Having a lower work function, LaB<sub>6</sub> needs only be heated to a temperature of about 1500°C [203]. To understand why this type of electron gun is now favoured over those using a tungsten filament, it is important to understand two main factors which influence the quality of an electron gun: the spatial coherence and the temporal coherence [201]–[203]. The former describes the degree to which electrons come from a single “point” in the source. The latter depends on the variation of the energy between the emitted electrons (i.e. the energy spread).

Typically, the colder is the source, the less this latter varies and the better is the temporal coherence of the source. Tungsten filaments are relatively low-cost and simple to look after when it comes to their maintenance. However, they offer less coherence than LaB<sub>6</sub> which are more expensive but deliver electrons with better spatial (due to finer tips) and temporal coherence (due to a lower temperature required during emission). As shown in figure 3.2, in thermionic sources the use of a Wehnelt cylinder placed below the source focuses the electron beam to a position called the gun crossover, additionally by repelling some of the electrons (i.e. the less temporally coherent) it may improve the coherence of the electron beam [201]–[203].

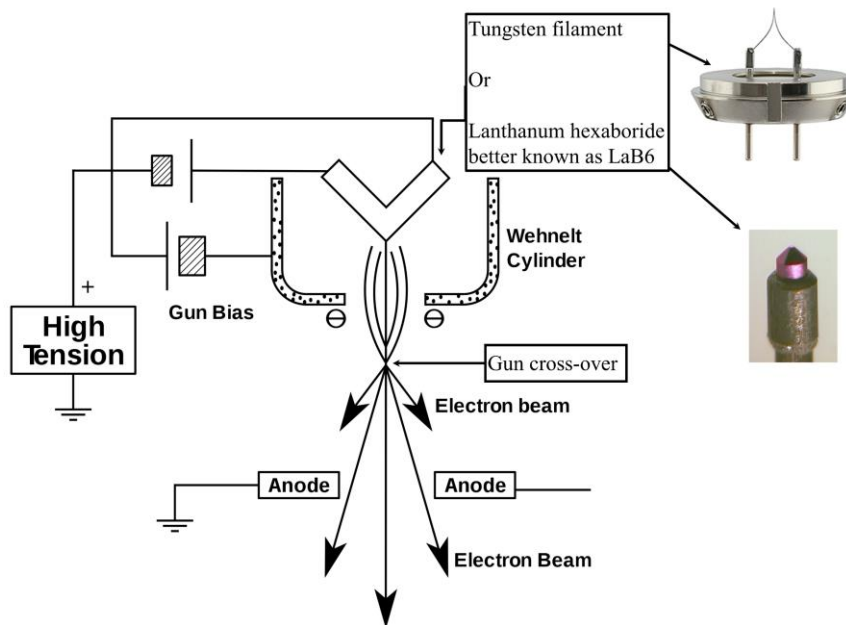


**Figure 3.2:** Schematic showing a typical thermionic electron gun structure with photographs of the two most common thermionic sources used in TEM (tungsten and LaB<sub>6</sub>). From [204]–[206].

An alternative to the thermionic emission source is shown in figure 3.3: the electrons are stripped from a cathode tip by applying a tension of a few thousand volts relative to the anodes. The applied voltage generates a strong electric field that extracts electrons from the tip of the

cathode. This type of emission is used in a field emission gun (FEG). FEG sources offer the best spatial and temporal coherence. For these reasons, they are therefore often used in microscopes which are specialised in imaging at high resolution or when high resolution is required for spectroscopy. It is worth noting that a hybrid type of field emission gun is also often used: the hot FEG. In a hot FEG, in addition to the electric field, the source is heated to avoid contamination and to provide thermionic assistance to extract more electrons and thus attain a higher beam current. However, as can be seen in table 3.1, this happens at the expense of the coherence compared to cold field emission guns which rely solely on the electric field to extract the electrons [201]–[203].

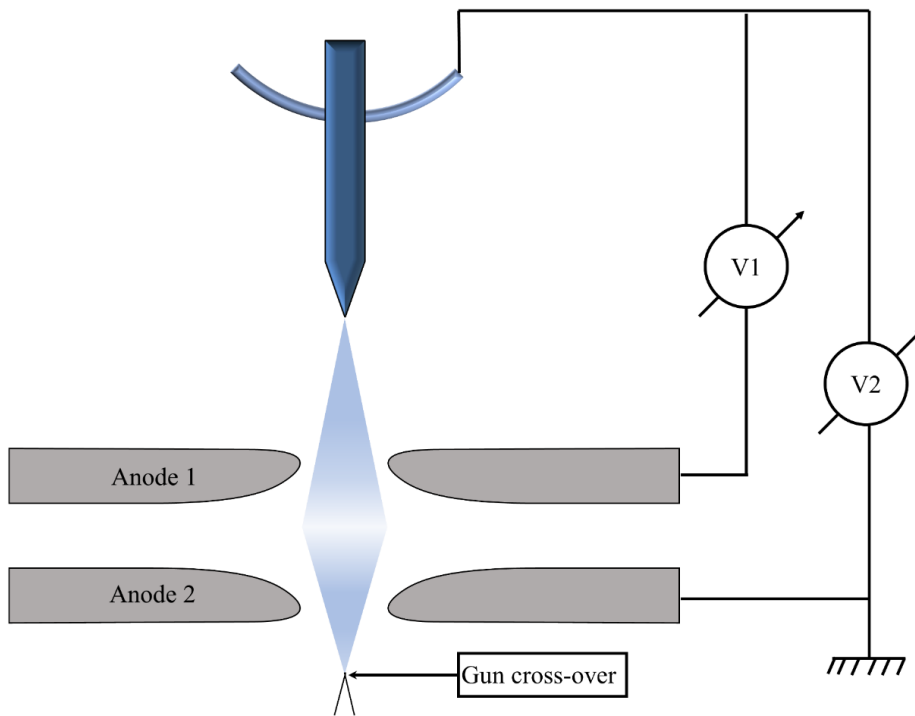


**Figure 3.3:** Schematic showing a field-emission type of electron gun where two anodes under a voltage shown in the picture by V1 and V2 are used as electrostatic lens to guide and focus the beam. Furthermore, as stated in [203], V1 typically delivers a voltage to extract the electrons from the tip whilst anode 2 is used to accelerate the electrons.

Type of source	Energy distribution (eV)	Size of the source's tip
Tungsten	2.5	50 $\mu$ m
LaB <sub>6</sub>	1	5 $\mu$ m
Thermal FEG	0.75	25nm
Cold FEG	0.35	5nm

**Table 3.1** Typical values of energy distribution and source sizes of the main type of sources used in TEM according to [207].

Another feature which differentiates the various types of electron gun is the brightness,  $\beta$ , of the source. The calculation of  $\beta$  is shown in equation 3.2, where  $i_e$  is the emission current,  $d_0$  is the diameter of the electron beam at its cross-over point (located below the Wehnelt cylinder as discussed below) and  $\alpha_0$  is the divergence which can be approximated as the semi-angle formed by the electron beam when it emerges from the gun crossover:

$$\beta = \frac{i_e}{\pi(\frac{d_0}{2})^2\pi(\alpha_0)^2} \quad (3.2)$$

It is intuitive that the higher the brightness is, the easier it potentially will be to extract information from the portion of the specimen being illuminated. However, increased brightness is more likely to damage a specimen susceptible to such effects. Typically, the brightness increases with the acceleration voltage. Furthermore, for a given acceleration voltage, the brightness also depends on the type of source. Usually, the lowest brightness comes from tungsten-type electrons gun followed by LaB<sub>6</sub>, then hot FEG, whilst the greatest brightness are found in TEMs equipped with cold FEG sources.

Once the electrons leave the source, they are accelerated to several hundreds of kilo electron-volts (in most TEM) [201]–[203]. To achieve this, a voltage between the ground and the source is created by holding the source at a high negative voltage (typically between –80 kV and –300 kV in the TEMs at the MIAMI facility) [208].

### 1.3.2. Lens system

#### 1.4.2.1. *The electromagnetic lens*

As described above, the invention of the TEM was in part dependent on the design of a new type of lens which could influence the trajectory of electrons using magnetic fields instead of

the traditional lenses used to bend light. In this type of lens, a magnetic field is created by running a current in a set of coils wrapped in metallic cases called pole pieces.

As stated by the Lorentz law, a force ( $\vec{F}$ ) dependent on the velocity  $\vec{v}$  of an electron in a magnetic field  $\vec{B}$  is generated such that:

$$\vec{F} = -e(\vec{v} \times \vec{B}) \quad (3.3)$$

Looking at this equation, it is therefore evident that the direction of the electron going through the magnetic lens will be modified depending on its initial direction as the force generated will take the direction of the cross product between  $\vec{v}$  and  $\vec{B}$ . Consequently, the direction of the force acting upon the electrons will also vary as  $\vec{v}$  changes direction [201]–[203].

Except for a rotation of the position of electrons when they escape from the field, the net effect of the TEM lens on electrons will be similar to a convergent optical lens on photons. The magnetic lens will converge electrons unless they are aligned with the optical axis of the lens (as  $\vec{v}$  and  $\vec{B}$  are collinear in this instance) and can therefore be used to create a magnified image of an object, similarly to the example illustrated in figure 3.1 [203].

The analogy with optical lenses also holds for the aberrations than they can both suffer. One of the most important aberrations is spherical aberration. In a lens, the strength with which electrons are bent depends on the distance they are from the optical axis – the further they are from the optical axis, the more strength with which they will be bent. In some modern TEMs, there are now systems which enable the correction of the spherical aberration. Indeed, often, TEMs dedicated to high resolution offer the correction of both this aforementioned aberration and a less severe one: the chromatic aberration corrected. Chromatic aberration is the result of the electron beam not being perfectly monochromatic (i.e. monoenergetic). Consequently, the electron beam is not bent uniformly by the lens as the Lorentz force depends on the velocity of

the electrons. Whilst most TEMs are not equipped with spherical and chromatic aberration correcting systems, they are fitted with other features which, as discussed below, are essential in order to correct other factors which can interfere with the image formation [202], [203].

#### *1.4.2.2. Feature of the Lens system*

In a TEM, several magnetic lenses can be found along the column, focusing the electrons and ultimately projecting a magnified image onto the viewing system. However, as the features which need to be observed are often on the order of nanometres, angstroms or even less in size, it is evident that any slight deviation of the electron beam or electron energy such as small imperfections in the lenses can be deleterious for the resolution. Therefore, each lens system is equipped with a set of features which are shown in figure 3.4 [202], [203].

As expected, even in the best-case scenario, at the scale considered in a TEM, the incoming electrons cannot be considered as coming exactly parallel to the lens' optical axis. To consider this, magnetic fields are generated by deflectors in order to bend the electron beam. As seen in figure 3.4, the first set of deflectors can be used to deflect the beam towards the axis, whilst further deflection via a second set will enable further correction of the misalignment between the incoming electrons and the lens. It is, however, worth noting that deflectors may be used to purposely deflect the beam off the optical axis to perform techniques that will be addressed below (e.g. dark-field (DF)) [202], [203].

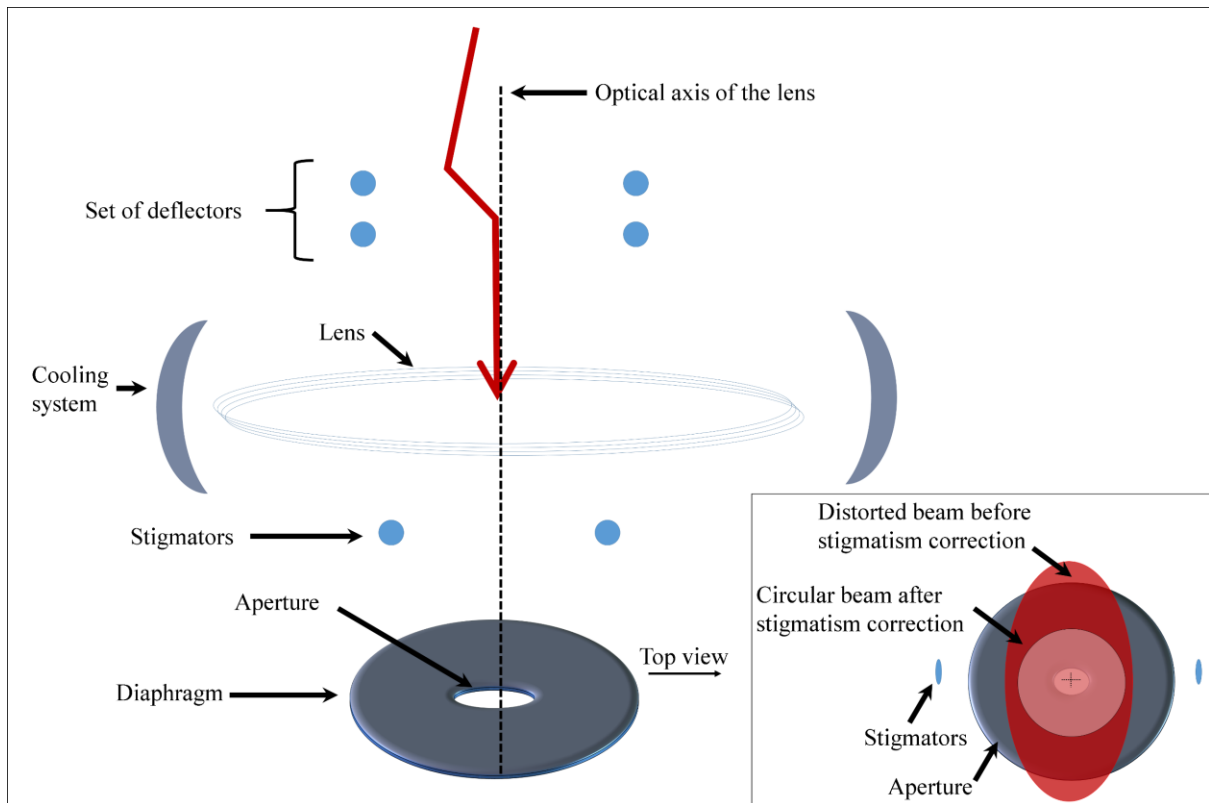


**Figure 3.4:** Schematic of an electromagnetic lens system and associated components. In the example depicted in the figure the electron beam shown in red is tilted towards the optical axis of the lens by the deflectors. As illustrated in the image on the right bottom-corner the astigmatism (represented by a distorted electron beam) is corrected when the electron beam passes through the stigmators (or more precisely by the field they generate) and is then skimmed by the aperture.

Another feature of TEM that can be considered is the non-perfect uniformity of the magnetic field generated by the lens. An unequal magnetic field can result in a lens being stronger in some directions than in others, which is called astigmatism. In the same way that optical lenses can suffer from astigmatism and bend a beam of photons in an uneven manner, the same effect occurs in magnetic lenses. As shown in figure 3.4, stigmators are used to correct this problem

by slightly distorting the electron beam via a magnetic or an electromagnetic field to correct for the distortion introduced by the associated lens

Lastly, the current running into the coils can be influenced by heat which, in metal, reduces the conductivity. As changing temperature will thus affect the magnetic field, the magnetic lenses are maintained at a constant temperature via a cooling system [202], [203].

### 1.3.3. Vacuum system

To enable the electrons to travel within the TEM column, a good vacuum must be maintained (about  $10^{-6}$  Pa in a typical TEM) as electrons would otherwise be scattered by gas atoms. To reach and maintain a desired level of vacuum, a set of pumps are used. These pumps operate at different pressures and are complementary [203]. Indeed, it is important to understand that if a pump is operated at an insufficient level of vacuum relative to its normal use, damage can result.

Typically, at a low level of vacuum from atmospheric level to  $\approx 10^{-1}$  Pa, the first pump used to lower the pressure is called a backing pump. Figure 3.5(a) shows a type of backing pump known as a rotary pump in which the gases will be dragged via a rotating fan. The gas which leaves via the exhaust is filtered to remove any vacuum pump oil and then released outside the column [203].

When the level of vacuum is sufficient, the oil diffusion pump carries on lowering the pressure. In a diffusion pump, oil is heated at the bottom of the pump so that molecules evaporate and travel up the centre of the pump at relatively high speed before being deflected back in the opposite direction down the outer region of the pump. They then collide with gas molecules and transfer momentum in the direction of the exhaust at the bottom of the pump. As the outside of the pump is maintained at a lower temperature, the oil will condense and re-join the liquid

oil being heated at the bottom of the pump as shown in figure 3.5(b). Diffusion pumps can be very efficient and are able to provide ultra-high vacuum ( $\approx 10^{-9}$  Pa). In this work, these pumps are mainly used to reach a vacuum of  $10^{-7}$  Pa [203].

To achieve higher vacuum, turbo molecular pumps are used. As shown in figure 3.5(c), the principle is in fact quite simple as it relies on a set of propellers which spin at very high speed (typically up to 60,000 rotations per minute) to drive the gases out [203].

Lastly, ion getter pumps permit vacuum to reach ultra-high vacuum (UHV) but can be operated only at pressures starting from  $10^{-3}$  Pa. As shown in figure 3.5(d), the principal components of an ion pump are a positively and a negative-charged plate which operate within a magnetic field. The cathode emits electrons that remain within the magnetic field. These electrons can ionise the molecules in the gas to form positively-charged ions. These will then be accelerated by the anode towards the cathode to be trapped. Additionally, titanium is sputtered away from the cathode by the impinging ions and tends to form compounds with gas molecules and so trap them within the pump [202], [203].

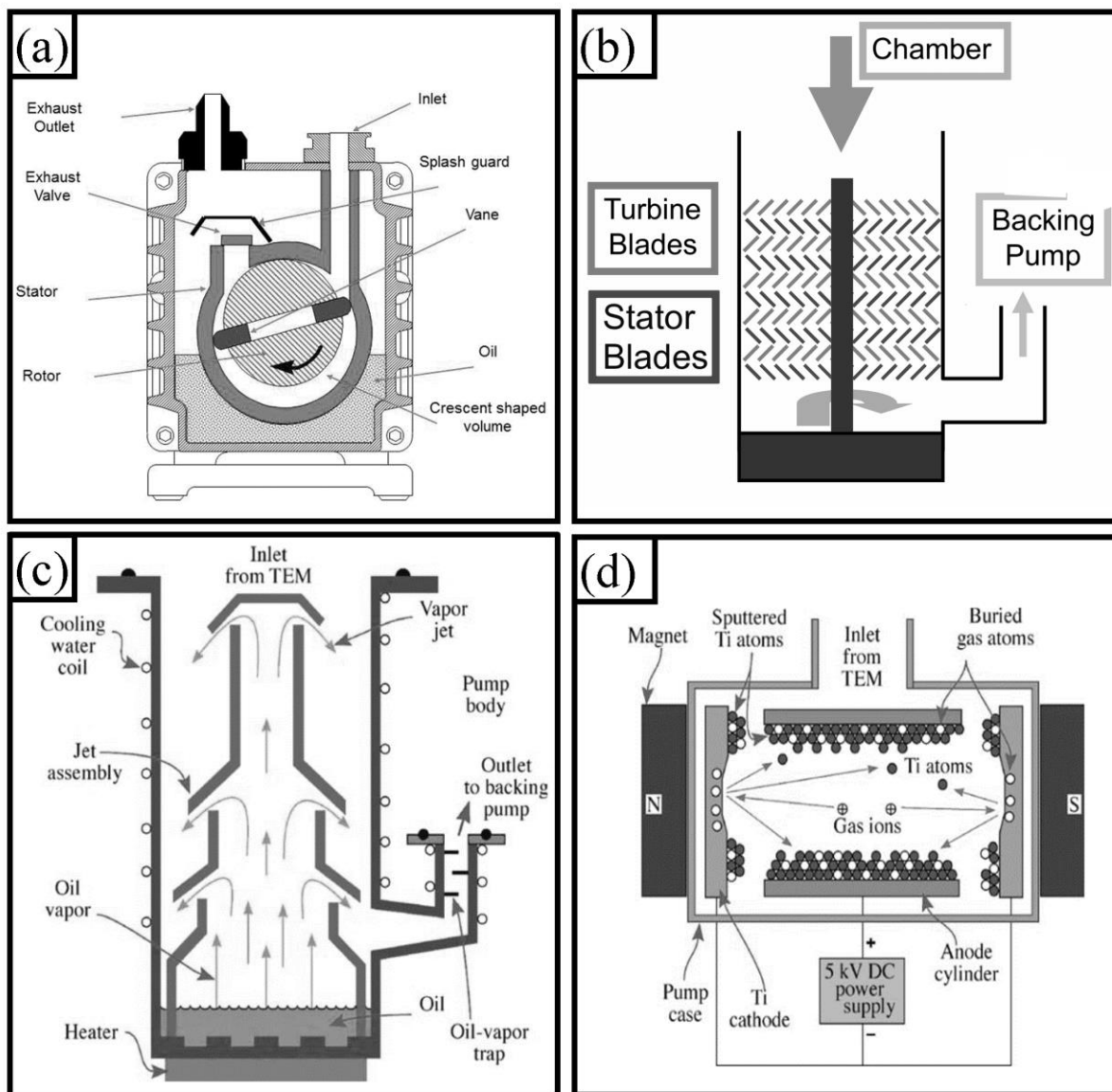


**Figure 3.5:** Schematics of: (a) a rotary pump, from [209]; (b) a turbo-molecular pump, from [210]; (c) an oil diffusion pump, from [203]; and (d) an ion getter pump, from [203].

#### 1.3.4. Sample Chamber

Samples need to be moved in and out the microscope without significant deterioration of the vacuum. The goniometer airlock permits the insertion of the sample without exposing the column to a sudden rise of pressure.

The sample holder (or rod) into which the sample is placed is inserted in the antechamber. Once sealed in this position, a roughing pump starts to evacuate the antechamber of gases until the required pressure has been reached (approximately below  $10^{-6}$  Pa in the microscope in the MIAMI facility). Once such a pressure is attained, the sample holder can be inserted fully into the microscope. When operating the TEM, contamination of the sample can occur even under vacuum as traces of gases including hydrocarbons, for example, will remain in the chamber or because the electron and/or ion beam causes outgassing, sputtering or hydrocarbon cracking. To reduce contamination of the sample, liquid nitrogen is poured into a reservoir on the microscope so as to cool a metal surface called a “cold finger” surrounding the sample. The cold finger acts as a trap for impurities as these will tend to condense onto the trap rather than going onto the sample [202], [203].

#### 1.3.5. Type of sample holders

There are several types of sample holders which can be used in a TEM. One of the most common options that sample holders offer is the possibility of tilting the sample. In the TEM, the sample can be moved by shifting the sample along the x-axis or the y-axis to bring the area of interest under the electron beam. However, as explained below, it is often also necessary to tilt the sample to fully determine the morphology of the sample, to perform high-resolution microscopy or to excite an electron beam reflection off a specific set of crystallographic planes. Some holders are single-tilt which allow an x-tilt whilst double-tilt holders permit both x-tilt and y-tilt as shown in figure 3.6 [202], [203].

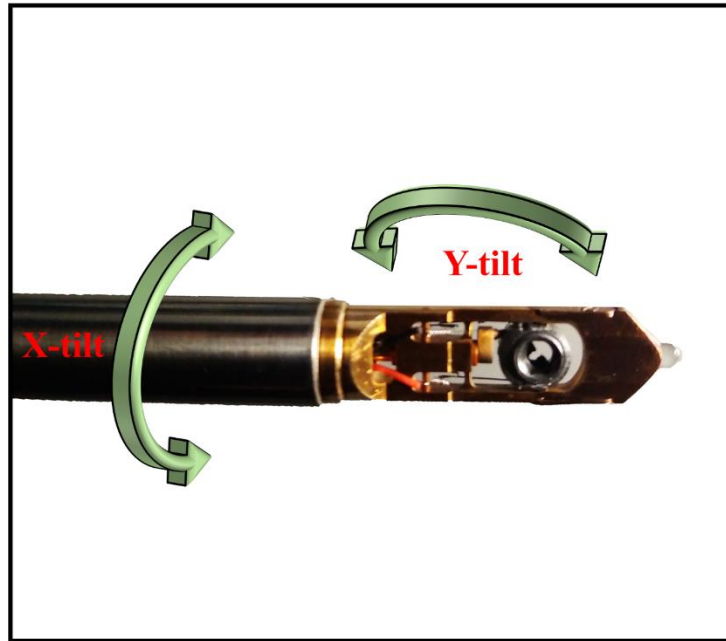


**Figure 3.6:** TEM holder with the two tilting directions represented by the green arrows.

Furthermore, there are holders which allow the rotation of the sample about the z-axis. They have proven in the current work to be especially useful during in situ irradiation of nanowires as they allow the orientation of the specimen into a position with the desired angle with respect to the ion beam.

For radiation damage investigations, the temperature often plays an important role. For instance, as explained in the literature review, the mobilities of defects are greatly influenced by the temperature of the specimen. For this reason, holders allowing control of the temperature by heating the sample or on the contrary by bringing down the temperature via the use of liquid nitrogen or liquid helium are often used. These types of holder may also be able to tilt the sample such as the heating double-tilt holders used in the current work.

Additionally, other types of holder can also be found such as straining or gas-flow holders which permit the sample to be mechanically tested or to allow the study of specimens in low-pressure gaseous environments [202], [203].

#### 1.3.6. Eucentric height

As will be explained later, the image seen on the phosphorescent screen (or any other viewing system) is the magnified version of the image formed by the objective lens. However, there is a plane of reference in which the object of interest should be placed: the eucentric plane. When the sample and the objective lens strength are adjusted so that the image is formed based on an object placed in this particular plane, the sample is said to be positioned at the eucentric height. If the height is not properly adjusted, using a tilt will also induce a shift and a change of height of the specimen. To have the sample at the eucentric height, the sample's plane must both be perpendicular to the lens optical axis and include the sample holder axis (to avoid the specimen to move during the tilt). As it is defined above, there is obviously not only one plane that satisfy these conditions, however, the eucentric height is unique because the sample height must also be adjusted when the objective lens' current is fixed at a reference value. In fact, in a TEM all the planes in the imaging system are (by default) arranged and set based on this current reference value.

In most TEMs, the electron beam travels from the top to the bottom of the TEM column passing through the magnetic fields generated by the different lenses. In such a TEM column, the settings are typically adjusted in a way that makes one (or several) of the lower lenses form a magnified image from an object at a fixed position above it. This fixed position will therefore be the object plane that lens, this object plane should also be in an ideal condition the image plane of the lens located directly above it. In fact, due to the multiple magnifications, each object plane should correspond to the image plane of an above-located lens leading to an in-

focus image. However, this is not always the case and the final image formed might not correspond to an in-focus image, meaning that one (or several lenses within the column) have formed an image from an object plane which did not correspond to the image plane of the above-located TEM lens. Typically, setting the focus is done via the objective lens which as shown in figure 3.7 may lead to a focused or a defocused image. As shown in figure 3.7 if we consider that the lens directly below the objective lens has its object plane defined at a fixed height (i.e. such a plane is shown in the figure via a dashed line) and that the specimen position and the objective lens strength are set in such a way that the image of the specimen will be formed at the height defined by the red rays, the image formed will be in focus. On the other hand, if the position and the strength of the objective lens are such that the rays are too strongly converged (illustrated by the green rays) and thus forming an image of the specimen above the object position of the lens below, this would lead to an overfocused image. Similarly, if the image is formed relatively too low (e.g. illustrated by the blue rays) the image will be in underfocus [202], [203].

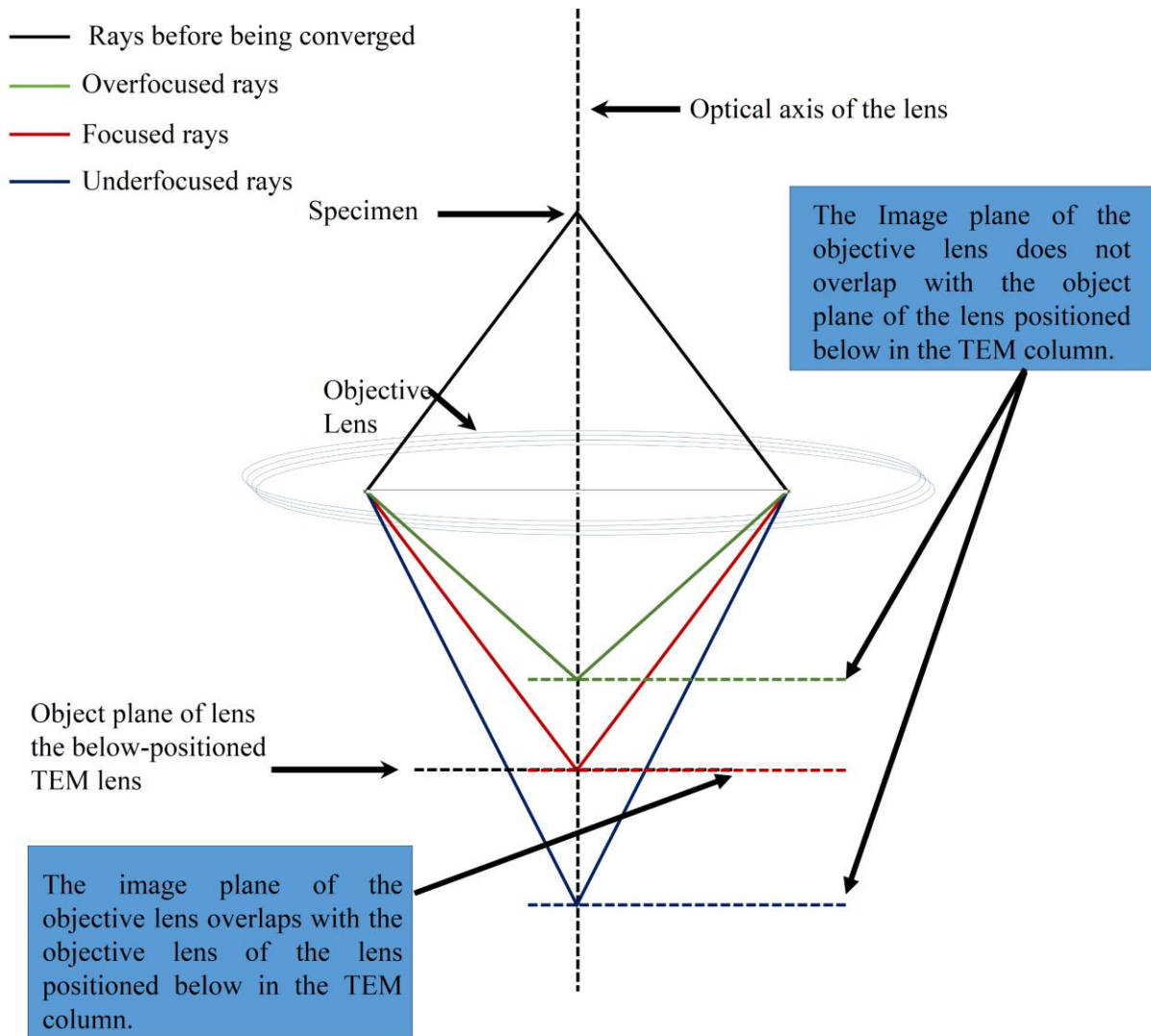


**Figure 3.7:** Schematic illustrating situations where the conjugate image of an object is either well focused onto the object plane of the lens positioned below in the TEM column (red line), overfocused (green lines) and underfocused (blues lines). In the example shown here the lens below in the TEM (not shown for clarity of the figure) is set such as its object plane is at a fixed height.

### 1.3.7. Viewing system

In TEM, the images formed by the electrons are observed using a viewing system which allows the formation of an image that is visible to the human eye. One of these is photographic films, which are electron sensitive and can therefore be used to capture images.

Another method of observation is the fluorescent screen, typically a phosphor screen, which is not used to capture images but rather to monitor the live image in the TEM.

“Direct” electron detectors directly produce a signal as the electrons hit the detector. An example is the complementary metal-oxide-semiconductor (CMOS) device. They are thus, used as a way of providing image and live observation using the flux of electrons hitting the device at each position [211], [212]. Typically, with such detectors as the signal is directly generated by the electrons there is a relatively good correlation between the signal detected and the position or the number of the impinging electron. As it will be addressed below, this is not the case for charge coupled device (CCD) cameras because they are indirect electron detectors.

Lastly, the CCD camera also allows live observation and imaging of the specimen. As CCD cameras were used routinely in this work (and in most modern TEMs) they are described in more detail below.

As shown in figure 3.8, the top part of the CCD camera is made of a material which performs the function of a scintillator. In a CCD camera, the scintillators are usually made from a single crystal of yttrium aluminium garnet (YAG) and have the ability to convert electrons into photons. Below the scintillator, typically a fibre optic bundle will carry the photons generated by the electrons to the CCD. The CCD will count the signal at each pixel available and therefore compile an image in which the intensity at each pixel depends on the number of counts detected by the CCD. Thus, the intensity of the image will depend on how the sample has interacted with the electrons [202], [203], [213].

However, unlike in this ideal description the photons generated by the electrons are in fact emitted in many directions so not all will enter the fibre optic bundle, thus affecting the conversion between electrons and photons. The conversion between electrons and photons is one of the main limiting factors of CCD camera as other effects might affect this conversion. For instance, an electron impacting the scintillator material might induce more than one photon. In some cases, the electrons can also leave the scintillator material only to be scattered back into the scintillator at positions unrelated to the original point of entry thus leading to the generation of photons at a position unrelated to its original position. Furthermore, some photons can also be transmitted to the CCD laterally far from the position hit by the electron when entering the camera and thus contribute to noise. For all these reasons, the signals transmitted by the fibre optic bundle are not perfectly representative of the initial position where the CCD has been hit by the electrons nor perfectly representative of the number of electrons.

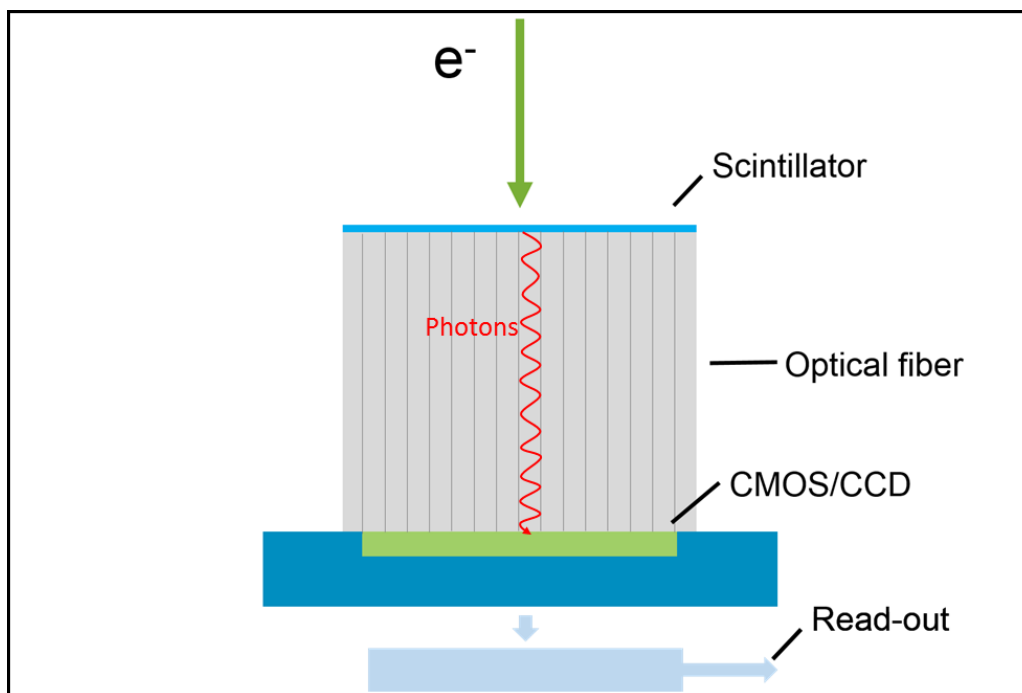


**Figure 3.8:** Schematic of a camera based on a CCD showing how an electron is captured by the scintillator that translates the electronic signal into photons to ultimately give rise to a signal via the CMOS. Modified from [214].

## 1.4. Image formation

### 1.4.1. Ensemble view

Figure 3.9 shows how the parts of the TEM previously presented are used in order to form a magnified image or a diffraction pattern. Firstly, an electron beam is generated by the electron gun and accelerated to the desired energy using the accelerator stack. The electron beam is then formed into a probe on the sample using the condenser lens system [202], [203].

Once the electron beam goes through the sample it is converged by the objective lens system the purpose of which, is to form the first magnified image (and diffraction pattern) of the sample. This is then further magnified using the intermediate and projector lens systems, which comprise one or several intermediate lenses and a final projector lens that will deliver a final magnified image to the viewing system. The object will thus be observed magnified by a factor of several thousand times (or million times), owing to the multiple lenses in the column [202], [203].

As described above, most lens systems are equipped with deflectors and stigmators allowing adjustment of the electron beam relative to the optical axis and to reduce astigmatism, respectively. Furthermore, apertures are used to select the electron beams which will be used to form the image and diffraction pattern. In the following section, going from the top of the microscope to the bottom, the different functions of the microscope are described in more detail.

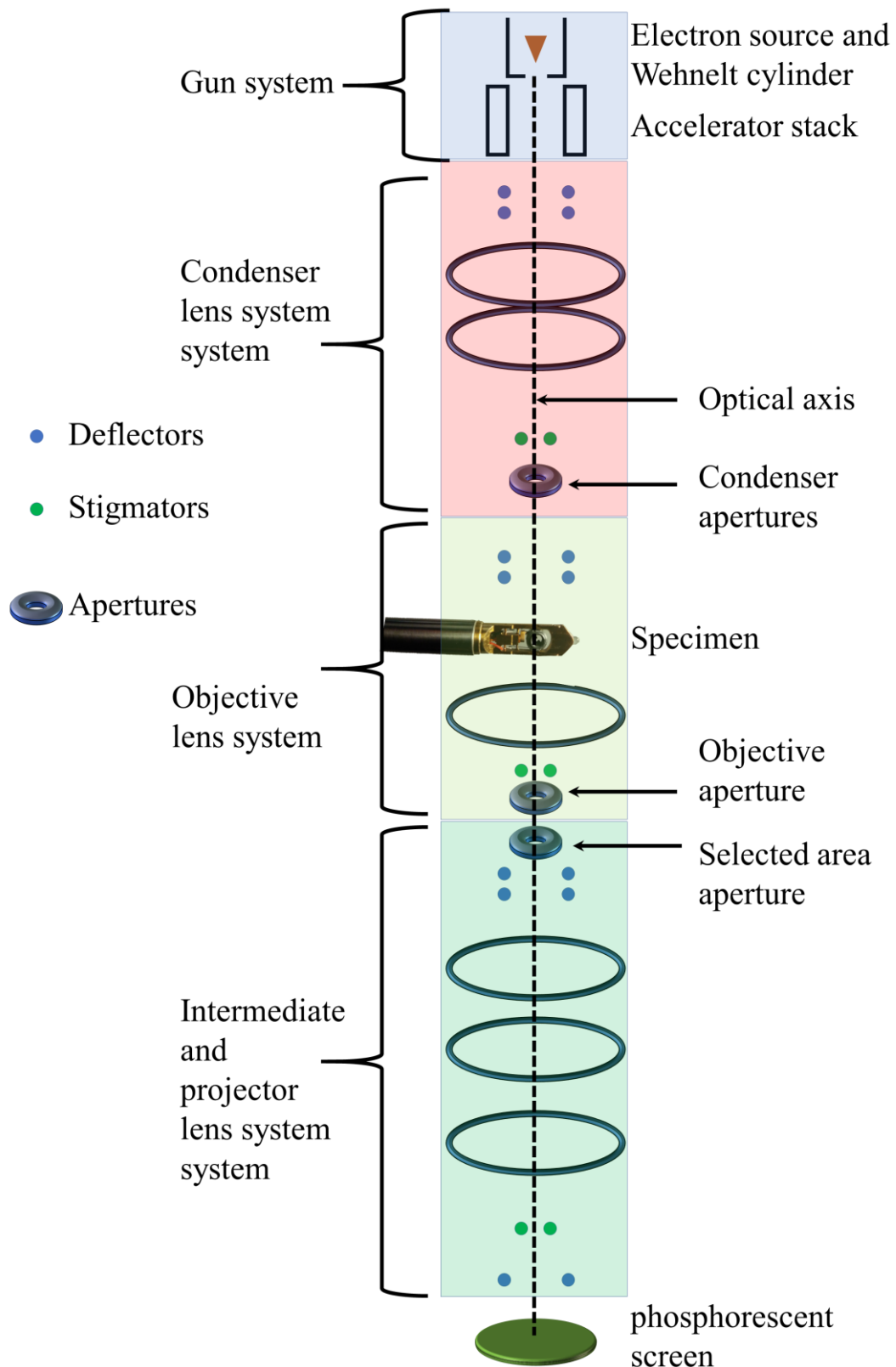


**Figure 3.9:** Ensemble view showing the main sections of the TEM. The image shown in the figure illustrates a simplified example as the actual TEM is more complex and may possess more lenses.

#### 1.4.2. From the Electron Gun to the sample

The illumination system takes the flux of electrons generated by the electron gun to the specimen. Using the Wehnelt cylinder, an image of the source is formed at the position where the beam coming from the gun has been condensed (the gun cross-over). As shown in figure 3.10, this image of the source serves as an object for the C1 lens which will condense (or de-condensed) its image at the C1 cross-over position.

Typically, in the simplest condenser lens system, a second lens C2 is used to illuminate the specimen. The C2 lens can be used to send a condensed beam onto the specimen thus performing techniques such as convergent-beam electron diffraction (CBED). In this work, the illumination system was mostly exploited to bring an (almost) parallel electron beam onto the specimen. For this reason, the illumination is underfocused and the C2 cross-over will be below the sample position. However, as can be seen in figure 3.10, the nominally-parallel beam is not really parallel as there is a very small angle  $\beta$  which typically is under  $0.006^\circ$ , which means that the electrons are not exactly spatially coherent [202], [203]. In theory, the C2 lens should be as underfocused as possible so that the angle  $\beta$  is minimised. However, in order for the specimen to be illuminated with sufficient electron intensity (i.e. a more condensed less-parallel beam) a compromise must be found. Lastly, as shown in figure 3.10 a diaphragm (with a hole in its centre called an aperture) can also make the beam more parallel but will reduce the number of electrons hitting the sample as it skims part of it.

There are many instances where the beam will need to be translated or tilted (e.g. when performing centred dark-field (CDF) as discuss below). As described above, coils can be used to deflect the electron beam along the column. Indeed, the set of deflectors can be used to shift or tilt the beam before it enters the sample. However, a calibration of the deflectors is often

necessary to perform a controlled tilting or shifting procedure so that tilting the beam does not shift it, and shifting the beam does not tilt it.

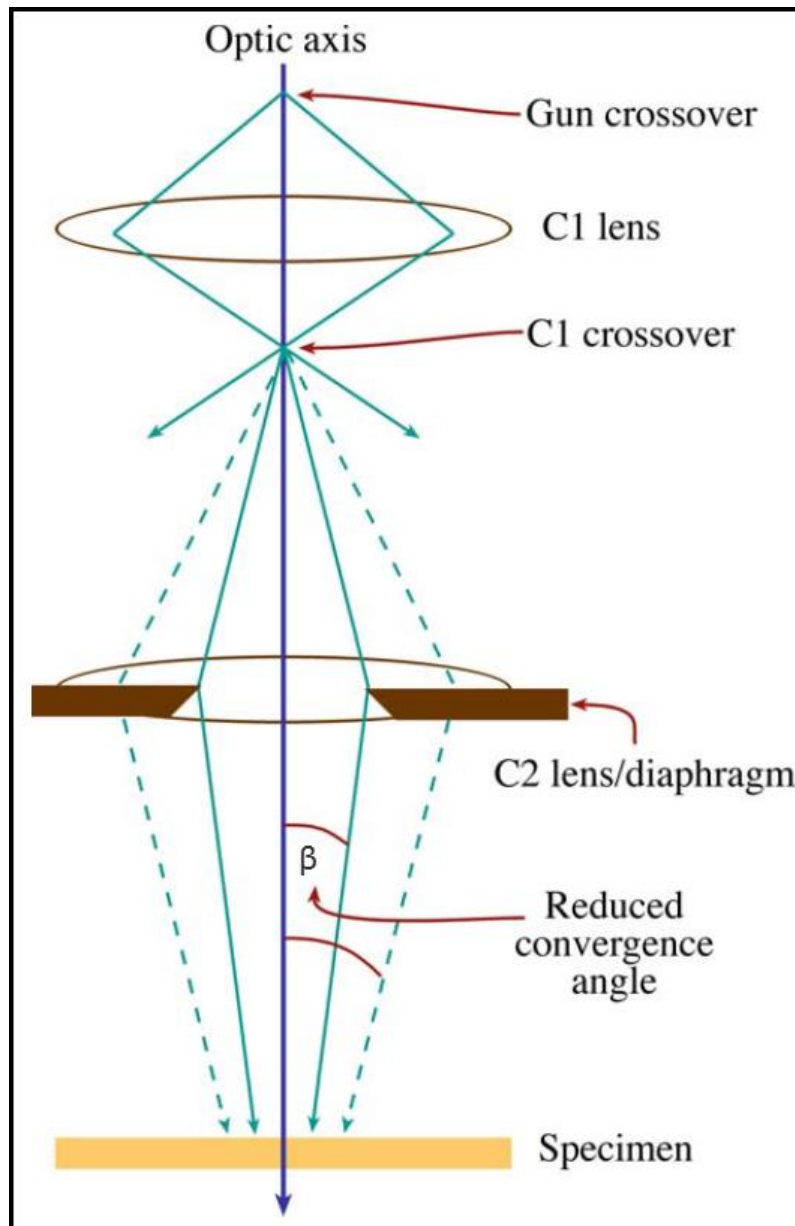


**Figure 3.10:** Electron ray path from the gun crossover to the sample showing how the C2 lens focuses the beam onto the specimen and how the diaphragm can act as a beam skimmer in a simplification of an actual TEM which is more complex and typically will possess more lenses. From [203].

### 1.4.3. Sample and objective lens

As stated above, the sample should be in the eucentric plane to avoid sample shift whilst tilting via the goniometer. As shown in figure 3.11, the objective lens will condense the electron beam in such a way that a diffraction pattern will be formed at its back focal plane. As will be shown later, the diffraction pattern gives valuable information regarding the microstructure of the specimen in the diffraction mode of the TEM. Lower in the column, the magnified image of the sample is formed in the image plane. In imaging mode, this is further magnified by the intermediate and projector lenses onto the viewing system [202], [203].

As shown in figure 3.11, choosing whether an image or a diffraction pattern is projected onto the viewing system is determined by setting the object plane of the intermediate lens to coincide with either the back focal or image plane of the objective lens in diffraction or imaging mode, respectively [202], [203].

During this PhD, most of the diffraction patterns were acquired whilst employing the selected area diffraction (SAD) aperture. This aperture was used to select the area of the specimen which was of interest. To do so, the SAD aperture cannot be physically placed at the sample position and so the aperture is therefore positioned in the image plane of the objective lens. Using the image of the specimen to select which area is used to create the diffraction is equivalent to having a virtual aperture at the position of the specimen [202], [203].

In imaging mode, an objective aperture might be utilized to select whether the image is formed using one of the diffracted electron beams or the direct beam (which is made mostly of unscattered electrons) to perform operations such as bright field (BF) and dark field (DF) imaging.

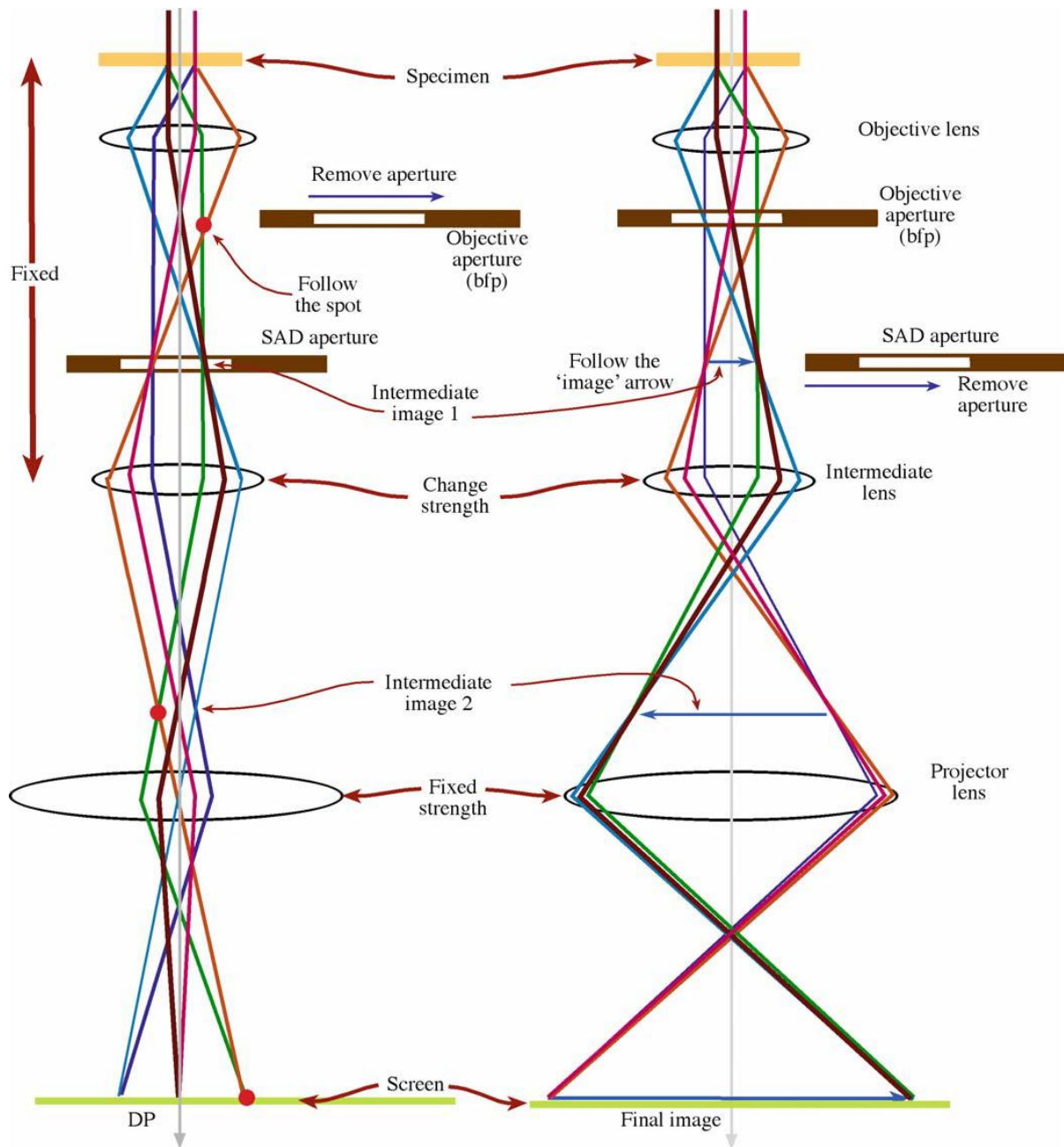


**Figure 3.11:** The ray diagram on the left shows an example of how a TEM can be operated to produce a diffraction pattern on the viewing system and on the right to produce an image. As shown in the picture the projector lens has a fixed height at which its object plane is positioned (i.e. Intermediate image 2). Consequently, the formation of a DP or an image will depend on whether at this position (i.e. the intermediate image 2) the intermediate lens forms a DP or an image. From [203].

#### 1.4.4. Bragg angle

As will be summarised below, the electron beam impinging on the specimen can lead to different kinds of interaction. Electrons can for instance be scattered without significant loss of energy (elastic scattering). The geometrical construction in figure 3.12 will be used to describe how coherent elastic scattering events constructively interact [202], [203].

In figure 3.12, two planes separated by a distance  $d$  in a crystal are shown as well as elastic scattering events and the resulting wave fronts. The wave front  $W_1$  is scattered and becomes  $W_d$ . The geometrical construction shows that there is a difference in path-length of two beams that encounter the adjacent scattering points, B and C. Indeed,  $\vec{R}_1$  travels a distance that is longer than  $\vec{R}_2$  by a quantity equal to:  $AC + CD = 2d \sin \theta$

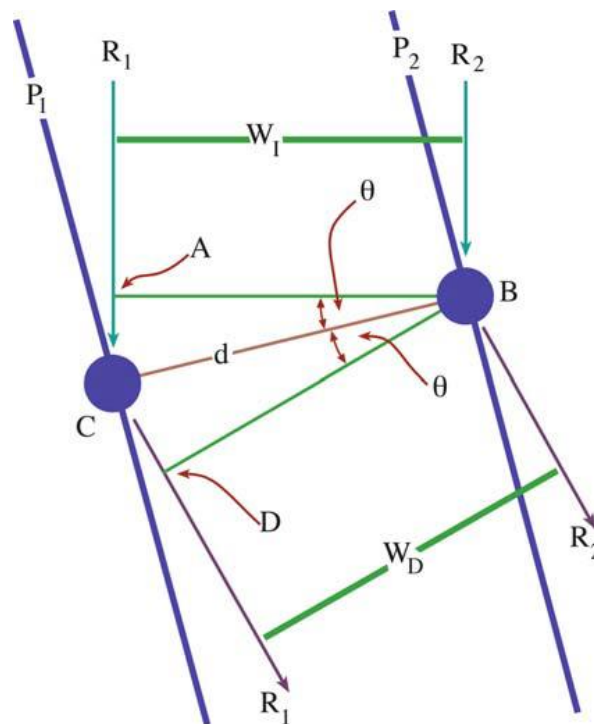


**Figure 3.12:** Scattering occurs from B and C, which are two points lying on the planes P1 and P2. The path difference between the two beams is equivalent to AC+CD. From [203].

In figure 3.12, the diagram shows two beams,  $\vec{R}_1$  and  $\vec{R}_2$ , from the same wavefront. Before scattering  $\vec{R}_1$  and  $\vec{R}_2$  are in phase as they come from the same wave front. However, after being scattered the difference of path length which depends on the angle  $\theta$  will determine whether they still are in phase. In fact, there are values of  $\theta$  called Bragg angles  $\theta_B$  at which the two beams will be in phase.  $\vec{R}_1$  and  $\vec{R}_2$  will be in phase when  $AC + CD = n\lambda$  (where  $n$  is an integer), thus when equation 3.4 is satisfied. This is the Bragg law and is equivalent to equation 3.5 (when  $n=1$ ) [203].

$$n\lambda = 2d \sin \theta_B \quad (3.4)$$

$$2 \sin \theta_B = \frac{\lambda}{d} \quad (3.5)$$

When the Bragg law is satisfied, thus when  $\theta = \theta_B$ , the beams may constructively interfere thus adding their intensities. The beams reflected through the Bragg angle correspond to the diffracted spots in the back focal plane of the objective lens.

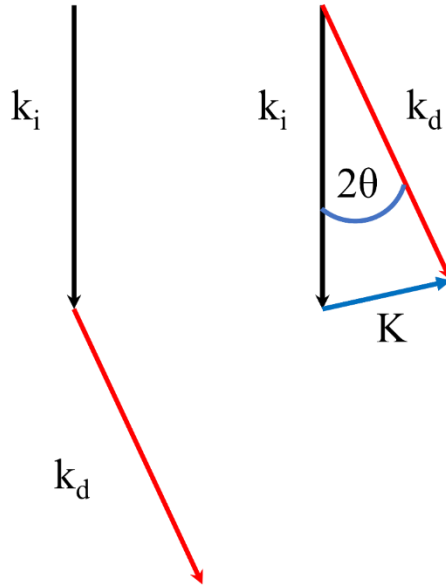


**Figure 3.13:** Illustration of vectors, which represent the wavefront prior to scattering,  $\vec{k}_i$ , and after diffraction,  $\vec{k}_d$ . The difference between these two is the vector  $\vec{K}$ .

The wave propagation vector  $\vec{k}$  (of magnitude  $\frac{1}{\lambda}$ ) can also be shown during the scattering keeping in mind that because it is elastic scattering that is considered here, the magnitude of the propagation vectors remains unchanged before and after scattering. As can be deduced from figure 3.13, the change in the vector due to the interaction is given by equation 3.6 and the magnitude of  $\vec{K}$  can be expressed as equation 3.7.

$$\vec{K} = \vec{k}_D - \vec{k}_I \quad (3.6)$$

$$|\vec{K}| = \frac{2 \sin \theta}{\lambda}. \quad (3.7)$$

Whilst  $\vec{K}$  represents the general case, if it takes values at which the Bragg law conditions are met then  $\vec{K}$  is called the diffraction vector,  $\vec{g}$ , whose magnitude is equal to  $(1/d)$ . As stated above, constructive interference will occur when  $\theta = n\theta_B$ . So, at the Bragg angle it can be written:

$$|\vec{g}| = \frac{2 \sin \theta_B}{\lambda} \quad (3.8)$$

#### 1.4.5. Reciprocal space and Ewald Sphere

As  $\vec{g}$  can be expressed as  $\frac{1}{d}$  it therefore has units of reciprocal length and exists in reciprocal space in which the lattice is expressed with reciprocal vectors  $\vec{r}^*$  which depend on reciprocal unit-cell vectors  $\vec{a}^*$ ,  $\vec{b}^*$ ,  $\vec{c}^*$ :

$$\vec{r}^* = m_1 \vec{a}^* + m_2 \vec{b}^* + m_3 \vec{c}^* \quad (3.9)$$

Where,  $m_1, m_2, m_3$  are integers

Furthermore, these reciprocal vectors are defined with respect to the unit lattice in real space such that:

$$\vec{a}^* \cdot \vec{b} = \vec{a}^* \cdot \vec{c} = \vec{b}^* \cdot \vec{c} = \vec{b}^* \cdot \vec{a} = \vec{c}^* \cdot \vec{a} = \vec{c}^* \cdot \vec{b} = 0 \quad (3.10)$$

$$\vec{a}^* \cdot \vec{a} = 1; \vec{b}^* \cdot \vec{b} = 1; \vec{c}^* \cdot \vec{c} = 1 \quad (3.11)$$

Consequently, these vectors are defined such that  $\vec{a}^*$  is normal to  $\vec{c}$  and  $\vec{b}$ ,  $\vec{b}^*$  to  $\vec{c}$  and  $\vec{a}$ ,  $\vec{c}^*$  to  $\vec{b}$  and  $\vec{a}$ . Also, the bigger the unit lattice represented by  $\vec{a}$ ,  $\vec{b}$  and  $\vec{c}$  in real space the smaller is the reciprocal unit lattice. The Bragg conditions correspond to value of  $\vec{g}$  equal to  $\frac{1}{d}$  and can therefore be expressed via vectors  $\vec{g}_{hkl}$  defined in reciprocal space, such as:

$$\vec{g}_{hkl} = h\vec{a}^* + k\vec{b}^* + l\vec{c}^* \quad (3.12)$$

One way of thinking about diffraction conditions is to consider an “Ewald sphere” in reciprocal space. As shown in figure 3.14 this sphere is usually drawn using the wave vector  $\vec{k}_i$  to represent CO where C is the origin of the sphere and O is the origin of the lattice in reciprocal

space. As vectors  $\vec{k}_i$  and  $\vec{k}_d$  have the same magnitude which is  $\frac{1}{\lambda}$ , the surface of the sphere of radius  $\frac{1}{\lambda}$  can only intersect reciprocal lattice points satisfying Bragg's law. In figure 3.14, a 2D representation of the Ewald sphere in the reciprocal lattice is shown. The surface of the Ewald sphere may intersect two reciprocal lattice points such that  $\vec{k}_D - \vec{k}_I = \vec{g}$  and in this situation the Bragg conditions are met and diffraction will occur [202], [203].

However, whilst in a reciprocal lattice discrete points are considered. The diffraction conditions are represented by a lattice made of relrods (which are ovoids centred on the reciprocal lattice points), meaning that even if the sphere does not exactly fall on the reciprocal lattice point it might still intersect a relrod and diffraction can occur. The shape of the relrods comes from the shape of the electron-irradiated section of the sample, which can be approximated as a thin cylinder or short-fat ovoid in real space. In reciprocal space, their shape is preserved, however, the relationship between length in real and reciprocal space being inverted, the thin illuminated region of the sample is a long column (or ovoid) in reciprocal space.

As stated above, the Ewald sphere does not need to exactly fall on lattice points for diffraction to occur. Furthermore, because the magnitude of  $\vec{k}_i$  and  $\vec{k}_d$  is  $\frac{1}{\lambda}$ , a small wavelength will result in an Ewald sphere with a bigger radius, which, consequently will have much more opportunities to encounter a relrod. It is worth stating that this correlation between the wavelength and the probability of diffraction phenomenon is the reason why diffraction occurs more readily in a TEM compared with X-ray diffraction which typically occurs at a larger wavelength [203].

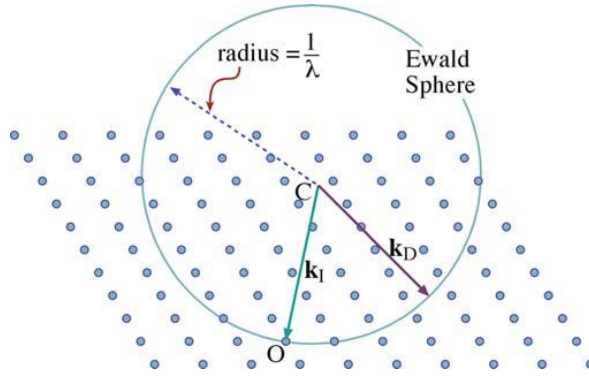


**Figure 3.14:** The Ewald sphere and the relrods in 2 D: as the relrods are not discrete points, a sphere with a large radius may encounter numerous relrods. From [203].

#### 1.4.6. Diffraction patterns

Each set of planes might give a diffraction spot at the back focal plane of the objective lens and the region of the specimen to generate those diffraction spots can be selected via the selected area aperture. In the selected region, however, some planes which satisfy the Bragg condition might not give a diffraction spot in the diffraction patterns if they are “forbidden reflections” and the intensity of the diffraction spots can vary for similar reasons as discussed below [203].

To describe the strength of a reflection or to know if they are forbidden, the structure factor  $F$  is determined using equation 3.13 where  $f_i$  is the scattering factor of the atoms in the lattice and where  $F^2$  is proportional to the intensity of the reflections. In germanium there is only one type of atom, therefore the amplitude of the diffracted beam will just be dependent on the scattering factor of germanium and to the eight  $(x,y,z)$  positions occupied by the atoms in the unit cell of:  $(0,0,0)$ ;  $(0.5, 0, 0.5)$ ;  $(0, 0.5, 0.5)$ ;  $(0.5, 0.5, 0)$ ;  $(0.25, 0.25, 0.25)$ ;  $(0.25, 0.75, 0.75)$ ;  $(0.75, 0.25, 0.75)$ ; and  $(0.75, 0.75, 0.25)$ :

$$F(\theta) = \sum_j f(\theta)_j e^{2\pi i(hx_j + ky_j + lz_j)} \quad (3.13)$$

When the different values of  $hkl$  in germanium are replaced in equation 3.13, some reflections are found to be forbidden (i.e.  $F = 0$ ): when  $h$ ,  $k$  and  $l$  are not all even or all odd; and when  $h$ ,  $k$  and  $l$  are all even and not divisible by four. Otherwise, when  $h$ ,  $k$  and  $l$  are all odd then  $F^2 = 32f$  and when  $h$ ,  $k$  and  $l$  are all even and divisible by four then  $F^2 = 64f$ .

Clearly, if the area producing the diffraction pattern contains more than one crystal then this will affect the diffraction pattern. For instance, crystals spatially oriented in different ways might give two sets of diffracted spots in the same diffraction pattern and these will appear misoriented relative to each other [202], [203].

Three typical types of microstructure that have been observed in this work are shown below. Figure 3.15(a) shows the diffraction pattern of a single crystal; the bright spots are characteristic of the sets of reciprocal lattice points that intersect the surface of the Ewald sphere. The diffraction pattern in Figure 3.15(b) is typical of a polycrystalline material; many spots are located at the same distance from the direct beam indicating that many crystallites with different spatial orientations are present. Lastly, in Figure 3.15(c) amorphous germanium has been used to generate the diffraction pattern. In this case, there are no bright spots, but only faint rings are observed. Stated in the previous chapter, even though the material is amorphous there is still some order within the material. A short-range order is ensured by the interatomic potential, meaning that there is an equilibrium distance between atoms. Indeed, as shown in figure 2.14 where germanium's RDF is presented, even in an amorphous material there are certain distances from an atom where there is higher probability of finding another atom. As there is a relatively high probability of finding neighbouring atoms at some distance  $d$ , diffraction will occur due to these neighbouring atoms and will cause rings in the diffraction pattern. It should be noted that in an amorphous material the distance  $d$  has a broader spread of

values than in a crystal (as illustrated by the RDF in figure 2.14). The amorphous rings are therefore relatively diffuse [202], [203].

It is worth noting that in this work, as ion irradiation was performed some of the material underwent amorphisation whilst other areas were perfect or defected crystal. In such cases, amorphous rings and bright spots might both appear in the diffraction pattern at a ratio which is representative of the level of disorder induced by the irradiation [202], [203].

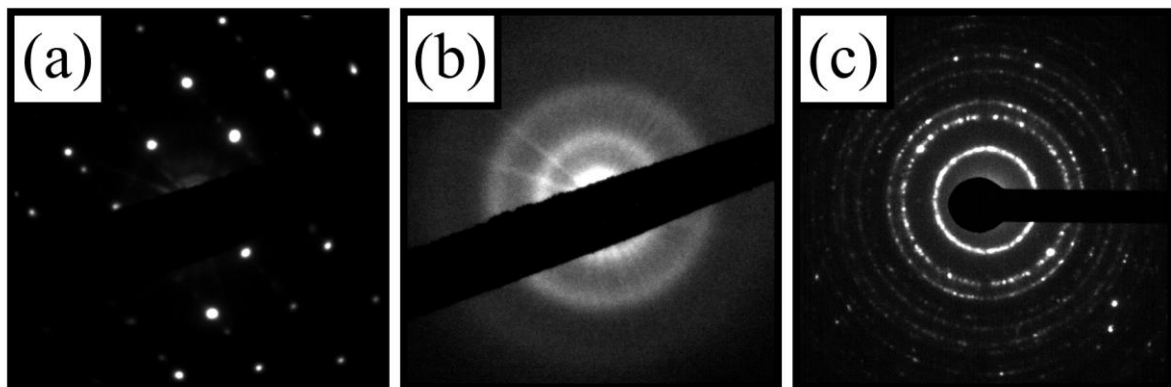


**Figure 3.15:** Examples of typical diffraction patterns: (a) single crystal diffraction pattern with the characteristic distinct bright spots; (b) fully amorphous specimen diffraction pattern with the characteristic faint rings and no bright spot apart from the 000 spot and (c) polycrystalline crystal diffraction pattern with the characteristic rings made from a multitude of bright spots.

#### 1.4.7. Kikuchi line

There is a useful type of diffraction called Kikuchi diffraction, which becomes intense if the sample is thick enough to cause sufficient amounts of incoherent elastic scattering (the incoherent electrons waves are not in phase) but still thin enough to be electron transparent. If those conditions are met, Kikuchi lines can be observed in the diffraction pattern [202], [203].

As shown in figure 3.16, Kikuchi lines are the result of scattering occurring in all directions (but mainly forwards). Thus, some of the scattered beams will be in the Bragg condition. However, unlike in a diffraction pattern, electrons which are in a Bragg condition come as stated above, from all directions. There is consequently a range of vectors  $k_i$  and likewise a range of vectors  $k_d$  satisfying the Bragg condition. As geometrically described via figure 3.16, this results in cones of diffracted electrons called Kossel cones. In projection on the viewing system, these cones will appear as parabolas, which are often approximated as straight lines due to the relatively long camera length of the TEM. As shown in figure 3.16, Kikuchi lines appear in pairs separated by an angle of  $2\theta_B$  with one line appearing brighter as it results from the scattering of the beams which were closer to the optical axis. Kikuchi lines are useful indicators of the orientation of the crystal because if the crystal moves then the Kikuchi lines will move with it which is not the case for DPs [202], [203].

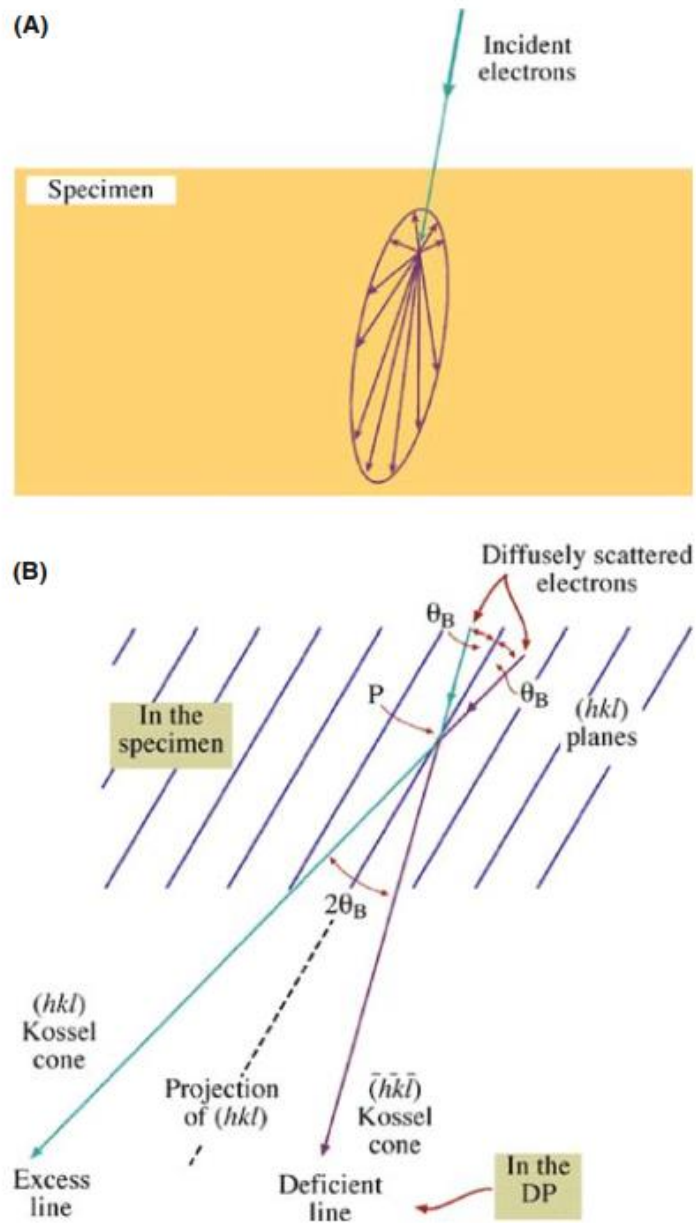


**Figure 3.16:** Illustration of the formation of Kikuchi lines during interaction of the electron beam with a sample: (a) the intensities of the two lines which each represents one Kossel cone differ as they emerge close to the incident electron beam; and (b) are approximated as lines on the camera or the phosphorescent screen. From [203].

In this work, basic use of Kikuchi lines was made as they were used whenever the sample needed to be tilted to conditions where the intensities of the spots in the diffraction pattern were symmetric (i.e. down-zone axis conditions). As will be described below, this type of crystal orientation was used when investigating amorphisation mechanisms and when performing high-resolution microscopy using the phase contrast mechanism.

#### 1.4.8. Bright Field and Dark Field

As the electron beam encounters the sample, different kinds of interactions can arise as summarised in figure 3.17. Three main pathways shown are: (a) electrons go through the sample without being subject to scattering; (b) electrons interact and transfer energy, they are inelastically scattered (these electrons might for instance generate X-rays, or secondary electrons) or absorbed; and (c) electrons which are scattered without losing energy might be elastically scattered forwards (forming diffraction patterns) or backscattered.

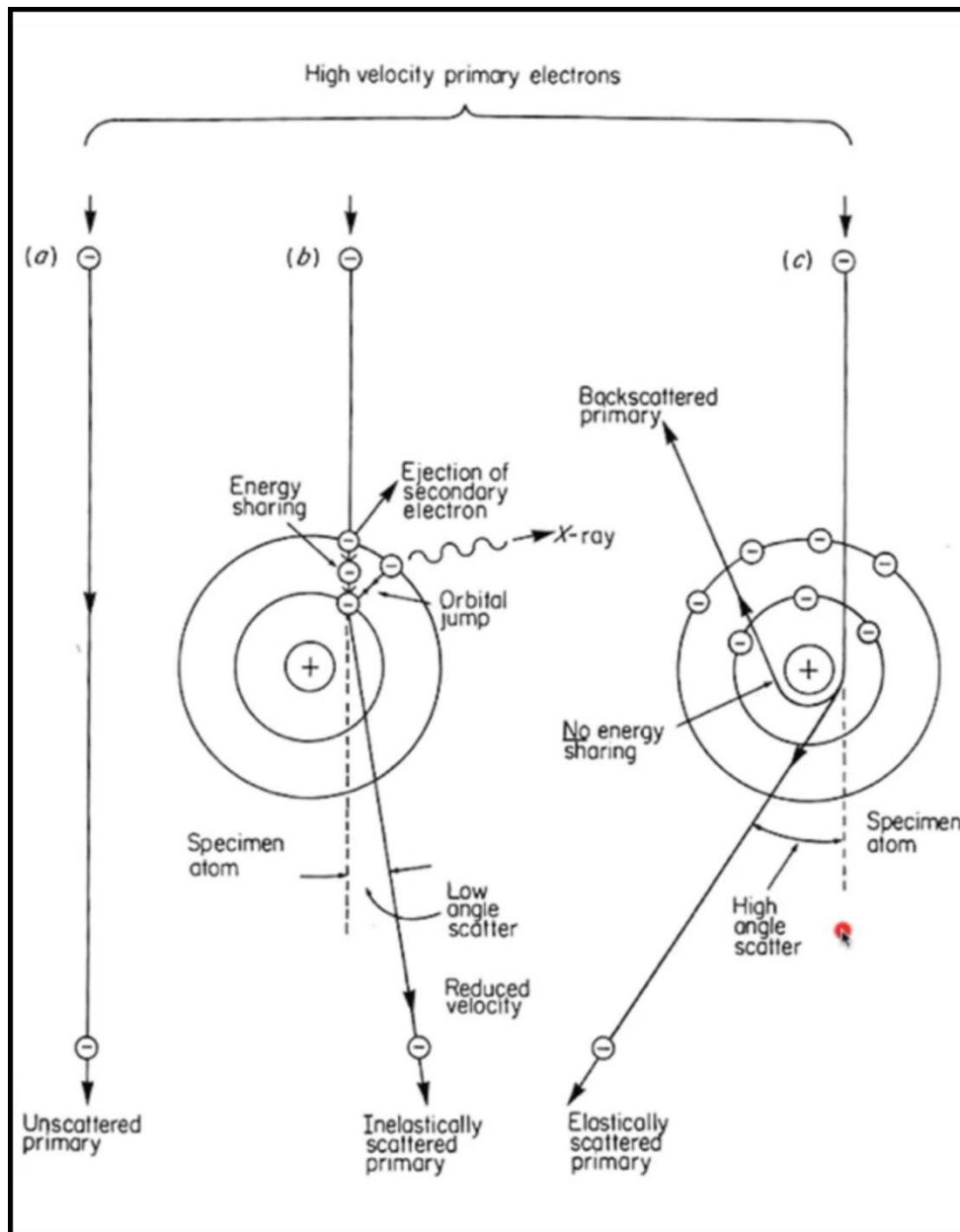


**Figure 3.17:** Summary of the principal possibilities for the electrons which are accelerated towards a specimen: (a) unscattered; (b) inelastically scattered; or (c) elastically scattered. From [215].

Thus, electrons can be blocked by the specimen, transmitted with little or no deviation from the optical axis and interact strongly at certain angles (i.e. diffraction). One particularly important point is that, diffraction effects are dependent on the microstructure of the specimen.

Indeed, as stated above, diffraction may induce scattering of intense electron beams at certain angles (i.e. the diffracted beams). Those diffracted beams can be observed in the back focal plane of the objective lens where they form the diffraction pattern. To understand BF and DF-TEM images, it must be recalled that in the diffraction pattern, the intensities of the spots are related to how strongly the electron beam diffracts and is transmitted in a given direction. Diffraction effects thus contain information about the directions taken by the diffracted beams (and consequently about the crystal structure). As explained earlier and shown in figure 3.11, it is possible to observe an image formed by only a selected diffracted electron beam by inserting an objective aperture into the back focal plane so that only the selected beam will be able to propagate down the TEM column and contribute to the image. This is shown in figure 3.18(a), assuming the direct beam has not been tilted off the optical axis. The aperture can be positioned so that it allows the passage of only the direct beam, where most of the specimen is not strongly diffracting the electrons. Positioning the objective aperture like this allows the formation of an image which is mostly bright and for this reason, such an image is called a bright-field image [202], [203].

Similarly, as shown in figure 3.18(b) the objective aperture may be positioned so that a single diffracted beam is allowed through to the image plane and therefore used to form the image. As only the part of the incident beam scattered by the sample in a particular direction is used to form the image, the image is typically dark except for the regions which have interacted with the electron beam and scattered it in the selected direction. For these reasons, the image is bright where such diffraction events have taken place and dark everywhere else. These type of images are therefore called dark-field images. However, in most cases displacing the aperture off the optical axis to create a dark-field image should be avoided as off-axis electrons tend to suffer from greater aberrations and astigmatism. Consequently, a better methodology is to

perform centred dark-field imaging by tilting the incident beam to bring the desired diffracted beam onto the optical axis is as shown in figure 3.18(c) [202], [203].

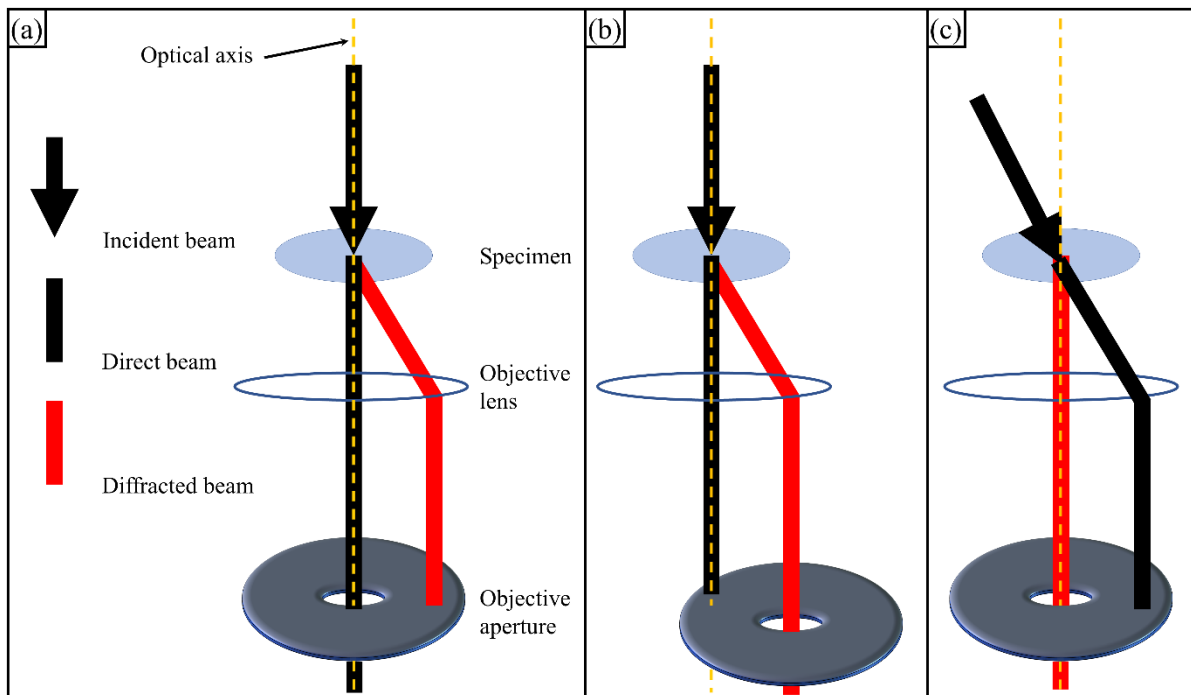


**Figure 3.18:** Schematic illustrating various imaging modes using the objective aperture: (a) BF imaging by selecting the direct beam on the optical axis; (b) a DF imaging mode by moving the objective aperture to select an off-axis diffracted beam; and (c) centred DF imaging where the incident electron beam is tilted in such a way that the diffracted beam becomes aligned with the optical axis.

#### 1.4.9. Amplitude and mass-thickness contrast

The contrast,  $C$ , between region 1 and region 2 is defined as the difference in intensity,  $I$ , between these two regions divided by the lower intensity [203]:

$$C = \frac{(I_2 - I_1)}{I_1} \quad (3.4)$$

For a human eye to notice the difference of intensity between two adjacent regions, the image of those two regions must form two distinct points and thus satisfy the so-called Rayleigh criterion (which defines the minimum resolvable distance two points) and, the contrast must be approximately above 5% [203]. In a TEM, the intensity depends on the number of electrons which contribute to the image in different regions of the image. Therefore, the contrast between two areas of a specimen is related to a difference between the way in which the electrons interact with these.

To comprehend amplitude contrast, it might be more convenient to mainly consider the particle-like nature of electrons instead of their wave-like nature. Secondly, it is important to note the fact that the scattering events increase with the thickness of the sample, the atomic number of the sample and its density. Amplitude contrast can be seen as a variation of the amount of the electron beam that is able to get through or be given to a given direction to form the image. For instance, in BF image mode two grains made of distinct chemical elements can be differentiated due to their respective cross section, the higher the atomic number is of an element the more it may scatter the electron beam. In this view, if a specimen contains a volume with atoms of a higher atomic number and/or atomic density, then the surrounding matrix will appear brighter as the electrons will have relatively higher probability of passing through from that region. In BF mode, scattering events can prevent electrons from contributing to the image formed via the direct beam. An example of amplitude contrast can be seen in figure 3.19, where the difference of thickness of a monoatomic specimen is clearly apparent. It is worth noting that amplitude contrast is not only relevant in BF image mode as diffraction contrast can also be used to form a DF image in which the contrast will be inverted [202], [203].

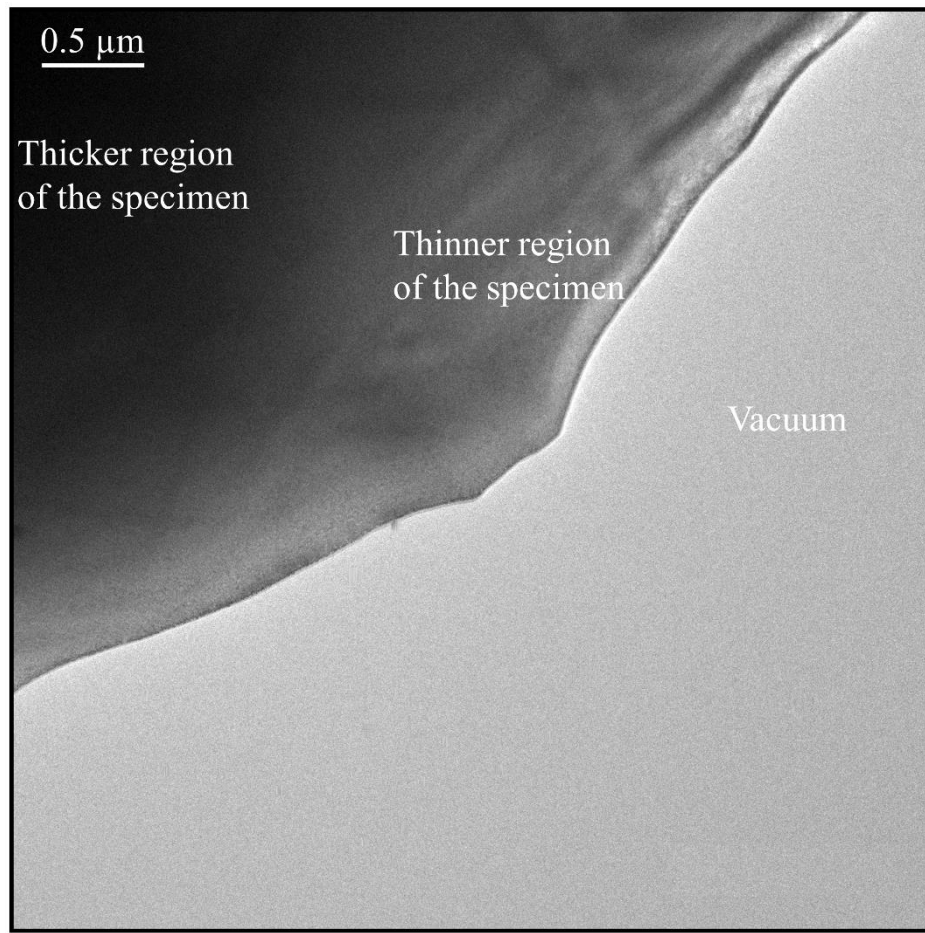


**Figure 3.19:** BF-TEM image of a wedge-shaped single-crystal germanium specimen, the darker regions corresponds to the thicker parts.

#### 1.4.10. Phase contrast

Whilst most of the work regarding radiation-induced damage using in situ TEM relies on characterisation of defects via diffraction contrast, another main type of contrast is phase contrast. Explaining phase contrast in detail would be outside the scope of this work; however, a basic explanation of phase contrast can be given by considering the incoming electrons as waves with a wave function [202], [203].

As the electron has a wave function, it will have a certain amplitude and an oscillating phase before interacting with the sample. Because only elastic scattering is considered in this type of

contrast, the amplitude will remain the same after scattering but the phase of the electron wave will be strongly affected by all the scattering events in the sample. These scattering events will induce phase shifts which can result in a change of contrast. The change of contrast being characteristic of the scattering events, the image will provide information regarding the scattering events (for instances atoms) in high resolution TEM (HRTEM) micrographs [202], [203].

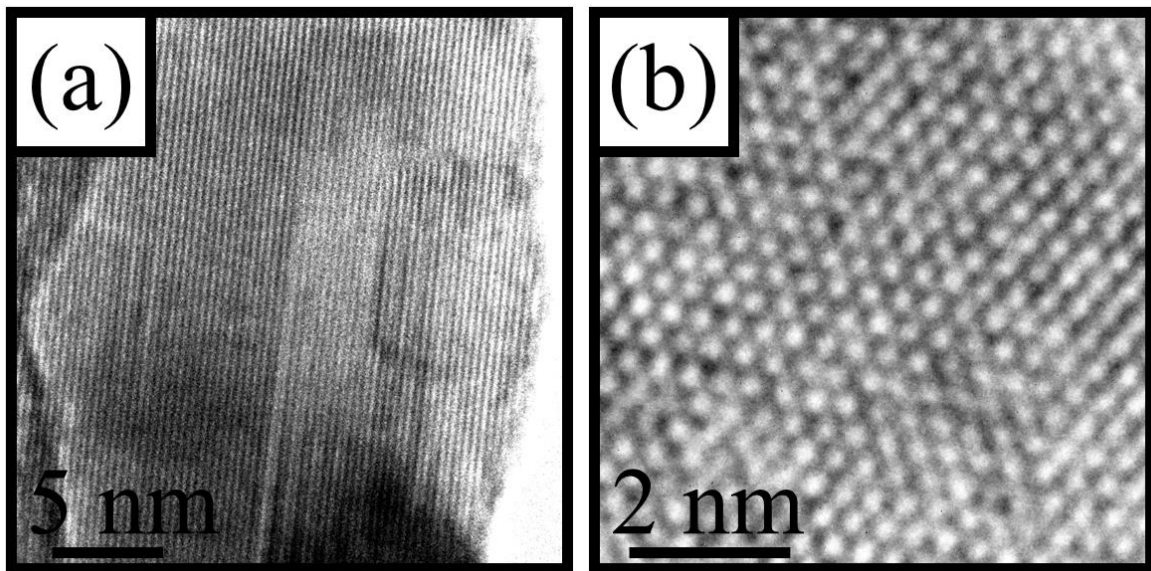


**Figure 3.20:** (a) HRTEM micrograph of a germanium nanowire obtained at the MIAMI-2 facility on a Hitachi H-9500. Measurements have confirmed that the representation of (111) lattices are shown in the image. (b) HRTEM micrograph captured at the MIAMI-1 facility on a JEOL JEM-3010 showing of a gold nanoparticle.

As shown in the examples of high-resolution images obtained in the MIAMI facilities during this work, in figure 3.20 using HRTEM lattice fringes or even columns of atoms can be resolved.

## 1.5. EELS and EFTEM

### 1.5.1. Basic idea

The interaction between electrons and the specimen can lead to emissions which are specific to the bombarded material. Such emissions include X-rays and Auger electrons. In the same way as analysing these emitted signals to probe the material characteristics (i.e. via techniques such as X-ray photoelectron spectroscopy XPS or Energy-dispersive X-ray spectroscopy XEDS), the analysis of the energy lost during the interaction can also provide valuable information. In this work, this aspect of the interaction between electrons and specimens has been used when the thickness of the sample needed to be characterised, thus the basic idea behind such analysis will be summarised below [202], [203], [216].

When inelastic scattering occurs, the energy loss can give useful information if its quantity is known. Typically, this is done first by using apparatus such as a magnetic prism which both acts as spectrometer and a lens. The magnetic field will deflect the electrons. The prism will converge the electrons onto the prism's image plane and their position will depend on the energy they have lost as the prism will deflect electrons that have lost more energy at a higher angle. In an electron energy loss spectroscopy (EELS) system, a spectrum will thus be acquired showing the electron intensity against energy loss. Furthermore, via energy-filtered TEM (EFTEM), it is also possible to form an image which includes only those electrons which have lost a specific amount of energy or conversely to form an image which does not include electrons having lost specific energies.

### 1.5.2. Typical EELS spectra

As shown in figure 3.21, the most intense signal in an EELS spectrum is generally the zero loss peak consists of electrons transmitted without noticeable energy loss [202], [203], [216].

Electrons can also lose energy exciting phonons. Phonons are collective vibrations of the atoms. They correspond to a temperature rise in the specimen. However, because they have a wide range of energy losses their signal is spread on the EELS spectra and contribute to the background noise. Lastly, as they can induce very small energy losses ( $< 0.1$  eV), the zero loss peak in a conventional TEM contains some of the electrons which have lost energy to phonons [202], [203], [216], [217].

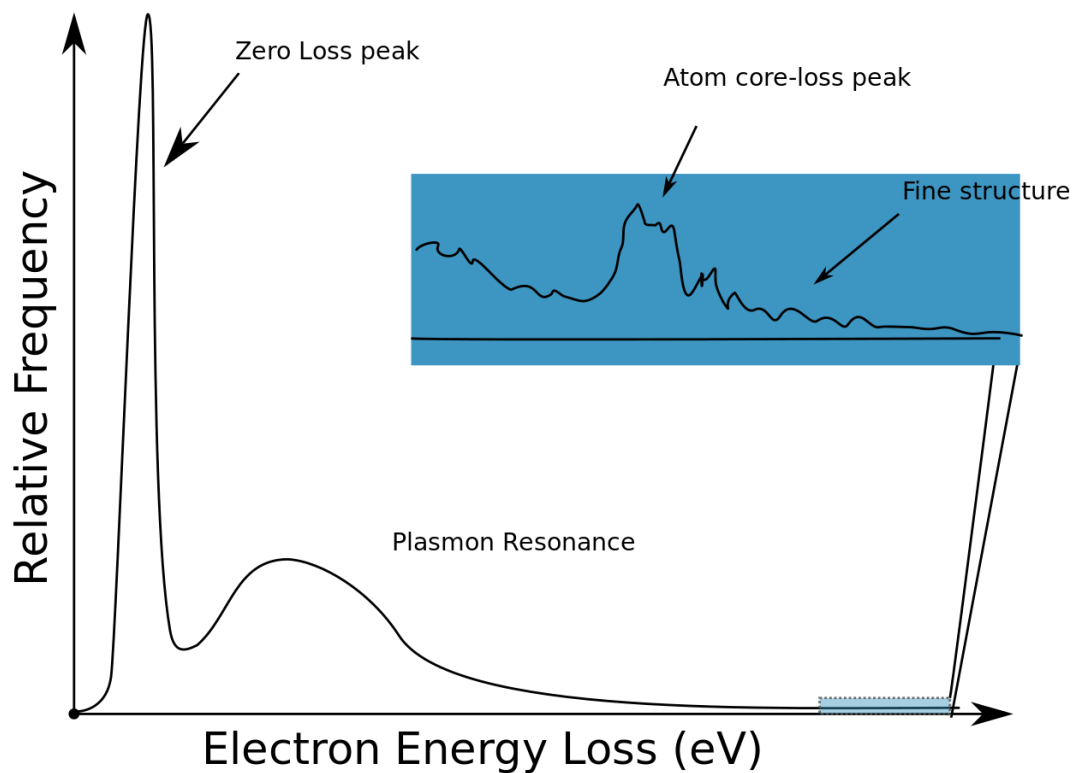


**Figure 3.21:** Typical EELS spectrum with the typical most-intense signals in the spectrum, (the zero loss peak and the plasmon resonance) as well as the less-intense signals which can be found at higher energy losses. From [218].

As shown in figure 3.21, at higher energy losses in the spectrum are plasmons, which are a collective excitation of the “free electrons” in the valence or conduction band. Because they are damped quickly, these oscillations are quite localised ( $\approx$  tens of nm). The energy losses due to plasmons are confined below 50 eV and can be used for band gap characterisation or to

determine the thickness of a sample. The former requires EELS to be performed at low temperature and to have a high enough resolution to see the minimum energy loss due to plasmons (that is the energy lost to electrons at the bottom of the band gap). In germanium, the band gap is around only 0.6 eV and the first plasmon peak will be hidden by the zero loss peak since in conventional TEMs with thermionic emission electron guns the zero loss peak typically has a width of 1 eV. Therefore, in this work, as the composition of the materials was known, electron energy loss has been used only to determine the thickness of the region of the sample which is irradiated [202], [203], [216], [217], [219]. The thickness was determined using the following expression 3.14:

$$\frac{t}{\lambda_p} = \ln \left( \frac{I_t}{I_0} \right) \quad (3.14)$$

With  $\lambda_p$ ,  $F$  and  $E_m$  determined via equations 3.15, 3.16 and 3.17, respectively. In these expressions,  $\lambda_p$  is the mean free path for inelastic scattering (mainly from plasmons),  $t$  is the thickness of the specimen,  $I_t$  is the integrated intensity of the spectrum,  $I_0$  is the integrated intensity of the zero loss peak,  $E_0$  is the incident energy,  $E_m$  is the mean energy loss,  $F$  is a factor which is used to take into account relativistic effects and  $Z$  is the mean atomic number of the specimen [203].

$$\lambda_p \approx \frac{106F \frac{E_0}{E_m}}{\ln \left( 2\beta \frac{E_0}{E_m} \right)} \quad (3.15)$$

$$F = \frac{1 + \frac{E_0}{1022}}{\left( 1 + \frac{E_0}{511} \right)^2} \quad (3.16)$$

$$E_m \approx 7.6Z^{0.36} \quad (3.17)$$

It is worth noting that while most of the experiments have been performed at a reduced acceleration voltage of 200 kV for reasons which will be addressed in chapter 6, the thickness of the samples was calculated at the normal operating voltage where the EELS system was accurately calibrated which is 300 kV .

As shown in figure 3.21, the energy losses described above are found in the low-loss region near the zero-loss peak. Nevertheless, in the higher-loss region there can be found signals which are specific to the energy given to electrons of the inner-shell of the atoms and thus are used to identify the atoms involved in the interactions. Typically, an atom-core-loss results in a relatively easily identifiable edge in the spectrum (as shown in figure 3.21). However, in their vicinity they are fine structures signals which are more complex to analyse but may provide details about the composition of the specimen such as the energy-loss near-edge structure (ELNES) which is very sensitive to electronic structure and the extended energy-loss fine structure (EXELFS) which may provide information about the chemical arrangement of the specimen [202], [203], [216], [217].

## 2. Sample Preparation

### 2.1. Nanowires

High purity (99.999%), single-crystal germanium nanowires were purchased commercially (product reference: GNWsI15) from Nanowire Tech Ltd. The nanowires were grown on a silicon wafer by a chemical vapour deposition VLS process. The wafer was put into an ethanol solution and the nanowires were harvested using an ultrasonic bath. A few minutes were sufficient to dislodge the nanowires from the wafer.

The sample preparation aimed at producing a sufficient density of nanowires in the ethanol solution and dispersion on a TEM grid so as to permit to easy location of nanowires in the

TEM. However, as experiments regarding bending of nanowires were to be performed, it was necessary to limit the density of the nanowires in solution as entangled nanowires might be less inclined to bend during IIB experiments. Typically, for about 1 cm<sup>2</sup> of wafer, 2 ml of solution was produced to achieve this.

A drop of solution was transposed onto a molybdenum TEM grid with no support film, which was then left to air dry. As a result, some nanowires were left hanging freely from the mesh of the TEM grid. In figure 3.22, a TEM micrograph shows a typical distribution of nanowires at the edge of a grid. The nanowire lengths ranged from 200 to 1500 nm with diameters ranging from 15 to 60 nm. Molybdenum grids with no film were chosen instead of the typical copper grids with a carbon support film as often used in TEM nanoparticle experiments because the carbon film might interfere with the bending of the nanowires, be sputtered away or curl during irradiation. Furthermore, it has been observed during experiments using copper grids that the copper can diffuse into the nanostructures at elevated temperature and during irradiation.

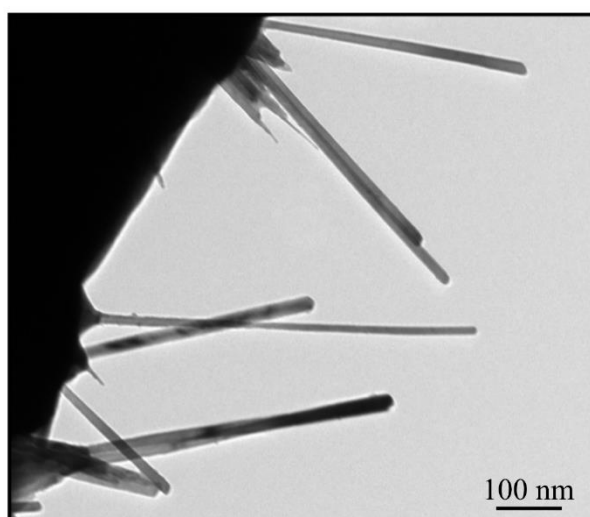


**Figure 3.22:** BF-TEM image of germanium nanowires. Some nanowires are potentially entangled together whilst others are isolated enough to bend without interference from neighbouring nanowires.

## 2.2. Bulk Germanium

High purity (5n), (111) single crystalline germanium was purchased from Goodfellow (product reference: GE003051) in the form of discs of diameter 2 cm and a thickness of 0.5 mm. Using wax which can be dissolved in acetone, each disc was attached to a metallic support in order to be cut into small discs measuring a diameter of 3 mm (a diameter at which they can be placed in a TEM sample holder) via a TEM specimen disc grinder. To reduce the thickness of the small discs, silicon carbide abrasive grinding paper (grit P800) was used to mechanically polish each side of the disc until it reached a thickness of approximately 100  $\mu\text{m}$ . The thickness of the sample was further reduced at the centre of the sample via a dimpler. The dimpler allowed mechanical thinning and polishing in the centre of the disc. It was operated using diamond paste (grade: 2  $\mu\text{m}$ ) to polish a disk-shaped region in the centre of the specimen, which after the process was about 20  $\mu\text{m}$  thick in the vicinity of the dimple.

The samples were then thinned to electron-transparency via a Gatan precision ion polishing system (PIPS). Using argon ions typically at energies from 0.5 to 6 keV, the PIPS was used as a way to sputter away material from the sample. Thus, as shown in figure 3.23 which summarises the sample preparation, the samples were thinned and polished by the dual ion beam at low angles (typically between  $1^\circ$  to  $6^\circ$ ). During the process, the ion beam located above the sample is thus used to polish the top of the sample and the ion beam located below the sample polishes the bottom of the sample. The operation is stopped once a hole is made at the centre of the sample (making the region in the vicinity of the hole is electron-transparent). It is worth noting that choosing a relatively high polishing angle (e.g.  $6^\circ$ ) enables to polish the sample at a faster rate but results to specimens with a steeper wedge.

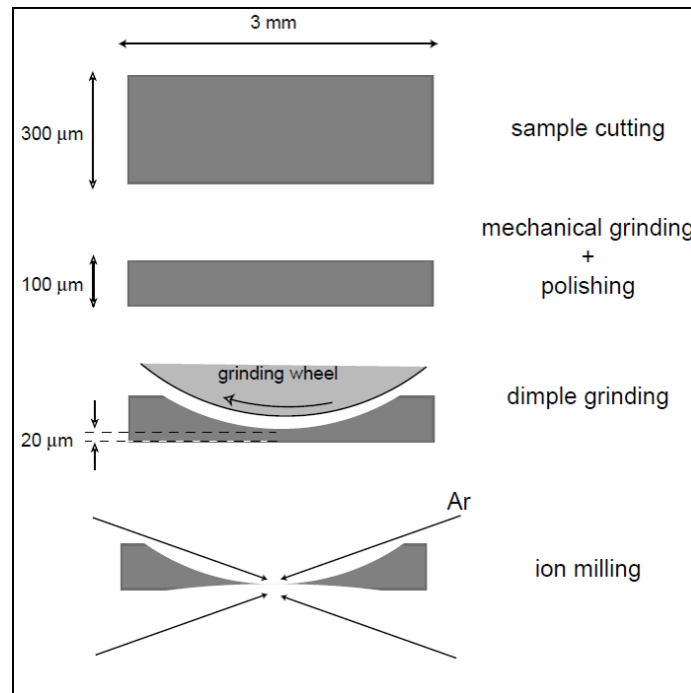


**Figure 3.23:** Schematic showing the main steps of the preparation of an electron transparent germanium foil. The electron transparent region is located in the vicinity of the hole made by ion milling. From [220].

### 3. SRIM calculation tools

SRIM was used to compute the interaction between ions and target materials. It considers the scattering cross section of the target material as well as its density and uses the binary collision approximation for its calculations. When a collision occurs, an evaluation of how much energy is lost by the ion during the discrete event is made. Afterwards, the trajectory of the ion is considered as a straight line until it collides with a subsequent atom. Furthermore, as the ion routinely transmits enough energy to PKAs for them to induce recoils in the materials, SRIM can be utilised to take into account the subsequent collisions of the PKAs using the same binary collision and conditions [75]. The calculations are performed for every collision at least until the total energy lost by the ion is such that it cannot displace other atoms of the target material or until it leaves the target material. Applying a Monte Carlo method, the calculations are

performed with a large number of ions in order to acquire enough statistics about the average characteristics of the interaction between the ions and the target material. When run in “detailed calculation for full damage cascade” mode SRIM is, according to the software designer able to better evaluate all collisional damage induced by an ion as it follows the collisions induced by each recoil. This mode was thus used to estimate the dpa. Indeed, using the SRIM output files: vacancy.txt and novac.txt, which, give the displacement per ion per depth ( $\kappa$ ), the dpa averaged in the region of thickness  $t$  can be readily calculated using equation 3.18 where  $a$  is the atomic density of the target material and  $\psi$  is the fluence [25]:

$$dpa = \frac{\kappa \times \psi}{a} \times t \quad (3.18)$$

To consider the damage rate and therefore determine how fast the damage will accumulate ( $dpa \cdot s^{-1}$ ), the fluence in equation 3.18 must be replaced by the flux. Other information is given by SRIM, such as an estimation of the sputtering yield, the nuclear energy loss as a function of depth, the average range of the ions or the percentage of electronic energy loss.

As stated in chapter 2, SRIM only computes the interaction of ions with flat targets. Therefore, to study the interaction of ions with nanowires an in-house developed MATLAB code has been used. This code is named IDRAGON for *Ion Damage and RAnge in the Geometry Of Nanowires* and allows the use of SRIM for the circular cross section of a nanowire by cutting it into slices which can be calculated individually. As shown in figure 3.24, the SRIM calculations are run on each slice that together represent a section of the nanowire. Typically, IDRAGON was used by dividing a nanowire into 100 slices for which SRIM performed a calculation using 5000 ions for each slice. For each slice was thus determine the damage and the implantation depth of the ions via the use of the SRIM output files, range.txt, which provides the range of the ions, or the files vacancy.txt and novac.txt, which as stated above

provide the displacements induce by the ions. Furthermore, the normalised damage depth,  $\Omega$ , which corresponds to the average damage depth normalised with respect to the diameter of the nanowire was calculated by IDRAGON using equation 3.19 where the number of atomic displacements given by SRIM is  $a_{m,n}$  and has been calculated in slice  $n$  at depth  $x_m$  and where  $\emptyset$  is the nanowire diameter [80]. Please note that the straggle, hence the profiles generated via IDRAGON may not be truly accurate close to the nanowires' edges (i.e. slices one and ten in figure 3.24). A qualitative explanation of this discrepancy lies in the fact that the IDRAGON code does not take into account that collision cascades might escape from a slice in the lateral direction. However, as it will be explained in the example below, for most slices the influence of the lateral projection of the collision cascades does not affect the profile generated by the code. For instance, a collision cascade initiated in slice six of figure 3.24 might also induce some displacements in the adjacent slices (i.e. slices seven and five). However, the damage induced by the volume of the cascade leaving slice six will be compensated by this of the cascades leaving slices seven and five and entering slice six. Thus, meaning that as the collision cascades initiated in the adjacent slices will also affect slice six, the overall effect of collision cascades leaving slice six will be counteracted by those entering it.

$$\Omega = \frac{\sum_{n=1}^{100} \left( \frac{\sum_{m=1}^{100} (a_{m,n} x_{m,n})}{\sum_{m=1}^{100} a_{m,n}} \right)}{100 \times \emptyset} \quad (3.19)$$

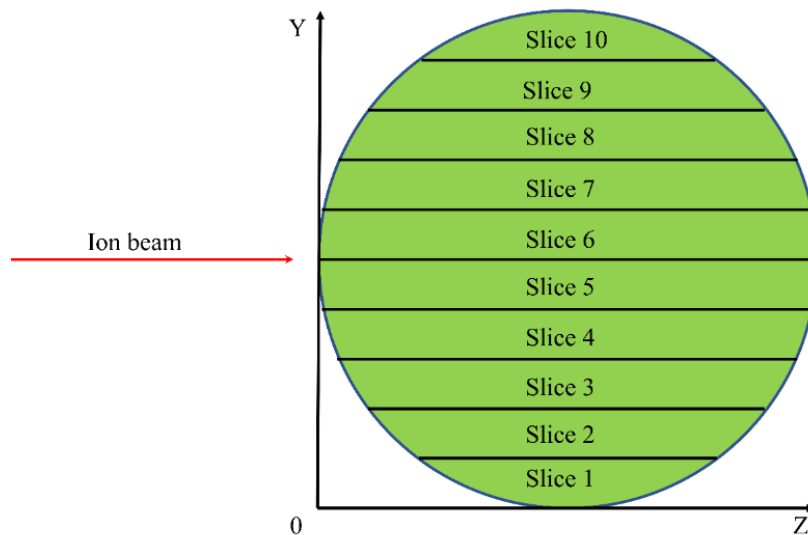


**Figure 3.24:** The cross-section of a nanowire is divided into slices that will be treated individually in SRIM as flat targets. Typically, the nanowires were divided into 100 slices that were recomposed in the IDRAGON MATLAB code to model the nanowire cross-section. For clarity, the nanowire is divided in only 10 slices in the figure.

Furthermore, a variant of IDRAGON has also been used to model the collision cascades in 3D via the output file: Collision.txt, which, provides the position of each recoil and PKA in the collision cascade. Like IDRAGON, the variant uses SRIM the output files within the program MATLAB. As this file can provide the position of recoils and PKAs, the modified version of IDRAGON was used to reconstruct a 3D model of the collision cascade. An example of a zirconium sample irradiated with 5 xenon ions at an energy of 300 keV at normal incidence is shown in figure 3.25. In the figure, the PKAs generated along the tracks of the ions can be clearly observed (in red) as well as the numerous recoils (in blue). Furthermore, using this modified version of IDRAGON, the average position and density of the recoils was determined. To do so, SRIM was run with 1 ion and after reconstruction of the collision cascade, the MATLAB code was used to count in the 3D plot the number of recoils within cylinders of

radius  $r_x$  whose axis is centred with the ion beam direction as inputted in SRIM. The density of recoils was then determined within each of the cylinders of radius  $r_x$ , for a range of cylinders whose radius  $r_x$  ranged between 0.1 nm to a radius large enough to include all recoils and using the increment in  $r_x$  0.05 nm. It should be noted that this code is designed for flat target materials unlike IDRAGON which is used for nanowires.

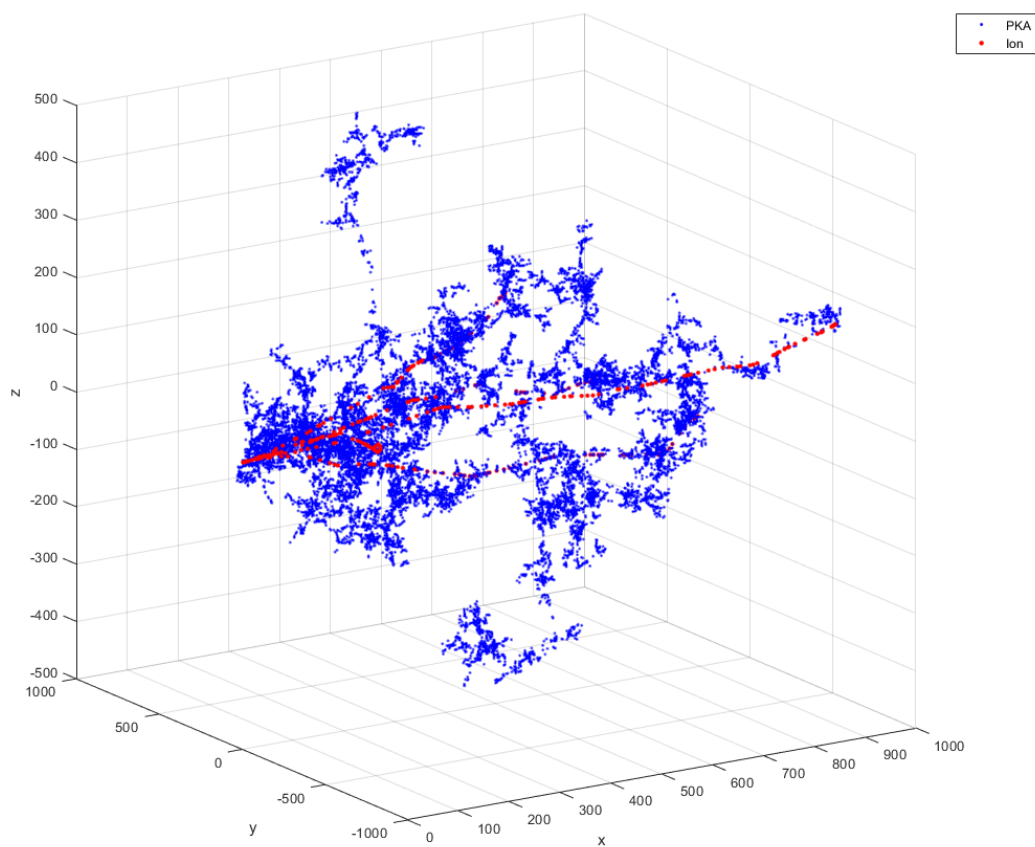


**Figure 3.25:** The modified DRAGON 3d plot showing the recoils (in blue) and the PKAs (in red) after a zirconium flat target is irradiated with 5 xenon ions accelerated to 300 keV at normal incidence.

## 4. MIAMI-1 and -2

### 4.1. Overview

The study of radiation damage often requires the emulation of radiation that occurs in extreme environments such as a nuclear plant, in space or during ion beam doping of semiconductors [31], [221]–[223]. Subsequently to the irradiations performed on the specimens, they are analysed via techniques such TEM or X-ray microscopy [224], [225]. However, by exploring the effect of radiation damage in this way (i.e. *ex situ*), information regarding the evolution of the material during irradiation is lost [137], [223], [226]. Irradiation performed *in situ* in a TEM allows access to dynamic effects such as bubble formation and growth or to alternate bending direction of nanowires during irradiation (as will be demonstrated later in this thesis) [80], [173], [208], [221], [223]. For those reasons, *in situ* ion irradiations have attracted a lot of attention; indeed, since the first system to perform ion irradiation *in situ* a TEM was designed in 1968 more than 30 other facilities have been built of which 13 were operational in 2014 [208], [227].

In this work, the irradiations were performed at the MIAMI facilities, which is home to two of *in situ* systems, namely MIAMI-1 and MIAMI-2. As will be described in more detail below, in addition to allowing the use of TEM and associated sample holders (e.g. temperature control), it is possible in the facility to investigate the effect of radiation damage of most ions (from hydrogen to lead) accelerated to various energies from low to medium (2 keV- to 350 keV for singly charged ions) [208].

### 4.2. Creation of ions

In MIAMI-1 and MIAMI-2, the ions are generated via an electric current which is run through a metallic filament thus heating it. Electrons are then emitted by the filament via thermionic

emission once the energy given to the electrons is high enough for them to exceed the work function described by equation 3.1. As a gas is flowing in the source, the emitted electrons will then react and ionize the gas. During this work, only inert gases were used as a means to produce singly-charged ions. However, ions with multiple charges can also be run in both MIAMI-1 and MIAMI-2 if needed [208].

#### 4.3. Mass selection

As other ions might be generated during the process described above, a bending magnet is operated as a way to mass select the ion species. Depending on the mass of the incoming ions, these will be more or less bent by the magnetic field. To go through the bending magnet section, ions must be bent to the right extent by the magnetic field, indeed, those which are too heavy will not be bent enough to go through the magnet section whilst those too light will be bent too much to go through it, as dictated by Lorentz law. Therefore, using a bending magnet at a given value will ensure that only one ion species is selected. Furthermore, as the force acting upon the ion is also sensitive to its charge, the bending magnet can equally be used to select its charge state [208].

#### 4.4. Accelerations of ions

To avoid having to apply an excessive strength field in the bending magnet, most of the acceleration is typically performed only after mass selection. The ions enter the acceleration column with an energy of a few keV and are accelerated by a set of elements spanning the voltage gradient from a high voltage to the ground state [208].

#### 4.5. Targeting with ions

For the ions to target the specimen, they must be guided and focused. In MIAMI, this is done by several sets of deflectors and Einzel lenses, which modify the trajectory of the ions using

electric and magnetic fields. The deflectors are placed along the track of the ions and enable them to enter the microscope at the desired angle whilst the purpose of the Einzel lenses is mainly to focus the ion beam [208].

#### 4.6. Monitoring the ion beam

To monitor the ion beam, (its shape, its position and flux) a few devices are positioned along its track.

The ion beam goes through rotating wires, which serve to monitor the shape of the beam by measuring the current of secondary electrons which are emitted by the wires when they are being hit by ions; skimming diaphragms are used to both skim the beam and measure the ion beam current; and Faraday cups which can be inserted or retracted are also used to measure the ion beam current [208].

As shown in the schematics of MIAMI-1 and MIAMI-2, all these components are placed within the ion beam system along the ion track so that measurements can be achieved at different positions from the source to the sample. However, to exactly know the beam current at the sample position, an in-house designed TEM-rod has been built allowing a Faraday cup to be placed exactly at the sample position before and after each experiment. It thus, allows the measurement of the flux of ions on the specimen. This current metering rod is also equipped with a negatively charged plate the purpose of which is secondary electrons suppression [208].

#### 4.7. MIAMI-1

Used in this thesis to investigate the IIB effects, MIAMI-1 is able to deliver low energy ions and therefore implant light ions such as helium into TEM specimens. Whilst undergoing a reconfiguration at the time of writing, a schematic and picture of the system at the time when the work reported here was carried out are shown in figure 3.26. Some specifications of both

the ion beam system and the microscope attached to it (a JEOL JEM-2000FX) are given in table 3.2.

It is worth noting that the angle between the incident ion beam and the electron beam is  $30^\circ$  and the angle between the projection of ion beam onto the sample plane and the x-axis (the axis running along the TEM rod) and the y-axis is  $45^\circ$ .

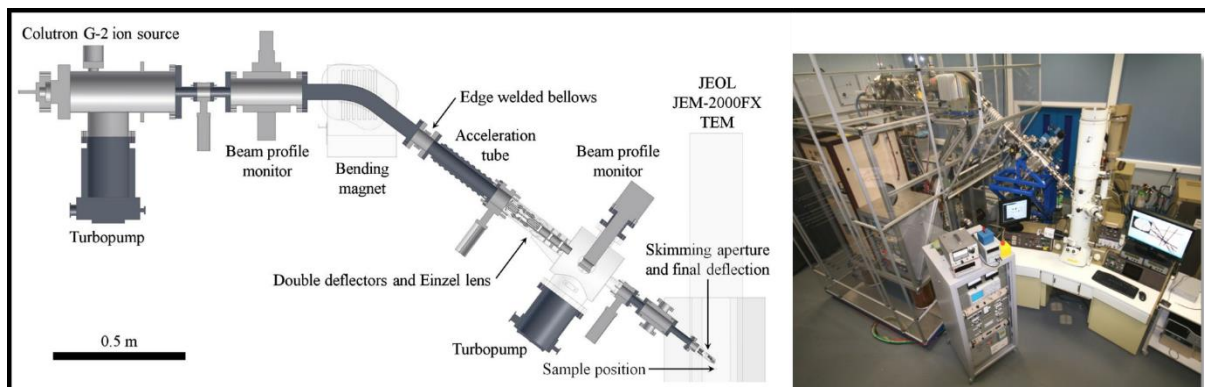


**Figure 3.26** Picture of MIAMI-1 and schematic displaying the layout of the system. From [208].

Specifications	
TEM	JEOL JEM-2000FX
Electron acceleration voltage	80 to 200 kV
Ion acceleration voltage	1 to 100 kV
Ion species	Most ions from H to W
Angle between electron and ion beams	30°
Ion flux	Up to $1.5 \times 10^{14} \text{ cm}^{-2} \text{ s}^{-1}$ for 6 kV He (for example)
Temperature	100 to 380 K or RT to 1570 K
Image capture	Gatan ES500W and Gatan Orius SC200 (4 MP)

**Table 3.2:** The table shows the main characteristics of the MIAMI-1 system. It is worth noting that these characteristics were accurate at the time when the work presented in this thesis was undertaken and consequently may not reflect the newest upgrades made to MIAMI-1.

#### 4.8. MIAMI-2

The newer system, MIAMI-2, started to be operational in March 2017 and offers numerous advantages compared with MIAMI-1 such as the possibility to perform spectroscopy techniques such as EELS and EFTEM, to accelerate ions to higher energy and to use dual ion beam system. Some specifications of both the ion beam system and the microscope attached to it (a Hitachi H-9500 TEM) are given in table 3.3. A schematic and a picture of the system are shown in figure 3.27. In MIAMI-2 the ion beam forms an angle of about  $18.7^\circ$  with the electron beam and its projection onto the sample plane is parallel to the y-axis.

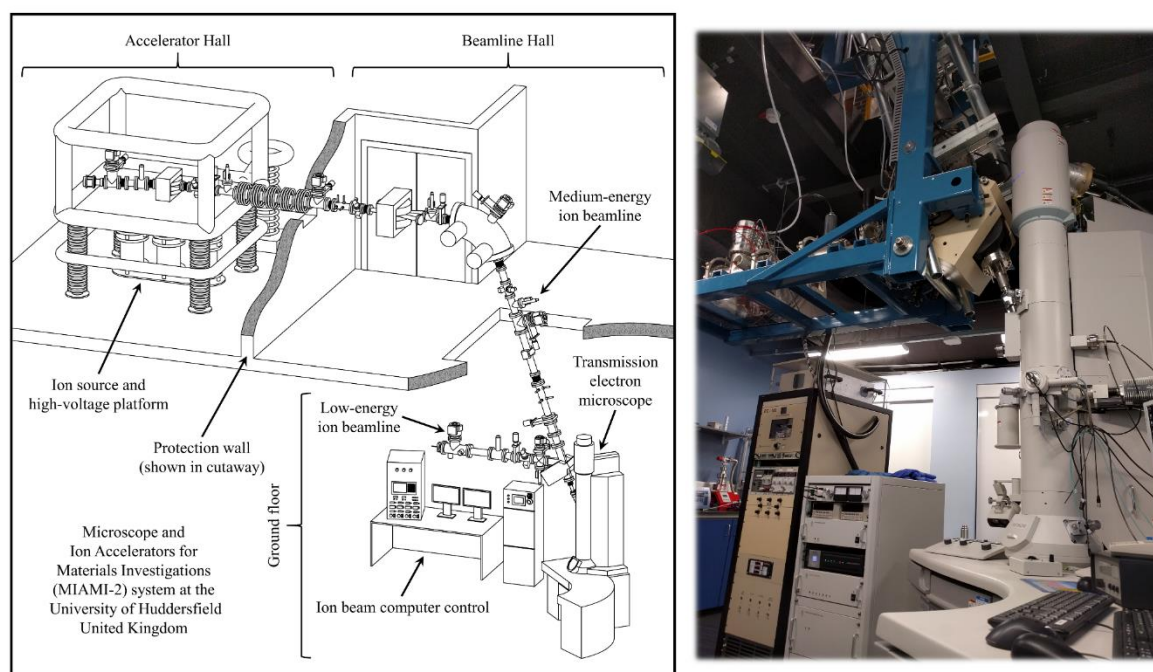


**Figure 3.27:** Picture of MIAMI-2 and schematic displaying the layout of the system. From [228].

<b>Specifications</b>	
TEM	Hitachi H-9500
Electron acceleration voltage	60 to 300 kV
Ion acceleration voltage	20–350 kV (NEC) and 1–20 kV (Colutron)
Ion species	Mass 1 –200 amu
Angle between electron and ion beams	18.7°
Environment	Temperature: 100 to 1570 K  Gas injection system
Image capture	Gatan OneView  25 fps (4K)  300 fps (512×512 pixels)
Analysis	EELS (Gatan Imaging Filter)  and Bruker EDS
Tomography	Tomography holder  and software

**Table 3.3:** The table shows the main characteristics of the MIAMI-2 system.

## 5. Angle between freely hanging nanowires and the ion beam

### 5.1. Reasons for the calculation

Because nanowires are seen in projection in the TEM, the correct interpretation of the image can be counter-intuitive and result in an erroneous judgement regarding the shape, the length or the position of a nanowire if not performed correctly. For this reason, a tilting procedure is needed to interpret TEM images of nanowires. For example, as seen in figure 3.28 a bent nanowire might seem straight when observed in a TEM. In this example, the curvature of the nanowire is normal to the image plane and tilting the nanowire using the goniometer permits its curvature to be revealed. It is worth noting that the curvature always appears less pronounced than it really is, unless the circular part of the nanowire lies parallel to the image plane.

Furthermore, as stated above, when nanowires are deposited onto a molybdenum grid with no carbon film they are attached to it only on one end and therefore hang free. Even if such a nanowire is straight, interpreting the image can still be problematic as it might be inclined if there is a slope which can be characterised by an inclination angle  $\hat{i}$ . This angle  $\hat{i}$  influences how the nanowire appears in the TEM image and the length of the nanowire is underestimated unless the nanowire is parallel to the image plane (i.e.  $\hat{i} = 0$ ). Most importantly within the context of this work, knowing  $\hat{i}$  is crucial as the angle between the ion beam and the nanowire depends on it and consequently impacts the ion beam induced damage in the target nanowire.

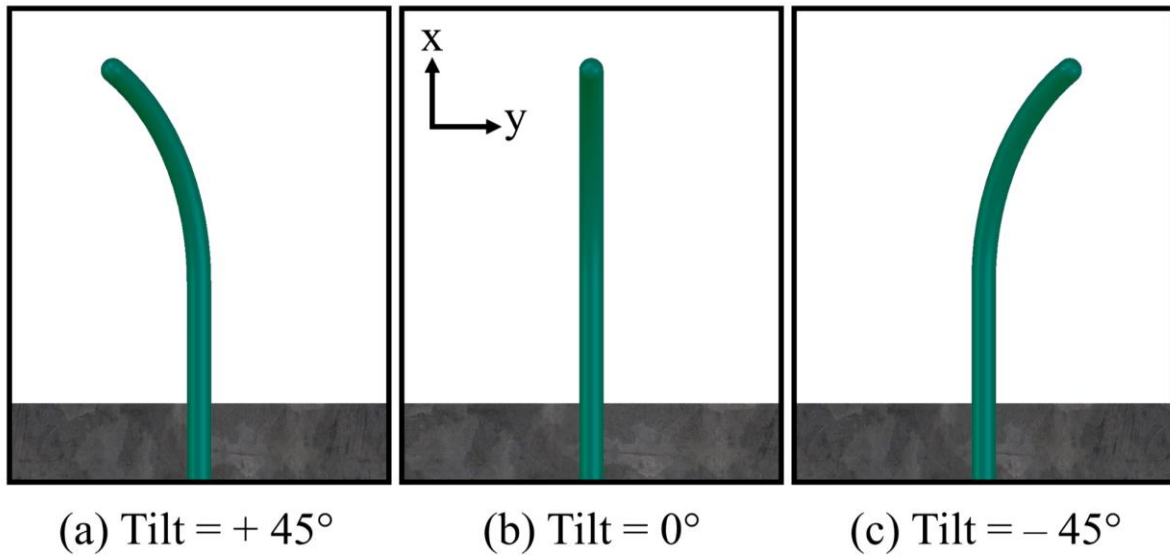


**Figure 3.28:** Example of how tilting can reveal the bent shape of a nanowire using the x-tilt of a TEM holder: (a) the nanowires appears bent towards the left when tilted at +45°; (b) straight when untilted; and (c) bent towards the right when tilted at -45°. At 0° the nanowire is actually bent upward as revealed by the tilting. It is worth noting that if the nanowire were bent downward it would appear bent towards the right when tilted at +45° and bent towards the left when tilted at -45°.

### 5.2. Calculation of $\hat{t}$

A nanowire of length  $l$  can be tilted by an angle  $\hat{t}$  with respect with the x-axis or the y-axis of the goniometer. As seen in figure 3.29, by doing so the angle of inclination  $\hat{i}$  might be modified to become  $\hat{i}'$  and the free end of the nanowire might also rotate. To simplify the calculation of  $\hat{t}$ , an imaginary vector (in orange in the figures) of length  $t$  attached to the free end of the nanowire and connected perpendicularly to the axis of tilt is introduced in figure 3.29(a).

The axis of tilt lies on a plane  $P$  which remains still and onto which the nanowire of length  $l$  is projected before and after tilting. As shown in figure 3.29 (b) and (c), before tilt, the nanowire is represented by  $[AB]$  and its projection by  $[A'B']$  (projection of which will be referred as

$Nw_1$ ). After the tilt, the nanowire is illustrated via  $[AC]$  and its projection via  $[A'C']$  will be referred as  $Nw_2$ . As stated above (in addition to the tilting angle  $\hat{t}$ ), in a TEM the only information that the observer has access to are the projections and thus the projection of the nanowire before tilting and after tilting.

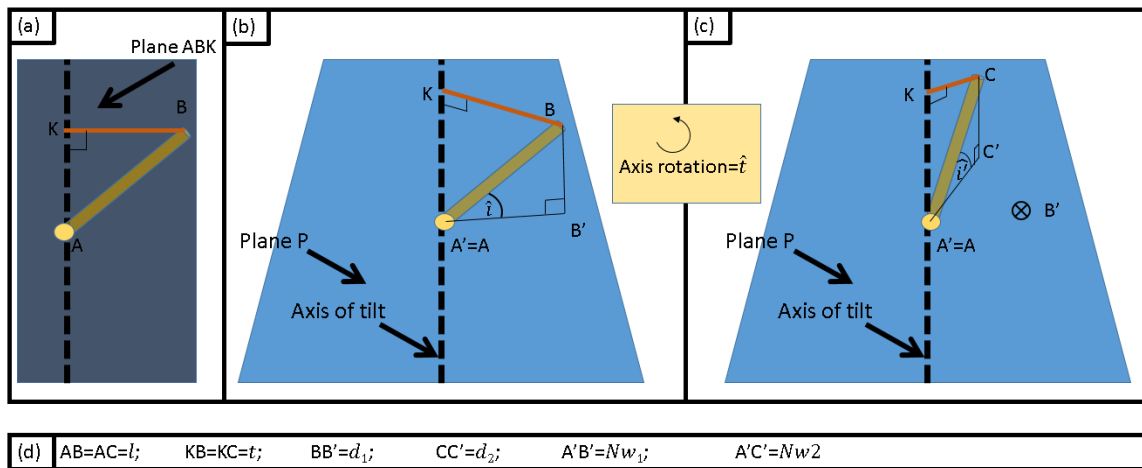


**Figure 3.29:** (a) Schematic showing the nanowire (brown) and the vector (orange) of length  $t$  (i.e.  $KB = KC = t$ ), (b) the nanowire and its projections are shown (b) before and (c) after tilting. The abbreviations used to name distances are shown in (d).

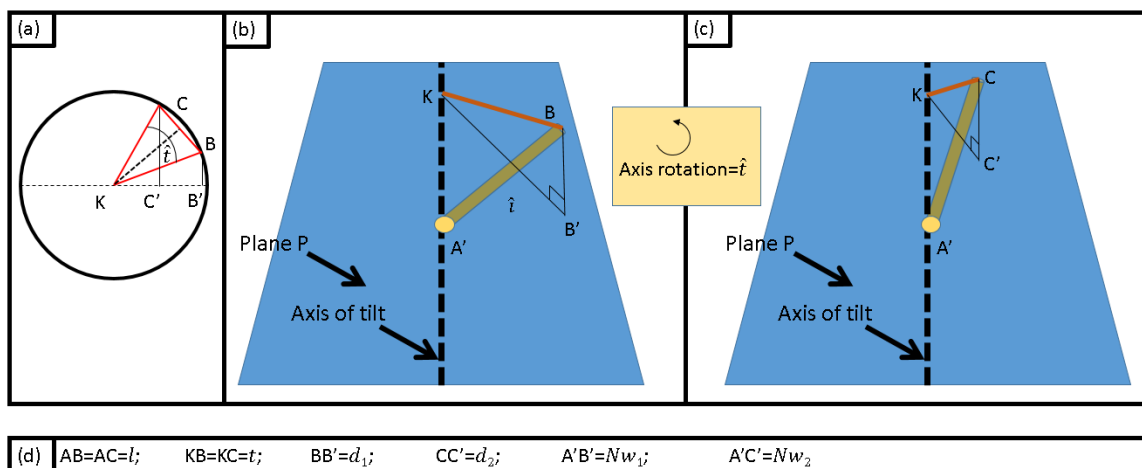


**Figure 3.30:** (a) Schematic showing the vector (orange) of length  $t$ , and its projection as seen along the axis of the tilt before and after tilting, (b) the nanowire (brown) and its projections are shown before and (c) after tilting. The abbreviations used to name distances are shown in (d).

As shown in figure 3.30, the vector of length  $t$  is normal to the axis, therefore both the projection of  $B$  and  $B'$  are aligned with  $K$ , meaning that  $KBC$  is a straight line and  $[B'C']$  can be defined by equation 3.20

$$KB' - KC' = B'C' = (t^2 - d_1^2)^{1/2} + (t^2 - d_2^2)^{1/2} \quad (3.20)$$

From figure 3.30(a), figure 3.31 and figure 3.29(b) and (c) it can be seen that:

- $t = \frac{BC}{2\sin(\frac{\hat{t}}{2})}$  (3.21)

- $BC = ((B'C')^2 + (d_2 - d_1)^2)^{1/2}$  (3.22)

- $d_1 = (l^2 - Nw_1^2)^{\frac{1}{2}}$  (3.23)

- $d_2 = (l^2 - Nw_2^2)^{\frac{1}{2}}$  (3.24)

If  $t$ ,  $d_1$  and  $d_2$  are replaced from equation 3.20, using equations 3.21, 3.22, 3.23 and 3.24  $l$  can be determined via equation 3.25 as  $Nw_1$ ,  $Nw_2$  and  $B'C'$  are known from the TEM image and  $\hat{t}$  is the tilting angle which is chosen by the experimenter:

$$B'C' = \left( \left( \frac{((B'C')^2 + ((l^2 - Nw_2^2)^{\frac{1}{2}} - (l^2 - Nw_1^2)^{\frac{1}{2}})^2)^{1/2}}{2\sin(\frac{\hat{t}}{2})} \right)^2 - (l^2 - Nw_1^2) \right)^{1/2} + \left( \frac{((B'C')^2 + ((l^2 - Nw_2^2)^{\frac{1}{2}} - (l^2 - Nw_1^2)^{\frac{1}{2}})^2)^{1/2}}{2\sin(\frac{\hat{t}}{2})} \right)^2 - (l^2 - Nw_2^2) \right)^{1/2} \quad (3.25)$$

As it can be seen from figure 3.29(b), once  $l$  is known,  $\hat{i}$  can be calculated via equation 3.26:

$$\text{Cos}(\hat{i}) = \frac{NW_1}{l} \quad (3.26)$$

### 5.3. Calculation of the angle between the ion beam and the nanowires

Once the position of the nanowire is known, the angle between the ion beam and the nanowire can be determined. An example of such a calculation is shown below and in figure 3.31 based on the geometry of the MIAMI-1 system. In the figure, the nanowire is inclined upward ( $\hat{i}$  is thus defined as being positive) and its projection forms an angle  $\hat{x}$  with the x-axis. In the MIAMI-1 system, the ion beam forms an angle of  $30^\circ$  with the electron-beam (and the z-axis) and its projection is at  $45^\circ$  to the x- and the y-axis.

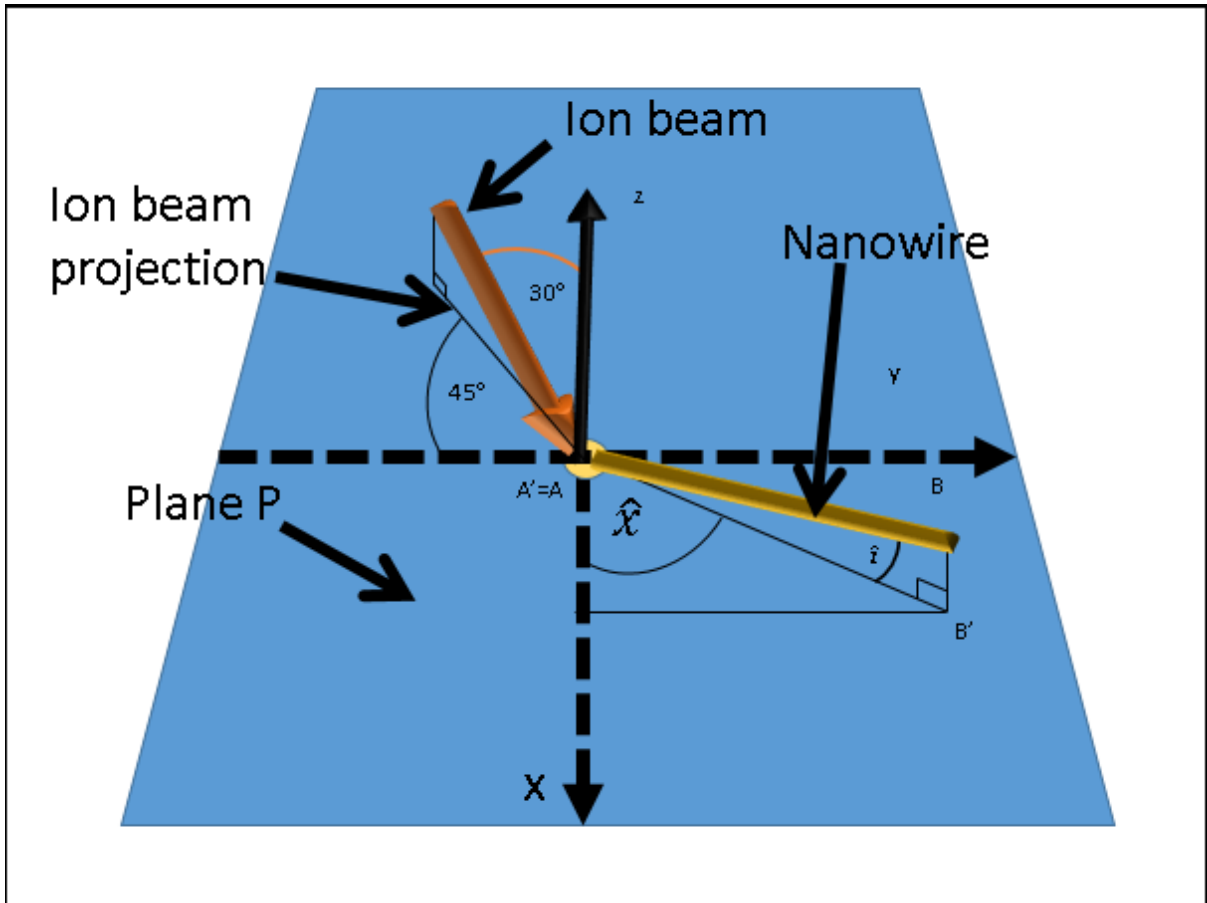


**Figure 3.31:** Schematic showing a nanowire in the MIAMI-1 system. The ion beam forms an angle of  $30^\circ$  with the x-axis whilst its projection forms an angle of  $45^\circ$  with x-axis and the y-axis.

As can be deduced from figure 3.31:

- The length of the projection of the ion beam vector onto the image plane is defined as  $I_{bpro} = \cos 60^\circ$  with the length of the ion beam vector chosen such as it is equal to 1.
  - The projection of the ion beam onto the x-axis is  $I_{bpro} \cos 45^\circ$
  - The projection of the ion beam onto the y-axis is  $I_{bpro} \sin 45^\circ$
  - The projection of the ion beam onto the z-axis is  $-\cos 30^\circ$
- Therefore the ion beam vector can be defined via equation 3.27

$$\vec{I}_b = (\cos 60 \times \cos 45)\vec{x} + (\cos 60 \times \cos 45)\vec{y} - (\cos 30)\vec{z} \quad (3.27)$$

The vector representing the nanowire  $\overrightarrow{AB}$  can also be deduced from figure 3.31 where, in the following example,  $\hat{x}$  will be chosen as being equal to  $45^\circ$ .

- The projection of the nanowire onto the x-axis is  $A'B' \times \cos 45^\circ$
- The projection of the nanowire onto the y-axis is  $A'B' \times \sin 45^\circ$
- The projection of the nanowire onto the z-axis is  $\cos \hat{t}$  with the length of the nanowire vector  $\overrightarrow{AB}$  also chosen such that it is equal to 1.

➤ Therefore, the nanowire vector can be defined via equation 3.28

$$\overrightarrow{AB} = (A'B' \times \cos 45^\circ)\vec{x} + (A'B' \times \sin 45^\circ)\vec{y} + (\cos \hat{t})\vec{z} \quad (3.28)$$

Consequently, after being tilted, the angle between the ion beam and the nanowire ( $\alpha'$ ) can be determined via equation 3.29. However, it is worth noting that if the ion beam induces a motion of the tilted nanowire, then  $\alpha'$  will only be representative of the initial spatial configuration of the nanowire:

$$\cos \alpha' = \overrightarrow{AB} \cdot \vec{I}_b \quad (3.29)$$

In the previous example  $\vec{I}_b$  has been defined for MIAMI-1. However, in this thesis some irradiations were performed in MIAMI-2 where the ion-beam forms an angle of  $18.7^\circ$  with the electron beam and is normal to the x-axis, in a direction opposite to  $\vec{y}$ . Therefore, using the same reasoning as previously, in MIAMI-2,  $\vec{I}_b$  is defined via equation 3.30.

$$\vec{I}_b = (\sin 18.7)\vec{y} - (\cos 18.7)\vec{z} \quad (3.30)$$

In many instances, the determination of  $\alpha'$  will permit valuable information such as the dpa or the range of the ions using SRIM to be obtained. However, in SRIM the input regarding the spatial configuration of the ion beam and its target material is not  $\alpha'$  but  $\alpha$  which is the angle between the ion beam and the normal to the nanowire. Therefore, in order to avoid confusion, the angle  $\alpha$  will be used and be defined as in SRIM (i.e. the angle between the ion beam and the normal to the surface onto which the calculations are performed).

# Chapter 4: Ion induced bending of nanowires at elevated temperatures

## 1. Motivation for irradiation at elevated temperatures

In this chapter, experiments designed to induce bending of germanium nanowires via the use of ion beams at elevated temperatures will be presented. As will be shown, the results presented herein are of both a practical and a fundamental interest. Indeed, they aim to engineer bent single crystalline germanium and silicon nanowires in a context where previous results in the literature have shown that such an outcome is unlikely via IIB at RT [177], [184]. From a more fundamental perspective, they will give an insight on the mechanisms responsible for the IIB phenomenon.

To introduce this chapter, the six main mechanisms proposed in the literature to explain the bending of nanostructures are summarised below:

- i. A mechanism based on uneven thermal expansion within the structure during irradiation which has been proposed to leading the nanowires to bend towards the ion beam [179].
- ii. A rearrangement of the surface and its vicinity as a way to stabilise the highly damaged structure via mass transport. Such rearrangement leading to bending towards the ion beam was proposed as readily occurring during irradiation and to benefit from both the displacement of atoms via nuclear stopping and the increased atomic mobility due to the input of thermal energy [122], [175], [176], [178].
- iii. A third mechanism proposed in the literature was based on an uneven distribution of point defects resulting in an uneven volume change (volume

expansion for regions rich in self-interstitials or volume contraction in volume rich in vacancies) which depending on the distribution of the point defects could lead to IIB away from or towards the ion beam [97], [114].

- iv. To explain the bending away from the ion beam, a mechanism based on a difference of density within the nanowire was proposed after experiments on germanium nanowires. As amorphous germanium has been reported to be less dense than its crystalline phase it has been stated that if amorphisation occurs on the ion-beam-facing side of the nanowire (whilst the opposite side remains crystalline) the uneven volume density may cause bending of the nanowire [20].
- v. A viscoelastic flow process that occurs in amorphous materials and leads to an anisotropic deformation (the ion hammering effect) was reported as being responsible for the bending towards the ion beam. This mechanism which was first proposed after experimental work on germanium and further developed after experiments on silicon nanowires is supposedly only effective enough to bend the nanowires towards the ion beam when they are fully amorphous [20], [177], [184].
- vi. A change of density in irradiated amorphous material was briefly introduced in the literature as causing the bending towards the ion beam. The authors stated that, during irradiation, a contraction of the irradiated side of the amorphous nanowire could induce the bending moment leading to IIB towards the ion beam [20].

Out of the proposed mechanisms, mechanisms iii to vi are based on an internal volume change. However, in all these cases, the volume changes occur due to the accumulation of damage induced by the ion beam. Indeed, mechanisms iv, v and vi can occur only when the

accumulation of damage is such that amorphisation is induced. For its part, mechanism iii can occur only via an accumulation of point defects during irradiation. For these reasons, it is of interest to verify whether or not bending can still occur (and in which direction) when the accumulation of defects is prevented.

Another motivation for preventing damage accumulation is associated with the experiments reported by Pecora et al. in [177], [184]. In their irradiation experiments, the authors caused bending of single-crystal silicon nanowires towards the ion beam. As explained in the literature review, the bending of nanostructures towards the ion beam is probably more convenient as a nanomanipulation technique compared to bending away as it allows better control of the orientation of the structure. Regrettably, such bending was observed to occur only when full amorphisation was observed [20], [177], [184]. As a crystalline seed would not be present to induce recrystallisation via SPEG, the impossibility of having a nanowire bend towards the ion beam whilst it is still crystalline is problematic. However, by irradiating tapered silicon nanowires the authors managed to bend only the fully amorphous narrow tip of a nanowire whilst the wider base was still partially crystalline. Unfortunately, during SPEG the nanowire shape changed becoming straight again [177], [184]. Therefore, even in this example, the engineering of single crystalline nanowires bent towards the ion beam was unsuccessful and therefore performing IIB without the deleterious effect of amorphisation was an additional motivation for this work.

To answer both fundamental questions regarding the IIB phenomenon and to overcome the challenge of engineering bent single crystalline germanium nanowires, irradiations at elevated temperatures have been performed.

## 2. Design of the experiment

As stated in the experimental methods chapter, germanium nanowires were deposited onto a molybdenum TEM grid and were in most cases isolated enough to be free to move during IIB without any interference from adjacent nanowires.

The thickness of the nanowires varied from one to another. For this reason, the prepared samples contained nanowires which according to the literature could exhibit opposite behaviour when subject to ion irradiation as the bending direction has been reported to be influenced by the nanowire diameter [97], [114].

The nanowires were irradiated in situ of a TEM in the MIAMI-1 facility with a 30 keV xenon ion beam. To follow whether bending occurred, the microscope was operated in BF image mode. The microstructural evolution was also monitored using DF imaging as well as the SADP which enables the detection of the amorphous rings to identify any regions in which major amorphisation was induced [31].

The nanowires were irradiated at either RT or at elevated temperature as it had been verified in previous work that such temperatures could prevent amorphisation [33], [150], [152], [229]. The ion irradiations were performed at a temperature of 400°C using a double-tilt heating holder with fluxes ranging from  $5 \times 10^{12}$  to  $2.5 \times 10^{13}$  ions.cm<sup>-2</sup>.s<sup>-1</sup>. Whilst the flux was chosen to have values high enough to rapidly induce IIB during the experiments, higher fluxes were avoided as they might induce an accumulation of damage that surpassed the dynamic annealing and thus lead to the amorphisation of the nanowires [152].

### 3. Results and discussion

#### 3.1. Bending of germanium nanowires towards the ion beam at 400°C

The bending of germanium nanowires towards the ion beam when irradiated at elevated temperature (400°C) was observed during these experiments. It has been shown in the literature that there is a competition between the annealing rate and the damage rate [27], [152]. Therefore, as the elevated temperature does not necessarily guarantee that amorphisation will not occur, the selected area diffraction patterns (SADPs) before and after irradiation were captured to verify whether the nanowires were still single crystalline after irradiation. The presence of strong diffraction spots without accompanying amorphous rings indicated that the nanowires were indeed still crystalline after irradiation [125]. To illustrate this, an example of a bent single crystal germanium nanowire is shown in figure 4.1 with a BF-TEM image of the nanowire and its SADP (a) before and (b) after irradiation. In both SADPs, the presence of amorphous rings was not observed indicating that the irradiation conditions were adequate to prevent any major amorphisation. SADPs were captured along the length of the nanowires to ensure that the existence of diffraction spots and the absence of the amorphous rings were consistent – particularly in the bent regions. This procedure has confirmed that, even in the most curved regions of the nanowires, amorphisation was not detected.

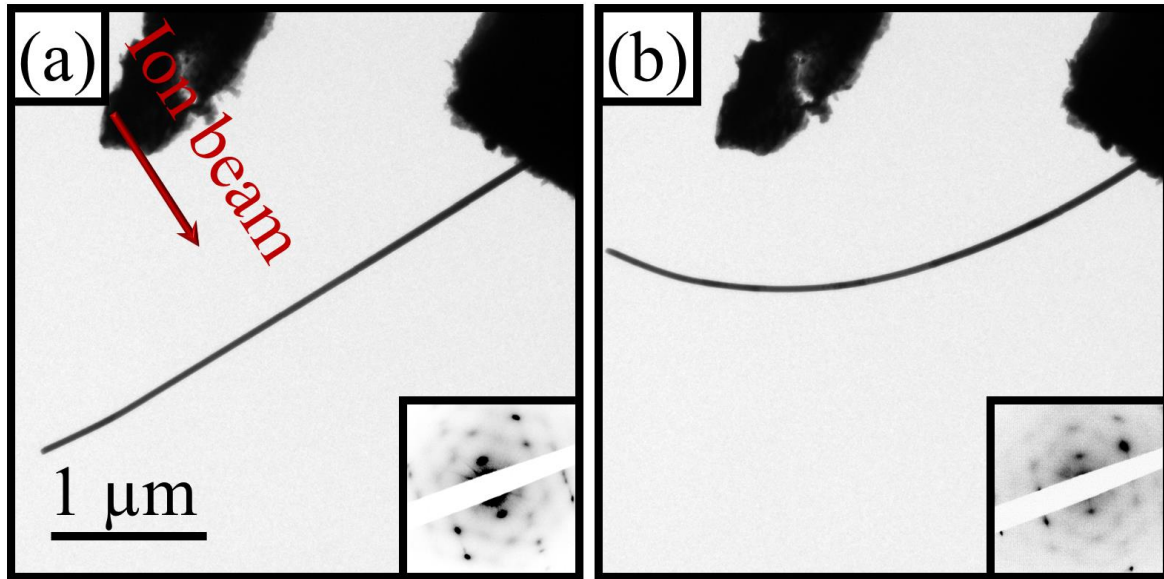


**Figure 4.1:** BF-TEM images and SADP of a nanowire: (a) before irradiation; and (b) after 30 keV xenon ion irradiation at 400°C to a fluence of  $7.1 \times 10^{14}$  ions.cm<sup>-2</sup>. The projection of the ion beam direction onto the image plane is indicated by the red arrow in (a). The scale bar in (a) also applies to image (b). The SADPs before and after irradiation are characteristic of single crystalline material.

It might be argued that major amorphisation has in fact occurred during the IIB and that the amorphous material induced by the ion was stable enough during the bending of the nanowire but had recrystallised when the SADP was captured (the elevated temperature of 400°C is known to be elevated enough to prompt SPEG in germanium) [22], [26]. To limit this possibility, the SADPs were captured immediately after the ion irradiation. Furthermore, an additional irradiation was performed during which the SADP was monitored whilst the nanowire was bending due to the irradiation. It should be noted that execution of such an experiment can be problematic as the specimen can move due to the ion irradiation and that consequently the area selected by the aperture can change requiring constant readjustment and may briefly include surrounding nanowires or other material. However, as can be observed from the SADPs in figure 4.2, amorphisation was prevented and a rotation of diffraction spots

around the 000 spot was induced. To accurately interpret the SADPs, it must be understood that some spots may appear or disappear during the irradiation depending on which planes happen to satisfy the Bragg conditions as the bending proceeds [203]. Therefore, in the SADP at two different fluences shown in figure 4.2(a) and (b) only selected diffraction spots indicated by the blue arrows are chosen to illustrate the rotation which was caused by the bending of the nanowire during IIB.

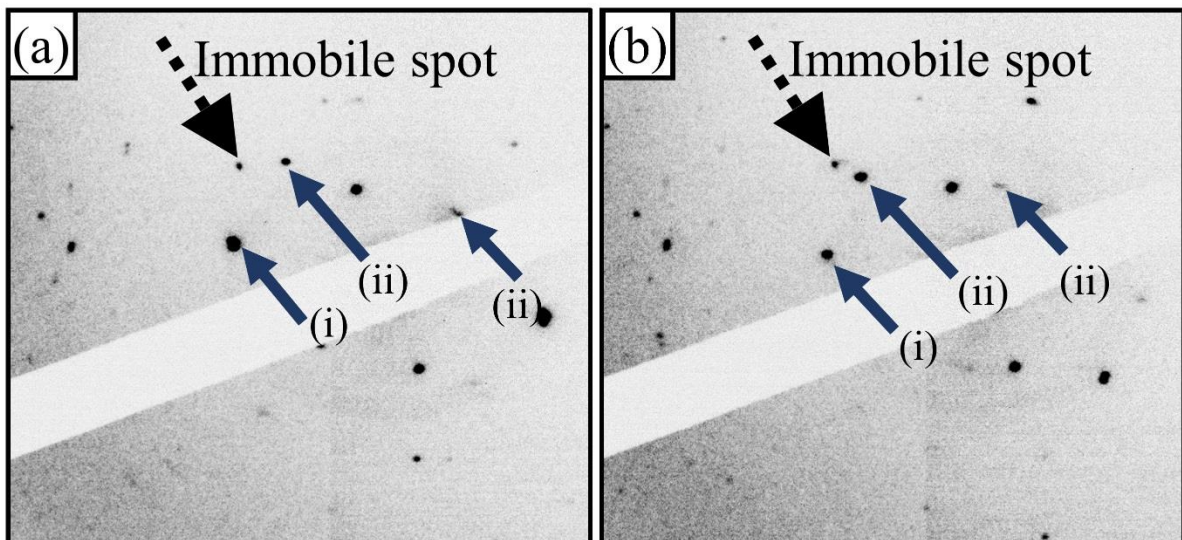


**Figure 4.2:** SADPs of a nanowire captured during irradiation to fluences of (a)  $8.8 \times 10^{14}$  ions.cm<sup>-2</sup> and (b)  $9.6 \times 10^{14}$  ions.cm<sup>-2</sup>. The diffraction spots indicated by the blue arrows have been chosen to illustrate the evolution of the SADP. A diffraction spot chosen as reference is indicated by the dashed black arrow. During the bending of the nanowires, several spots such as spots (i) and (ii) moved during the motion of the nanowire. However, whilst the intensity of the diffraction spot chosen as a reference varied, it did not move during irradiation. Indeed, the intensities of the diffraction spots may vary during the ion irradiation and some may appear and disappear as the intensities of the spots depend on how close to the Bragg conditions the diffracting planes are during the nanowire motion.

Further evidence of the single-crystal character of the bent germanium nanowires comes from the centred dark-field (CDF) TEM images. In figure 4.3(a) and (b), BF-TEM images of a nanowire are shown before and after irradiation, respectively. After irradiation the nanowire is aligned with the ion beam similar to the nanowire presented above in figure 4.1(b), the SADP in figure 4.3(b) shows that no major amorphisation has occurred. However, another effect of radiation damage is observable in that the nanowire is clearly thinner after irradiation. The thinning of the nanowire is attributed to sputtering and may be a factor which limits the degree of manipulation of the nanowires (especially if IIB is to be induced multiple times on the same nanowires) [230]–[234]. Figure 4.3(c)–(e) shows the nanowire at another tilt angle with (c) featuring a BF-TEM image and (d)–(e) CDF images. As can be observed, the nanowire is bright across its whole diameter in the CDF images. If one side of the nanowire were amorphous and the incident electron beam were parallel to the interface between the amorphous and the crystalline phase, the nanowire would have been only partially bright on the crystalline side and dark on the amorphous side. In other configurations, (i.e. the incident electron beam not exactly parallel to the interface), it is very likely that the side most exposed to the ion beam (the one facing the ion beam in projection) would have appeared more or less dark depending on how much of the amorphous phase cut across the incident electron beam [203]. In contrast, in figure 4.3 the contrast can be considered as uniformly bright across the nanowire. On the other hand, it must be noted that even if only regions along the nanowires are bright, it is to be expected that not all of a bent nanowire will be in the same Bragg condition. For this reason, two different Bragg conditions have been selected to generate the CDF-TEM images which are shown in figure 4.5(d) and (e).

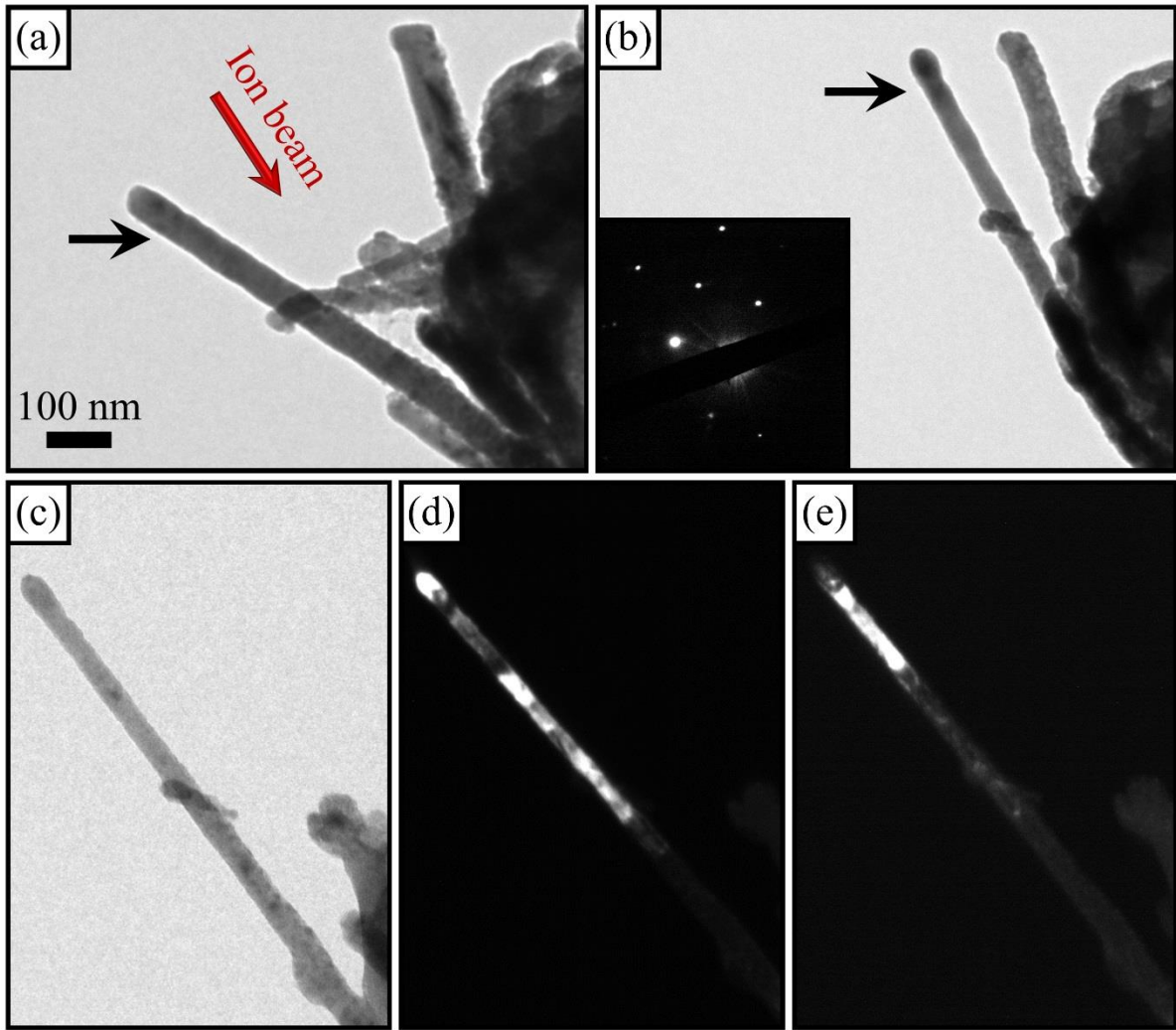


**Figure 4.3:** (a) BF-TEM image of a nanowire before irradiation at 400°C temperature and (b) after irradiation to a fluence of  $2.4 \times 10^{15}$  ions.cm<sup>-2</sup> inducing bending and sputtering of the nanowire. The SADP in (b) shows that amorphisation has not been detected after the bending of the nanowire towards the ion beam. The same nanowire after irradiation is shown in (c) at another tilt angle in BF-TEM image mode and in a CDF-TEM image mode which correspond to (d) a (004) condition and in (e) to a ( $\bar{1}31$ ) condition. The projection of the ion beam direction onto the image plane is indicated by the red arrow in (a). The scale bar in (a) is also valid for the other images in the figure. It must be specified that the images (b), (c) and (d) were taken at a different tilt angle (close to zone axis) for the reason that they were captured during a post-analysis whose aim was to perform HRTEM.

### 3.2. IIB mechanisms

In the literature, the first work reported on the bending of germanium nanowires via the use of ion beams has defined amorphisation as a requirement for the IIB to occur [20]. Indeed, in [20] bending away was observed to occur when partial amorphisation was induced, whilst the bending of the nanowires towards the ion beam was said to be possible only when full amorphisation was achieved and ion hammering was identified as being the cause of IIB towards the ion beam. It is therefore interesting to have induced bending of germanium nanowires towards the ion beam without amorphisation. It is worth noting that the same conclusion has also been reported for the bending of silicon nanowires towards the ion beam [177], [184]. To compare to that work in a similar manner, an equivalent experiment has been carried on silicon nanowires again at elevated temperature. The results of this experiment are presented in Appendix A and demonstrate that silicon nanowires too can be bent towards the ion beam without becoming amorphous. For these reasons, ion hammering as a cause of the bending of nanowires irradiated at elevated temperatures can be dismissed. More generally, this mechanism is not to be totally ruled out as it may still play a role during bending at RT. However, these experiments cast doubt on the influence of ion hammering as it is now clear that another mechanism can induce the bending of nanowires towards the ion beam under conditions where ion hammering cannot occur.

An important feature of irradiations performed at elevated temperature is that the thermal energy provided must be great enough to prevent the damage accumulation that would otherwise lead to the amorphisation of the structure. If full crystallinity is to be retained, the thermal energy must ensure that the recombination of defects is able to occur at a higher rate than their accumulation. As stated in the literature, the requisite temperatures to perform such irradiations depend on numerous factors and can therefore vary depending on the experimental

conditions [152]. In the work presented here, even at high fluences the nanowires remained crystalline. For instance, the nanowire shown in figure 4.4 is still crystalline after being irradiated at 400°C to a fluence of  $2.7 \times 10^{15}$  ions.cm<sup>-2</sup> corresponding to a peak of 35 dpa (i.e. the dpa is calculated in the region containing the peak of the damage profile with a width measuring  $\pm 0.1$  of the total damage range). Knowing that germanium has been reported to become amorphous above 0.3 dpa when irradiated at RT with germanium ions [23], it is reasonable to assume that the nanowire shown in figure 4.4 would have suffered amorphisation if the irradiation had been performed under the same conditions but at RT as the peak dpa is two orders of magnitude greater than 0.3. As amorphisation has not been observed even at this relatively high fluence, it is reasonable to conclude that the elevated temperature has prevented major damage accumulation. This observation regarding the prevention of damage accumulation is in disagreement with a proposed mechanism based on the distribution of point defects within the nanowires used to explain the bending [97], [114]. Indeed, for this mechanism to operate, point defects must generate enough volume expansion and/or contraction to induce an imbalance sufficient to make a nanowire bend towards or away from the ion beam. As major damage accumulation has been prevented in the experiments reported here, this mechanism is also unlikely to explain how the germanium (and silicon) nanowires have bent towards the ion beam at elevated temperature.

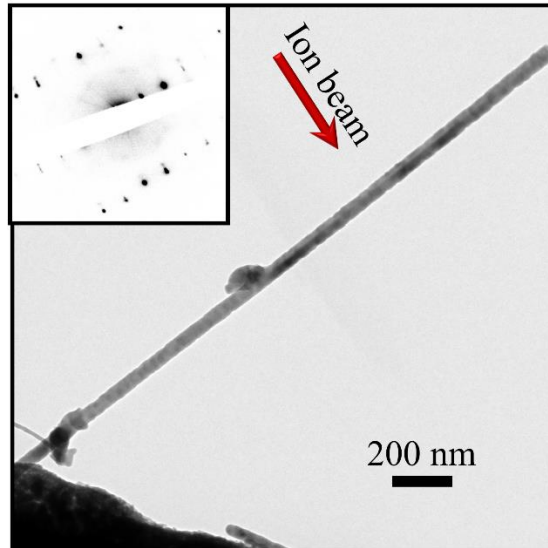


**Figure 4.4:** BF-TEM image and SADP of a germanium nanowire irradiated at 400°C to a fluence of  $2.7 \times 10^{15}$  ions.cm<sup>-2</sup> showing that in this case the elevated temperature may have prevented the bending from occurring. The projection of the ion beam direction onto the image plane is indicated by the red arrow.

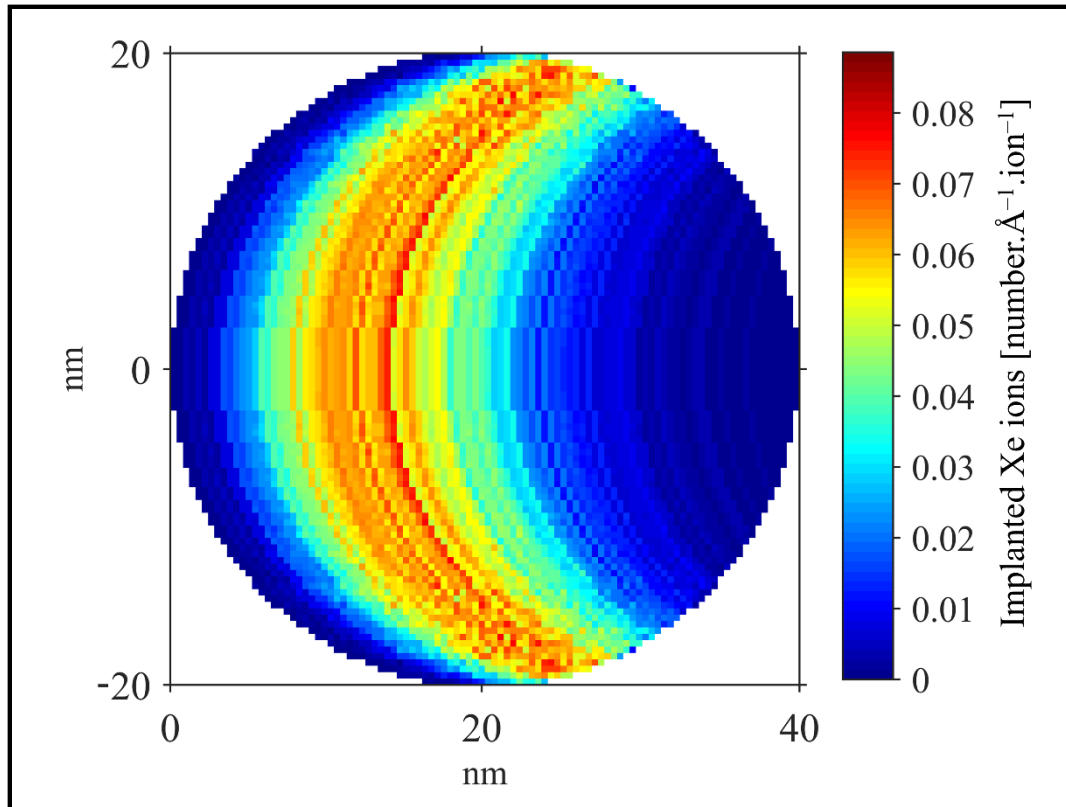


**Figure 4.5:** IDRAGON profile showing the distribution of implanted xenon atoms in the cross section of the nanowire shown in figure 4.1. According to this calculation, most of the ions were implanted within the half of the nanowire nearest to the irradiated surface.

Whilst major accumulation of damage has been prevented, the effect of xenon ions which might have been implanted into the nanowire must be considered as they may induce volume expansion. Indeed, even though inert gases have often been reported to diffuse out of the target material as they do not bond with the lattice [97], TEM observations have also shown that they could remain implanted and agglomerate in the vicinity of their average implantation depth [235]. To consider this possibility, IDRAGON was run for the nanowire shown in figure 4.1 to determine where the xenon ions would be implanted. The outcome of the calculation is shown in figure 4.5 and indicates that unless atomic diffusion or channelling occurred, the majority of the ions were implanted closer to the ion-beam-facing side of the nanowire. If the xenon ions

did not diffuse out of the structure and remained close to this implantation depth, they may have induced a volume expansion in that side of the nanowire. In such a situation, similar to the mechanism described by Borschel et al. [97], [114] and detailed in the literature review of the current work, a volume expansion of the ion-beam-facing side of the nanowire could induce a bending of the nanowire away from the ion beam [97], [114]. As the nanowire in this case has instead bent towards the ion beam then it can be assumed that if a volume change due to the implanted ions were operating then it is not a primary cause of bending as it has been overcome by another mechanism.

The mechanism based on the uneven thermal expansion was proposed on a material whose thermal expansion coefficient was negative. However, in the case of germanium and many other materials such as silicon [184], gallium arsenide [97], aluminium [175] and zinc oxide [114], bending towards the ion beam has been observed despite a positive thermal expansion coefficient over a large range of temperature [236]–[239].

In [20], IIB has been induced on germanium nanowires irradiated with a 30 keV gallium ion beam at RT at an angle of  $45^\circ$  relative to the ion beam. Via the IDRAGON implantation profile of such a nanowire, it was determined in the present work that most of the ions were implanted in the ion-beam-facing side of the nanowires irradiated in [20]. In such a case, if the thermal energy provided by the ion beam were responsible for internal volume changes then it would induce an expansion in the ion-beam-facing side of the nanowire. This swelling could consequently lead the nanowire to bend away from the ion beam. However, in reality the nanowire bent towards the ion beam meaning that some other mechanism must be responsible for the bending. Likewise, in [176] a 100 nm wide silver cantilever was irradiated by a 30 keV gallium ion beam at an initial angle  $\alpha$  of  $52^\circ$ . According to SRIM, the ion range and most of the energy loss to phonons are within the first 10 nm of the target material. However, similar to the germanium nanowires given as examples above in figures 4.1 and 4.3, the cantilever also

bent towards the ion beam whereas a mechanism based on thermal expansion would have driven it in the opposite direction.

In conclusion, out of all the mechanisms proposed in the literature, only those reported in [122], [175], [176], [178] and based on the dynamic atomic rearrangement of the surface and subsurface are capable of explaining the bending of the nanowires towards the ion beam as reported here.

In figure 4.6(a), the BF-TEM image of a germanium nanowire before irradiation is shown and in figure 4.6(b) the BF-TEM image of the nanowire bent after irradiation is shown as well as the SADP, which attests that the nanowire remained crystalline. However, in addition to the shape modification of the nanowire, it can be observed that the ion irradiation has caused a degree of sputtering.

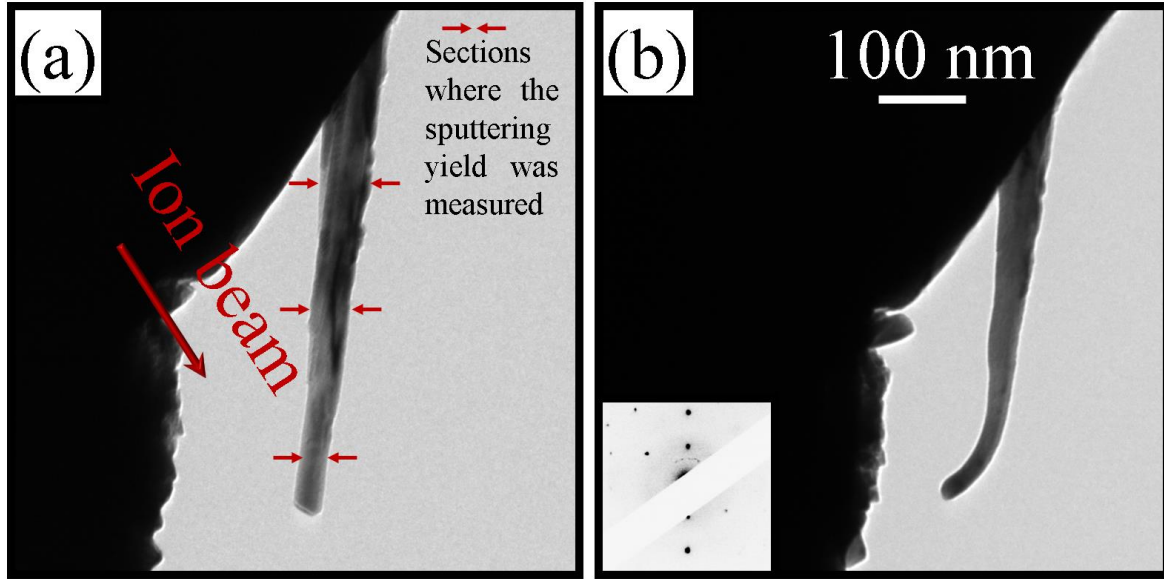


**Figure 4.6:** BF-TEM images of a nanowire (a) before and (b) after 30 keV xenon ion irradiation at 400°C to a fluence of  $1.2 \times 10^{15}$  ions.cm<sup>-2</sup>. The projection of the ion beam direction onto the image plane is indicated by the red arrow in (a) and the zones corresponding to the sections where the sputtering yield was measured are shown by the red arrows. The scale bar in (b) also applies to image (a). The SADP after irradiation is indicative of single crystal material.

The method to evaluate the sputtering yield ( $S_y$ ) during irradiation at an initial angle  $\alpha$  of the nanowire of radius ( $R$ ) (cm) based on its radius ( $r$ ) (cm) after sputtering is described below.

The number of atoms  $N_{at}$  removed from a nanowire irradiated surface per cm<sup>2</sup> (atoms.cm<sup>-2</sup>) at a fluence  $\phi$  is expressed by equation 4.1.

$$N_{at} = S_y \times \phi \quad (4.1)$$

Therefore, the number of atoms sputtered away ( $A_s$ ) when a nanowire of length 1 cm has reached a radius ( $r$ ) is expressed in equation 4.2 with the approximation that the nanowire is cylindrical and remains cylindrical during irradiation.

$$A_s = S_y \times \phi \times 2 \times r \times 1 \text{ cm} \quad (4.2)$$

The volume sputtered ( $V_s$ ) from the nanowire can therefore be calculated as a function of the atomic density ( $a_d$ ) in  $\text{atom.cm}^{-3}$  of germanium as shown in equation 4.3.

$$V_s = \frac{S_y \times \phi \times 2 \times r}{a_d} \times 1 \text{ cm} \quad (4.3)$$

The volume sputtered can also be expressed as a function of the radius of the nanowire before irradiation ( $R$ ) and after and irradiation step ( $r$ ) as expressed in equation 4.4.

$$V_s = (R^2 - r^2) \times \pi \times 1 \text{ cm} \quad (4.4)$$

The expression 4.4 can be rearranged to equation 4.5.

$$r = \sqrt{R^2 - \frac{V_s}{\pi}} \quad (4.5)$$

Finally, an equation 4.6 which formulates the decrease of the radius of the nanowire as a function of the sputtering yield is deduced below. Indeed, as  $R^2 - r^2 = (R - r) \times (R + r)$ , the value of  $(R - r)$  can be express using equations 4.4 and 4.5 and is shown to be a function of  $V_s$  which itself depends on the sputtering yield  $S_y$ .

$$R - r = \frac{R^2 - r^2}{R + r} = \frac{V_s}{\pi(R + \sqrt{R^2 - \frac{V_s}{\pi}})} \quad (4.6)$$

It is worth noting that in equation 4.6  $V_s$  varies during irradiation as it depends on the value of  $r$  which obviously decreases during the irradiation.

After 30 keV xenon ion irradiation to a fluence of  $1.2 \times 10^{15} \text{ ions.cm}^{-2}$ , the sputtering yield from the nanowire shown in figure 4.6 has been calculated at three different positions along its length using the equations above. As the nanowire diameter was uneven before irradiation, three positions were used to examine whether the sputtering differed along its length.

A sputtering yield has been estimated in the region which has bent during irradiation (i.e. the tip of the nanowire) using a section whose diameter went from 33 to 22 nm during irradiation. Sputtering yields were also deduced for regions: just below the bending tip using a section for which the diameter was 44 nm before irradiation and 33 nm after; and close to the base of the nanowire in a section measuring 63 nm before irradiation and 52 nm after. The calculations have shown that the sputtering yield was constant along the nanowire and was between 63 and 64 atoms per xenon ion. The sputtering yield measured has been compared with the SRIM calculation applied to this nanowire. According to the SRIM calculation, the sputtering yield is expected to have a value of approximately four atoms per ion. The discrepancy between SRIM and the experimental observations is considerable. However, it is worth noting that sputtering of nanowires is often substantially higher than that predicted for the bulk as SRIM does not take into account the cylindrical shape of the nanowire [35], [171] and that the sputtering yields of materials bombarded at elevated temperature has also been reported as being often greater than those observed at lower temperature [230], [232], [240].

Regardless of any enhancement to sputtering yield, the sputtering yield was consistent along the nanowire meaning that the whole nanowire must have been subject to irradiation. Nevertheless, one clear observation is that, as shown in figure 4.6, the nanowire did not react in the same manner to the ion bombardment as only the tip has bent during irradiation. As only the thinner part has experienced IIB, parallels can be drawn with [97], [114] in which it was observed that the value of the ratio  $\frac{\text{range of the ion}}{\text{nanowire diameter}} = \theta$ , dictates the bending direction during ion irradiation. According to [97], [114], an elevated value of  $\theta$  (i.e. above 0.5) would induce a bending towards the ion beam and a lower one (i.e. below 0.5) would induce bending away from it. As this nanowire displays a clear difference regarding its diameter at the thin tip and the rest of its body, it might be suggested based on these publications that the thicker part of the nanowire, which represents most of the nanowire length, should have a tendency to bend

away from the ion beam. However, bending away from the ion beam has not occurred anywhere in this nanowire. In fact, only a small section of the nanowire has been subject to IIB and this was towards the ion beam. This section would have had a higher value of  $\theta$  and has bent towards the ion beam whilst the rest of the nanowire which might have been expected to have a tendency to bend away from it, remained straight. This observation might imply the irradiation at 400°C has allowed bending to occur only towards the ion beam whilst bending away was prevented. Although the behaviour of this nanowire only suggests such a conclusion, more evidence of such hindrance due to the temperature of irradiation will be shown below via the comparison between the effects of irradiations performed at elevated temperature and those performed under the same conditions but at RT.

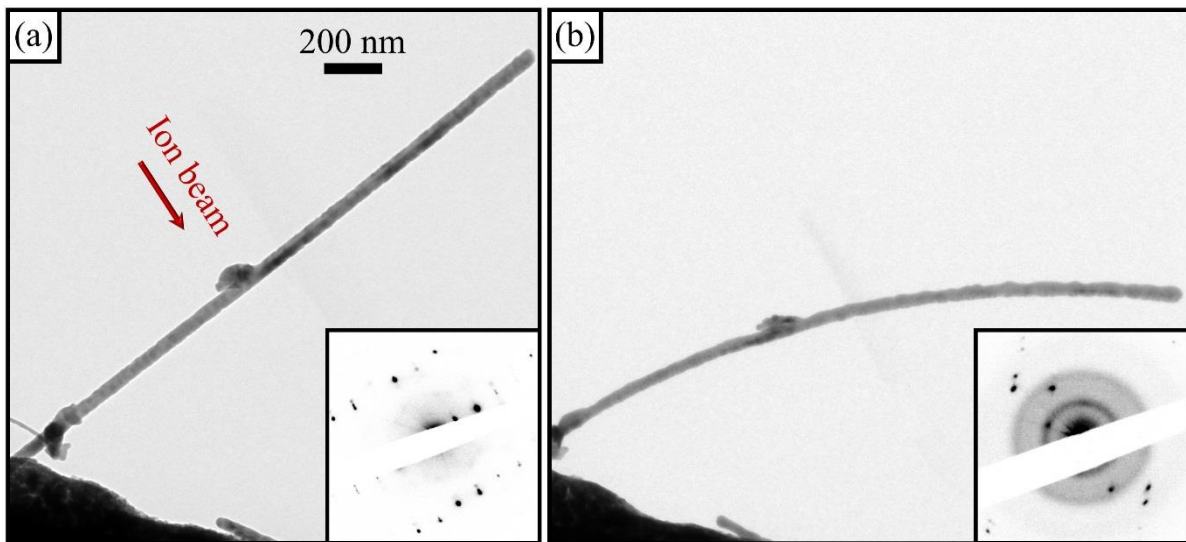


**Figure 4.7:** BF-TEM images and SADPs of a nanowire (a) after a 30 keV xenon ion irradiation at 400°C to a fluence of  $2.7 \times 10^{15}$  ions.cm<sup>-2</sup> and (b) after a subsequent irradiation at RT to a further fluence of  $7.5 \times 10^{13}$  ions.cm<sup>-2</sup>. The projection of the ion beam direction onto the image plane is indicated by the red arrow in (a). The scale bar in (a) applies to image (b). The SADPs show that the irradiation induced considerably more damage accumulation (leading to amorphisation) when it was performed at RT.

One important element of the experiments performed at elevated temperature is that not all nanowires were observed to bend, but that those that did always bent towards the ion beam. This contrasts with several experiments that have been performed under the same conditions at RT. In these cases, some nanowires bent towards and others bent away from the ion beam. Considering this difference of behaviour of the nanowires irradiated at elevated temperature, it can be hypothesised that at the elevated temperature the mechanisms, which prompted the bending away, are suppressed. Interestingly, all mechanisms, which would induce bending away from the ion beam, require some degree of damage accumulation to lead to either amorphisation or to a non-uniform distribution of point defects. As major damage accumulation is prevented at 400°C, it is therefore perhaps understandable that bending away was not observed. Figure 4.7 is a clear example of the difference in behaviour of the same nanowire irradiated at these two different temperatures. The nanowire is initially irradiated at elevated temperature under the conditions described in the experimental section. The elevated temperature prevents major damage accumulation and the nanowire remained crystalline as shown by the SADP inset into the BF-TEM image in figure 4.7(a). The nanowire was irradiated to a relatively-high fluence of  $2.7 \times 10^{15}$  ions.cm<sup>-2</sup> but still remained unbent. The assumption is that the damage accumulation was prevented as was the mechanism responsible for bending away. In figure 4.7(b) the BF-TEM image and the inset SADP show how a subsequent irradiation performed at RT affected the nanowire. In this second irradiation, an additional fluence which is more than one order of magnitude below the total irradiation performed at the elevated temperature has a tremendous effect on the nanowire. As shown by the SADP, at RT the accumulation of damage during irradiation occurs and the nanowire consequently suffered from amorphisation with the characteristic amorphous rings visible in the SADP [31], [203].

In addition, the nanowire has bent away from the ion beam, presumably because the mechanisms based on damage accumulation were free to operate.

#### 4. Conclusion, remarks and perspectives

Following experiments reported in the literature on tapered silicon nanowires [177], [184], doubts can be cast upon the possibility of recovering the crystallinity of nanowires whilst preserving the bending induced via IIB. Consequently, the results of the experiments presented here can have a practical interest as they demonstrate the possibility of inducing bending of germanium nanowires towards an ion beam whilst still preserving their single-crystal character by performing the irradiation at elevated temperature. Furthermore, as silicon nanowires have also been successfully subject to nanomanipulation via IIB at elevated temperature and still remained crystalline (see Appendix A), the process used in this work seems to be transferable to other materials.

As stated above, IIB towards the ion beam is probably the most effective way of aligning nanostructures as compared to IIB away as alignment of nanostructures can be readily controlled by positioning the ion beam parallel to the desired orientation. However, in both directions, IIB can be an unwanted effect of the doping of nanostructures using ion beams and thus a way to prevent such bending is desirable. From this view, the current work indicates that if doping is performed at elevated temperatures then the bending can be avoided as long as the nanowire is under conditions where it would normally bend away from the ion beam. Indeed, as the experiments have indicated that the occurrence of bending away from the ion beam requires major damage accumulation, the irradiations performed at elevated temperatures can constitute an easy way to prevent IIB away. However, more investigations are needed in order to understand which conditions lead to the nanowire bending towards the ion beam at elevated temperature or to the nanowire remaining straight (as it cannot bend away at elevated

temperature). In fact, in a more general sense than just irradiations performed at elevated temperatures, determining the conditions which lead to particular bending directions is highly desirable for both nanoengineering and to have a better fundamental understanding of the IIB phenomenon. For these reasons, this challenge will be addressed in the next chapter.

An obvious question arising from these results is how the lattice which is preserved at elevated temperatures can accommodate the bending. During these experiments, it has been observed that some of the nanowires subject to IIB towards the ion beam did not assume the circular shape which they consistently have during irradiation at RT. Figure 4.8 shows an example of such a nanowire that did not bend along an arc at elevated temperature. From the superimposed images (taken from an in situ video) it can be seen that the nanowire remains straight during the alignment with the ion beam, thus suggesting that the crystal lattice prevents it from taking the typical curved shape observed during irradiation at RT.

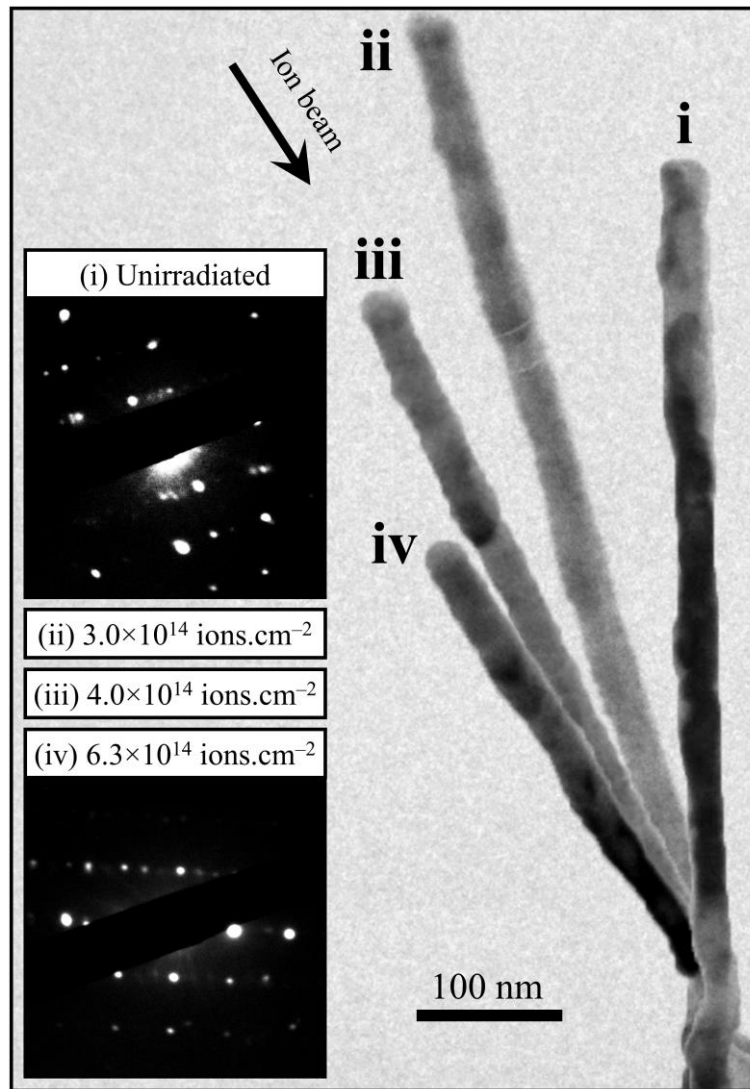


**Figure 4.8:** Superimposed BF-TEM images taken from an in situ video showing the evolution of a germanium nanowire during a 30 keV xenon ion irradiation at 400°C. The projection of the ion beam direction onto the image plane is indicated by the red arrow in (a). The SADP before and after irradiation are characteristic of crystalline material. The nanowire is shown to align towards the ion beam without taking a curved shape.

The nanowire shown in figure 4.6(b) took a curved shape close to its tip whilst remaining unbent further along its length. An attempt has therefore been made to compare via HRTEM the impact of the ion beam on these two distinctly different regions of the nanowire.

Unfortunately, acquiring lattice images of the bent section of the nanowires was found to be challenging using conventional TEM techniques. Thus, the question remains as to how the lattice adjusts to the circular shape of the nanowire and should be a focus of future work. For instance, the bending might induce dislocations to accommodate internal stress. Furthermore, as shown in figure 4.9, when a nanowire takes a curved shape the lattice might be under compressive strain on the inside of the arc and tensile strain on the outside.

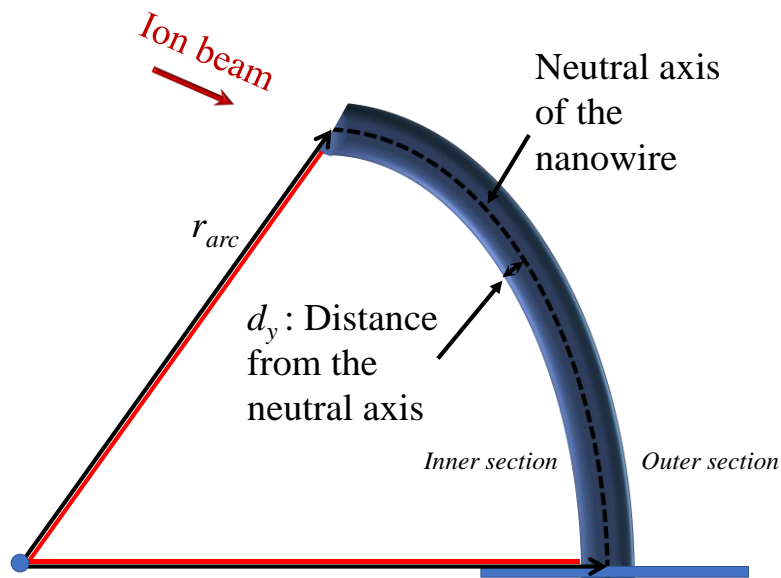


**Figure 4.9:** Schematic of a nanowire bending towards the ion beam whilst taking a circular shape. The radius ( $r_{arc}$ ) should be measured using the neutral axis of the nanowire to determine the strain as a function of  $d_y$  according to equation 4.7.

If the nanowires are under strain, a simple “beam theory” argument can be made regarding the magnitude of the internal strain [241]. In the inner section of the nanowire, an internal compressive strain can be expected whilst on its outer section the strain will be tensile. The absolute term of the strain ( $\epsilon$ ) increases as a function of the distance ( $d_y$ ) from the centre of the nanowire (known as the neutral axis) as shown in figure 4.9.

According to this model, the strain,  $\varepsilon$ , can be expressed via equation 4.7 as a function of the radius made by the nanowire ( $r_{arc}$ ) and  $d_y$ .

$$\varepsilon = \frac{d_y}{r_{arc}} \quad (4.7)$$

Using equation 4.7 on germanium nanowires bent via IIB at 400°C, values of strain above 3% have been calculated. It must be recalled that (as stated in the experimental method chapter) the radius observed in the TEM and used for such calculation is most likely underestimated as it is measured based on the projection of the nanowires onto the image plane. Consequently, whilst the exact curvature can be determined in future work via tilting the TEM-rod, here, based on the available BF-images, the deformation of the nanowires out of the image plane is not taken into account and the calculated values of strain are thus also underestimated.

As a strain of a few percent [165], [167], (or alternatively a combination of strain and heavy n-type doping [242]) have been reported to induce a direct band gap behaviour of germanium, IIB at elevated temperatures may be a promising technique for optoelectronic applications as direct band gap transitions can allow light emission. Furthermore, as the bending is not limited to the use of inert gases, a combination of strain and heavy doping can be readily achieved during IIB to facilitate band gap engineering of germanium [97].

To conclude, on a more general note there is a lack in the literature regarding how the IIB might affect other characteristics of the bent nanostructures (such as the influence of the IIB on the band gap of nano-semiconductors as well as its potential impact on piezoelectric nanostructures such as ZnO nanowires).

# Chapter 5: Ion induced bending of nanowires at RT and subsequent annealing

## 1. Context

In the experiments reported in the previous chapter, the bending of germanium nanowires towards the ion beam was achieved via ion irradiation at 400°C. These experimental conditions have allowed the nanowires to remain crystalline during IIB, thus suggesting that bending towards the ion beam can occur without the operation of mechanisms based on damage accumulation.

In chapter 4 experiments were also performed at RT and comparison between these and the irradiations achieved at elevated temperature have shown that the nanowires were observed to bend away only at RT (i.e. only under conditions where major radiation damage was not prevented by the elevated temperature).

To be truly accurate, whilst these results have shown that damage accumulation was required for bending away, the question remain as to whether damage accumulation is also responsible for the bending towards the ion beam when the irradiation is performed at RT. Besides, the irradiation conditions which dictates the bending direction are yet to be defined.

The bending of nanostructures via the use of ion beams can be used reliably only if the direction of the bending can be controlled. In the experiments presented in the current chapter, the germanium nanowires were irradiated at RT by xenon ions in order to determine which factors influence their bending direction. For this reason, a great use of the tilting procedure was made: whereas in the previous chapter, it was principally utilised to verify the bending direction of the nanowires, here the tilting procedure was also performed to fully characterise the

orientation between the ion beam and the nanowires as described in the experimental method chapter. As the angle between the nanowire and the ion beam was known, the IDRAGON implementation of SRIM was extensively exploited allowing verification of whether the bending direction could be correlated to the average damage depth. Furthermore, through this comparison of the simulation and the experimental results, insights into the mechanisms behind IIB were gained.

The IIB phenomenon, and particularly its use to align an array of nanowires towards an ion beam, makes it a powerful tool for nanomanipulation. However, the annealing step which is routinely performed to remove the damage accumulated during ion irradiation has been observed to undo the alignment obtained during IIB towards the ion beam [177], [184]. This observation was made by Pecora et al. [177], [184] after experimentations performed on tapered silicon nanowires and the geometry of these structures may therefore have influenced the outcome [177], [184]. The stability of IIB curvature during annealing remains to be investigated for the case of non-tapered nanowires. In the literature, experiments performed on both silicon and germanium nanowires have indicated that bending towards would occur only when the nanowires were fully amorphous thus making the use of SPEG problematic as it requires the presence of a buried crystal within the nanostructure [20], [177], [184]. In the experiments reported in this chapter, the nanowires were irradiated at RT to induce bending (away from or towards the ion beam) and then it was verified whether the nanowires were fully amorphous. Afterwards, the nanowires were subjected to annealing to investigate the stability of the bent structures. The conclusion of the annealing experiments provides valuable information for nanoengineering applications as well as giving further insights on the mechanisms which regulate the IIB phenomenon.

## 2. Method

The samples were prepared in the same way as those irradiated at elevated temperature (see chapter 3 and 4) resulting in single-crystal germanium nanowires with lengths ranging from 100 nm to 2  $\mu\text{m}$  and average diameters ( $\varnothing$ ) ranging between 15 to 60 nm. The nanowires chosen to study the IIB effect were those left extending into free space from the TEM molybdenum grids. As the diameter and orientation varied between nanowires, this resulted in a range of values for the initial normalised average damage depth ( $\Omega$ ) (the ratio of the average damage depth to the diameter of the nanowire).

The TEM was operated at 200 kV in the MIAMI-1 system where the nanowires were irradiated by a 30 or 70 keV xenon ion beam at RT with a typical flux of  $10^{13}$  ions.cm<sup>-2</sup>.s<sup>-1</sup>. Two different energies were chosen to further increase the range of values taken by  $\Omega$ . To evaluate  $\Omega$ , the IDRAGON code was used as described in the experimental section with SRIM 2013 run in “Detailed calculation with full damage cascades” where the displacement energy for germanium was set to 21 eV. The dpa were calculated in the same way as described in chapter 3.

A tilting procedure was performed before the irradiation to determine how the nanowires were oriented with relation to the ion beam at the beginning of the irradiation using the equations and the method detailed in the experimental methods chapter. Via the tilting procedure the initial angle  $\alpha$  was thus determined, which, as stated in the experimental chapter, corresponds to the angle between the ion beam and the normal to the nanowire’s axis. After irradiation, the specimen stage was tilted once more to determine the bending direction.

The TEM was operated in BF mode to follow the morphological evolution of the nanowires whilst SADPs and DF images were used to further monitor the microstructure of the nanowires.

### 3. Results and discussion

#### 3.1. Irradiation of germanium nanowires at RT

##### 3.1.1. Results

In figure 5.1(a) and (b), a  $\varnothing = 52$  nm germanium nanowire is shown before and after irradiation by a 30 keV xenon ion beam at RT, respectively. On the bottom row of figure 5.1 ((c) and (d)) a germanium nanowire whose average diameter is smaller ( $\varnothing = 39$  nm) is also shown before and after irradiation by a 30 keV xenon ion beam. During these irradiations performed at RT, both nanowires bent and suffered from radiation damage. The accumulation of radiation damage is clearly demonstrated by the SADPs in figure 5.1(b) and (e) which indicate that the nanowires are partially amorphous after irradiation as evidenced by the coexistence of both amorphous rings and diffraction spots [203]. However, even though both the nanowires are partially amorphous their behaviour differs. Indeed, it can be seen in these figures (and confirmed via the tilting procedure) that the nanowires have bent in opposite directions: the nanowire in the top row has bent away from the ion beam and the thinner nanowire in the panel (c) and (d) has bent towards it. It is worth recalling that an individual TEM image does not give complete information regarding the angle between the nanowire and the ion beam. For example, the nanowire shown in figure 5.1(a) is inclined in such a way that it forms before irradiation an angle  $\alpha = 37^\circ$  whilst the BF-TEM image could be interpreted as  $\alpha \approx 0^\circ$ . As detailed in chapter 3, the calculation of  $\alpha$  was determined via a tilting procedure performed before irradiation. The ratio  $\Omega$  was thus calculated using IDRAGON for the two germanium nanowires shown in figure 5.1(a) and (c).

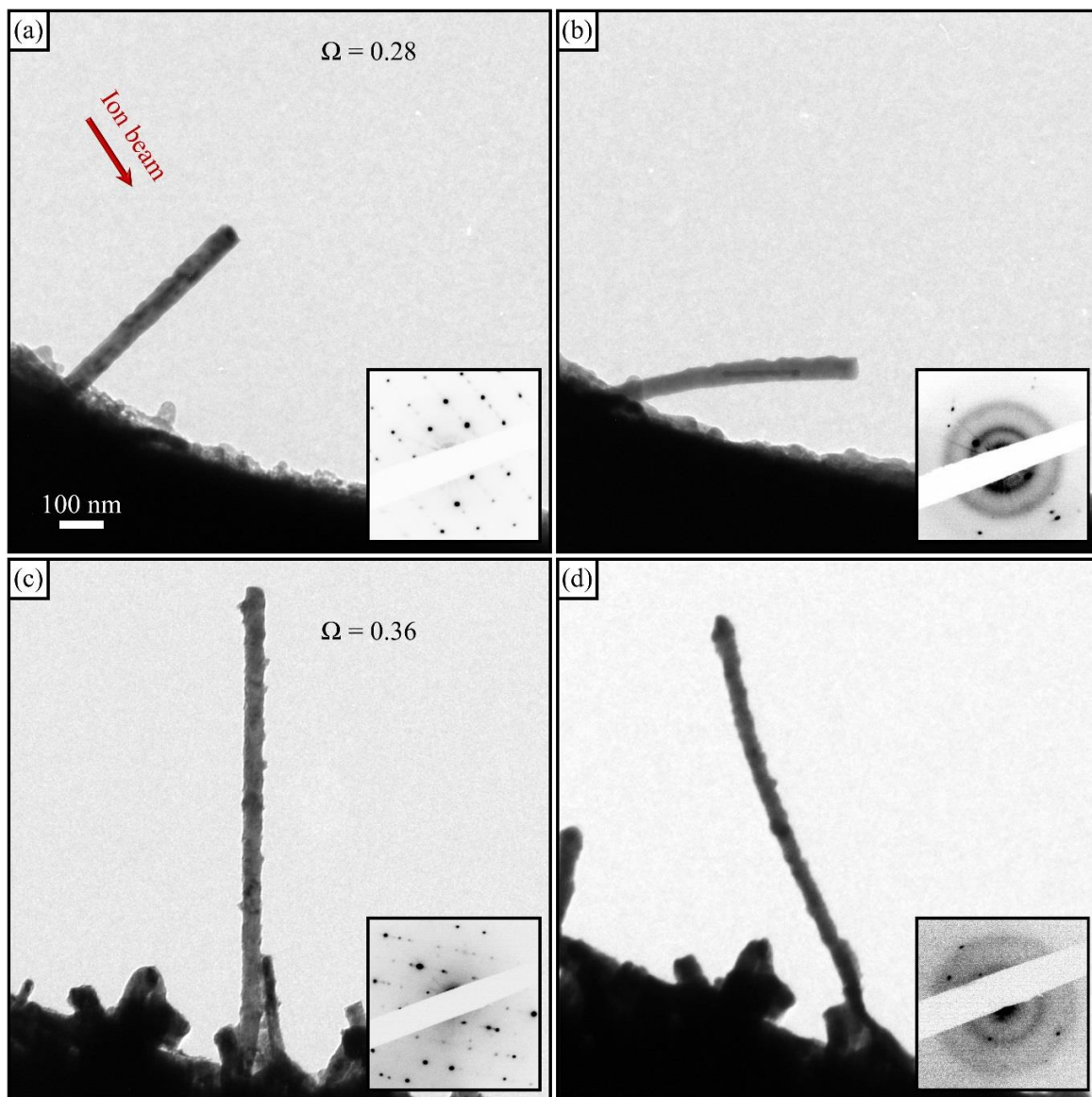


**Figure 5.1:** BF-TEM images and SADPs of (a) a germanium nanowire before a 30 keV xenon irradiation at RT and (b) after the irradiation at a fluence of  $3.3 \times 10^{14}$  ions.cm<sup>-2</sup> which has prompted IIB away from the ion beam. On the bottom row the BF-TEM images and the SADPs show (c) a germanium nanowire before a 30 keV xenon irradiation at RT and (d) after the irradiation at a fluence of  $3.9 \times 10^{14}$  ions.cm<sup>-2</sup> which has prompted IIB towards the ion beam. For each case,  $\Omega$  is given in (a) and (c). The projection of the ion beam onto the image plane is indicated by the red arrow in (a). The scale bar in (a) also applies to the other images in the figure. The conditions of irradiation of the nanowire in (a), (b) and in (c),(d) are resumed in table 1(xi) and (vi), respectively.

Similar IDRAGON calculations were performed for a total of 11 nanowire irradiations (including those shown in figure 5.1) and are summarised in table 5.1 which also gives the average diameter, the xenon ion energy used, the bending direction and the damage profile generated by IDRAGON. It is striking that all nanowires but one (which will be discussed below) follow a trend where the bending direction can be related to the damage profile. Indeed, nanowires with low  $\Omega$  ( $\leq 0.34$ ) have bent away from the ion beam whilst those with a higher  $\Omega$  ( $\geq 0.36$ ) have bent towards it. Consequently, it is evident that table 5.1 strongly suggests that the normalised damage depth  $\Omega$  is a crucial parameter for the bending direction and that a threshold value for reversing the bending direction is found around 0.35.

$\emptyset$ (nm)	$\alpha$ ( $^{\circ}$ )	Energy (keV)	$\Omega$	Bending direction	IDRAGON
i 18	37	70	0.54	Towards	
ii 43	26	70	0.46	Away	
iii 27	67	70	0.39	Towards	
iv 37	10	30	0.38	Towards	
v 51	42	70	0.38	Towards	
vi 39	20	30	0.36	Towards	
vii 40	31	30	0.34	Away	
viii 43	29	30	0.33	Away	
ix 48	1	30	0.33	Away	
x 40	44	30	0.31	Away	
xi 52	37	30	0.28	Away	

0 Maximum

**Table 5.1** The table summarises the experimental conditions and results obtained when 11 germanium nanowires were irradiated by xenon ion irradiation at RT. The colour scale under

the table is valid for all the IDRAGON profiles with “maximum” referring to the highest level of damage within each individual nanowire (i.e. not the maximum damage level across all 11 nanowires).

As illustrated by the image and SADP of the nanowire in figure 5.1(d), the nanowire has bent towards the ion beam but is not fully amorphous [243]. This constitutes an inconsistency with the mechanisms proposed in [20], [177], [184] (i.e. A modification of the density of the amorphous phase during irradiation and the ion hammering) which require that full amorphisation must occur for the nanowire to bend towards the ion beam. Indeed, it has been proposed that before full amorphisation of the nanowire the presence of a crystalline strip would preserve the rigidity of the nanowire and therefore prevent bending towards the ion beam [184]. In the work presented here, bending of nanowires towards the ion beam has been observed to occur immediately or rapidly after irradiation. In these cases, as the fluence is very low the nanowires must be crystalline at least in the region outside the damage range. For instance, the nanowire whose initial experimental conditions are summarised in table 5.1 (iv) rapidly bent towards the ion beam (at fluences lower than  $2 \times 10^{13}$  ions.cm<sup>-2</sup>). At this fluence, the region beyond the damage range ( $>0.38$  of  $\varnothing$ ) has a dpa of only 0.06, thus, well below the dpa at which amorphisation is expected to occur under these conditions [25], [244]. Consequently, as the nanowire was mostly crystalline when it started bending, the mechanisms based on amorphisation to explain the bending towards the ion beam (described in the literature review) cannot be regarded as valid for the bending of germanium nanowires.

To further investigate the other proposed mechanisms that could potentially explain the bending phenomenon, the case of nanowires which have bent towards the ion beam but that have most of the radiation damage closer to their irradiated side (i.e.  $\Omega < 0.5$ ) will be discussed in the following section.

### 3.1.2. Case of nanowires bending towards the ion beam whilst $\Omega < 0.5$

As discussed previously, a few mechanisms proposed in the literature are based on internal density changes occurring due to damage accumulation. In this subsection each of these proposed mechanisms will be considered (along with other consequences of ion irradiation which may similarly induce density changes) on nanowires where  $\Omega < 0.5$ . It will then be demonstrated that nanowires with  $\Omega < 0.5$  which in the current work were observed to bend towards the ion beam should in fact have bent away from it, if indeed, density-change-based mechanisms were to be invoked as the main driving mechanisms in operation.

Before considering the mechanisms proposed in the literature, the overall effect of Frenkel pairs must be considered (in contrast with the mechanism proposed by Borschel et al. [97], [114]. which is based on the way in which the point defects are distributed within the nanowire) as it can potentially induce an overall density change in the damaged region. As detailed in the literature review in chapter 3, there is a relaxation around point defects which can lead to a volume contraction or expansion depending on the type of defect (i.e. vacancies or interstitials, respectively) [86]. However, in germanium the amount of swelling around interstitials is considered to be either equal to or greater than the volume contraction around vacancies [52], [98]. For this reason, when  $\Omega < 0.5$ , if density changes due to point defects are considered as the only driving mechanisms for the bending of the nanowires the overall result would be swelling to the ion-beam-facing side. As stated in the literature review, a stress between a less-dense ion-beam facing side and the opposite side should lead to bending away [20], [97], [114]. Consequently, the result of such a mechanism operating in isolation would be opposite to that which has been observed in the work reported here: that bending towards the ion beam should occur for nanowires under initial conditions where  $\Omega < 0.5$ .

Similarly, a stress between regions of different density has been proposed by Romano et al. to explain the bending away from the ion beam [20]. The authors described how amorphisation localised on the ion-beam-facing side of the nanowire should induce a stress between the amorphous region and the crystalline region of the nanowire, and ultimately drive the nanowire to bend away from the ion beam. However, whilst this explanation is reasonable, several of the experiments presented herein have indicated otherwise. For instance, as shown by its SADP, the nanowire in figure 5.1(c) and (d), for which  $\Omega < 0.5$ , has become partially amorphous during the irradiation but has bent towards the ion beam until being aligned with it. This is in contradiction with the mechanism proposed in [20], showing that such a nanowire (with  $\Omega < 0.5$ ) should bend away from the ion beam due to the stress between the amorphous phase and the crystalline phase.

Similarly, a density change due to the presence of implanted ions should also lead nanowires having a ratio  $\Omega < 0.5$  to bend away from the ion beam, even though nanowires under these experimental conditions ( $\Omega < 0.5$ ) have instead been observed to bend towards the ion beam. An example of such behaviour contradicting the major role of the implanted ions in the bending effect can be demonstrated when analysing the nanowire shown in figure 5.1(c). As illustrated by figure 5.2 showing the IDRAGON-generated implantation profile of the nanowire in figure 5.1(c), most of the implanted ions are expected to be located in the ion-beam-facing side of the nanowire. They will thus, (assuming they do not diffuse out of the nanowire or otherwise significantly redistribute), lead to a volume expansion of the ion-beam-facing side and consequently make it bend away from the ion beam and not, as observed, towards the ion beam.

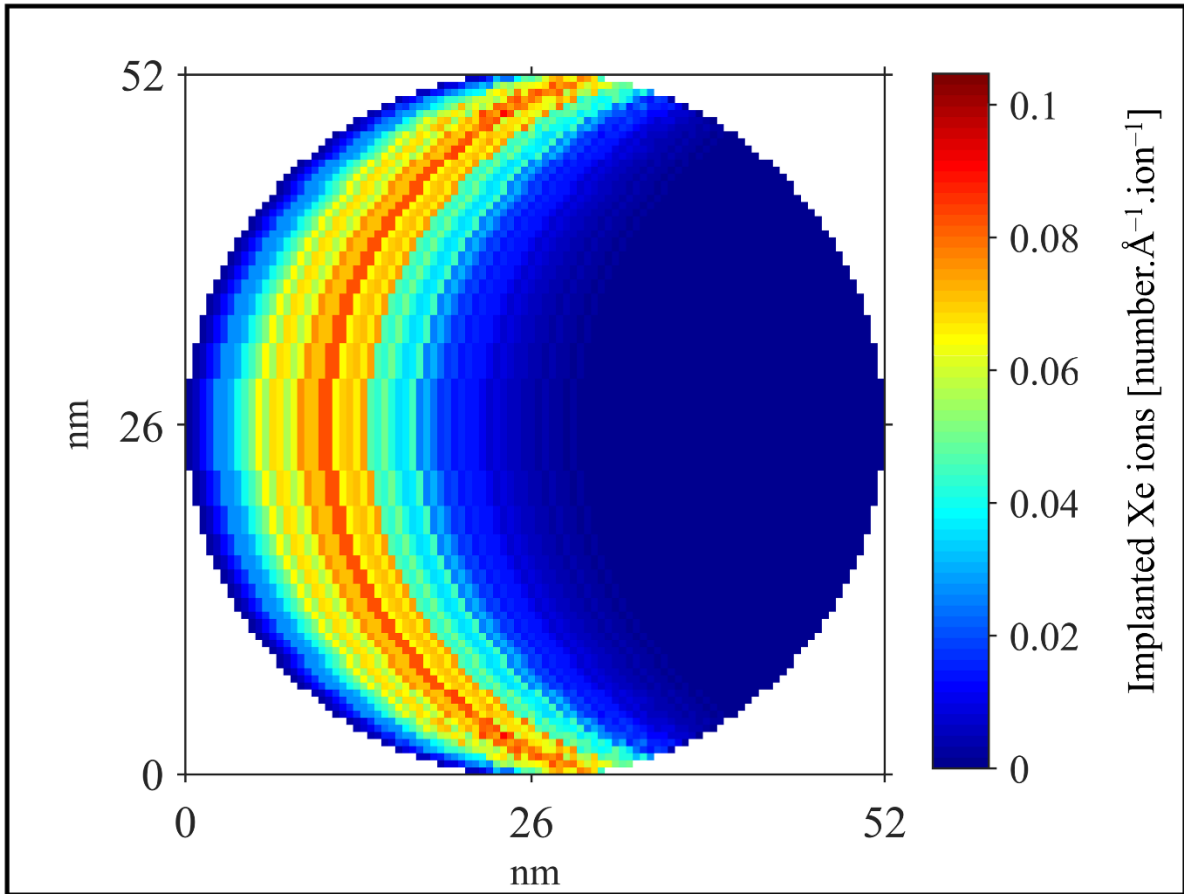


**Figure 5.2:** IDRAGON implantation profile of the nanowire shown in figure 5.1 under irradiation by a 30 keV xenon ion beam at  $\alpha=37^\circ$ .

Similarly to Romano et al. [20], an internal density change occurring during ion irradiation has been proposed as a cause for the bending by Borschel et al. [97], [114]. Indeed as detailed in the literature review, the authors described in [97] and [114] how the distribution of self-interstitials and vacancies induced by the ion beam can cause a density imbalance. However, in their experiments when the damage was produced mainly on the ion-beam-facing side of the nanowires, they were observed to bend away from the ion beam whilst they bent towards it when the damage was induced in the whole nanowire cross-section. Considering again nanowires like the one shown in figure 5.1(c), it can be observed that most of the damage is

located near the surface as evidenced by the IDRAGON profile in table 5.1 (vi), where  $\Omega = 0.36$ . In such a case, the separation of point defects is unlikely to generate the bending moment which would lead to the nanowire bending towards the ion beam. In fact, as stated in [97] and [114], the population of point defects which is almost entirely induced in the ion-beam-facing side of the nanowire might lead to a net excess of self-interstitials even though the irradiation induces Frenkel pairs. This excess has been said to be the result of ion-beam-induced sputtering [97], [114]. Indeed, as recoils may travel in the target material leaving vacancies closer to the irradiated surface, the sputtering (as it occurs relatively closer to the surface) is more likely to remove more material rich in vacancies than material rich in interstitials. This argument was proposed by Borschel et al. [97], [114] and detailed in the literature review chapter to explain how shallow irradiation should prompt nanowires to bend away as a result of the volume expansion in the front facing side of the nanowire [97], [114].

It is worth noting that in the case of the irradiations summarised in table 5.1(iv), where the nanowire had a value of  $\Omega < 0.5$  but still bent towards the ion beam the tilting analysis can be used to both determine  $\alpha$  before bending and thus provide information regarding its evolution during the bending, (thus revealing how the range of the damage would have evolved once the nanowire started to bend). Before irradiation the nanowire in table 5.1(iv) is inclined with an angle of  $5.3^\circ$  upwards (towards the electron beam) and its configuration is such that at the beginning of the irradiation both its motion relative to the z-axis (i.e. an upward bending in the TEM) and its motion in the xy-plane (i.e. relative to the motion of the projection of the nanowire in the image plane) would reduce the average damage depth in this nanowire. Consequently, as soon as the bending started the range of the ions started to be even more reduced thus enhancing the conditions which according to the mechanisms stated above, should have made the nanowire bend away from the ion beam as proposed by both Romano et al. [20] and Borschel et al. [97], [114] instead of towards it as observed in the work presented here.

To conclude, the way in which all the mechanisms based on radiation damage induce density changes should have made nanowires having values of  $\Omega < 0.5$  bend away from the ion beam have been described above. Therefore, the observation that they have instead bend towards is at odds with all of these proposed mechanisms. As these do not explain the bending of the nanowires towards the ion beam, the only valid mechanisms proposed so far in the literature as an explanation for such bending are those based on dynamic damage rearrangement proposed in [122], [175], [176], [178]. However, it must be stated that the mechanisms so far proposed in the literature and based on density changes cannot be entirely dismissed and that the influence they may have on the bending of nanowires will be addressed below.

### 3.1.3. Competition of mechanisms

The previous chapter has provided strong indications that IIB away from the ion beam at RT was due to damage accumulation and thus could be the consequence of the proposed mechanisms based on density changes. However, as discussed above, germanium nanowires may bend towards the ion beam mainly via mechanisms based on surface and near-surface rearrangement of atoms. The influence of several mechanisms on the bending of nanowires is of utmost importance as a competition between different mechanisms may dictate the IIB direction of irradiated nanostructures depending on which is the dominant mechanism.

As the experiments reported here were performed in situ in a TEM, they allowed the monitoring of the bending direction in real-time. From the video recordings, it can be seen that in some instances the nanowires seemed to “hesitate” between bending in a continuous direction at the beginning of the ion irradiation. When the irradiation was started, these nanowires were observed to “tremble” under the action of the ion beam or to briefly bend in one direction before reversing. Such an example is shown in the still frames taken from a BF-TEM video in figure 5.3(a)-(c) where a 40 nm diameter nanowire was irradiated by a 30 keV xenon ion beam. It can

be seen in this figure that the nanowire first bent towards the ion beam as shown in figure 5.3(b) before permanently bending away from it at higher fluences as shown in figure 5.3(c). The nanowire in this figure was irradiated under conditions where  $\Omega$  at the beginning of irradiation was 0.31. In fact, all the nanowires that seemed to “hesitate” before assuming a definite bending direction had  $\Omega$  between 0.31 and 0.36. It can therefore be suggested that these values of  $\Omega$  (being close to the tipping point where the bending direction reverses between away or towards the ion beam) are also the values at which the competition between the mechanisms is more clearly visible as they lead to the bending “hesitation” of the nanowires. It can be argued that, because  $\Omega$  only represents the initial experimental conditions, the reversal of bending is due to the change of  $\alpha$  and thus of the damage range during bending. However, during the reversal of the bending direction, the nanowire seems to come back to its initial position (and inclination) and still keeps bending away. For this reason, the evolution of the damage range cannot alone be responsible for the bending reversal. Instead, the irradiation may modify the structure in a way which has slightly favoured conditions for bending away, or “unfavoured” conditions for bending towards the ion beam, thus leading to the bending reversal.

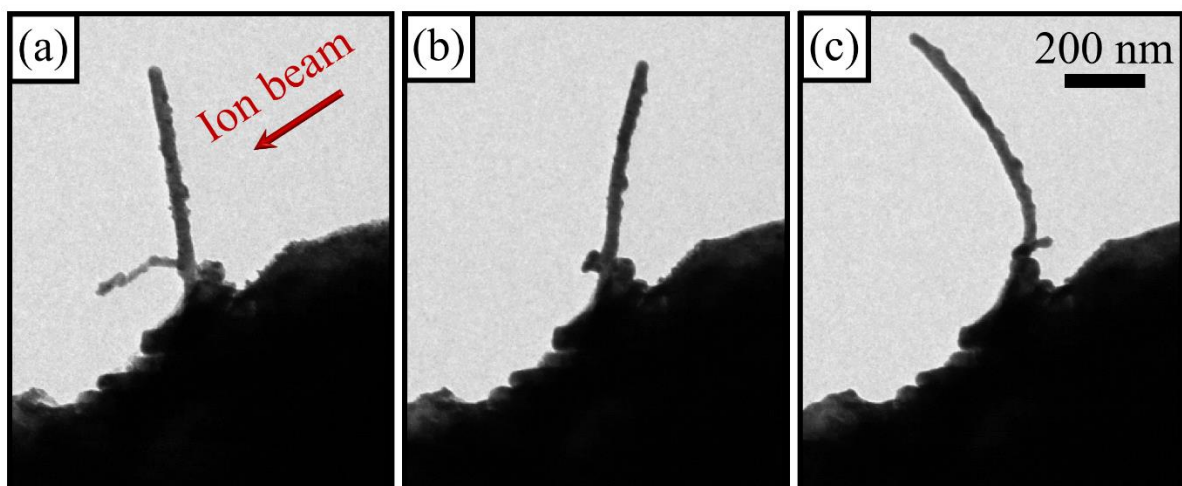


**Figure 5.3:** BF-TEM images of (a) a germanium nanowire before 30 keV xenon irradiation at RT, (b) after irradiation at a fluence of  $1 \times 10^{14}$  ions.cm<sup>-2</sup> which has prompted IIB towards from the ion beam and (c) at a fluence of  $3 \times 10^{14}$  ions.cm<sup>-2</sup> showing that the nanowire bending direction has changed during subsequent irradiation as it then bends away from the ion beam. The projection of the ion beam onto the image plane is indicated by the red arrow in (a). The scale bar in (a) also applies for the other images in the figure. The ratio  $\Omega$  illustrating the initial condition of irradiation corresponds to a value of 0.35 and is thus close to the threshold value for bending direction reversal.

As stated above, when the range of the ion is low, damage accumulation may induce both the presence of a crystalline phase and an amorphous phase in the nanowire. For instance, the presence of both these phases is evidenced by the SADP of the nanowire shown in figure 5.1(b) and by the DF-TEM shown in figure 5.4. As the nanowire must have bent away from the ion beam due to the stress between the two phases there is a similarity with the situation where bending occurs in structures made of thin films deposited on a substrate. Indeed, bending of such bimaternal (i.e. material made of the combination of a substrate and a thin film) has been reported as occurring due to the juxtaposition of two materials with different densities [245]–[247], similarly to the mechanisms based on internal density differences proposed to explain

nanowires bending away [20], [97], [114]. To consider the bending of thin films (having a radius of curvature,  $r$ ), the stress and the strain can be quantified using the Stoney equation 5.1 which depends on the thickness ( $t$ ), Young's modulus ( $E$ ) and Poisson's ratio ( $\nu$ ) of the substrate and the film as shown in figure 5.5 [248]. Therefore, quantifying the forces ( $\sigma$ ) behind the bending of the nanowire using the Stoney equation (or a modified version as in [20]), and replacing the terms relating to the film and the substrate ( $t, E, \nu$ ) for those of the two phases in the nanowire may seem like a sensible thing to do; however, as will be addressed below, doing so may require too many simplifications of the problem.

$$r = \frac{E_s \times t_s^2}{(1-\nu)_s \times 6 \times \sigma_f \times t_f} \quad (5.1)$$

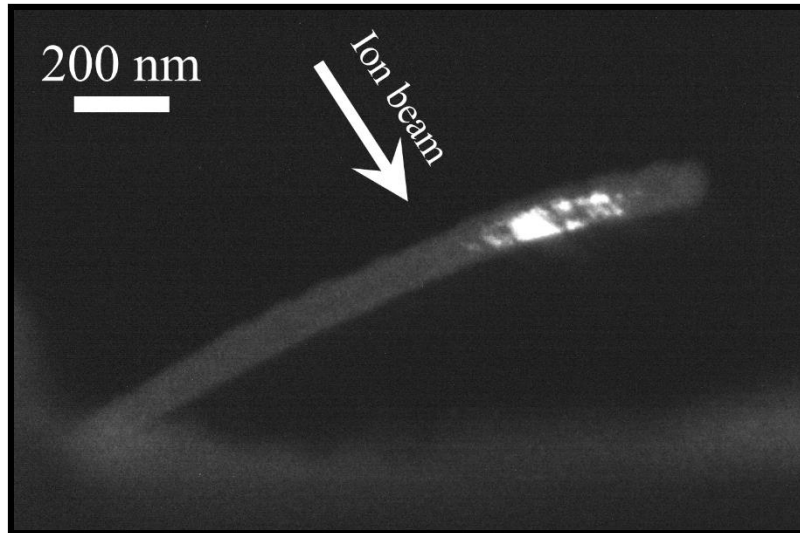


**Figure 5.4:** DF-TEM image of a germanium nanowire after a 30 keV xenon irradiation at RT to a fluence of  $4.7 \times 10^{14}$  ions.cm<sup>-2</sup> which has prompted IIB away from the ion beam. The presence of a crystalline structure is evidenced by the bright features. The nanowire was single crystalline before irradiation (as shown by its SADP in figure 5.1(a)). On the ion-beam-facing side, the nanowire is dark all along its length in the DF image even in the vicinity of the bright section – thus suggesting that the side facing the ion beam is fully amorphous as a result of the damage accumulation due to the xenon ion beam irradiation. The projection of the ion beam onto the image plane is indicated by the white arrow.

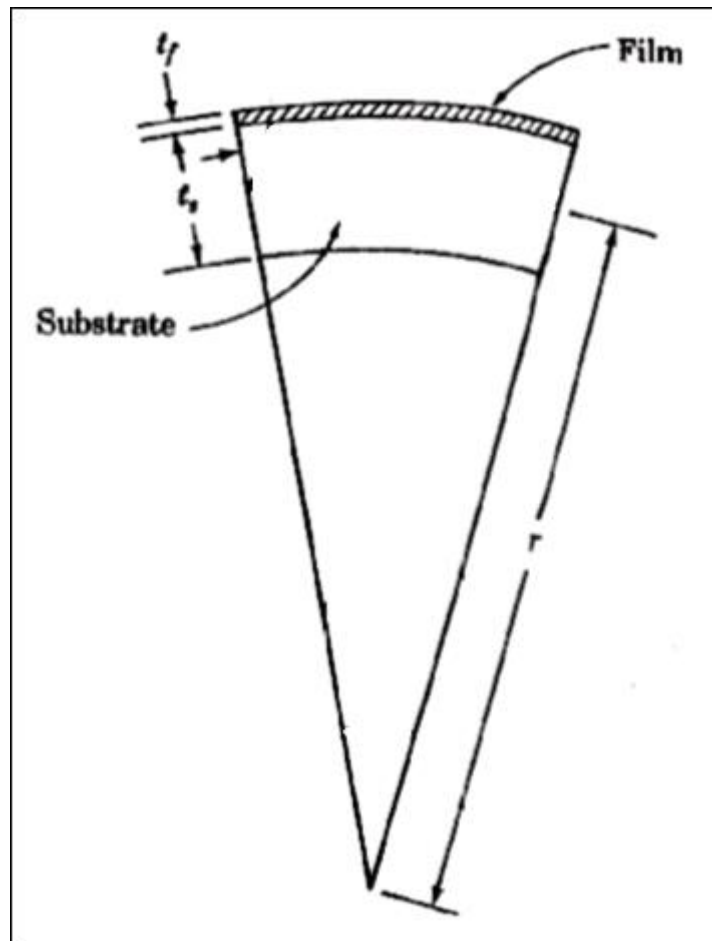


**Figure 5.5:** Schematic of the bending of a thin film and its substrate. On the figure the variables (described in the text) required for the calculation via the Stoney equation are based on two distinct portions, which are the thin film and the substrate. However, as stated above, in a nanowire the two distinct portions must be replaced by two phases of the irradiated nanowire for which properties and thickness are difficult to determine and which will evolve during the irradiation. From [248].

In the Stoney model, which is illustrated in figure 5.5 and equation 5.1, the radius of curvature,  $r$ , can be expressed as a function of Young's modulus,  $E$ , and the Poisson ratio,  $\nu$ , of the two phases whose densities differ. However, these variables (i.e.  $E$  and  $\nu$ ) would be difficult to define in the case of a nanowire. For instance, even if the thickness of each phase could be

determined precisely via DF-TEM image mode, the density of the ion-beam-facing-side of the nanowire might evolve during irradiation. Indeed, the ion-beam-facing-side of the nanowire might be of different nature depending on the fluence as it can become a damaged crystal, be made of a mix of the amorphous phase and highly damage crystal or at higher fluence be an amorphous phase [27], [117], [125]. Furthermore, as stated in the literature review in chapter 2, the properties of amorphous germanium are particularly complex as the nature of the amorphous phase can evolve during irradiation and even take on a sponge-like structure [121], [134], [249]. Furthermore, as the equation only considers the effect of the two phases on the curvature of the material, a modification of an equation such as equation 5.1 may need to be done in order to take into account other forces arising from competing mechanisms (which in this work are suspected to be the result of dynamical rearrangements of the defects induced during irradiations).

According to table 5.1, the tipping point value of  $\Omega$  at which the irradiation will drive the bending away from or towards the ion beam is between 0.34 and 0.36. However, some of the reasons which make the use of Stoney equations inaccurate also make this value valid only for relatively similar irradiation conditions. Indeed, the density changes due to damage accumulation are necessarily related to the ion used; different ions do not produce the same types of defects and the same amount of dynamic annealing even when they have the same range [116], [250]. For instance, light ions will tend to generate fewer clusters of defects than heavy ions and the heaviest ions might even directly induce amorphous pockets in a single ion strike [27], [116]. Furthermore, electronic energy loss also differs depending on the ion species and might lead to a dynamical annealing of the defects thus affecting bending mechanisms based on damage-induced density changes and based on dynamical surface rearrangement [25], [133]. It is worth noting that the type of defects and their dynamic annealing induced during the ion irradiation might also depend on the energy used during irradiation, thus altering the

threshold value of  $\Omega$  [116]. For these reasons, even if the threshold value has been determined for a particular range of experimental conditions, a reassessment might be necessary to refine it for significantly different ion masses and energies.

An example of the influence of the irradiation conditions on the threshold  $\Omega$  can be found by comparing the work of Romano et al in [20] and the present experiments. In their publications they irradiated single crystalline germanium nanowires with gallium ions at 30 keV at an initial angle  $\alpha = 45^\circ$ . Via IDRAGON, a comparison of their experimental results and those reported in the work presented in this chapter has shown that the dissimilarities regarding the experimental conditions have resulted in a difference in the behaviour of the germanium nanowires. In the work by Romano et al. [20] the nanowires bent towards the ion beam when  $\Omega$  was 0.32. At this value, according to the present work, if the germanium nanowires irradiated here with xenon ions were under this relatively low  $\Omega$  value, they would have bent away from the ion beam. Therefore, it can be proposed that  $\Omega$ , in addition to being a powerful way of forecasting the bending direction, might also be indicative of the type of damage and/or dynamic annealing induced by the ions as the threshold value of  $\Omega$  may depend on these factors. It is worth noting that for obvious reasons the value of the ratio will also change depending on the irradiated materials as damage accumulation will be impacted by the nature of the material. Lastly, because there are mechanisms involved in the IIB phenomenon which are correlated with the rearrangement of defects at the surface of the material, it is highly possible that the nature of the surface also influences the bending direction. In fact, it has been reported that both the build-up and the release of stress can be altered by the nature of the surface (i.e. surface roughness, surface contamination etc.) [251]–[253]. Therefore, in the current work, the surface of some nanowires may have influenced the bending direction. For instance, one could speculate that the only nanowire which did not follow the trend related to  $\Omega$  (nanowire (ii) in table 5.1) might have been subject to such surface effects.

## 3.2. Annealing of nanowires bent via IIB

### 3.2.1. Annealing of fully amorphous nanowires

Figure 5.6(a) and (b) present the BF-TEM images and SADPs of a germanium nanowire before and after irradiation by a 30 keV xenon ion beam at RT, respectively. As demonstrated by the SADP, the nanowire, which was a single crystal before irradiation, became fully amorphous after irradiation to a fluence of  $7.3 \times 10^{13}$  ions.cm<sup>-2</sup> and bent towards the ion beam as shown in figure 5.6(b). After the irradiation, the sample was heated to a temperature of 440°C in order to induce SPEG in the event that a remaining crystalline seed had been shielded by the TEM grid (or otherwise) at the base of the nanowire and was thus not bombarded by the ion beam (but also not detected in the SADP). However, as shown in figure 5.6(c), the BF-TEM image and SADP after 25 minutes of annealing indicated that the nanowire morphology and its microstructure did not evolve as it remained bent and fully amorphous. As the temperature of annealing was substantially above the minimum temperature at which SPEG is activated ( $\approx 300^\circ\text{C}$  in bulk [26]) it can be assumed that the nanowire was indeed fully amorphous. However, at relatively higher temperatures than that required for SPEG, nucleation of crystalline seeds and growth may occur during annealing due to RNG [31]. As stated in the literature review in chapter 3, in the event of RNG the nanowire would have become polycrystalline and thus this experiment shows that the necessary minimum temperature for RNG was not reached at 440°C.

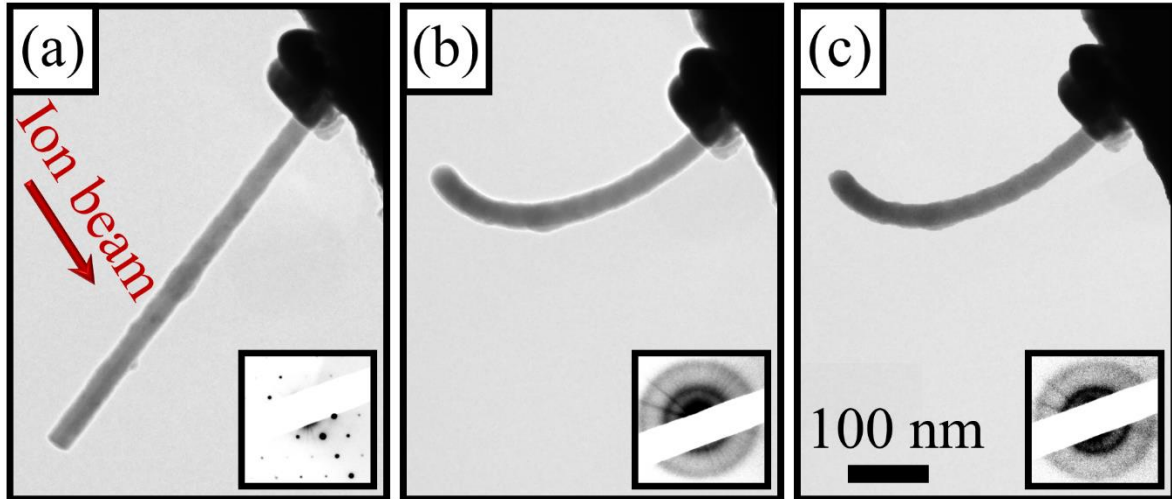


**Figure 5.6:** BF-TEM images and SADPs of (a) germanium nanowire before 30 keV xenon irradiation at RT and (b) after irradiation to a fluence of  $7.3 \times 10^{13}$  ions.cm<sup>-2</sup> which has prompted IIB towards the ion beam. The SADPs indicate that the nanowire was single crystalline before and became fully amorphous during irradiation. (c) Annealing at a temperature of 440°C was performed on the bent nanowire for 25 minutes. No noticeable change of shape was observed during the annealing and the SADP remained unchanged showing that neither SPEG nor RNG has been induced by the thermal treatment. The projection of the ion beam onto the image plane is indicated by the red arrow in (a). The scale bar in (c) also applies for the other images in the figure.

### 3.2.2. Annealing of partially amorphous nanowires

As most of the nanowires in the current work were only partially amorphous after IIB, annealing was able to recover a single crystalline character via SPEG. As shown below, the way the nanowires responded to this annealing treatment was dependent on their bending direction during IIB; however, a different behaviour was observed when annealing was

performed on partially amorphous nanowires that were bent away from the ion beam compared to those that were bent towards it.

### 3.2.3. Annealing of the partially amorphous nanowires which bent away from the ion beam

Figure 5.7(a) and (b) show the BF-TEM images and SADPs of a germanium nanowire before and after irradiation by a 30 keV xenon ion beam at RT, respectively. As can be observed from the SADPs, the nanowire which was a single crystal became partially amorphous after irradiation as evidenced by the coexistence of diffraction spots and amorphous rings. It can be seen in figure 5.7(b) that the nanowire has bent away from the ion beam.

In figure 5.7(c) the nanowire is shown after annealing at 440°C for 5 minutes. The SADP after irradiation illustrates that the annealing has been effective in inducing SPEG and the nanowire has recovered its single crystal character. Moreover, the nanowire shape has drastically changed as it regained its straightness. This change of shape during annealing was observed in all the partially amorphous nanowires which bent away from the ion beam; they recovered their single crystalline character and tended to become straight during the process. Sometimes, after annealing, they recovered a shape that was nearly the same as before irradiation as shown in figure 5.7.

As discussed above, these nanowires have most probably bent away from the ion beam as a result of damage accumulation (i.e. of point defects and amorphisation) which has induced a density change within the nanowires. However, during the heat treatment the damage can be repaired and the amorphous regions can become crystalline again. Consequently, it can be concluded that the density changes which were initially responsible for IIB away from the ion beam are reversed and the nanowire shape can thus be restored.

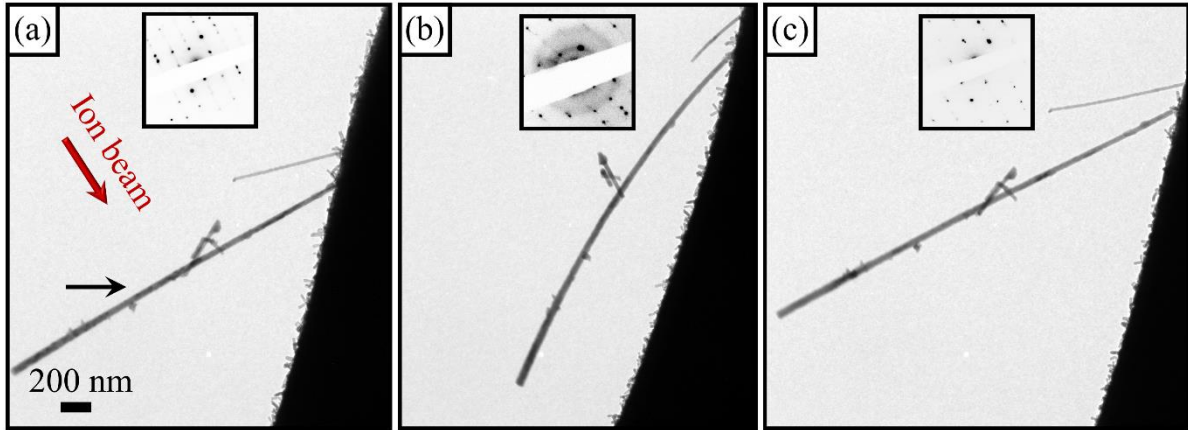


**Figure 5.7:** BF-TEM images and SADPs of (a) germanium nanowire (indicated by the black arrow) before a 30 keV xenon irradiation at RT and (b) after the irradiation to a fluence of  $9.1 \times 10^{13}$  ions.cm<sup>-2</sup> which caused IIB away from the ion beam. (c) Annealing at a temperature of 440°C was performed on the bent nanowire for 5 minutes during which time the shape of the nanowire changed becoming straight once more. The projection of the ion beam onto the image plane is indicated by the red arrow in (a). The scale bar in (a) is also valid for the other images of the figure.

#### 3.2.4. Annealing of the partially amorphous nanowires which bent towards the ion beam

Contrary to the experiments reported in [20] on the IIB of germanium nanowires where germanium nanowires bent only towards the ion beam when full amorphisation was reached, the nanowires in the current work bent towards the ion beam whilst remaining partially crystalline. Under the conditions used, performing a subsequent anneal allowed the recovery to a single crystal via SPEG. This behaviour is illustrated by an example showing the BF-TEM images and SADPs of a germanium nanowire in figures 5.8(a)-(c). The nanowire before irradiation is a single crystal and straight as shown in figure 5.8(a) and bent towards the ion

beam and became partially amorphous under irradiation as shown in figure 5.8(b). To better interpret the figure and avoid confusion regarding the bending direction, it must be specified that a smaller nanowire is attached to the tip of the main (longer) nanowire. The small nanowire is visible in the three BF-TEM images but is made more apparent after the main (longer) nanowire has bent. In figure 5.8(c) the SADP indicates that the annealed nanowire is polycrystalline. As will be explained below, the polycrystalline nature of the nanowire after annealing is related to the bent shape of the nanowire.

Indeed, the change of shape of nanowires during IIB at RT raises the question of how the microstructure evolves during this process. The possibilities of how the atomic planes might be oriented in the nanowire after being bent are shown in figure 5.9(a) and (b). After irradiation, the atomic planes of the bent nanowires might remain oriented in the same way relative to each other as before the bending. In this case as illustrated in figure 5.9(a), the crystallites within the nanowire will share the same orientation. Consequently, the regrowth from these crystallites via SPEG will result in a single crystal (with potentially a number of twinning defects). On the other hand, if as illustrated in figure 5.9(b), the crystal rotates as the nanowires bend then the crystallites within the nanowires can be highly misoriented relative to each other. In this case, the annealing would induce SPEG from many crystallite seeds that are misoriented relative to each other within the secondary amorphous phase – thus making the nanowires polycrystalline. Hence, considering that the nanowire shown in figure 5.8(c) was polycrystalline after SPEG, it can be concluded that the IIB has led to a misorientation of the crystallites in the nanowires before annealing. It is worth noting that the misorientation of the crystallites in the bent nanowire is expected considering results reported in [114] by Borschel et al. The authors performed HRTEM on a ZnO nanowire bent via IIB at three different positions along the nanowire axis. Using lattice imaging, they observed that at each of these three positions the crystal preserved its orientation with the nanowire axis even though the nanowire was bent

[114]. Thus, showing that similarly to the germanium nanowires shown here, the motion of the nanowire during bending also led to the motion of the crystal.

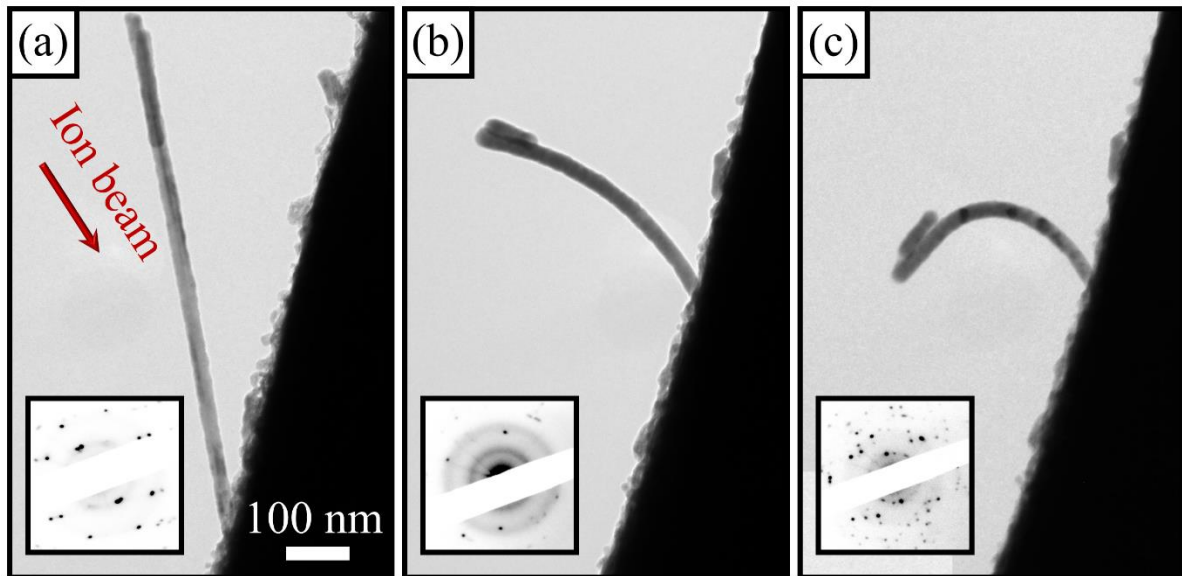


**Figure 5.8:** BF-TEM images and SADPs of (a) a germanium nanowire before a 30 keV xenon irradiation at RT and (b) after irradiation to a fluence of  $7.3 \times 10^{13}$  ions.cm<sup>-2</sup> which has prompted IIB towards the ion beam. The SADPs indicate that the nanowire was a single crystal and (b) became partially amorphous after irradiation. (c) Annealing at a temperature of 440°C was performed on the bent nanowire for 18 minutes during which the shape of the nanowire changed as the curvature increased during annealing. Additionally, as evidenced by the SADP, recrystallisation occurred during the thermal treatment making the nanowire polycrystalline. The projection of the ion beam onto the image plane is indicated by the red arrow in (a). The scale bar in (a) also applies for the other images in the figure.

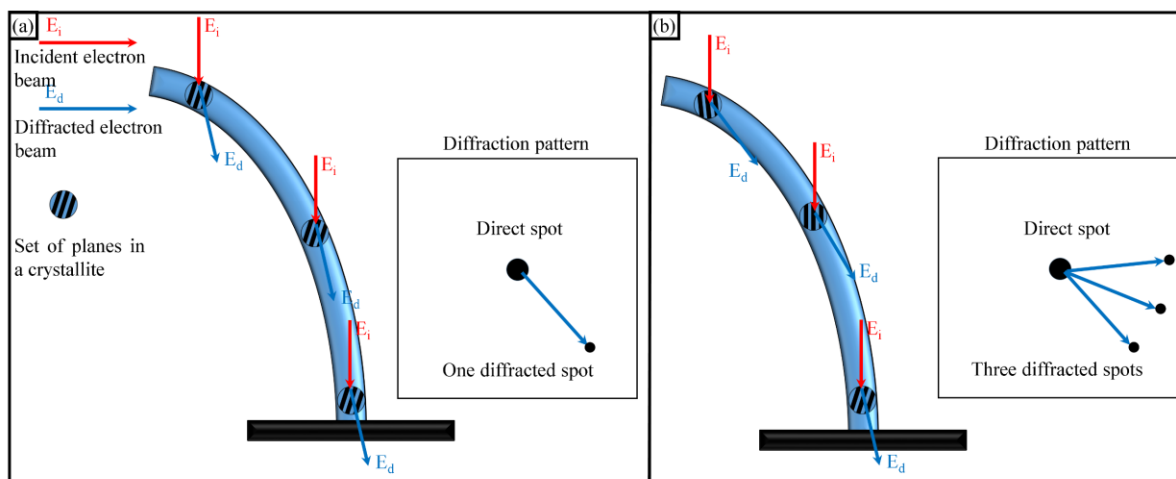


**Figure 5.9:** The orientation of crystallites relative to each other in a partially amorphous nanowire and the way it can impact the diffraction pattern is shown (a) in the case where the crystallites did not rotate during the bending, thus, making sets of planes in several crystallites parallel and consequently diffracting in the same fashion, whilst in (b) the crystallites have rotated during the bending making a similar set of planes misoriented relative to each other and consequently leading to a rotation of the diffracting spots from the crystallites. In order to make the figure clearer, only one diffracted beam is taken into account for each set of planes.

In figure 5.8(c) another crucial observation is that the nanowire has bent even more during annealing. However, in reality, the shape of the nanowire after annealing differs to what it would have been if it was further irradiated as the nanowire did not align towards the beam but has instead had an increase in its curvature. This behaviour during annealing also contrasts with that of nanowires which were initially bent away from the ion beam. As the mechanisms responsible for the bending of the nanowires towards the ion beam can be assumed to differ from the ones responsible for the nanowires bending away from it, a different outcome from the annealing process is not surprising. In the mechanisms based on surface energy reduction via dynamic rearrangement, the bending towards the ion beam is said to be the result of a

shrinkage of the surface exposed to the ion beam. Looking closely at figure 5.9(c), it can be seen that the annealing did not prompt a straightening of the nanowire nor an alignment of the nanowire towards the direction of the ion beam. Instead, interestingly, the annealing might have led to an increase of the shrinking of the surface which was initially facing the ion beam as this surface can be considered as the inner side of a bending beam. As detailed in the literature review, one of the phenomena that has been highlighted as potentially responsible for the rearrangement of irradiated surfaces during IIB is the heat deposited by the ion beam. The MD simulations reported in [122] which studied the IIB of silicon nanowires indicated that, after the impact of an ion, the rearrangement of the damaged surface and subsurface which led to bending occurs during the period where the temperature resulting from the heat spike was about a few hundred degrees Celsius. However, there is no reason that after the last ion has collided with the nanostructure all the damage making the surface unstable should be repaired. In fact, it is likely that the rearrangement will stop because the temperature resulting from irradiation has fallen below a certain threshold. Consequently, providing thermal energy to an irradiated nanowire may reactivate the rearrangement of the damaged surface and make it bend even more as appears to have been the case for the nanowire shown in figure 5.9(c).

#### 4. Conclusion, remarks and perspectives

In the work presented here, germanium nanowires were observed to bend either towards the ion beam or away from it. It is worth stating that, following this work, subsequent experiments were also performed using the MIAMI-2 system (under the same experimental conditions) but with the electron beam off and that the bending away from and towards the ion beam was still observed, thus, showing that the IIB could occur without the aid of the electron beam.

The correlation between the experimental results presented here and the MC calculations have shown that the bending direction of the nanowires was dependent on the average damage depth relative to the nanowire diameter,  $\Omega$ . Indeed, a threshold value of  $\Omega \approx 0.35$  has been identified for the reversal of the bending direction. Below this value, nanowires were observed to bend away from the ion beam whilst higher values led the nanowires to bend towards it. Consequently, future users of the IIB technique should consider the utilisation of such a ratio as it allows a reliable, yet simple, manner of forecasting the bending direction of nanowires, making IIB a more predictable tool for the manipulation of nanostructures.

This chapter has also confirmed what was suspected based on IIB experiments at elevated temperatures reported in chapter 4, that several mechanisms are involved in the IIB phenomenon. It has been concluded that the nanowires which bent away from the ion beam did so due to the dominance of damage accumulation leading to internal volume changes whilst bending towards the ion beam was mainly the result of the rearrangement of the damaged surface and subsurface during irradiation. As the nanowires are subject during irradiation to several mechanisms, it was proposed that the outcome of the competition between the mechanisms (reflected by the bending direction) depended on which mechanism(s) dominated. This opposition between mechanisms was more clearly illustrated when the irradiations were performed under conditions where  $\Omega$  was close to its tipping point value as the nanowires were observed to “hesitate” between bending direction and thus, between which mechanism would dominate.

As it was observed that the nanowires could remain partially crystalline after IIB towards and away from the ion beam, annealing was performed to induce SPEG. Interestingly, the behaviour of the nanowires during this process was correlated to the bending direction and could consequently be related to the mechanisms leading to the IIB. The nanowires that bent away from the ion beam may have straightened during the recrystallization due to the apparent

removal of the internal density variations and those that bent towards the ion beam during IIB may have bent even more due to activation of further surface rearrangement via the thermal energy provided during annealing.

Whilst chapter 4 has shown that IIB at elevated temperature could be used to align silicon and germanium nanowires whilst preserving their crystalline structures, this chapter has reinforced the findings of chapter 4 as it has now been shown that the alignment of germanium nanowires via IIB at RT could not sustain epitaxial recrystallisation. The experiments reported in this chapter have also shown that if the nanowires bend away from the ion beam (at low  $\Omega$ ) during IIB at RT then there is a way to recover their straightness. This could be particularly useful in situations where IIB is a deleterious effect of ion beam doping. However, whilst for the reasons stated above IIB towards the ion beam may often be a more convenient way of manipulating the nanowires than IIB away. The fact that IIB away is not stable during SPEG can be problematic as the bending away offers certain advantages compared to IIB towards. For instance, as shown in figure 5.10, when nanowires bend away from the ion beam they can attain a high degree of curvature and almost form loops. This shape is not readily achievable via IIB towards because, as stated in the literature review, the curvature of the nanowires saturates upon alignment with the ion beam.

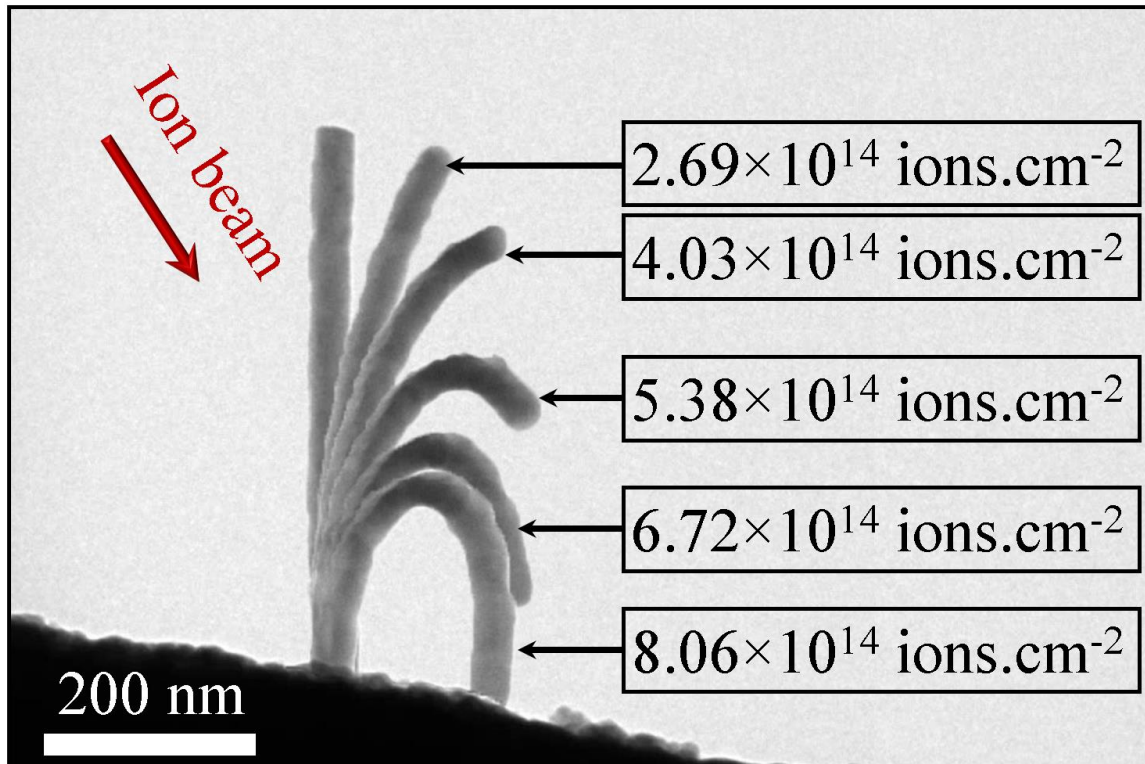


**Figure 5.10:** Superimposed BF-TEM images taken from an in situ video showing the evolution of a germanium nanowire during a 30 keV xenon ion irradiation at RT. The projection of the ion beam onto the image plane is indicated by the red arrow. The nanowire is shown to have bent away from the ion beam as the fluence increased. It is worth noting that the curvature of the nanowire has increased until the nanowire came into contact with the TEM grid.

In view of how sensitive nanowires are to both radiation and temperature, these experiments suggest that nanowires (and especially germanium nanowires) might be used as novel types of heat and radiation detectors if their deformation is finely correlated with the degree of radiation and/or heat received.

Furthermore, as stated in the previous chapter, the possible presence of strain within a nanowire can be of utmost importance. Indeed, residual strain might be expected in bent nanowires and

especially where  $\Omega$  is low. As the nanowire shown in the DF-TEM image in figure 5.4 demonstrates, such nanowires can be damaged and become amorphous on their ion-beam-facing side and yet be single crystalline on the opposite side. The lattice of the crystal may therefore be under some residual tensile strain which should be characterised in future work.

In these experiments, it has been concluded that different mechanisms dominate in the two opposite bending directions. Consequently, it might be postulated that under different experimental conditions these mechanisms may induce the nanowires to bend in the direction opposite to that reported here. For instance, at higher values of  $\Omega$  the radiation damage may induce the separation of self-interstitials and vacancies as proposed by Borschel et al. [97], [114] to induce bending towards the ion beam and their consequential alignment to it. On the other hand, it might be possible to perform experiments where the range of the ion is such that the surface rearrangement occurs on the rear side of the nanowire thus leading the nanowire to bend away from the ion beam contrary to that induced by the mechanism in the current work.

Another question concerns the fact that the fully amorphous nanowires did not bend more during annealing. As the temperature was not high enough to induce RNG, it might be important to know if such a transformation would occur at higher temperatures when crystals nucleate.

# Chapter 6: Amorphisation mechanisms in germanium

## 1. Introduction

Numerous studies have been reported regarding the amorphisation of silicon and its mechanisms [25], [27], [70], [125]–[127], [129], [254], [255]. For the past few decades, amorphisation mechanisms in silicon have been explored due to its technological relevance and because ion beam doping methods have often been used on this material during the manufacture of microelectronic devices [25], [256], [257]. As described in chapter 2, during the ion beam doping of a semiconductor the accumulation of defects may lead to amorphisation [84], [85], [258]. The processes leading to amorphisation can be complex and depend on several factors including the temperature of the target material (this has for instance been clearly shown in chapter 4 where the elevated temperature has prevented amorphisation of the germanium nanowires during ion irradiation), the ion used for the irradiation (as discussed in the literature review and suggested in chapter 5) and by the target material itself. Typically, the amorphous state of the implanted material is considered detrimental for the properties of transistors and an annealing step is often required [257]. However, a pre-amorphisation step before ion-beam doping is routinely performed intentionally as it facilitates the control of the dopant implantation depth by eliminating channelling effects [72], [73]. The pre-amorphisation step is usually performed via self-ion or inert-gas irradiation [72], [73].

Currently, the limitations of the silicon-based semiconductor technology present a challenge to develop new materials for future microelectronic devices [13], [259]. As stated in Chapter 2, germanium has been proposed as a replacement or as a complementary material in tomorrow's devices as the mobility of the charge carriers is higher than in silicon [34]. Furthermore, even more than now, on tomorrow's devices the control and characterisation of the damaged or

amorphous region are of paramount importance due to their reduced scale. For instance, the dpa at which amorphisation will be induced, the size and distribution of isolated amorphous regions as well as the depth and the thickness of amorphous material must be predictable as their impact on electronic properties will be even greater in these nanoscale transistors. It is worth noting that the comparison between the ability of different ions to make the target material amorphous is often made via the use of the threshold dpa for amorphisation [25], [133].

To fully predict how and when amorphisation will occur, the mechanisms behind it must be understood. Yet, whilst numerous studies related to amorphisation have been performed on silicon there is still no consensus regarding the mechanisms which lead to it [27]. As stated in the literature review, the main models which describe amorphisation are the homogeneous model, the heterogeneous model (and its modified version developed by Gibbon in [128]) and combinations of the heterogeneous and homogeneous models [23], [25]–[27], [89], [125], [127], [128], [145], [260].

As has been detailed in the literature review chapter, in the homogeneous model the structure is described as collapsing into an amorphous phase when the density of defects reaches a certain level [23], [26]. Typically, as the density of defects can be correlated to the nuclear energy deposited in the target material, the threshold for amorphisation can be described via the critical energy deposited per atom (i.e. the critical dose energy density ( $E_{dc}$ )) at which the material becomes amorphous) and can be described by equation 6.1 [26]:

$$\psi \cdot E_d(z) = E_{dc} \cdot \rho \quad (6.1)$$

The evidence of amorphous pockets during irradiation of semiconductors by heavy ions has pointed towards a mechanism based on the build-up of amorphous material via the

accumulation of amorphous pockets each of volume,  $V$ , and where the evolution of the amorphous fraction,  $f_a$ , during irradiation is described by equation 6.2 as a function of the ions per unit volume dose,  $D$  (in ions.cm<sup>-3</sup>) [25], [27].

$$f_a = 1 - e^{-V.D} \quad (6.2)$$

This heterogeneous model, referred to for clarity as the purely heterogeneous model in this chapter, is however considered unlikely to happen for lighter ions as they are less likely to induce amorphous pockets via a single impact. A modified version of this heterogeneous model has therefore been proposed by Gibbon et al. [128] in which the amorphous regions are induced after  $m$  overlaps of damaged regions of volume  $V$  [27], [116], [128]. Accordingly, the build-up of amorphous material can be described by equation 6.3.

$$f_a = 1 - \sum_{k=0}^{m-1} \frac{(V.D)^k}{k!} e^{-V.D} \quad (6.3)$$

Furthermore, it has recently been proposed that instead of an accumulation of either amorphous regions or crystalline damaged regions, amorphisation occurred via the accumulation of volumes  $V$  made of an amorphous core of volume  $V_a$  surrounded by a shell of crystalline but highly damaged material of volume  $V_d$  as shown in figure 6.1. In this scenario, amorphisation would result from the accumulation of volume  $V = V_a + V_d$  where  $V_d$  could become amorphous after  $m$  overlaps [145]. The evolution of the amorphous fraction,  $f_a$ , in this model, is described by equation 6.4 [145].

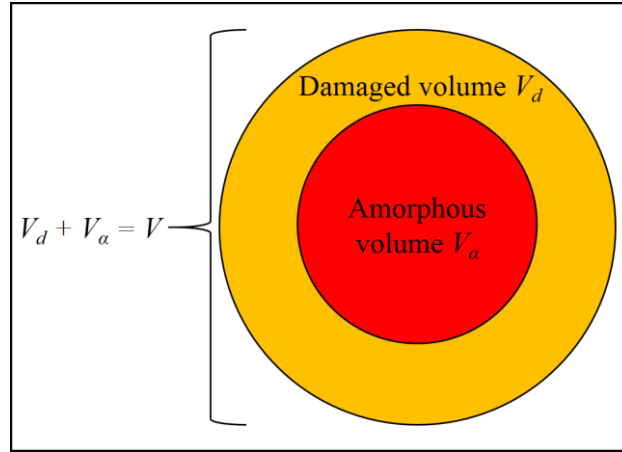


**Figure 6.1:** Schematic showing the cross section of a calculated volume  $V$  made of an amorphous core  $V_\alpha$  (in red) and a crystalline damaged region  $V_d$  (in orange) requiring  $m$  overlaps to become amorphous.

$$f_a = 1 - e^{-V_\alpha \cdot D} e^{-V_d \cdot D} \left( 1 + \sum_{k=0}^m \frac{(V_d \cdot D)^k}{k!} \right) \quad (6.4)$$

It is important to note that if amorphisation occurs only via the accumulation of amorphous regions due to single ion impacts then  $V = V_\alpha$ ,  $m = 0$  (i.e. there is no overlap) and then equation 6.4 becomes equation 6.2. On the other hand, if amorphisation occurs only via the accumulation of clusters of defects  $V = V_d$ ,  $m \neq 0$  and equation 6.4 is thus equivalent to equation 6.3.

The four mechanisms described above (and in the literature review) lead to different evolution of the amorphous fraction  $f_a$  which can be illustrated by figure 6.2 [125]. It shows examples where, for all mechanisms, the target material becomes amorphous at the same fluence and where the value of  $V$  in equation 6.4, 6.3 and 6.2 is also similar, thus meaning that in the figure the heterogeneous amorphisation occur via accumulation of amorphous zones of the same volume.

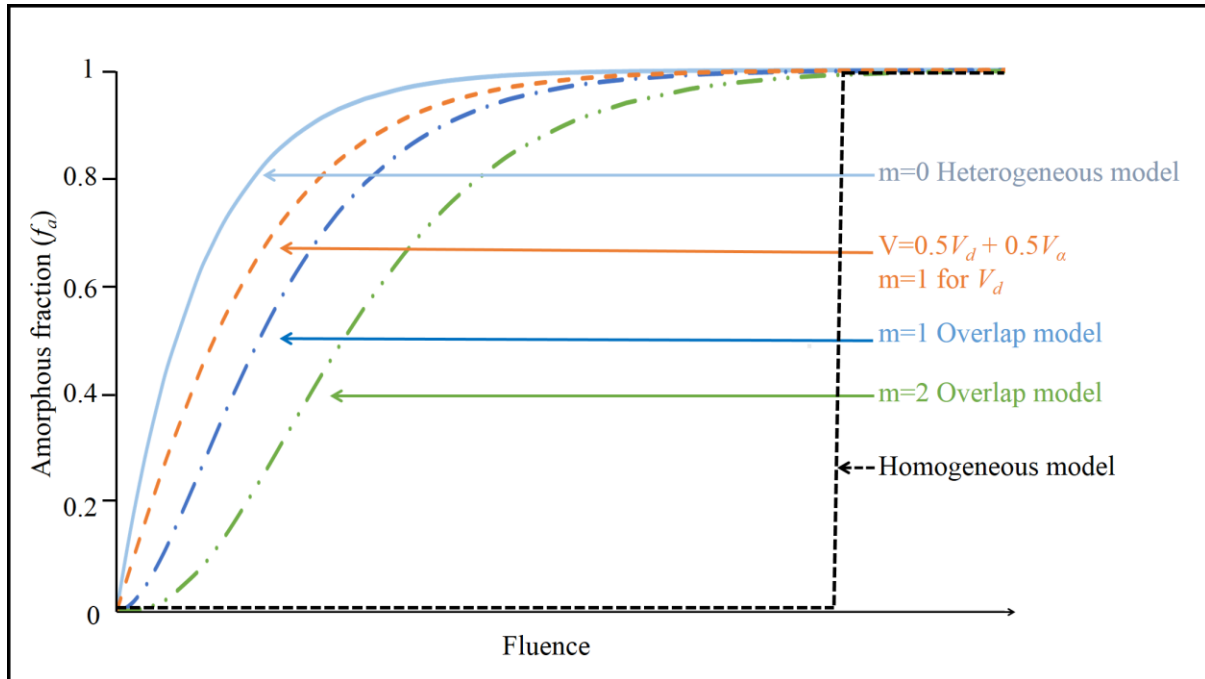


**Figure 6.2:** Evolution of the amorphous fraction as a function of fluence for different amorphisation mechanisms. In this simple illustration, the target material is considered fully amorphous (i.e.  $f_a = 1$ ) at the same fluence for each mechanism. In the three heterogeneous models the curves have been generated using equation 6.4 whilst keeping the value of  $V$  similar whether  $V = V_a$ ,  $V = V_d$ , or  $V = V_a + V_d$ .

As germanium is considered as an important material for future semiconductor devices [34], a set of experiments has been designed to better understand the mechanisms behind amorphisation, to provide a robust data set on the dose and dpa required to fully amorphise germanium. Furthermore, even though as detailed in chapter 2, lighter ions induce less damage than heavier ones under similar conditions [116], [117], the results reported in the current chapter reveal unexpected outcomes. Indeed, unlike what is typically observed [25], [125], [132], [133], [141], these experiments have shown that a lighter ion can induce a lower (or similar) dpa threshold for amorphisation than a heavier ion under conditions where the damage

rate ( $\text{dpa}\cdot\text{s}^{-1}$ ) and the ion range are the same. Consequently, this chapter will also aim at elucidating these intriguing experimental results.

In order to do this, during the experiments, germanium samples have been irradiated by an inert gas and the evolution of  $f_a$  has been monitored via SADPs. The irradiations have been performed using all the non-radioactive inert gases, thus, covering a large range of ion masses (i.e. from 4 to 132 amu) to provide information on how the mass of the ion affects the amorphisation process. Furthermore, by correlating the experimental results with equation 6.1, equation 6.4 and with the modified version of IDRAGON which allows the modelling and analysis of the 3D collision (as described in chapter 3), further insights into the mechanisms behind amorphisation have been gained. As will be addressed in the discussion, this work also demonstrates how the stochastic nature of the collision cascade is key to the build-up of amorphous material during irradiation by helium ions.

## 2. Experimental methods

Single crystalline germanium samples were mechanically polished using a dimpler and subsequently thinned to electron transparency using a PIPS as described in chapter 3. The samples were irradiated in the MIAMI-2 facility using 300 keV xenon, 200 keV krypton, 100 keV argon, 80 keV neon or 70 keV helium ions and were measured to have a thickness of 30, 23, 19, 23 and 23 nm, respectively, (the measurements were carried out using EELS spectroscopy as in [219] and as described in chapter 3). For reasons that will be addressed below, the energies for irradiation were selected such that the range of the ions was substantially larger than the specimen thickness, furthermore the ion ranges were relatively close for the specimens irradiated with xenon, krypton, argon and neon ions. Furthermore, the fluxes were chosen so that, for all irradiations, the damage rate was  $\approx 4.5 \times 10^{-4} \text{ dpa}\cdot\text{s}^{-1}$ . The samples were irradiated at approximately  $18.7^\circ$  from the [111] direction, thus avoiding

channelling effects. The SADPs of the samples were also taken at a direction parallel to the incident ion beam to confirm that the ion irradiations were not incident along low indexes directions.

The crystallinity of the samples was monitored between each irradiation step using the SADPs, thus following the progress of amorphisation. For the acquisition of the SADPs, the samples were carefully tilted to exactly the [111] down-zone condition. Because electron irradiation has been reported to retard or prevent amorphisation [153], [154], the electron beam was only briefly allowed to irradiate the sample during the capture of the SADP between each ion irradiation step. Furthermore, the TEM was operated at an acceleration voltage of 200 kV as such an acceleration voltage has been reported in [153], [154] to minimize recrystallization of germanium under a TEM electron beam.

For each experiment, both the area selected for the SADP and the lens settings were kept constant throughout. Indeed, as the intensity within the SADP was used to probe the amorphous state of the sample, it is important to exclude any effects (other of than those of the ion irradiation) that could result in a change to the intensity detected. As the information within the SADP obviously depends on the area selected, this area must be kept constant during irradiation. Similarly, changing the lenses setting could induce a change in the electron beam intensity, thus leading to an artefact regarding the evolution of the intensity of the amorphous rings in the SADPs.

The amorphous ring intensity is representative of how amorphous a sample is [25], and so was monitored to calculate the amorphous fraction  $f_a$ . The specimen were deemed to be amorphous when no diffraction spots were visible in the SADP and only the amorphous rings were observed in DigitalMicrograph [261], at which point the irradiation was continued (at a minimum, 12 percent above the fluence at which the diffraction spots were no longer visible)

to ensure full amorphisation of the samples. The intensity of the amorphous rings was determined from the raw data via the radial density function plugin in software routinely use for the analysis of TEM micrographs (ImageJ) [262].

The modified version of the IDRAGON code which, as stated in chapter 3, allows the analysis and the 3D modelling of collision cascades in planar targets, was used to determine some of the characteristics of the collision cascades for each irradiation conditions. As stated in chapter 3, using SRIM, the code allows tracking of the incident ion as well as the recoils thus providing information on how the damage is introduced into the material. In the code, for each irradiation case (i.e. ion species), one ion at a time was considered and an algorithm was run to count the number of recoils in a cylindrical volume whose axis was centred along the ion beam direction and having a length equal to the thickness of the irradiated sample (determined via EFTEM during the experiments as described above). The recoils were counted within cylindrical volumes of different radii,  $r_x$ , ranging from 0.1 nm to a value large enough to include all the recoils induced by the ion, thus enabling the code to plot and determine the number of recoils in a cylindrical volume as a function of  $r_x$ . These operations (the reconstruction of the 3D collision cascades and the counting of the recoils) were executed for each ion species for 1000 collision cascades via the use of 1000 distinct seed numbers in SRIM. It is worth noting that this cylindrical approximation of the damaged volume previously used in [128], [129], [140], [263], [264] is justified by the fact that the thickness of the target materials were smaller than the ion range (as it is also the case in the work presented herein). For each irradiation condition, SRIM was additionally used as described in chapter 3 in order to determine the dpa and the ratio ( $S_e/S_n$ ) using 99,999 ions.

### 3. Results

As described above, the heterogeneous mechanism of amorphisation occurs via the accumulation of volumes  $V$ . After a single ion impact these volumes might be amorphous zones ( $V = V_a$ ), be highly-damaged crystalline volumes (i.e. cluster of defects) which require  $m$  overlaps to induce an amorphous zone ( $V = V_d$  and  $m \neq 0$ ) or consist of an amorphous zone induced by a single impact within an outer shell of highly-damaged crystal ( $V = V_a + V_d$ ). Swanson et al. determined the minimum defect density needed for the collapse of a damaged crystal into an amorphous phase [138]. The value calculated was in agreement with the work of Gibbons in [128], where the authors showed that in the overlap model applied to a germanium crystal, the collapse of a region of volume  $V$  into an amorphous phase indeed occurred when the defect density reached 0.02 of the atomic fraction [138]. Assuming that for each vacancy a self-interstitial is also induced, the vacancy density at which such a fraction is reached corresponds to  $0.442 \text{ vacancies.nm}^{-3}.\text{ion}^{-1}$  (0.01 of the atomic fraction).

As stated above, the modified IDRAGON code was used to determine the distribution of recoils in the collision cascade. Furthermore, as a recoil generates a vacancy and considering that most of the vacancies are not replaced due to replacement collisions, the 3D plot can effectively be considered as showing where the vacancies have been induced during irradiation. Consequently, using the aforementioned defect fraction the volume  $V_a$  can be determined via the analysis of the 3D plots as schematically illustrated in figure 6.3(a). An example of volume  $V_a$  determined by this method is shown for the xenon case in figure 6.3(b). As shown in table 6.1, the results indicate that an amorphous region of volume  $V_a$  may have been formed for each irradiation case except for helium ions. Indeed, in the calculation corresponding to the helium case, the number of recoils induced on average by each helium ion is too low ( $3 \text{ recoils.ion}^{-1}$ ) to form such amorphous regions.

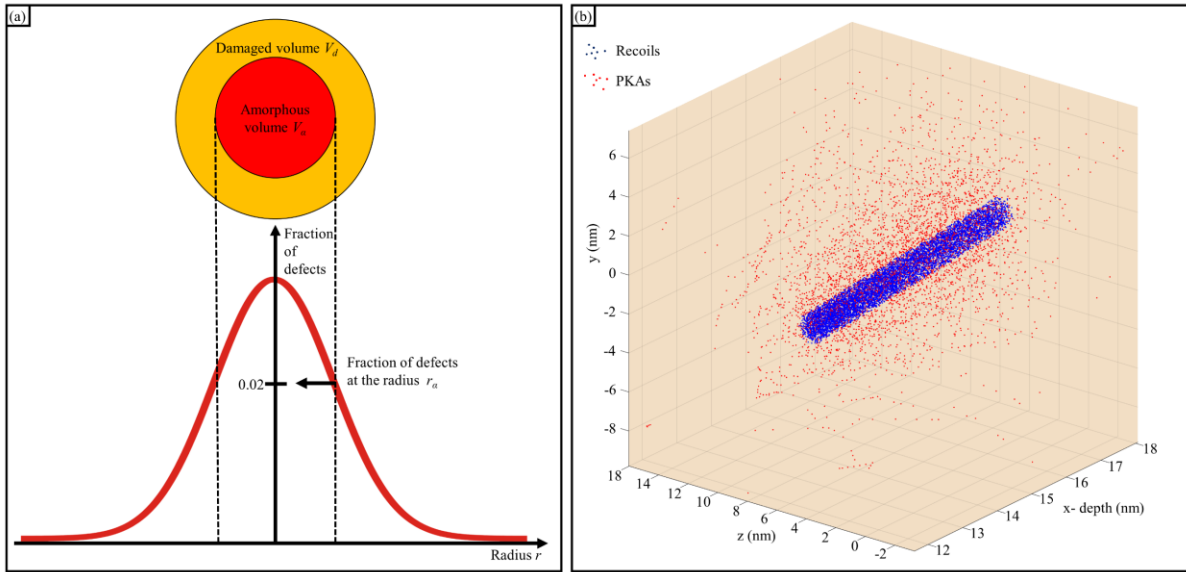


**Figure 6.3:** (a) Schematic showing how  $V_\alpha$  is determined based on the defect densities distribution indicated by the red line and (b) example showing a section of the 3D plot of the recoils within  $V_\alpha$  and the PKAs after irradiation by 300 keV xenon ions, where all the recoils within  $V_\alpha$  are indicated by a blue spot and the PKAs are shown by a red spot. The plot shown in (b) is generated after 1000 ions.

Ion	Total average number of recoils (recoils.ion <sup>-1</sup> )	<i>m</i>	<i>V<sub>a</sub></i> (nm <sup>3</sup> )	<i>V<sub>d</sub></i> (nm <sup>3</sup> )	Threshold dpa	<i>S<sub>e</sub>/S<sub>n</sub></i>	Fluence at full amorphisation (ions.cm <sup>-2</sup> )
Xenon	1595	1	108	700	0.37±0.02	0.63	3.0 × 10 <sup>13</sup>
Krypton	768	1	55	400	0.32±0.02	0.65	4.2 × 10 <sup>13</sup>
Argon	294	<i>m</i> = 1 or <i>m</i> = 2 (Fitting equivalent)	9	45 when fitted using <i>m</i> = 1 78 when fitted using <i>m</i> = 2.	0.72±0.04	1.03	1.8 × 10 <sup>14</sup>
Neon	147	2	2	38	0.83±0.04	1.51	5.1 × 10 <sup>14</sup>
Helium	3	3	0	0.17	11.3±0.6	40.67	3.5 × 10 <sup>17</sup>

**Table 6.1:** For each case, as well as the average total number of recoils per ion determined by SRIM are shown the value of *m* determined via the correlation between the experimental results and equation 6.4, *V<sub>a</sub>* determined via the MATLAB analysis of the collision cascades using the theoretical defect fraction for amorphisation, *V<sub>d</sub>* determined via the correlation between the experimental results and equation 6.4, the threshold dpa for amorphisation and the fluence at full amorphisation were determined using the experimental results (i.e. the SADPs) and *S<sub>e</sub>/S<sub>n</sub>* as given by SRIM.

After sufficient irradiation, all samples could be rendered fully amorphous and an example of the evolution of the SADP is shown in the case of the sample irradiated by xenon ions in figure 6.4. The pristine crystal structure is illustrated by the SADP in figure 6.4(a), at an intermediate fluence where the sample was partially amorphous (as evidenced by the presence of both the diffraction spots and the amorphous rings) in figure 6.4(b) and when amorphisation was completed (as evidenced by the presence of only amorphous rings) in figure 6.4(c).

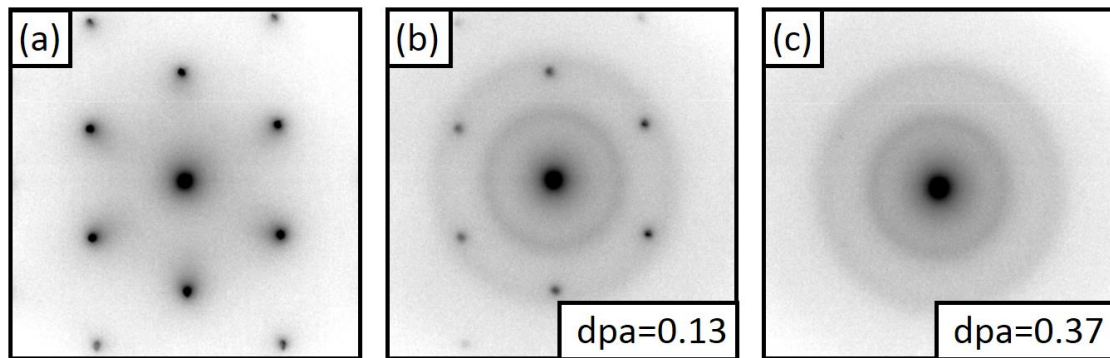


**Figure 6.4:** SADP of a germanium sample (a) before irradiation (b) after irradiation with 300 keV xenon ion at a fluence of  $1.3 \times 10^{13}$  ions.cm<sup>-2</sup> and a dpa of 0.13 and (c) at a fluence of  $3.0 \times 10^{13}$  ions.cm<sup>-2</sup> and a dpa of 0.37. The SADP in (c) was taken when the sample became fully amorphous as characterised by the presence of amorphous rings without any spots apart from the direct beam.

As shown in figure 6.5, using the SADPs as well as the volume  $V_a$  (determined via the MATLAB script) for each ion species, a correlation has been made between the intensity of the rings (which are proportional to the amorphous fraction) and equation 6.4 by finding the values of  $V_a$  and  $m$  which best matched the curves shown by the line in figure 6.5 with the experimental data points shown in the figure. In a few instances, some data points seem to be slightly off of the general trend for  $f_a$ . This might be due to the fact that the SADP aperture was

placed close to, or even on, the edge of the sample and therefore a small movement may have induced a variation in the captured intensities as more or less material contributed to the captured signal. It is also worth noting that a small decrease of the amorphous intensity is observed at the beginning of the irradiation on a few samples. This might be due to drift of the sample at the beginning of the irradiation which may have been undetected during the experiments or to the removal of surface oxide or contaminants by sputtering effects. However, as shown in figure 6.5, apart from these rare irregularities an appropriate fitting with equation 6.4 has been obtained. Furthermore, the quality of the fit is supported by the values of the coefficient of determination  $R^2$  calculated for each case. Note that this value is, in all fits, superior to 0.97 (where 1 is the target value for a perfect fit).

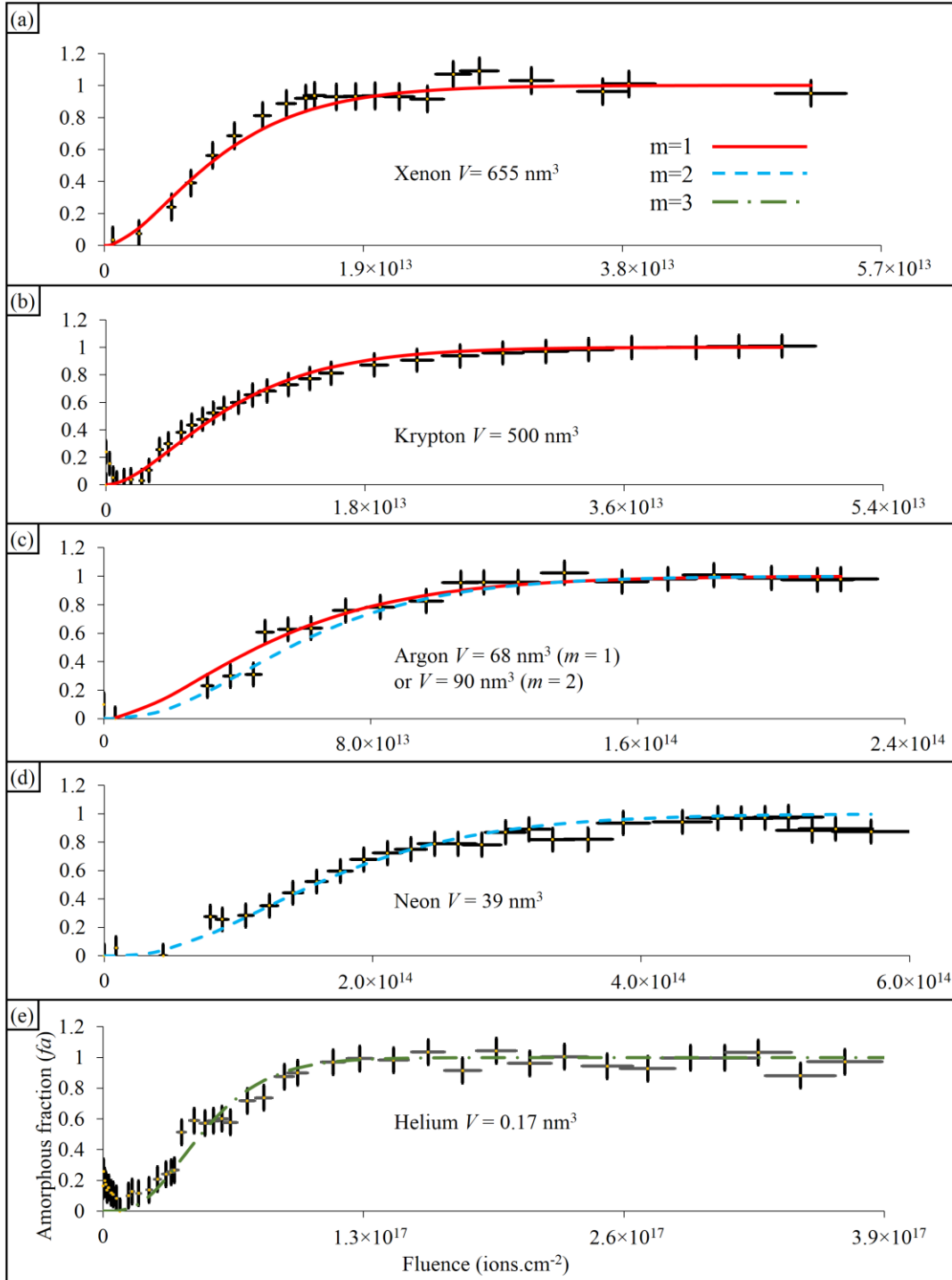


**Figure 6.5:** Evolution of  $f_a$  as function of the fluence during irradiation at RT according to equation 6.4 (as indicated by the curves) and according to the experiments (as shown by the data points) for the irradiation conditions: (a) 300 keV xenon (b) 200 keV krypton (c) 100 keV argon (d) 80 keV neon and (e) 70 keV helium ions. The labels of the axis in (e) also applies for (a) - (d).

The recoil densities were not determined only for the fraction of defects corresponding to the formation of volumes  $V_a$  but for all radii  $r_x$  (as explained in the experimental methods section above). The corresponding defect densities can therefore be shown for all ions (except for the helium ions due to the low number of recoils induced by helium) as a function of volume in figure 6.6. As detailed below, the MATLAB calculations confirmed previously published simulations and experimental work regarding the correlation between defect production and ion mass [27], [116], [132], [265]. Indeed, figure 6.6 shows that for matching ion ranges, the heaviest ions tend to induce regions with the highest defect concentrations as they have a higher nuclear collision cross-section and thus have a shorter mean free path between successive collisions [27], [116]. As shown in table 6.1 heavier ions also induce more defects per ion. These observations demonstrate that heavier ions are therefore more likely to generate clusters of defects  $V_d$  and amorphous regions  $V_a$  as there is a higher probability of finding regions with high densities of defects from a collision cascade and thus a higher probability of forming highly defective regions.

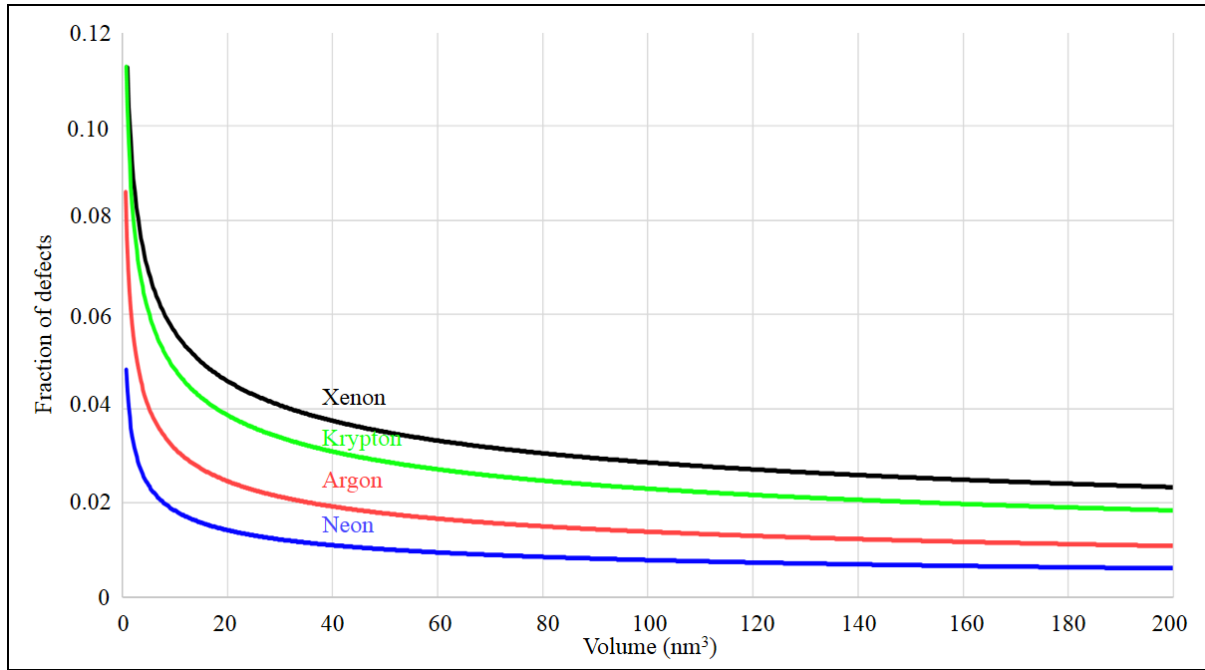


**Figure 6.6:** Using the MATLAB code and SRIM, the calculated fraction of defects as a function of the cylindrical volumes of radii,  $r_x$  defined in the experimental section is shown for all ions with the exception of the helium irradiation.

For each ion species, the fluence and the dpa for amorphisation as well as the ratio ( $S_e/S_n$ ) are summarised in table 6.1. Furthermore, the volumes  $V_a$ ,  $V_d$  and the required number of overlaps  $m$  required to make the volume  $V$  amorphous are also shown. It can be clearly seen that as previously reported in the literature  $V_a$ ,  $V_d$  (and therefore  $V$ ) increase with the mass of the ions used, whilst  $m$  and the ratio  $S_e/S_n$  have higher values when the ion is lighter [25], [125], [128]. Likewise, the threshold dpa value can be correlated with the mass of the ion as it is lower when the ion is heavier. This tendency regarding the threshold dpa is expected and generally accepted. However, a discrepancy is noticeable in the data presented here when comparing the threshold dpa of the krypton-irradiated sample with that of the xenon-irradiated one. Indeed, even though the mass of krypton is lower than that of xenon, the threshold dpa does not follow the trend identified here as it has a value of  $0.32 \pm 0.02$  versus a value of  $0.37 \pm 0.02$  for xenon.

It can be argued that the higher dpa threshold resulting from the xenon irradiation might be due to a spatial variation of the damage within the sample. Indeed, within the sample, if at a certain depth a region is less damaged than the rest of the sample, such a region could remain crystalline at higher fluence than the rest of the sample. In this case, whilst the rest of the sample would become amorphous more readily, the fact that a higher fluence would be required to make such region amorphous would contribute to increase the dpa threshold. To verify whether this could explain the observed discrepancy, the damage has been discretised within the sample. To do so, the dpa was calculated in 1 nm slices along the depth of the target material in SRIM at the fluence at which full amorphisation was established experimentally. The slice with the lowest dpa was compared for the xenon and for the krypton case indicating that the region with the lowest dpa was less damaged in the krypton case as compared with the xenon one. Therefore, this analysis indicates that in these experiments, the lower dpa threshold for krypton should not be the result of a spatial variation of damage.

Furthermore, the influence of the difference in thickness between the sample irradiated with krypton and that irradiated with xenon has also been examined. Because the sample irradiated with krypton was substantially thinner than that irradiated with xenon, repeat experiments were performed with both xenon and krypton ions, where instead the thickness of the sample irradiated with krypton was slightly thicker (25 nm) than that irradiated with xenon (23 nm). These additional experiments have resulted in the same trend in the dpa threshold for amorphisation with it again being lower for the krypton irradiation than for the xenon irradiation.

## 4. DISCUSSION

### 4.1. Mechanism for amorphisation according to the SADP

For all irradiation conditions, full amorphisation has been observed even when irradiation has been performed using helium ions. Furthermore, whilst previously reported experimental results have indicated that helium ions might not be able to make germanium fully amorphous [26], it is worth noting that full amorphisation under helium might have been not observed in those works for the simple reason that it requires a relatively high fluence to occur (i.e. in the helium irradiation shown in this chapter complete amorphisation was reached at a fluence of  $3.5 \times 10^{17}$  ions.cm<sup>-2</sup> corresponding to approximately 7 hours of irradiation at a flux of  $1.4 \times 10^{13}$  ions.cm<sup>-2</sup>.s<sup>-1</sup>).

Figure 6.5 shows that amorphisation must be the result of a heterogeneous process as the curves and the experimental data points representative of the  $f_a$  do not describe what would be expected if amorphisation was the result of a homogeneous mechanism. As previously reported in the literature and also shown in figure 6.2 [25], [125], the curve describing the amorphous fraction growth would be steeper if a homogeneous mechanism were responsible for the amorphisation process as amorphisation is supposed to occur via the abrupt collapse of the damaged material into its amorphous phase.

However, even when the sample was irradiated by the heaviest ion (xenon), the amorphisation build-up was not found to occur solely via an accumulation of amorphous volumes each induced by a single ion impact. Thus, precluding what can be considered as a pure heterogeneous mechanism (case where  $m = 0$ ) as the cause for amorphisation. Conversely, as the presence of volumes  $V_a$  is concluded to be involved in all conditions except for the sample irradiated with helium ions, it appears that amorphisation in most situations is due to complex

heterogeneous processes involving both amorphous volumes  $V_a$  and highly damaged regions  $V_d$ .

Investigating the presence of amorphous regions within a collision cascade based on the defect density determined via SRIM does have the shortcoming that the MC code does not consider dynamic processes that might enable defect recombination. However, as the timescales on which the recombination of point defects occurs are orders of magnitude longer than the collapse of the crystal into an amorphous phase [264], it can be assumed that the IDRAGON script based on SRIM provides a reasonable way of determining the direct formation of amorphous volumes  $V_a$  as its formation must thus precede the defect recombination. Additionally, the determination of the recoil density by SRIM, is by itself of fundamental interest as it provides a measure of the density distribution of the initially induced damage as the starting point for the process that subsequently unfolds and, as addressed below, is relevant to the amorphisation process and the dpa threshold.

#### 4.2. Influence of the distribution of defects on the dpa threshold for amorphisation

As highlighted above, whilst the trend regarding the values of the  $V$  and  $m$  are what is generally reported (i.e. the heavier the ion the smaller is  $m$  and the higher is  $V$ ) [25], [27], [125], [128], the comparison between the dpa threshold for amorphisation of the sample irradiated with xenon and krypton ions reveals an unanticipated result as it is lower for the case of krypton ion than for xenon. Whilst xenon and krypton ions are both relatively heavy ions and therefore may transfer a larger part of their kinetic energy per collision, in the germanium target material, the transmitted nuclear energy of a 300 keV xenon ion is on average 1.4 greater than this transmitted by a 200 keV krypton ion, thus meaning that the overall average energy loss via nuclear stopping cannot by itself explain the lower dpa threshold of the krypton case.

Furthermore, the electronic loss which is known to be able to retard amorphisation via bond-rearrangement repair mechanisms [133], is unlikely to be responsible for such discrepancy in this energy regime at which the ratio  $S_e/S_n$  is higher for the sample bombarded with krypton than that irradiated by xenon ions meaning that more repair would be induced (based on  $S_e/S_n$ ) in the case of krypton.

Even though a homogeneous mechanism is unlikely for these two relatively-heavy ions, the question should be raised as to whether such a mechanism (which, as described in detail in the literature review, is based on the energy deposited via nuclear stopping in the material [26]) can provide a valid explanation for the relative values of dpa threshold of krypton and xenon irradiated-samples. According to [26], the minimum energy deposited required to have the whole crystal collapse into an amorphous phase should be similar at room temperature for samples irradiated with different ions. As SRIM can calculate energy deposited via nuclear stopping per angstrom per ions in  $\text{eV}\cdot\text{\AA}^{-1}\cdot\text{ion}^{-1}$ , the energy minimum required to make the sample amorphous was calculated for each irradiation condition via equation 6.1 (in  $\text{eV}\cdot\text{atom}^{-1}\cdot\text{ion}^{-1}$ ). Consequently, it was shown that for the xenon, argon, and neon-irradiated samples the calculated threshold energy was between 27 and 29  $\text{eV}\cdot\text{atom}^{-1}\cdot\text{ion}^{-1}$  whilst it was significantly lower for the krypton-irradiated sample at 17  $\text{eV}\cdot\text{atom}^{-1}\cdot\text{ion}^{-1}$ ). This result further implies a discrepancy between the homogeneous mechanism and the experimental data as unlike what is described by this model, the nuclear energy deposition (or dpa) threshold for amorphisation did not solely depend on the target material but also on the irradiating species.

Interestingly, as shown in [116], in heterogeneous mechanisms, the proportionality between the number of defects and the amorphisation rate is not relevant as the amorphisation rate depends highly on the nature of the collision cascade. As this point is crucial for the understanding of this work, it will be explored further here. On heterogeneous mechanisms, one important point is that the build-up of amorphous material depends on the atomic

displacements induced within the regions which will subsequently go on to form a cluster of defects or an amorphous volume [27]. This is supported by several MD simulations which have shown that in a heterogeneous mechanism, regions with a high density of defects were responsible for amorphisation irrespective of the presence of defects generated outside those regions [116]. In the current work this can be considered as the region inside the volume  $V$ . In other words, according to [116] and to the heterogeneous mechanisms [27], recoils generated outside these volumes will not have a major impact on amorphisation. This element, as it will be shown below, has a major role on the correlation between the dpa and the threshold for amorphisation. Indeed, if the heterogeneous mechanism is the main mechanism contributing to amorphisation, then, during ion irradiation there will be displacements which are not induced within the highly damaged regions  $V$ . Consequently, those displacements which, in the heterogeneous mechanism can be considered as not participating in the amorphisation process, will still contribute to the calculated dpa threshold even though they can be considered as “non-amorphising” in the heterogeneous model. As stated in the literature review, one might expect the contribution of these so called “useless displacements” on the dpa threshold to be more pronounced for lighter ions. Indeed, it has been reported (and is shown in figure 6.6) that the lighter the ions were, the more dilute were the collision cascades and the greater the probability of inducing displacements outside  $V$  [116], [266]. Consequently, it will be likely that heavier ions will have a lower dpa threshold as the large number of the displacements they induce are concentrated in the regions of densest damage in their cascades and thus may be considered as “useful” for the amorphisation build-up. However, the comparison between the krypton and the xenon-irradiated samples in the current work seems to contradict this idea even though figure 6.6 shows that xenon ions induce larger defect-rich regions,  $V$  and  $V_a$ . Accordingly, consideration of neither of these calculated volumes seems to provide a complete explanation for the lower dpa threshold for krypton as their values are more elevated for the case of xenon.

Another approach has therefore been made based on the fact that in the heterogeneous model the dpa threshold must be related to the number of recoils generated within these volumes (i.e.  $V_a$  and  $V_d$ ). Indeed, it must be recalled that whilst the dpa threshold for amorphisation is an indicator commonly used to compare how different ion species amorphise a material, it is only indicative of the overall number of displacements induced when the material has been amorphised [267]. Such indicators do not solely capture the displacements generated within  $V_a$  and  $V_d$ , which might be the displacements contributing to the amorphisation process in the heterogeneous model. Comparing the displacements induced within these volumes with the overall number of displacements for each ion species should give a representative idea of how the dpa threshold for amorphisation should compare. Indeed, knowing what fractions of dpa can be considered as “useless” displacements is thus the same as knowing the displacements that will only contribute to increase of the threshold dpa.

As shown in figure 6.7, for each ion species the percentage of recoils induced within the volume  $V_a$  has been calculated which, as stated above, is the volume where dynamic annealing has been disregarded in the model being discussed here. Such calculations have shown that whilst the trend is generally that the calculated percentage of recoils inside  $V_a$  is higher when the ion mass is higher, an exception is observed when comparing the results relative to the krypton conditions which shows the highest value.

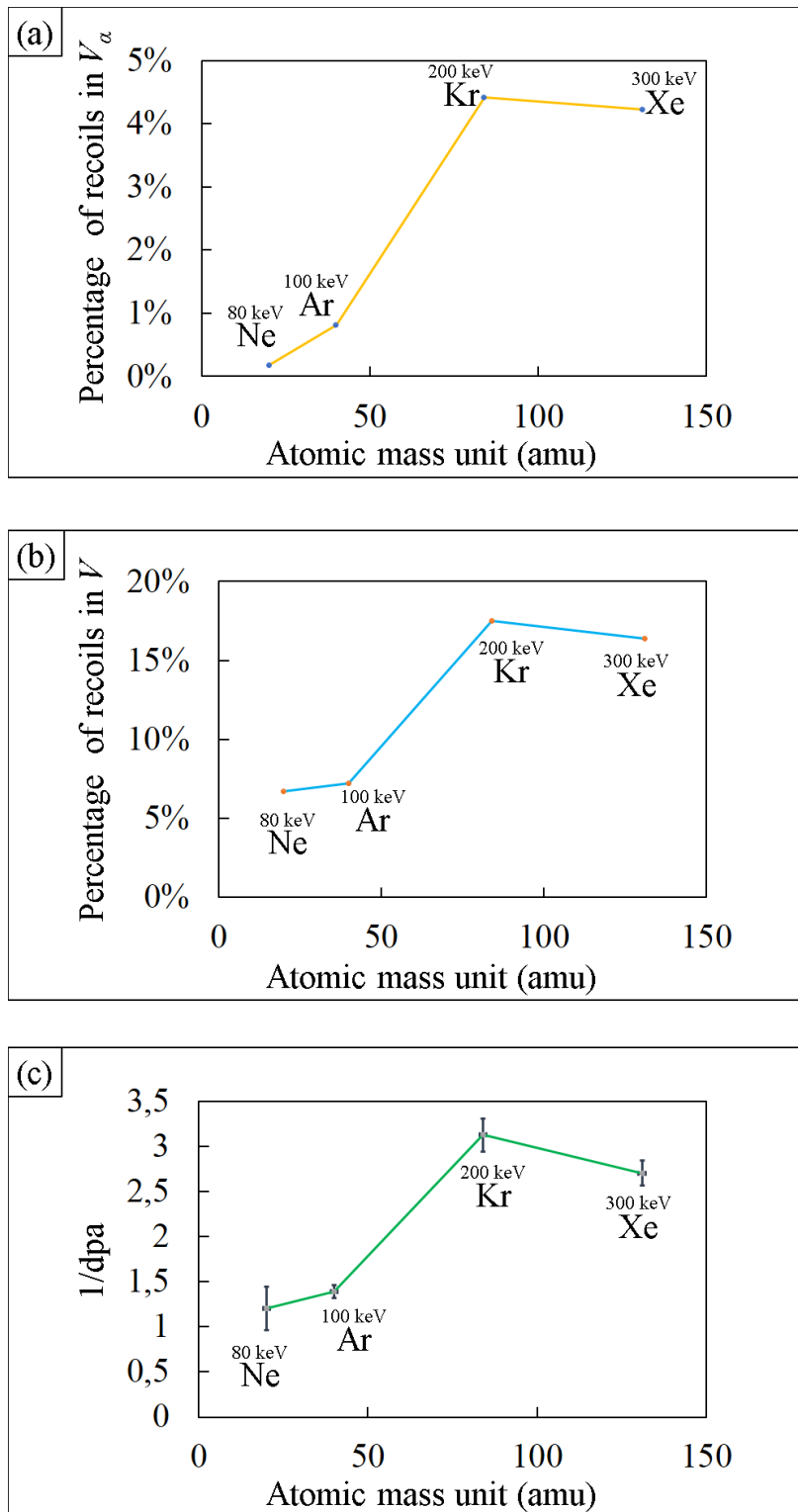


**Figure 6.7:** The percentage of recoils induced (a) in  $V_\alpha$  and in (b)  $V$  as function of the ion mass for each irradiation condition. In (c) is shown  $1/\text{dpa}$  as a function of the ion mass for each case. The ions labelled in (a) and are also applicable for (b) and (c). The lines in (a), (b) and (c) are included as guides for the eye.

As displacements are not induced only in  $V_\alpha$  but in the whole volume  $V$ , the same calculation has been repeated for  $V$  with the results shown in figure 6.7(b). Understandably, in this case, as the calculation is not based on  $V_\alpha$ , recombination of the defects cannot be disregarded and the calculation is thus only qualitative. However, it must be recalled that the calculation considers regions which demonstrate a high density of defects. Consequently as according to MD simulations reported in [116] and as discussed in the literature review, clusters of defects in semiconductors have been shown to be more likely to survive dynamic annealing than isolated point defects, the volumes  $V$  which include the defect rich volumes  $V_\alpha$  and  $V_d$  may be approximated as being relatively stable. Therefore, it is notable that when comparing the curves in figure 6.7(a) and (b) with the evolution of the dpa shown in figure 6.7(c), there is a resemblance regarding the evolution of the threshold dpa as a function of the ion mass. These results indicate that whilst both krypton and xenon ions have induced relatively dense cascades, xenon (which generates more displacements per ion than krypton) tends to induce more of them outside the highly damaged region thus resulting in a higher threshold dpa than krypton. Thus, this counter-intuitive result regarding the dpa threshold of the krypton and the xenon irradiated sample is an additional indication of the major role played by  $V_d$  and  $V_\alpha$  and thus of the heterogeneous process in the build-up of the amorphous layer. This also demonstrates that the dpa threshold for amorphisation (as it does not consider the mechanisms involved in the amorphisation process) can be a misleading indicator of the propensity of an ion to induce amorphisation. In fact, it must be specified that even though the threshold dpa is higher for a xenon irradiated sample, the xenon ion was still better able to amorphise the germanium target material as amorphisation will be reached with a number of ions per unit volume ( $D$ ) which is more than 45% lower than for the krypton case.

### 4.3. Influence on the stochastic nature of the collision cascade induce by helium ions on the dpa threshold for amorphisation

As stated above, it has previously been reported that lighter ions induce more dilute cascades [116], [266]. For the case of a very light ion such as helium, the production of regions with a high density of defects might at first seem unlikely as the MC calculations have indicated that each helium ion induces on average only three recoils in the sample. However, as will be discussed below, the irradiation performed with helium ions is a classic example of how an average value can be misleading when analysing stochastic events. Indeed, after examination of 1000 collision cascades it was shown that whilst 949 ions induce fewer than ten recoils in a 23 nm target, four ions were able to induce more than 100 recoils and even values of  $V_\alpha$  as large as 65 nm<sup>3</sup>.

Amorphisation build-up can occur even if only a small fraction of the ions contribute to the formation of volumes  $V$ . Obviously, the rarer these collision cascades, the higher will be the number of ions (i.e. the fluence) required to induce the damaged volumes  $V$ . In the helium case, as only 1% of the helium ions generate more than 50 recoils, it can be concluded that it is the stochastic nature of the collision cascades that causes the build-up of an amorphous layer via a heterogeneous process. Consequently, it can be stated that there is a “useful” fluence that induces amorphisation whilst most of the other ions induce isolated point defects and therefore “useless” atomic displacements. This explain the reason why the dpa and the fluence threshold for amorphisation for helium are orders of magnitude greater than those of the other inert gas ions. Furthermore, the fact that the whole fluence is considered in equation 6.4 instead of the “useful fluence” is the reason why the calculated volume  $V$  is excessively small (0.17 nm<sup>3</sup>). Indeed, by not taking into account that only a fraction of the fluence contributes to the amorphisation build up, the results of equation 6.4 are biased as it calculates only the value of  $V$  if each of the helium ions were inducing a (small) volume  $V$ . This approach can reasonably

be applied for other materials and more particularly other semiconductors. For instance, it is interesting that using similar in situ methods to monitor the evolution of  $f_a$  during 60 keV helium irradiation of silicon in [25], a similarly small volume  $V$  ( $0.13 \text{ nm}^3$ ) has been determined via equation 6.3 and is likely also due to the indirect consequence of the stochastic nature of the collision cascades.

## 5. Conclusion and remarks

Via the use of SADPs, the fluence and the dpa thresholds for amorphisation of germanium samples irradiated with xenon, krypton, argon, neon and helium ions at RT have been determined. As the ions used during the experiments have masses ranging from 4 to 132 amu, the results presented here will provide a useful set of data for material scientists wishing to either amorphise germanium or to avoid such effects.

Using in situ ion irradiation, the evolution of the SADP has been monitored to determine the amorphous fraction  $f_a$  during irradiation by the inert gases. A correlation between the amorphisation rate characterised by the amorphous fraction  $f_a$ , equation 6.4 and a modified version of IDRAGON allowing the analysis of the 3D collision cascades calculated using SRIM has shown that amorphisation occurs (mainly) via a heterogeneous mechanism in all cases. It was demonstrated that amorphisation is the result of a complex mechanism which involves the accumulation of a single-ion-strike amorphous region within a shell of heavily damaged crystalline material requiring  $m$  overlaps to become amorphous.

The observation that the dpa threshold for amorphisation can be lower for a lighter ion (krypton) than for a heavier one (xenon) was inconsistent with an amorphisation process based on a homogeneous mechanism whilst being in better agreement with the heterogeneous mechanism. Indeed, unlike the homogeneous mechanism, heterogeneous mechanisms do not solely depend on the overall nuclear energy deposited in the target material as only the

collisions induced within the volume  $V$  are responsible for participating in the amorphisation process. In agreement with this, it was shown that the dpa threshold for amorphisation and the percentage of displacements generated within the volumes responsible for amorphisation could be correlated, thus, providing further evidence regarding the crucial role played by these volumes in the build-up of the amorphous layer.

The sample irradiated by helium ions became amorphous after a fluence and a threshold dpa for amorphisation orders of magnitude above that for all other ions. It was shown in this case that the stochastic nature of the collision cascades was key to understanding this. Indeed, whilst on average each ion induced only three recoils, the analysis of 1000 collision cascades via the MATLAB code showed that rare collision cascades where ions induce more than 100 recoils (up to 230 recoils per ion) could induce highly damaged volumes and possibly even amorphous regions.

Lastly, it is worth noting that even if the experimental results have shown that amorphisation may have occurred mainly via a heterogeneous model, other contributions cannot be completely dismissed. Indeed, the influence of stable point defects generated outside  $V$  cannot be totally neglected. Such defects may, for instance, interact with clusters of defects or amorphous pockets leading either to the growth or the shrinking of their initial volume, as suggested in [143] and described in the literature review. Thus, during irradiation, the amorphisation rate of the material might be altered depending on the nature and the shape of the collision cascade (i.e. the distribution of the point defects within  $V$ ).

## Chapter 7: Conclusion

### 1. Ion induced bending of nanowires at elevated temperatures

Germanium and silicon nanowires were irradiated by xenon ions in situ in a TEM. By performing irradiations at elevated temperatures, it was shown that both silicon and germanium nanowires could be bent whilst still remaining crystalline. Such a methodology will potentially be beneficial if IIB is to be performed on nanowires for electronic applications which require them to be crystalline. Indeed, whilst IIB has been patented in the hope that it might be useful for tomorrow's electronic devices (e.g. the patent belonging to a company which is closely related to the electronic industry, Samsung [185]), the effect of annealing on the bent nanowires indicates that performing the irradiation at elevated temperatures might be valuable. Indeed, without irradiation at elevated temperature it might be impossible to use IIB and obtain bent single crystalline nanowires as these either become fully amorphous or suffer shape deformation during post-irradiation annealing [80], [177], [184]. Furthermore, these experiments have cast doubts on the necessity of the accumulation of point defects and amorphous material for the bending of nanowires using an ion beam.

As the nanowire bent via ion irradiation at elevated temperatures are single-crystals, it would be of interest to investigate the detailed atomic arrangement in lattice of the nanowires having a curved shape. To do so, collaboration with other laboratories on nanowires bent using the MIAMI facilities will enable further study using scanning TEM (STEM) in future works.

The feasibility of using EELS for band gap examination is currently also being investigated. Using EELS might enable the analysis of the nanowires' band gap and determine whether it varies across the curved nanowires. The motive of this procedure is the fact that the presence

of internal compressive and tensile stresses within such nanowires might affect the electronic band structure.

Furthermore, instead of using inert gases, it might be of interest also to use dopant ions to simultaneously dope and bend the nanowire. As explained in the literature review, two main outcomes are likely to be observed: a better activation of the dopant (as reported in the experiments by Fukata et al. [33]) and a possibility for the nanowire under stress to become optically active due to the combination of stress and also facilitated by the heavy doping (as reported in [242]).

## 2. 1. Ion induced bending of nanowires at RT and subsequent annealing

Germanium nanowires were irradiated at room temperature and subsequently annealed at 440°C. Using MC calculations, it was shown that the bending direction could be correlated to the ratio between the damage depth and the nanowire diameter. Apart from the applied interest of showing a way to control the bending direction, the results in chapter 5 also have fundamental importance as the experiments have studied the bending direction in the context of the mechanisms proposed in the literature. Indeed, it was shown that several of these mechanisms compete and that the bending direction is determined by the outcome of a competition between some or all of these.

Subsequent annealing showed that the shape of the germanium nanowires changed during SPEG. Interestingly, the shape deformation during SPEG was dependent on the initial bending direction as an increase of the curvature was observed in nanowires which were bent towards the ion beam, whilst those bent away tended to unbend. The shape deformation during annealing was proposed as being associated with the main mechanism which initially causes the bending during irradiation at room temperature.

These experiments showed that annealing could be used to prevent the bending (when it is an undesired effect of ion irradiation) but conversely could be problematic when the bending is desired.

Future experiments should be performed to verify how the threshold ratio of damage depth to nanowire diameter changes with energy, ion species and temperature. Indeed, such parameters should influence both the damage and the dynamical rearrangement of the defects within the nanowires, and thus the bending behaviour. (By influencing the outcome of the competition between mechanisms).

As with the nanowires irradiated at elevated temperature, for the RT-irradiated nanowires it is also planned to analyse them using STEM to determine the distribution and the arrangement of defects in nanowires bent away and towards the ion beam. Heating these nanowires in situ in a STEM would allow monitoring of the evolution of defects during the subsequent shape transformation. Lastly, it is of interest to evaluate whether the shape of fully amorphous bent nanowires could evolve if the annealing temperature is elevated enough to induce RNG. However, it is worth noting that experiments currently performed in the MIAMI-2 facility are showing that RNG in germanium nanowires typically occurs at a much higher temperature than in the bulk.

### 3. Amorphisation

Irradiations were performed using inert gases on germanium samples within the MIAMI-2 facility. The samples prepared via PIPS became fully amorphous as a result of the ion bombardment. The evolution of the amorphous fraction during irradiation was monitored using diffraction patterns. Furthermore, the collision cascades (from MC calculations) were analysed in 3D.

From the comparison of the experimental data and the analysis of the 3D collision cascades, the mechanism for amorphisation was deduced to be a heterogeneous mechanism where amorphisation occurs via the overlap of dense defect regions as well as accumulations of amorphous pockets induced by single ion impacts.

It was also shown that such a mechanism means that the trend for the dpa threshold for amorphisation does not always follow what is normally accepted; that is that the heavier the ion, the lower the threshold dpa. The reason for this observation was shown to be the result of the dissimilarity between the overall number of atomic displacements (given by the dpa) and the actual atomic displacements directly involved in the heterogeneous mechanism. Indeed, it was demonstrated that if an ion species induces a large number of atomic displacements outside the regions participating in the build-up of the amorphous fraction, the dpa threshold might be particularly high due to a large number of “useless-for amorphisation” displacements. Conversely, if a large proportion of atomic displacements are involved in the amorphisation process, the threshold dpa will be relatively low as observed in the case of the sample bombarded by krypton ions.

The case of the sample irradiated with helium ions showed that the stochastic nature of the collision cascades was of utmost importance as amorphisation could not be predicted using the average collision cascade induced by such light ions. Instead, the amorphisation was shown to be dependent on the more exceptional instances where a helium ion induces much more damage than in an average cascade.

In future work, similar analyses of collision cascades should reveal other irradiation conditions where the dpa threshold for amorphisation does not follow the typical trend described above. This may arise in germanium with ions of different energies or mass but also in other materials such as silicon. Consequently, after preliminary MC calculations, a set of such situations could

be revealed and experiments could subsequently be performed to confirm the conclusion suggested by the MC calculations.

Furthermore, it will be interesting to perform experiments at lower flux in order to induce isolated damage clusters and/or amorphous pockets via single impacts. The sample then irradiated could be studied using X-TEM as a way of giving an insight into the real damage induced in the sample (as opposed as the damage calculated via models and MC calculations). This should ultimately lead to a more accurate way of describing amorphisation as well as better ways of interpreting the MC calculations.

## References

- [1] J. Vallverdú I Segura, “Computational epistemology and e-science: A new way of thinking,” *Minds Mach.*, vol. 19, no. 4, pp. 557–567, 2009.
- [2] B. K. Jesiek, “The origins and early history of computer engineering in the united states,” *IEEE Ann. Hist. Comput.*, vol. 35, no. 3, pp. 6–18, 2013.
- [3] G. O’Regan, “Early Computers,” in *A Brief History of Computing*, no. February, London: Springer London, 2012, pp. 35–52.
- [4] V. Coroama, J. Bohn, and F. Mattern, “Living in a smart environment implications for the coming ubiquitous information society,” in *2004 IEEE International Conference on Systems, Man and Cybernetics (IEEE Cat. No.04CH37583)*, 2004, vol. 6, pp. 5633–5638.
- [5] A. Schmidt, B. Pfleging, F. Alt, A. Sahami, and G. Fitzpatrick, “Interacting with 21st-century computers,” *IEEE Pervasive Comput.*, vol. 11, no. 1, pp. 22–30, 2012.
- [6] R. S. Rosenberg, B. Isbn, A. Press, P. Date, and P. Count, “The social impact of computers,” *Choice Rev. Online*, vol. 30, no. 2, pp. 30-975-30–0975, 2013.
- [7] M. Friedewald and O. Raabe, “Ubiquitous computing: An overview of technology impacts,” *Telemat. Informatics*, vol. 28, no. 2, pp. 55–65, 2011.
- [8] D. R. Hartree, “The ENIAC, an electronic computing machine,” *Nature*, vol. 158, no. 4015, pp. 500–506, Oct. 1946.
- [9] Y. C. C. Yeh, “Triple-triple redundant 777 primary flight computer,” in *IEEE Aerospace Applications Conference Proceedings*, 2002, vol. 1, pp. 293–307.
- [10] P. E. Dodd, M. R. Shaneyfelt, J. R. Schwank, and J. A. Felix, “Current and future

- challenges in radiation effects on CMOS electronics,” *IEEE Trans. Nucl. Sci.*, vol. 57, no. 4 PART 1, pp. 1747–1763, 2010.
- [11] R. R. Schaller, R.R. Schaller, R. R. Schaller, and R.R. Schaller, “Moore’s law: past, present, and future,” *IEEE Spectr.*, vol. 34, no. 6, pp. 52–55, 57, 1997.
- [12] M. Kanellos, “ENIAC: A computer is born,” *CNET news*, 2006.
- [13] A. M. Ionescu, “Nanoelectronics roadmap : evading Moore’s law,” no. January 2008, pp. 4–6, 2016.
- [14] M. Roser, “Moore’s Law Transistor Count 1971-2016.” [www.OurWorldData.org](http://www.OurWorldData.org), 2018.
- [15] J. Vanhellemont and E. Simoen, “Brother Silicon, Sister Germanium,” *J. Electrochem. Soc.*, vol. 154, no. 7, p. H572, 2007.
- [16] C. Claeys and E. Simoen, *Germanium-based technologies. From materials to devices*. 2007.
- [17] M. Gong *et al.*, “Superhydrophobicity of hierarchical ZnO nanowire coatings,” *J. Mater. Chem. A*, vol. 2, no. 17, pp. 6180–6184, 2014.
- [18] . A West , T Tumlin, A Fakner, M Griep, “Nanostructured Superhydrophobic Surfaces for Nanoeducation and Science , Technology , Engineering , and Mathematics ( STEM ) Outreach,” *Academia.Edu*, no. February, 2015.
- [19] J. Wang, J. W. Luo, L. Zhang, and A. Zunger, “Reinterpretation of the expected electronic density of states of semiconductor nanowires,” *Nano Lett.*, vol. 15, no. 1, pp. 88–95, 2015.
- [20] L. Romano, N. G. Rudawski, M. R. Holzworth, K. S. Jones, S. G. Choi, and S. T.

- Picraux, "Nanoscale manipulation of Ge nanowires by ion irradiation," *J. Appl. Phys.*, vol. 106, no. 11, pp. 1–6, Dec. 2009.
- [21] J. R. Weber, A. Janotti, and C. G. Van de Walle, "Defects in Germanium," in *Photonics and Electronics with Germanium*, K. Wada and L. C. Kimerling, Eds. Weinheim, Germany: Wiley-VCH Verlag GmbH & Co. KGaA, 2015, pp. 1–23.
- [22] R. A. Kelly *et al.*, "Epitaxial Post-Implant Recrystallization in Germanium Nanowires," *Cryst. Growth Des.*, vol. 15, no. 9, pp. 4581–4590, 2015.
- [23] G. Impellizzeri *et al.*, "Ion implantation damage and crystalline-amorphous transition in Ge," *Appl. Phys. A Mater. Sci. Process.*, vol. 103, no. 2, pp. 323–328, 2011.
- [24] Y. L. Chao, S. Prussin, J. C. S. Woo, and R. Scholz, "Preamorphization implantation-assisted boron activation in bulk germanium and germanium-on-insulator," *Appl. Phys. Lett.*, vol. 87, no. 14, pp. 1–3, 2005.
- [25] P. D. Edmondson *et al.*, "An in situ transmission electron microscopy study of the ion irradiation induced amorphisation of silicon by He and Xe," *Scr. Mater.*, vol. 113, pp. 190–193, 2016.
- [26] A. Claverie, S. Koffel, N. Cherkashin, G. Benassayag, and P. Scheiblin, "Amorphization, recrystallization and end of range defects in germanium," *Thin Solid Films*, vol. 518, no. 9, pp. 2307–2313, 2010.
- [27] L. Pelaz, L. A. Marqús, and J. Barbolla, "Ion-beam-induced amorphization and recrystallization in silicon," *J. Appl. Phys.*, vol. 96, no. 11, pp. 5947–5976, 2004.
- [28] Y. Kamata, "High-k/Ge MOSFETs for future nanoelectronics," *Mater. Today*, vol. 11, no. 1–2, pp. 30–38, Jan. 2008.
- [29] R. Wittmann and S. Selberherr, "A study of ion implantation into crystalline

- germanium,” *Solid. State. Electron.*, vol. 51, no. 6, pp. 982–988, 2007.
- [30] L. Z. Pei and Z. Y. Cai, “A review on germanium nanowires,” *Recent Pat. Nanotechnol.*, vol. 6, no. 1, pp. 44–59, 2012.
- [31] P. Das Kanungo *et al.*, “Characterization of Structural Changes Associated with Doping Silicon Nanowires by Ion Implantation,” *Cryst. Growth Des.*, vol. 11, no. 7, pp. 2690–2694, 2011.
- [32] R. A. Kelly, J. D. Holmes, and N. Petkov, “Visualising discrete structural transformations in germanium nanowires during ion beam irradiation and subsequent annealing,” *Nanoscale*, vol. 6, no. 21, pp. 12890–12897, 2014.
- [33] N. Fukata, R. Takiguchi, S. Ishida, S. Yokono, S. Hishita, and K. Murakami, “Recrystallization and reactivation of dopant atoms in ion-implanted silicon nanowires,” *ACS Nano*, vol. 6, no. 4, pp. 3278–3283, 2012.
- [34] D. Wang *et al.*, “Germanium nanowire field-effect transistors with SiO<sub>2</sub> and high- $\kappa$  HfO<sub>2</sub> gate dielectrics,” *Appl. Phys. Lett.*, vol. 83, no. 12, pp. 2432–2434, 2003.
- [35] A. Johannes, H. Holland-Moritz, and C. Ronning, “Ion beam irradiation of nanostructures: Sputtering, dopant incorporation, and dynamic annealing,” *Semicond. Sci. Technol.*, vol. 30, no. 3, p. 33001, 2015.
- [36] Y. Li *et al.*, “Dopant-free GaN/AlN/AlGaN radial nanowire heterostructures as high electron mobility transistors,” *Nano Lett.*, vol. 6, no. 7, pp. 1468–1473, 2006.
- [37] H. Bracht, S. Schneider, and R. Kube, “Diffusion and doping issues in germanium,” *Microelectron. Eng.*, vol. 88, no. 4, pp. 452–457, 2011.
- [38] A. Colli, A. Fasoli, C. Ronning, S. Pisana, S. Piscanec, and A. C. Ferrari, “Ion beam doping of silicon nanowires,” *Nano Lett.*, vol. 8, no. 8, pp. 2188–2193, 2008.

- [39] G. Dearnaley, "Ion implantation," *Nature*, vol. 256, no. 5520, pp. 701–705, Aug. 1975.
- [40] A. Chroneos, E. N. Sgourou, C. A. Londos, and U. Schwingenschlögl, "Oxygen defect processes in silicon and silicon germanium," *Appl. Phys. Rev.*, vol. 2, no. 2, p. 21306, Jun. 2015.
- [41] T. Yoshida, M. Nagao, and S. Kanemaru, "Characteristics of ion-induced bending phenomenon," *Jpn. J. Appl. Phys.*, vol. 49, no. 5 PART 1, pp. 0565011–0565015, 2010.
- [42] I. Spectrum, "Germanium can take transistors where silicon cant." [Online]. Available: <http://spectrum.ieee.org/semiconductors/materials/germanium-can-take-transistors-where-silicon-cant>. [Accessed: 24-Jun-2019].
- [43] Y. Cai, R. Camacho-Aguilera, J. T. Bessette, L. C. Kimerling, and J. Michel, "High phosphorous doped germanium: Dopant diffusion and modeling," *J. Appl. Phys.*, vol. 112, no. 3, 2012.
- [44] J. C. Bourgoin and M. Lannoo, "On self-diffusion in silicon and germanium," *Radiat. Eff.*, vol. 46, no. 3–4, pp. 157–161, 1980.
- [45] M. Posselt, A. A. Gabriel, M. Posselt, and A. A. Gabriel, "Atomistic simulation of amorphous germanium and its solid phase epitaxial recrystallization," *Phys. Rev. B*, vol. 80, no. 4, pp. 1–12, 2009.
- [46] C. Kittel, *Intro to solid state physics*. 1996.
- [47] N. Ashcroft, D. Mermin, *Solid State Physics.*, vol. 9, no. 1. 1976.
- [48] P. Y. Yu and M. Cardona, *Fundamentals of Semiconductors*, vol. 107, no. 50. Berlin, Heidelberg: Springer Berlin Heidelberg, 2005.

- [49] T. Fischer, *Materials Science for Engineering Students Chap 1 (Types of Materials, Electron Energy Bands, and Chemical Bonds)*. Elsevier Book, 2008.
- [50] Bernard BOITTIAUX, “Bandes d’énergies - Porteurs : 2.2 Énergie des électrons dans un cristal.” [Online]. Available: <http://www.polytech-lille.fr/cours-atome-circuit-integre/phys/sc220.htm>. [Accessed: 27-Mar-2019].
- [51] M. Grundmann, *The Physics of Semiconductors*. Springer Berlin Heidelberg, 2006.
- [52] P. Ehrhart and H. Zillgen, “Vacancies and interstitial atoms in e<sup>-</sup>-irradiated germanium,” *J. Appl. Phys.*, vol. 85, no. 7, pp. 3503–3511, Apr. 1999.
- [53] B. Yu, X. H. Sun, G. A. Calebotta, G. R. Dholakia, and M. Meyyappan, “One-dimensional Germanium Nanowires for Future Electronics,” *J. Clust. Sci.*, vol. 17, no. 4, pp. 579–597, Dec. 2006.
- [54] R. A. Serway, J. W. Jewett, and R. V Mcgrew, *Principles of Physics 2ND EDITION*, vol. 1. Saunders Colege Division.
- [55] W. Chen, D. Qi, X. Gao, and A. T. S. Wee, “Surface transfer doping of semiconductors,” *Prog. Surf. Sci.*, vol. 84, no. 9–10, pp. 279–321, 2009.
- [56] J. F. Ziegler, “Section V. Semiconductors: (a) High energy implantation HIGH ENERGY ION IMPLANTATION,” *Nucl. Instruments Methods Phys. Res.*, vol. 6, pp. 270–282, 1985.
- [57] M. Goorsky, *Ion implantation*, INTECHOPEN. InTech, 2012.
- [58] Coll. and Kai Nordlund et al., “Primary Radiation Damage in Materials,” *OCDE / Nucl. Sci.*, p. NEA/NSC/DOC(2015)9, 2015.
- [59] C. P. Race, D. R. Mason, M. W. Finnis, W. M. C. Foulkes, A. P. Horsfield, and A. P.

- Sutton, "The treatment of electronic excitations in atomistic models of radiation damage in metals," *Reports Prog. Phys.*, vol. 73, no. 11, p. 116501, Nov. 2010.
- [60] A. V. Krasheninnikov and K. Nordlund, "Ion and electron irradiation-induced effects in nanostructured materials," *J. Appl. Phys.*, vol. 107, no. 7, 2010.
- [61] F. Aumayr, S. Facsko, A. S. El-Said, C. Trautmann, and M. Schleberger, "Single ion induced surface nanostructures: A comparison between slow highly charged and swift heavy ions," *J. Phys. Condens. Matter*, vol. 23, no. 39, 2011.
- [62] M. T. Robinson, "Attractive interaction potentials and the binary collision approximation," *Radiat. Eff. Defects Solids*, vol. 141, no. 1–4, pp. 1–19, 1997.
- [63] T. Díaz De La Rubia and T. D. de la Rubia, "Irradiation-Induced Defect Production in Elemental Metals and Semiconductors: A Review of Recent Molecular Dynamics Studies," *Annu. Rev. Mater. Sci.*, vol. 26, no. 1, pp. 613–649, 2003.
- [64] G. Greaves *et al.*, "Enhanced sputtering yields from single-ion impacts on gold nanorods," *Phys. Rev. Lett.*, vol. 111, no. 6, 2013.
- [65] E. Holmström, A. Kuronen, and K. Nordlund, "Threshold defect production in silicon determined by density functional theory molecular dynamics simulations," *Phys. Rev. B - Condens. Matter Mater. Phys.*, vol. 78, no. 4, p. 45202, Jul. 2008.
- [66] G. S. Was, I. Obodovskiy, G. S. Was, S. Gary, G. S. Was, and S. Gary, "Fundamentals of Radiation Materials Science," *Radiation*, pp. 367–371, 2007.
- [67] G. H. Kinchin and R. S. Pease, "The Displacement of Atoms in Solids by Radiation," *Reports Prog. Phys.*, vol. 18, no. 1, p. 301, Jan. 1955.
- [68] A. J. McKenna, T. Trevethan, C. D. Latham, P. J. Young, and M. I. Heggie, "Threshold displacement energy and damage function in graphite from molecular

- dynamics,” *Carbon N. Y.*, vol. 99, pp. 71–78, 2016.
- [69] W. K. Hofker, D. P. Oosthoek, N. J. Koeman, and H. A. M. De Grefte, “Concentration profiles of boron implantations in amorphous and polycrystalline silicon,” *Radiat. Eff.*, vol. 24, no. 4, pp. 223–231, 1975.
- [70] R. Mikšová, A. Macková, A. Jagerová, P. Malinský, P. Slepíčka, and V. Švorčík, “Structural study and ion-beam channelling in Si  $\langle 100 \rangle$  modified by Kr<sup>+</sup>, Ag<sup>+</sup>, 2<sup>+</sup> and Au<sup>+</sup>, 2<sup>+</sup> ions,” *Appl. Surf. Sci.*, vol. 458, no. March, pp. 722–733, 2018.
- [71] M. A. Razali, A. J. Smith, C. Jeynes, and R. M. Gwilliam, “Temperature-dependant study of phosphorus ion implantation in germanium,” vol. 193. AIP Conference Proceedings. Vol. 1496. No. 1. AIP, 2012, pp. 193–196, 2012.
- [72] L. Capello *et al.*, “Influence of preamorphization on the structural properties of ultrashallow arsenic implants in silicon,” *J. Appl. Phys.*, vol. 100, no. 10, 2006.
- [73] Jinning Liu, U. Jeong, M. Meloni, S. Mehta, and Che-Hoo Ng, “Effects of pre-amorphization on junction characteristics and damage behavior in low energy boron implantation,” in *2000 International Conference on Ion Implantation Technology Proceedings. Ion Implantation Technology - 2000 (Cat. No.00EX432)*, 2000, pp. 191–194.
- [74] E. Simoen *et al.*, “Ion-implantation issues in the formation of shallow junctions in germanium,” *Mater. Sci. Semicond. Process.*, vol. 9, no. 4–5 SPEC. ISS., pp. 634–639, 2006.
- [75] J. F. Ziegler, M. D. D. Ziegler, and J. P. P. Biersack, “SRIM - The stopping and range of ions in matter (2010),” *Nucl. Instruments Methods Phys. Res. Sect. B Beam Interact. with Mater. Atoms*, vol. 268, no. 11–12, pp. 1818–1823, Jun. 2010.

- [76] W. Möller, “TRI3DYN – Collisional computer simulation of the dynamic evolution of 3-dimensional nanostructures under ion irradiation,” *Nucl. Instruments Methods Phys. Res. Sect. B Beam Interact. with Mater. Atoms*, vol. 322, pp. 23–33, Mar. 2014.
- [77] G. Demange, E. Antoshchenkova, M. Hayoun, L. Lunéville, and D. Simeone, “A rational use of BCA code MARLOWE for ballistic effects of ion beam irradiation in the ion mixing formalism: comparison to Molecular Dynamics,” *arXiv Prepr. arXiv1610.08659 (2016)*, pp. 1–8, Oct. 2016.
- [78] C. Borschel, “Iradina Manual,” *Solid State Phys.*, 2011.
- [79] D. Schwen, M. Huang, P. Bellon, and R. S. Averback, “Molecular dynamics simulation of intragranular Xe bubble re-resolution in UO<sub>2</sub>,” *J. Nucl. Mater.*, vol. 392, no. 1, pp. 35–39, 2009.
- [80] O. Camara *et al.*, “Shape Modification of Germanium Nanowires during Ion Irradiation and Subsequent Solid-Phase Epitaxial Growth,” *Adv. Mater. Interfaces*, vol. 5, no. 13, p. 1800276, Jul. 2018.
- [81] N. Cowern *et al.*, “Extended Point Defects in Crystalline Materials: Ge and Si,” *Phys. Rev. Lett.*, vol. 110, no. 15, p. 155501, Apr. 2013.
- [82] K. Jaichan, “CREATION OF SURFACE AND BULK DEFECTS OF Ge AND SURFACE ROUGHENING OF Ge DURING HIGH ENERGY ION IRRADIATION (Chapter 4 Surface defects created by keV Xe ion irradiation on Ge).”
- [83] D. Fink and L. T. Chadderton, “Ion-solid interactions: Current status, new perspectives,” *Radiat. Eff. Defects Solids*, vol. 160, no. 3–4, pp. 67–83, 2005.
- [84] A. Chroneos and H. Bracht, “Diffusion of n -type dopants in germanium,” *Appl. Phys. Rev.*, vol. 1, no. 1, p. 11301, Mar. 2014.

- [85] H. Bracht, “Defect engineering in germanium,” *Phys. Status Solidi Appl. Mater. Sci.*, vol. 211, no. 1, pp. 109–117, 2014.
- [86] S. A. Centoni, B. Sadigh, G. H. Gilmer, T. J. Lenosky, T. Díaz De La Rubia, and C. B. Musgrave, “First-principles calculation of intrinsic defect formation volumes in silicon,” *Phys. Rev. B - Condens. Matter Mater. Phys.*, vol. 72, no. 19, pp. 1–9, 2005.
- [87] T. Steinbach, A. Reupert, E. Schmidt, and W. Wesch, “Ion beam induced stress formation and relaxation in germanium,” *Nucl. Instruments Methods Phys. Res. Sect. B Beam Interact. with Mater. Atoms*, vol. 307, pp. 194–198, 2013.
- [88] N. Kalyanasundaram, M. C. Moore, J. B. Freund, and H. T. Johnson, “Stress evolution due to medium-energy ion bombardment of silicon,” *Acta Mater.*, vol. 54, no. 2, pp. 483–491, 2006.
- [89] L. Pelaz *et al.*, “Stability of defects in crystalline silicon and their role in amorphization,” *Phys. Rev. B - Condens. Matter Mater. Phys.*, vol. 64, no. 4, pp. 1–9, 2001.
- [90] E. S. Structures, Z. Suo, J. H. Hollomon, R. Maurer, F. Seitz, and C. S. Smith, “Lecture 2 The Vacancy,” *Spring*, pp. 1–11, 2004.
- [91] R. E. Whan, “Investigations of oxygen-defect interactions between 25 and 700 Å°K in irradiated germanium,” *Phys. Rev.*, vol. 140, no. 2A, 1965.
- [92] D. Kiselev, “Activation and Radiation Damage of Components in the Environment of Proton Accelerators,” *CAS - Cern Accel. Sch. Course High Power Hadron Mach.*, pp. 437–463, 2011.
- [93] A. Chroneos, “Dopant-vacancy cluster formation in germanium,” *J. Appl. Phys.*, vol. 107, no. 7, pp. 2009–2011, 2010.

- [94] H. Bracht, “Copper related diffusion phenomena in germanium and silicon,” *Mater. Sci. Semicond. Process.*, vol. 7, no. 3 SPEC. ISS., pp. 113–124, 2004.
- [95] H. Bracht *et al.*, “Interstitial-mediated diffusion in germanium under proton irradiation,” *Phys. Rev. Lett.*, vol. 103, no. 25, pp. 31–34, 2009.
- [96] S. Schneider and H. Bracht, “Suppression of donor-vacancy clusters in germanium by concurrent annealing and irradiation,” *Appl. Phys. Lett.*, vol. 98, no. 1, pp. 96–99, 2011.
- [97] C. Borschel *et al.*, “Alignment of semiconductor nanowires using ion beams.,” *Small*, vol. 5, no. 22, pp. 2576–80, 2009.
- [98] M. Tang, L. Colombo, J. Zhu, and T. Diaz de la Rubia, “Intrinsic point defects in crystalline silicon: Tight-binding molecular dynamics studies of self-diffusion, interstitial-vacancy recombination, and formation volumes,” *Phys. Rev. B*, vol. 55, no. 21, pp. 14279–14289, Jun. 1997.
- [99] H. Mehrer, *Diffusion\_in\_solids\_Helmut*. Springer, 2010.
- [100] M. Suezawa, Y. Iijima, and I. Yonenaga, “On the nature of thermal equilibrium point defects in Si: Are the thermal equilibrium point defects in Si crystals Frenkel pairs or Schottky defects?,” *Jpn. J. Appl. Phys.*, vol. 56, no. 4, p. 48005, 2017.
- [101] W. J. W. Donald R. Askeland, Pradeep P. Fulay, “Materials science and engineering,” *Mater. Sci. Eng. B*, vol. 12, no. 4, p. 393, Feb. 2010.
- [102] M. W. Valenta and C. Ramasastry, “Effect of Heavy Doping on the Self-Diffusion of Germanium,” *Phys. Rev.*, vol. 106, no. 1, pp. 73–75, Apr. 1957.
- [103] E. Hüger *et al.*, “Self-diffusion in germanium isotope multilayers at low temperatures,” *Appl. Phys. Lett.*, vol. 93, no. 16, p. 162104, Oct. 2008.

- [104] H. Reiss and C. S. Fuller, "Influence of Neutrons and Electrons on the Solubility of Lithium in Boron-Doped Silicon," *JOM*, vol. 8, no. 2, pp. 276–282, Feb. 1956.
- [105] R. A. Logan, B. T. Laboratories, M. Hill, and R. A. Logan, "Thermally induced acceptors in germanium," *Phys. Rev.*, vol. 101, no. 5, pp. 1455–1459, 1956.
- [106] H. Akiko, "Experimental Determination of Diffusion and Formation Energies of Thermal Vacancies in Germanium.pdf," *Journal of the Physical Society of Japan*, vol. 21, no. 1, pp. 34–41, 1965.
- [107] D. Shaw, "Self- and impurity diffusion in Ge and Si," *Phys. Status Solidi*, vol. 72, no. 1, pp. 11–39, 1975.
- [108] S. Mayburg, "Vacancies and interstitials in heat treated germanium," *Phys. Rev.*, vol. 95, no. 1, pp. 38–43, 1954.
- [109] M. Dionízio Moreira, R. H. Miwa, P. Venezuela, M. D. Moreira, and R. H. Miwa, "Electronic and structural properties of germanium self-interstitials," *Phys. Rev. B - Condens. Matter Mater. Phys.*, vol. 70, no. 11, pp. 1–5, 2004.
- [110] J. R. Silva *et al.*, "Self-interstitial defect in germanium," *Phys. Rev. B - Condens. Matter Mater. Phys.*, vol. 62, no. 15, pp. 9903–9906, 2000.
- [111] J. Vanhellefont *et al.*, "On the solubility and diffusivity of the intrinsic point defects in germanium," *J. Appl. Phys.*, vol. 101, no. 3, 2007.
- [112] B. L. Darby, B. R. Yates, I. Martin-Bragado, J. L. Gomez-Selles, R. G. Elliman, and K. S. Jones, "Substrate orientation dependence on the solid phase epitaxial growth rate of Ge," *J. Appl. Phys.*, vol. 113, no. 3, 2013.
- [113] D. R. Tobergte and S. Curtis, *Recrystallization and Related Annealing Phenomena*, vol. 53, no. 9. Cambridge: Elsevier, 2004.

- [114] C. Borschel *et al.*, “Permanent bending and alignment of ZnO nanowires,” *Nanotechnology*, vol. 22, no. 18, p. 185307, May 2011.
- [115] M. G. Grimaldi, L. Calcagno, P. Musumeci, N. Frangis, and J. Van Landuyt, “Amorphization and defect recombination in ion implanted silicon carbide,” *J. Appl. Phys.*, vol. 81, no. 11, pp. 7181–7185, 1997.
- [116] M.-J. Caturla *et al.*, “Ion-beam processing of silicon at keV energies: A molecular-dynamics study,” *Phys. Rev. B*, vol. 54, no. 23, pp. 16683–16695, 1996.
- [117] J. Nord, K. Nordlund, and J. Keinonen, “Amorphization mechanism and defect structures in ion-beam-amorphized Si, Ge, and GaAs,” *Phys. Rev. B*, vol. 65, no. 16, p. 165329, 2002.
- [118] M. T. Robinson, “Basic physics of radiation damage production,” *J. Nucl. Mater.*, vol. 216, no. C, pp. 1–28, 1994.
- [119] E. M. Bringa and R. E. Johnson, “Coulomb Explosion and Thermal Spikes,” *Phys. Rev. Lett.*, vol. 88, no. 16, p. 4, 2002.
- [120] J. A. Brinkman, “On the nature of radiation damage in metals,” *J. Appl. Phys.*, vol. 25, no. 8, pp. 961–970, 1954.
- [121] L. Bischoff, W. Pilz, and B. Schmidt, “Amorphous solid foam structures on germanium by heavy ion irradiation,” *Appl. Phys. A*, vol. 104, no. 4, pp. 1153–1158, Sep. 2011.
- [122] N. S. Rajput, Z. Tong, and X. Luo, “Investigation of ion induced bending mechanism for nanostructures,” *Mater. Res. Express*, vol. 2, no. 1, p. 15002, Dec. 2015.
- [123] E. Figueroa *et al.*, “Mechanical properties of irradiated nanowires - A molecular dynamics study,” *J. Nucl. Mater.*, vol. 467, pp. 677–682, 2015.

- [124] M. Lai, X. Zhang, and F. Fang, “Crystal Orientation Effect on the Subsurface Deformation of Monocrystalline Germanium in Nanometric Cutting,” *Nanoscale Res. Lett.*, vol. 12, 2017.
- [125] P. D. Edmondson, D. J. Riley, R. C. Birtcher, and S. E. Donnelly, “Amorphization of crystalline Si due to heavy and light ion irradiation,” *J. Appl. Phys.*, vol. 106, no. 4, pp. 1–8, 2009.
- [126] J. Huang *et al.*, “Si amorphization by focused ion beam milling: Point defect model with dynamic BCA simulation and experimental validation,” *Ultramicroscopy*, vol. 184, pp. 52–56, 2018.
- [127] A. Claverie, A. Roumili, N. Gessinn, and J. Beauvillain, “Kinetics of silicon amorphization by N<sup>+</sup> implantation: Dose rate and substrate temperature effects,” *Mater. Sci. Eng. B*, vol. 4, no. 1–4, pp. 205–209, Oct. 1989.
- [128] J. F. Gibbons, “Ion implantation in semiconductors—Part II: Damage production and annealing,” *Proc. IEEE*, vol. 60, no. 9, pp. 1062–1096, 1972.
- [129] L. A. Christel, J. F. Gibbons, and T. W. Sigmon, “Displacement criterion for amorphization of silicon during ion implantation,” *J. Appl. Phys.*, vol. 52, no. 12, pp. 7143–7146, Dec. 1981.
- [130] C.-T. Pan *et al.*, “In-situ observation and atomic resolution imaging of the ion irradiation induced amorphisation of graphene,” *Sci. Rep.*, vol. 4, no. 1, p. 6334, 2015.
- [131] X. Wang, L. Jamison, K. Sridharan, D. Morgan, P. M. Voyles, and I. Szlufarska, “Evidence for cascade overlap and grain boundary enhanced amorphization in silicon carbide irradiated with Kr ions,” *Acta Mater.*, vol. 99, pp. 7–15, 2015.
- [132] R. C. Birtcher, “Energy Dependence of Ge Amorphization by Ne , Ar or Kr Ion

Irradiation \* Argonne National Laboratory October 1994 Portions of this document may be illegible in electronic image products . Images are produced from the best available original document,” 1994.

- [133] G. Velis *et al.*, “Ion mass dependence of irradiation-induced damage accumulation in KTaO<sub>3</sub>,” *J. Mater. Sci.*, vol. 54, no. 1, pp. 149–158, 2018.
- [134] B. Stritzker, R. G. Elliman, and J. Zou, “Self-ion-induced swelling of germanium,” *Nucl. Instruments Methods Phys. Res. Sect. B Beam Interact. with Mater. Atoms*, vol. 175–177, no. 2001, pp. 193–196, 2001.
- [135] S. C. Moss and J. F. Graczyk, “Evidence of Voids Within the As-Deposited Structure of Glassy Silicon,” *Phys. Rev. Lett.*, vol. 23, no. 20, pp. 1167–1171, Nov. 1969.
- [136] A. L. Stepanov, V. V. Vorob’ev, V. I. Nuzhdin, V. F. Valeev, and Y. N. Osin, “Formation of Porous Germanium Layers by Silver-Ion Implantation,” *Tech. Phys. Lett.*, vol. 44, no. 4, 2018.
- [137] J. Yanagisawa, K. Takarabe, K. Ogushi, K. Gamo, and Y. Akasaka, “Nanoporous structure formations on germanium surfaces by focused ion beam irradiations,” *J. Phys. Condens. Matter*, vol. 19, no. 44, pp. 0–10, Nov. 2007.
- [138] M. L. Swanson, J. R. Parsons, and C. W. Hoelke, “Damaged regions in neutron-irradiated and ion-bombarded Ge and Si,” *Radiat. Eff.*, vol. 9, no. 3–4, pp. 249–256, Jun. 1971.
- [139] G. Otto, G. Hobler, L. Palmethofer, and P. Pongratz, “Amorphous pockets in Si: Comparison of coupled molecular dynamics and TEM image contrast simulations with experimental results,” *Nucl. Instruments Methods Phys. Res. Sect. B Beam Interact. with Mater. Atoms*, vol. 255, no. 1 SPEC. ISS., pp. 105–109, 2007.

- [140] F. F. Morehead and B. L. Crowder, "A model for the formation of amorphous Si by ion bombardment," *Radiat. Eff.*, vol. 6, no. 1, pp. 27–32, Jan. 1970.
- [141] E. C. Baranova *et al.*, "on Silicon Amorphization During Different Mass Ion Implantation.," *Radiat. Eff.*, vol. 18, no. 1–2, pp. 21–26, 1973.
- [142] E. C. Baranova, V. M. Gusev, Y. V. Martynenko, C. V. Starinin, and I. B. Hailbullin, "On Silicon Amorphisation During Different Mass Ions Implantation," in *Ion Implantation in Semiconductors and Other Materials*, Boston, MA: Springer US, 1973, pp. 59–71.
- [143] D. K. Sadana, "Mechanisms of amorphization and recrystallization in ion implanted III–V compound semiconductors," *Nucl. Instruments Methods Phys. Res. Sect. B Beam Interact. with Mater. Atoms*, vol. 7–8, pp. 375–386, Mar. 1985.
- [144] N. Hecking, K. F. Heidemann, and E. Te Kaat, "Crystalline Silicon During Ion Irradiation," *Nucl. Instruments Methods Phys. Res. B*, vol. 15, pp. 760–764, 1986.
- [145] O. Peña-Rodríguez, J. Manzano-Santamaría, A. Rivera, G. García, J. Olivares, and F. Agulló-López, "Kinetics of amorphization induced by swift heavy ions in  $\alpha$ -quartz," *J. Nucl. Mater.*, vol. 430, no. 1–3, pp. 125–131, Nov. 2012.
- [146] F. Agulló-López *et al.*, "Synergy between thermal spike and exciton decay mechanisms for ion damage and amorphization by electronic excitation," *Phys. Rev. B - Condens. Matter Mater. Phys.*, vol. 74, no. 17, pp. 1–6, 2006.
- [147] L. Csepregi, E. F. Kennedy, J. W. Mayer, and T. W. Sigmon, "Substrate-orientation dependence of the epitaxial regrowth rate from Si-implanted amorphous Si," *J. Appl. Phys.*, vol. 49, no. 7, pp. 3906–3911, 1978.
- [148] G. L. L. Olson and J. A. A. Roth, "Kinetics of solid phase crystallization in amorphous

- silicon,” *Mater. Sci. Reports*, vol. 3, no. 1, pp. 1–77, Jan. 1988.
- [149] W. E. Hong and J. S. Ro, “Kinetics of solid phase crystallization of amorphous silicon analyzed by Raman spectroscopy,” *J. Appl. Phys.*, vol. 114, no. 7, 2013.
- [150] J. W. Mayer, “A COMPARISON OF THE HOT IMPLANTATION BEHAVIOR OF SEVERAL GROUP-III AND -V ELEMENTS IN Si AND Ge,” *Appl. Phys. Lett.*, vol. 11, no. 12, p. 365, 1967.
- [151] F. Milési, J. Leveneur, V. Mazzocchi, F. Mazon, F. Gonzatti, and K. Yekache, “High temperature ion implantation evaluation in silicon & germanium,” *AIP Conf. Proc.*, vol. 1321, pp. 196–199, 2010.
- [152] R. D. Goldberg, J. S. Williams, and R. G. Elliman, “Amorphization of silicon by elevated temperature ion irradiation,” *Nucl. Inst. Methods Phys. Res. B*, vol. 106, no. 1–4, pp. 242–247, 1995.
- [153] I. Jenčič *et al.*, “Regrowth of heavy-ion implantation damage by electron beams,” *Mater. Sci. Semicond. Process.*, vol. 3, no. 4, pp. 311–315, Aug. 2000.
- [154] I. Jenčič *et al.*, “Electron-beam-induced crystallization of isolated amorphous regions in Si, Ge, GaP, and GaAs,” *J. Appl. Phys.*, vol. 78, no. 2, pp. 974–982, Jul. 1995.
- [155] F. Corticelli, G. Lulli, and P. G. Merli, “Solid-phase epitaxy of implanted silicon at liquid nitrogen and room temperature induced by electron irradiation in the electron microscope,” *Philos. Mag. Lett.*, vol. 61, no. 3, pp. 101–106, 1990.
- [156] G. Lulli, P. G. Merli, and M. V. Antisari, “Solid-phase epitaxy of amorphous silicon induced by electron irradiation at room temperature,” *Phys. Rev. B*, vol. 36, no. 15, pp. 8038–8042, 1987.
- [157] R. S. Wagner and W. C. Ellis, “VAPOR-LIQUID-SOLID MECHANISM OF SINGLE

- CRYSTAL GROWTH,” *Appl. Phys. Lett.*, vol. 4, no. 5, pp. 89–90, Mar. 1964.
- [158] F. Xu *et al.*, “Simple approach to highly oriented ZnO nanowire arrays: large-scale growth, photoluminescence and photocatalytic properties,” *Nanotechnology*, vol. 17, no. 2, pp. 588–594, 2006.
- [159] R. G. Hobbs, N. Petkov, and J. D. Holmes, “Semiconductor nanowire fabrication by bottom-up and top-down paradigms,” *Chem. Mater.*, vol. 24, no. 11, pp. 1975–1991, 2012.
- [160] D. Wang, B. a. Sheriff, M. McAlpine, and J. R. Heath, “Development of ultra-high density silicon nanowire arrays for electronics applications,” *Nano Res.*, vol. 1, no. 1, pp. 9–21, 2008.
- [161] K. K. Nanda, F. E. Kruis, and H. Fissan, “Energy Levels in Embedded Semiconductor Nanoparticles and Nanowires,” *Nano Lett.*, vol. 1, no. 11, pp. 605–611, 2001.
- [162] L. T. Ngo *et al.*, “Ultimate-Strength Germanium Nanowires,” *Nano Lett.*, vol. 6, no. 12, pp. 2964–2968, Dec. 2006.
- [163] B. S. Sahu *et al.*, “Effect of ion implantation energy for the synthesis of ge nanocrystals in sin films with hfo2/sio2stack tunnel dielectrics for memory application,” *Nanoscale Res. Lett.*, vol. 6, no. 1, p. 177, 2011.
- [164] A. M. Chockla, K. C. Klavetter, C. B. Mullins, and B. A. Korgel, “Solution-grown germanium nanowire anodes for lithium-ion batteries,” *ACS Appl. Mater. Interfaces*, vol. 4, no. 9, pp. 4658–4664, 2012.
- [165] J. Greil, A. Lugstein, C. Zeiner, G. Strasser, and E. Bertagnolli, “Tuning the electro-optical properties of germanium nanowires by tensile strain,” *Nano Lett.*, vol. 12, no. 12, pp. 6230–6234, 2012.

- [166] F. Zhang, V. H. Crespi, and P. Zhang, “Prediction that uniaxial tension along 111 produces a direct band gap in germanium,” *Phys. Rev. Lett.*, vol. 102, no. 15, pp. 1–4, 2009.
- [167] G. Audoit, É. N. Mhuirheartaigh, S. M. Lipson, M. A. Morris, W. J. Blau, and J. D. Holmes, “Strain induced photoluminescence from silicon and germanium nanowire arrays,” *J. Mater. Chem.*, vol. 15, no. 45, p. 4809, 2005.
- [168] H. Tahini, A. Chroneos, R. W. Grimes, U. Schwingenschlögl, and A. Dimoulas, “Strain-induced changes to the electronic structure of germanium,” *J. Phys. Condens. Matter*, vol. 24, no. 19, pp. 22–26, 2012.
- [169] S. Bao *et al.*, “Low-threshold optically pumped lasing in highly strained germanium nanowires,” *Nat. Commun.*, vol. 8, no. 1, pp. 1–7, 2017.
- [170] K. Guilloy *et al.*, “Tensile Strained Germanium Nanowires Measured by Photocurrent Spectroscopy and X-ray Microdiffraction,” *Nano Lett.*, vol. 15, no. 4, pp. 2429–2433, Apr. 2015.
- [171] A. Johannes, S. Noack, W. Wesch, M. Glaser, A. Lugstein, and C. Ronning, “Anomalous Plastic Deformation and Sputtering of Ion Irradiated Silicon Nanowires,” *Nano Lett.*, vol. 15, no. 6, pp. 3800–3807, 2015.
- [172] P. C. Millett, D. S. Aidhy, T. Desai, S. R. Phillpot, and D. Wolf, “Grain-boundary source/sink behavior for point defects: An atomistic simulation study,” *Int. J. Mater. Res.*, vol. 100, no. 4, pp. 550–555, Apr. 2009.
- [173] O. El-Atwani, J. E. Nathaniel, A. C. Leff, K. Hattar, and M. L. Taheri, “Direct Observation of Sink-Dependent Defect Evolution in Nanocrystalline Iron under Irradiation,” *Sci. Rep.*, vol. 7, no. 1, p. 1836, Dec. 2017.

- [174] O. El-Atwani *et al.*, “In-situ TEM observation of the response of ultrafine- and nanocrystalline-grained tungsten to extreme irradiation environments,” *Sci. Rep.*, vol. 4, pp. 4–10, 2014.
- [175] N. S. S. Rajput *et al.*, “Ion-beam-assisted fabrication and manipulation of metallic nanowires,” *Micro & Nano Lett.*, vol. 10, no. 7, pp. 334–338, 2015.
- [176] N. S. Rajput, A. Banerjee, and H. C. Verma, “Electron- and ion-beam-induced maneuvering of nanostructures: phenomenon and applications,” *Nanotechnology*, vol. 22, no. 48, p. 485302, Dec. 2011.
- [177] E. F. Pecora, A. Irrera, and F. Priolo, “Ion beam-induced bending of silicon nanowires,” *Phys. E Low-Dimensional Syst. Nanostructures*, vol. 44, no. 6, pp. 1074–1077, 2012.
- [178] M. Bettge *et al.*, “Ion-induced surface relaxation: controlled bending and alignment of nanowire arrays,” *Nanotechnology*, vol. 23, no. 17, p. 175302, May 2012.
- [179] S. K. Tripathi, N. Shukla, S. Dhamodaran, and V. N. Kulkarni, “Controlled manipulation of carbon nanopillars and cantilevers by focused ion beam,” *Nanotechnology*, vol. 19, no. 20, p. 205302, 2008.
- [180] A. Cui, W. Li, Q. Luo, Z. Liu, and C. Gu, “Controllable three dimensional deformation of platinum nanopillars by focused-ion-beam irradiation,” *Microelectron. Eng.*, vol. 98, pp. 409–413, 2012.
- [181] A. Cui *et al.*, “Ion-beam-induced bending of freestanding amorphous nanowires: The importance of the substrate material and charging,” *Appl. Phys. Lett.*, vol. 102, no. 21, pp. 1–6, 2013.
- [182] W. Y. Song *et al.*, “Bending of a Carbon Nanotube in Vacuum Using a Focused Ion

- Beam,” *Adv. Mater.*, vol. 18, no. 1, pp. 95–98, 2006.
- [183] T. I. Kamins, S. S. Williams, T. Hesjedal, and J. S. Harris, “Chemically vapor deposited Si nanowires nucleated by self-assembled Ti islands on patterned and unpatterned Si substrates,” *Phys. E Low-Dimensional Syst. Nanostructures*, vol. 13, no. 2–4, pp. 995–998, 2002.
- [184] E. F. Pecora, A. Irrera, S. Boninelli, L. Romano, C. Spinella, and F. Priolo, “Nanoscale amorphization, bending and recrystallization in silicon nanowires,” *Appl. Phys. A Mater. Sci. Process.*, vol. 102, no. 1, pp. 13–19, 2011.
- [185] and Y.-L. C. Kamins, Theodore I., “Method of aligning nanowires U.S. Patent No. 6,248,674,” 2001.
- [186] A. Hedler, S. L. Klaumünzer, and W. Wesch, “Amorphous silicon exhibits a glass transition,” *Nat. Mater.*, vol. 3, no. 11, pp. 804–809, 2004.
- [187] H. Trinkaus, “Dynamics of viscoelastic flow in ion tracks: Origin of plastic deformation of amorphous materials,” *Nucl. Instruments Methods Phys. Res. Sect. B Beam Interact. with Mater. Atoms*, vol. 146, no. 1–4, pp. 204–216, 1998.
- [188] G. Rizza *et al.*, “Saturation of the ion-hammering effect for large non-hydrostatic capillarity stresses in colloidal silica nanoparticles,” *Nanotechnology*, vol. 22, no. 47, 2011.
- [189] M. J. Smyth and M. W. L. Teng, “2018 Nobel Prize in physiology or medicine,” *Clin. Transl. Immunol.*, vol. 7, no. 10, pp. 2–5, 2018.
- [190] M. A. Tunes *et al.*, “Energetic particle irradiation study of TiN coatings: are these films appropriate for accident tolerant fuels?,” *J. Nucl. Mater.*, vol. 512, pp. 239–245, 2018.

- [191] T. D. Ladd, F. Jelezko, R. Laflamme, Y. Nakamura, C. Monroe, and J. L. O'Brien, "Quantum computers," *Nature*, vol. 464, no. 7285, pp. 45–53, Mar. 2010.
- [192] I. Newton, "Opticks: Isaac Newton's Theories of Light & Color," 1704.
- [193] E. Ruska, "The development of the electron microscope and of electron microscopy," *Rev. Mod. Phys.*, vol. 59, no. 3, pp. 627–638, Jul. 1987.
- [194] I. Falconer, "Corpuscles, Electrons and Cathode Rays: J.J. Thomson and the 'Discovery of the Electron,'" *Br. J. Hist. Sci.*, vol. 20, no. 3, p. 241, Jul. 1987.
- [195] J. J. Thomson, "XL. Cathode Rays," *London, Edinburgh, Dublin Philos. Mag. J. Sci.*, vol. 44, no. 269, pp. 293–316, Oct. 1897.
- [196] E. Paraskevopoulou and D. Koliopoulos, "Teaching the Nature of Science Through the Millikan-Ehrenhaft Dispute," *Sci. Educ.*, vol. 20, no. 10, pp. 943–960, 2011.
- [197] K. T. McDonald, "Birkeland, Darboux and Poincaré: Motion of an Electric Charge in the Field of a Magnetic Pole," *physics.princeton.edu*, vol. 8544, pp. 1–28, 2015.
- [198] P. Hawkes, "Recent advances in electron optics and electron microscopy," *Ann. la Fond. Louis Broglie*, vol. 29, no. SPEC. ISS. 1, pp. 837–855, 2004.
- [199] L. de Broglie, "La mécanique ondulatoire et la structure atomique de la matière et du rayonnement," *J. Phys. le Radium*, vol. 8, no. 5, pp. 225–241, 1927.
- [200] A. D. Tony Wilson, Martin Friedrich, "Basics of Light Microscopy & Imaging," *Imaging Microsc.*, pp. 1–4.
- [201] R. A. Schwarzer, "Emission electron microscopy - A review . Part 1 : Basic concepts and applications in physics," no. January 1981, 2015.
- [202] B. Fultz and J. Howe, *Transmission Electron Microscopy and Diffractometry of*

- Materials*. Berlin, Heidelberg: Springer Berlin Heidelberg, 2013.
- [203] D. B. William and B. C. Carter, *Transmission Electron Microscopy*. 2008.
- [204] E. Scientific, “Edge scientific.” [Online]. Available: <https://edgescientific.com/wp-content/uploads/2016/06/14-JL1208JEOL-K-Type-Base-Tungsten-Filaments-with-Metal-Ring-front.jpg>.
- [205] I. Kimball Physics, “LaB6HotCathode.” [Online]. Available: <https://commons.wikimedia.org/wiki/File:LaB6HotCat>.
- [206] Courtesy of Hat’nCoat, “2000px-Canon.” [Online]. Available: <https://commons.wikimedia.org/wiki/File:Canon.svg>. [Accessed: 22-Sep-2019].
- [207] B. Roth, H. H. T. A. Roth, Bill (Senior Applications Engineer, and B. Roth, “Advanced FE Applications Course,” *Hitachi*, 2009.
- [208] J. A. Hinks, J. A. van den Berg, and S. E. Donnelly, “MIAMI: Microscope and ion accelerator for materials investigations,” *J. Vac. Sci. Technol. A Vacuum, Surfaces, Film.*, vol. 29, no. 2, p. 21003, 2011.
- [209] E. Vacuum, “dd-vac-pump\_WS.” [Online]. Available: <https://vacaero.com/information-resources/vac-aero-training/180484-vacuum-systems-for-composite-manufacturing.html>. [Accessed: 12-Feb-2019].
- [210] Kkmurray, “Turbo\_pump\_schematic.” [Online]. Available: [https://commons.wikimedia.org/wiki/File:Turbo\\_pump\\_schematic.gif](https://commons.wikimedia.org/wiki/File:Turbo_pump_schematic.gif). [Accessed: 12-Feb-2019].
- [211] R. N. Clough, G. Moldovan, and A. I. Kirkland, “Direct detectors for electron microscopy,” *J. Phys. Conf. Ser.*, vol. 522, no. 1, 2014.

- [212] P. Date, “UC San Diego UC San Diego Electronic Theses and Dissertations Direct Electron Detection in Transmission Electron Microscopy,” 2009.
- [213] H. C. Shaw *et al.*, “Performance of Nanomaterials and Actively Running Nanocircuits During Heavy Ion Irradiation,” *12th NASA Symp. VLSI Des.*, 2005.
- [214] Gatan, “CCD.” [Online]. Available: <http://www.gatan.com/techniques/imaging>. [Accessed: 12-Feb-2019].
- [215] G. Jensen, “cryo-em-course-Caltech-University.” [Online]. Available: [internal-pdf://205.94.189.32/part\\_3\\_-\\_image\\_formation.pdf](internal-pdf://205.94.189.32/part_3_-_image_formation.pdf). [Accessed: 29-Mar-2019].
- [216] R. F. Egerton, “Electron energy-loss spectroscopy in the TEM,” *Reports Prog. Phys.*, vol. 72, no. 1, p. 16502, 2008.
- [217] R. . Egerton, “Electron Energy Loss Spectroscopy,” *Micron*, vol. 33, no. 7–8, p. 693, 2002.
- [218] Hat’nCoat, “Idealised EELS spectrum.” [Online]. Available: [https://commons.wikimedia.org/wiki/File:EELS\\_Idealised.svg](https://commons.wikimedia.org/wiki/File:EELS_Idealised.svg). [Accessed: 13-Feb-2019].
- [219] C. W. Lee, Y. Ikematsu, and D. Shindo, “Measurement of mean free paths for inelastic electron scattering of Si and SiO<sub>2</sub>,” *J. Electron Microsc. (Tokyo)*, vol. 51, no. 3, pp. 143–148, 2002.
- [220] C. Cayron, “TEM study of interfacial reactions and precipitation mechanisms in Al<sub>2</sub>O<sub>3</sub> short fiber or high volume fraction SiC particle reinforced Al-4Cu-1Mg-0.5Ag squeeze-cast composites,” *EMPA Act.*, no. 250, 2001.
- [221] R. W. Harrison, “On the use of ion beams to emulate the neutron irradiation behaviour of tungsten,” *Vacuum*, vol. 160, no. March 2018, pp. 355–370, 2019.

- [222] Y. Zhang *et al.*, “Ionization-induced annealing of pre-existing defects in silicon carbide,” *Nat. Commun.*, vol. 6, no. 1, p. 8049, Dec. 2015.
- [223] R. C. Birtcher, M. A. Kirk, K. Furuya, G. R. Lumpkin, and M. O. Ruault, “In situ transmission electron microscopy investigation of radiation effects,” *J. Mater. Res.*, vol. 20, no. 7, pp. 1654–1683, 2005.
- [224] C. F. Yu, D. S. Chao, H. S. Tsai, and J. H. Liang, “Influence of post-Annealing ambient gas on photoluminescence characteristics for ion beam synthesized Ge nanoparticles in SiO<sub>2</sub> and Si<sub>3</sub>N<sub>4</sub> films,” *Surf. Interface Anal.*, vol. 46, no. 12–13, pp. 1160–1164, 2014.
- [225] N. Kobayashi, M. Hasegawa, N. Hayashi, H. Tanoue, H. Shibata, and Y. Makita, “Ion-beam-induced epitaxial crystallisation of metastable Si<sub>1-x-y</sub>GexCy layers fabricated by Ge and C ion implantation,” *Nucl. Inst. Methods Phys. Res. B*, vol. 106, no. 1–4, pp. 289–293, 1995.
- [226] J. C. Kim, D. G. Cahill, R. S. Averback, C. Kim, D. G. Cahill, and S. Averback, “Formation and annihilation of nanocavities during keV ion irradiation of Ge,” *Phys. Rev. B*, vol. 68, no. 9, p. 94109, Sep. 2003.
- [227] J. A. Hinks, “Transmission electron microscopy with in situ ion irradiation,” *J. Mater. Res.*, vol. 30, no. 9, pp. 1214–1221, May 2015.
- [228] G. Greaves, A. H. H. Mir, R. W. W. Harrison, M. A. A. Tunes, S. E. E. Donnelly, and J. A. A. Hinks, “New Microscope and Ion Accelerators for Materials Investigations (MIAMI-2) system at the University of Huddersfield,” *Nucl. Instruments Methods Phys. Res. Sect. A Accel. Spectrometers, Detect. Assoc. Equip.*, vol. 931, no. March, pp. 37–43, 2019.

- [229] O. Lehtinen *et al.*, “Ion irradiation of multi-walled boron nitride nanotubes,” *Phys. Status Solidi Curr. Top. Solid State Phys.*, vol. 7, no. 3–4, pp. 1256–1259, 2010.
- [230] E. Vietzke, K. Flaskamp, M. Hennes, and V. Philipps, “The enhanced sputtering yield of graphite at elevated temperatures: The energy of the released carbon atoms,” *Nucl. Inst. Methods Phys. Res. B*, vol. 2, no. 1–3, pp. 617–622, 1984.
- [231] P. Sigmund, “Elements of Sputtering Theory,” *Nanofabrication by Ion-Beam Sputtering*, no. September 2016, pp. 1–40, 2012.
- [232] C. E. Carlston, G. D. Magnuson, A. Comeaux, and P. Mahadevan, “Effect of elevated temperatures on sputtering yields,” *Phys. Rev.*, vol. 138, no. 3A, pp. 3–7, 1965.
- [233] A. Oliva-Florio, R. A. Baragiola, M. M. Jakas, E. V. Alonso, and J. Fern, “Noble-gas ion sputtering yield of gold and copper: Dependence on the energy and angle of incidence of the projectiles,” *Phys. Rev. B*, vol. 35, no. 5, pp. 2198–2204, 1987.
- [234] M. P. Seah, “An accurate semi-empirical equation for sputtering yields, II: For neon, argon and xenon ions,” *Nucl. Instruments Methods Phys. Res. Sect. B Beam Interact. with Mater. Atoms*, vol. 229, no. 3–4, pp. 348–358, 2005.
- [235] I. Mica *et al.*, “Extended defect generation by Xenon implantation in silicon,” *AIP Conf. Proceedings. Vol. 1583. No. 1. AIP, 2014.*, vol. 68, no. January, pp. 64–68, 2014.
- [236] G. A. Slack and S. F. Bartram, “Thermal expansion of some diamondlike crystals,” *J. Appl. Phys.*, vol. 46, no. 1, pp. 89–98, 1975.
- [237] V. M. Glazov and A. S. Pashinkin, “Thermal expansion and heat capacity of GaAs and InAs,” *Inorg. Mater.*, vol. 36, no. 3, pp. 225–231, 2000.
- [238] F. C. Nix and D. MacNair, “The thermal expansion of pure metals: Copper, gold, aluminum, nickel, and iron,” *Phys. Rev.*, vol. 60, no. 8, pp. 597–605, 1941.

- [239] H. Ibach, "Thermal Expansion of Silicon and Zinc Oxide (II)," *Phys. Status Solidi*, vol. 33, no. 1, pp. 257–265, 1969.
- [240] M. Szymoński and R. S. Bhattacharya, "The sputtering of gallium arsenide at elevated temperatures," *Appl. Phys.*, vol. 20, no. 3, pp. 207–211, 1979.
- [241] T. Iwinski, E. P. Bernat, and P. L. Balise, "Theory of Beams The Application of the Laplace Transformation Method to Engineering Problems," *Phys. Today*, vol. 12, no. 7, Jul. 1959.
- [242] J. Liu *et al.*, "Tensile-strained, n-type Ge as a gain medium for monolithic laser integration on Si," *Opt. Express*, vol. 15, no. 18, p. 11272, 2007.
- [243] S. U. Campisano, S. Coffa, V. Raineri, F. Priolo, and E. Rimini, "Mechanisms of amorphization in ion implanted crystalline silicon," *Nucl. Inst. Methods Phys. Res. B*, vol. 80–81, no. PART 1, pp. 514–518, 1993.
- [244] L. M. Wang and R. C. Birtcher, "Amorphization, morphological instability and crystallization of Krypton ion irradiated germanium," *Philos. Mag. A Phys. Condens. Matter, Struct. Defects Mech. Prop.*, vol. 64, no. 6, pp. 1209–1223, 1991.
- [245] Y. Zhang and Y. Zhao, "Applicability range of Stoney's formula and modified formulas for a film/substrate bilayer," *J. Appl. Phys.*, vol. 99, no. 5, p. 53513, Mar. 2006.
- [246] M. J. Wenzel, F. Josse, and S. M. Heinrich, "Deflection of a viscoelastic cantilever under a uniform surface stress: Applications to static-mode microcantilever sensors undergoing adsorption," *J. Appl. Phys.*, vol. 105, no. 6, p. 64903, Mar. 2009.
- [247] S. Singamaneni *et al.*, "Bimaterial Microcantilevers as a Hybrid Sensing Platform," *Adv. Mater.*, vol. 20, no. 4, pp. 653–680, Feb. 2008.

- [248] G. G. Stoney, "The Tension of Metallic Films Deposited by Electrolysis," *Proc. R. Soc. A Math. Phys. Eng. Sci.*, vol. 82, no. 553, pp. 172–175, May 1909.
- [249] L. M. Wang and R. C. Birtcher, "Radiation-induced formation of cavities in amorphous germanium," *Appl. Phys. Lett.*, vol. 55, no. 24, pp. 2494–2496, 1989.
- [250] A. H. Mir *et al.*, "Understanding and simulating the material behavior during multi-particle irradiations," *Sci. Rep.*, vol. 6, no. 1, p. 30191, Sep. 2016.
- [251] N. V Medhekar, W. L. Chan, V. B. Shenoy, and E. Chason, "Stress-enhanced pattern formation on surfaces during low energy ion bombardment.," *J. physics. Condens. matter*, vol. 21, no. 22, p. 224021, 2009.
- [252] A. Moreno-Barrado *et al.*, "Nonuniversality due to inhomogeneous stress in semiconductor surface nanopatterning by low-energy ion-beam irradiation," *Phys. Rev. B - Condens. Matter Mater. Phys.*, vol. 91, no. 15, pp. 1–12, 2015.
- [253] P. C. Srivastava, V. Ganesan, and O. P. Sinha, "Evidence of plastic flow and recrystallization phenomena in swift ( $\sim 100$  MeV) Si<sup>7+</sup> ion irradiated silicon," *Nucl. Instruments Methods Phys. Res. Sect. B Beam Interact. with Mater. Atoms*, vol. 222, no. 3–4, pp. 491–496, 2004.
- [254] J. S. Williams *et al.*, "Preferential amorphization and defect annihilation at nanocavities in silicon during ion irradiation," *Appl. Phys. Lett.*, vol. 77, no. 26, pp. 4280–4282, 2000.
- [255] A. A. Lomov, A. V. Myakon'kikh, A. P. Oreshko, and A. A. Shemukhin, "Study of the amorphization of surface silicon layers implanted by low-energy helium ions," *Crystallogr. Reports*, vol. 61, no. 2, pp. 173–180, 2016.
- [256] F. Priolo, T. Gregorkiewicz, M. Galli, and T. F. Krauss, "Silicon nanostructures for

- photonics and photovoltaics,” *Nat. Nanotechnol.*, vol. 9, no. 1, pp. 19–32, 2014.
- [257] K. J. Kirkby and R. P. Webb, “Ion Implanted Nanostructures,” *Encyclopedia*, vol. 4, pp. 1–11, 2004.
- [258] G. I. S. M. M. G. Grimaldi, “Ion implantation damage and crystalline- amorphous transition in Ge Ion implantation damage and crystalline-amorphous transition,” no. May 2014, 2011.
- [259] D. J. Frank, R. H. Dennard, E. Nowak, P. M. Solomon, Y. Taur, and H. S. P. Wong, “Device scaling limits of Si MOSFETs and their application dependencies,” *Proc. IEEE*, vol. 89, no. 3, pp. 259–287, 2001.
- [260] A. Rivera, J. Olivares, M. L. L. Crespillo, G. García, M. Bianconi, and F. Agulló-López, “Assessment of swift-ion damage by RBS/C: Determination of the amorphization threshold,” *Nucl. Instruments Methods Phys. Res. Sect. B Beam Interact. with Mater. Atoms*, vol. 267, no. 8–9, pp. 1460–1463, May 2009.
- [261] Gatan, “DigitalMicrograph 3.4 User’s Guide,” *Gatan Guid.*, vol. 123, no. 6, pp. 407–408, Jun. 2011.
- [262] C. A. Schneider, W. S. Rasband, K. W. Eliceiri, and C. Instrumentation, “NIH Image to ImageJ: 25 years of image analysis,” *Nat. Methods*, vol. 9, no. 7, pp. 671–675, 2012.
- [263] A. Rivera, J. Olivares, M. L. Crespillo, G. García, M. Bianconi, and F. Agulló-lópez, “Nuclear Instruments and Methods in Physics Research B Assessment of swift-ion damage by RBS / C : Determination of the amorphization threshold,” *Nucl. Inst. Methods Phys. Res. B*, vol. 267, no. 8–9, pp. 1460–1463, 2009.
- [264] W. P. Maszara and G. A. Rozgonyi, “Kinetics of damage production in silicon during self-implantation,” *J. Appl. Phys.*, vol. 60, no. 7, pp. 2310–2315, Oct. 1986.

- [265] S. O. Kucheyev *et al.*, “Effect of ion species on the accumulation of ion-beam damage in GaN,” *Phys. Rev. B*, vol. 64, no. 3, pp. 1–10, 2002.
- [266] H. H. Andersen and H. L. Bay, “Heavy-ion sputtering yields of gold: Further evidence of nonlinear effects,” *J. Appl. Phys.*, vol. 46, no. 6, pp. 2416–2422, Jun. 1975.
- [267] R. E. Stoller, M. B. Toloczko, G. S. Was, A. G. Certain, S. Dwaraknath, and F. A. Garner, “On the use of SRIM for computing radiation damage exposure,” *Nucl. Instruments Methods Phys. Res. Sect. B Beam Interact. with Mater. Atoms*, vol. 310, pp. 75–80, 2013.

## Appendix

As with the germanium nanowires, single crystalline silicon nanowires were irradiated at elevated temperatures to induce bending whilst preserving their single crystalline characters. The nanowires, which, were also deposited onto a molybdenum grid via the method described in chapter 3 had lengths ranging from 300 nm to 5  $\mu\text{m}$  and diameters from 30 nm to 70 nm. For these experiments the irradiation condition were slightly different as the nanowires were irradiated with 40 keV xenon ions, with a flux of  $4.8 \times 10^{12}$  ions. $\text{cm}^{-2}.\text{s}^{-1}$  at a temperature of  $500^\circ\text{C}$ . Figure A.1 shows a superimposition of images of a silicon nanowire during irradiation and the SADP of the nanowire before and after irradiation. It is, thus observed that the nanowire has bent and remained single crystalline as evidenced by the inset SADP.

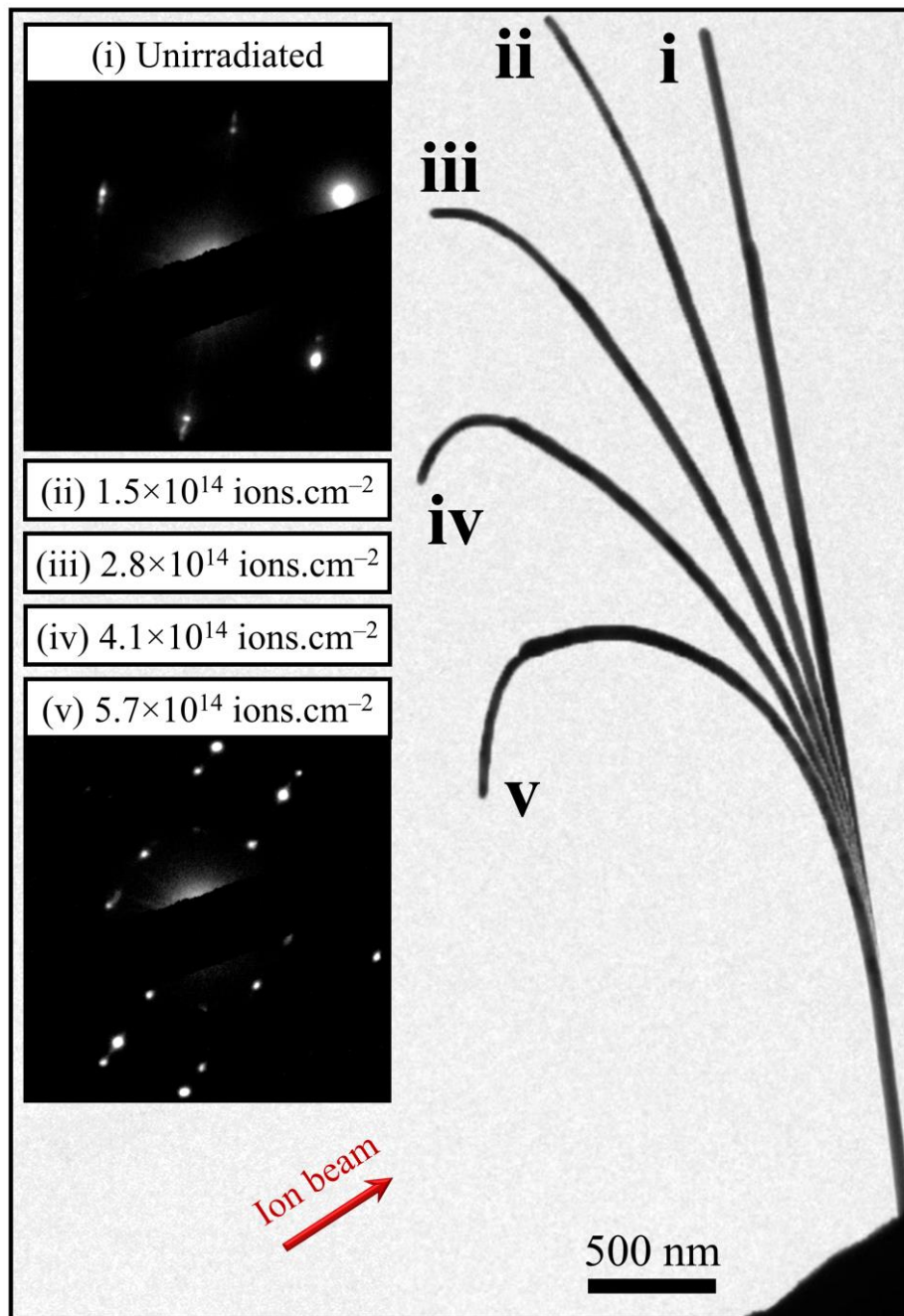


**Figure A.1:** Superimposition of BF-TEM images captured from a video during 40 keV xenon ion irradiation in situ in the TEM inducing the bending of the silicon nanowires at 500°C. The SADPs before irradiation and after irradiation are shown to illustrate the single crystalline character of the nanowire after bending.